

A sedimentological and geochemical study of the uranium mineralization at Rietkuil Mine, Beaufort West, Karoo Basin

By

MONIQUE MAREE

Thesis submitted in fulfillment of the requirements for the degree of

MASTERS OF SCIENCE

In the Faculty of Natural and Agricultural Science

Department of Geology

University of the Free State

Bloemfontein

South Africa

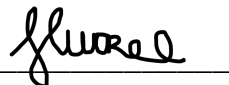
2020

SUPERVISOR: Mrs. J. Magson

CO-SUPERVISOR: Dr. L. Nel

Declaration

I, Monique Maree, declare that this dissertation is my own unaided work. The substance has not been submitted for any degree or examination in any other university in the past. All the sources I have used or quoted have been obtained by me, while I was a student at the University of the Free State, and have been indicated and acknowledged by complete reference.



Monique Maree

03/03/2020

Date

Acknowledgments

I would like to thank the National Research Fund (NRF) for making funds available for this project, without which this project would not have been able.

I thank the following staff from the Department of Geology, University of the Free State:

- First and foremost, I would like to thank my supervisors, Mrs. J. Magson and Dr. L. Nel for their guidance and insights that made an enormous impact on the outcome of this study.
- A.I. Odendaal for spending valuable time and effort in guiding me with the compilation of maps and sections in this thesis.
- J.C. Looock for sharing his vast knowledge of the Karoo and attributing valuable resources regarding uranium mineralization in the Karoo, that was used in this thesis.
- M. Welman-Purchase and laboratory staff for assisting with sample preparation and analytical procedures and making sure that the instruments are always calibrated.

I would also like to thank, Christel Tinguely, from the Department of Geology, University of Cape Town for assisting me in sample preparation and analysis for ICP-MS.

George van der Walt and team, at Peninsula Energy Limited, Beaufort West, for aiding in sample collection at Rietkuil Mine, and allowing me to conduct my research.

I would like to give a big thanks to Linda and Christy Mocke for their generosity and hospitality. They truly became a parental unit for me while I was conducting fieldwork in Beaufort West.

My dear family and friends who gave me much needed moral support and motivation to finish this dissertation.

Abstract

Despite a vast amount of research conducted on the Karoo Uranium Province there is no clear definitive model for the uranium mineralization. This thesis aims to create a mineralization model for the uranium deposit at Rietkuil mine making use of detailed field mapping and geochemical analyses. This information can possibly contribute to a revised uranium mineralization model for the Karoo Uranium Province.

The sediments from Rietkuil mine forms part of the Abrahamskraal Subgroup in the lower Beaufort Group (Late Permian age). It hosts uranium mineralization in horizontally bedded, very fine to fine-grained sandstone with a moderate sorting. Clay pellet conglomerate, cross-bedded sandstone, horizontally bedded sandstone, ripple cross-bedded sandstone, massive sandstone, parallel laminated siltstone and mudstone, massive mudstone, and mudstone with ball-and-pillow structures were the eight lithofacies identified at the study location. With the aid of petrographic and XRF data, the sandstone was classified as lithic-wacke and lithic-arenite.

The distribution of the carbonaceous matter was strongly controlled by lithology. Fieldwork revealed that the carbon was strongly associated with horizontally bedded units. LECO analysis (total carbon), Mebius titrations (organic carbon) and field observations show that there was a decrease in the amount of carbon upwards in the lithology.

Field and petrographic observations produced evidence of a Ca-rich hydrothermal fluid that intruded into the wacke. The porosity of the wacke was increased by tectonic features (joints, folds, and faults), lithological features (thin horizontally bedded layers, and interfingering sandstone lenses), mineralogical features (solution seams, absorption by a muddy matrix, and adsorption onto carbonaceous matter). These factors controlled the distribution of the uranium mineralization.

The geochemical data obtained from Rietkuil mine was evaluated by using Pearson's correlation coefficients indicating elemental relationships of identified minerals. It revealed strong positive relationships between elements hosted in detrital minerals as well as elements hosted in hydrothermal minerals. The elements of the two mineral parameters though show strong negative correlations with each other. Strong positive relationships between pyrite and organic carbon were observed. Uranium showed strong positive correlations with CaO (inorganic carbon). The uranium mineralization was confined to zones with high amounts of carbon. This indicated that the carbon and pyrite produced a suitable environment for the precipitation of uranium minerals.

Evidence suggests that the uranium mineralization at Rietkuil mine was a secondary uranium deposit. The uranium sourced from eroded granitic material and tuff deposits contained in underlying sedimentary rocks. XRD analysis revealed that the uranium occurred in the U^{+6} oxidation state thus being transported as uranyl complexes with ions like SO_4^{-2} , PO_4^{-2} , VO_4^{-2} , and AsO_4^{-2} by a Ca-rich low-temperature hydrothermal fluid. The joints were the feeder mechanism for the transportation of fluids. When these

fluids encounter the reduced environment produced by the carbon, uranium and sulfide minerals precipitated from the solution.

Table of Contents

Declaration	i
Acknowledgments	ii
Abstract	iii
List of Figures.....	viii
List of Tables.....	xii
List of Abbreviations	xiv

Chapter 1: Introduction..... 1

1.1 Geology of the Karoo Supergroup.....	1
1.1.1 <i>Development of the Main Karoo Basin</i>	1
1.1.2 <i>Stratigraphy of the Main Karoo Basin</i>	4
1.2 Uranium	7
1.2.1 <i>Uranium chemistry</i>	7
1.2.2 <i>Mobilization and deposition of uranium in aqueous systems</i>	7
1.2.3 <i>Sandstone-hosted uranium deposits</i>	9
1.2.4 <i>Karoo Uranium Province</i>	9
1.3 The aim and objectives of the study	12

Chapter 2: Materials and methods..... 13

2.1 Fieldwork at Rietkuil opencast mine	13
2.2 Sample preparation	14
2.2.1 <i>Thin section preparation</i>	14
2.2.2 <i>Preparation of samples for XRD</i>	14
2.2.3 <i>Preparation of samples for XRF</i>	14
2.2.4 <i>Preparation of samples for ICP-MS</i>	15
2.2.5 <i>Preparation of samples for LECO analyzer</i>	15
2.3 Analytical procedures	20
2.3.1 <i>Petrography</i>	20
2.3.2 <i>XRD</i>	20
2.3.3 <i>XRF</i>	21
2.3.4 <i>ICP-MS</i>	21
2.3.5 <i>LECO analyzer</i>	23

2.3.6	<i>Mebius method for titration of organic carbon</i>	23
Chapter 3: Results		25
3.1	Rietkuil opencast mine	25
3.1.1	<i>Geological map of Rietkuil area</i>	25
3.1.2	<i>Rietkuil mine</i>	27
3.1.3	<i>Lithology and lithofacies</i>	27
3.1.4	<i>Tectonic features</i>	50
3.1.5	<i>Uranium distribution (Gamma-Ray)</i>	57
3.1.6	<i>Carbon distribution</i>	63
3.2	Petrography.....	69
3.2.1	<i>Petrographic description</i>	69
3.3	Geochemical analysis	74
3.3.1	<i>XRD analysis</i>	74
3.3.2	<i>XRF analysis</i>	75
3.3.3	<i>ICP-MS analysis</i>	81
3.3.4	<i>Carbon analysis</i>	81
Chapter 4: Discussion		83
4.1	Mineralogy and whole-rock geochemistry	83
4.2	Controls on the uranium distribution.....	84
4.2.1	<i>Host sandstone</i>	85
4.2.2	<i>Porosity and hydrothermal fluid intrusion</i>	86
4.2.3	<i>Reductants</i>	87
4.3	Uranium mineralogy and geochemistry	88
4.4	Genetic uranium mineralization model for Rietkuil mine	88
Chapter 5: Conclusions		91
5.1	Conclusions.....	91
5.2	Suggestions for further study	93
References		94

Appendices:

Appendix A	99
A1 Analysis conducted on samples	99
A2 Petrography.....	100
 Appendix B	 101
B1 XRD	101
 Appendix C	 120
C1 XRF	120
 Appendix D	 122
D1 ICP-MS	122
 Appendix E	 123
E1 LECO analyzer.....	123
E2 Mebius titration method.....	124
 Appendix F	 126
 Appendix G	 128

List of Figures

Chapter 1

- Figure 1.1:** Represent the geological age of the generalized stratigraphy of the Karoo Basin (from the south to the northeast) along with time gaps in deposition. The tectonic evolution of the Karoo Basin is represented in the tectonic setting. The black and red bar, represents periods of tectonic pulses (black) and crustal relaxation (red) during the formation of the Cape Fold Belt with the onset of subduction (tectonic pulse) of the paleo-Pacific plate. The image was modified after Catuneanu, et al. (1998)..... 3
- Figure 1.2:** Represents the generalized stratigraphy of the western, eastern and northern Beaufort Group. It illustrates the geological age of the Beaufort Group, subgroups, formations, and members. It also shows hiatus (grey), sandstone-rich units (yellow) and the Rietkuil study area (red). The image was modified after Hancox & Rubidge (2001). 5
- Figure 1.3:** Represents the position of the Beaufort Group, the extent of the Karoo Uranium Province and the location of Rietkuil study area in South Africa. Within the Karoo Uranium Province known trail mining sites is also indicated in dotted-lines. The image was modified after Xu, *et al.* (2012)..... 9

Chapter 2

- Figure 2.1:** Represents the sample collection of Face 1 and 2 of the lower bench at Rietkuil mine. The sample number is displayed along with its positions. The red stars represent samples used for petrography and the yellow stars represents samples used for ICP-MS analysis..... 16
- Figure 2.2:** Represents the sample collection of Face 3 and 4 of the lower bench at Rietkuil mine. The sample name is displayed along with its positions. The red stars represent samples used for petrography and the yellow stars represents samples used for ICP-MS analysis..... 17
- Figure 2.3:** Represents the sample collection of Face 1 and 2 of the upper bench at Rietkuil mine. The sample name is displayed along with its positions. The red stars represent samples used for petrography and the yellow stars represents samples used for ICP-MS analysis..... 18
- Figure 2.4:** Represents the sample collection of Face 3 and 4 of the upper bench at Rietkuil mine. The sample number is displayed along with its positions. No petrography or ICP-MS analysis was conducted on these faces..... 19

Chapter 3

Figure 3.1: Mapped lithologies, tectonic structures, measured dips and flow directions at Rietkuil mine.....	26
Figure 3.2: Plan view of Rietkuil mine identifying the main faces and benches used in this thesis. The blue, green and red lines is a schematic representation of the major strikes of joints present in the area. The blue joints strike 88°; the green joints strike 168°; and the red joints strike 133°. The black arrow indicates the ramp into the mine.	27
Figure 3.3: Summary of the lithological features and lithofacies assemblage in the lower bench on Face 1, Profile 1 (see, Figure 3.11). HB = Horizontally Bedded.....	34
Figure 3.4: Summary of the lithological features and lithofacies assemblage in the upper bench on Face 1, Profile 1 (refer, Figure 3.12).....	35
Figure 3.5: Summary of the lithological features and lithofacies assemblage in the lower bench on Face 2, Profile 3 (refer, Figure 3.13). HB = Horizontally Bedded. ...	36
Figure 3.6: Summary of the lithological features and lithofacies assemblage in the upper bench on Face 2, Profile 1 (refer, Figure 3.14).....	37
Figure 3.7: Summary of the lithological features and lithofacies assemblage in the lower bench on Face 3, Profile 1 (refer, Figure 3.15). HB = Horizontally Bedded. ...	38
Figure 3.8: Summary of the lithological features and lithofacies assemblage in the upper bench on Face 3, Profile 1 (refer, Figure 3.16). HB = Horizontally Bedded....	39
Figure 3.9: Summary of the lithological features and lithofacies assemblage in the lower bench on Face 4, Profile 1 (refer, Figure 3.17). HB = Horizontally Bedded. ...	40
Figure 3.10: Summary of the lithological features and lithofacies assemblage in the upper bench on Face 4, Profile 1 (refer, Figure 3.18).....	41
Figure 3.11: Face 1 Lower Bench orientated WNW-ESE, as seen in the plan view. A) The extent of lithological units in Face 1. B) The extent of the lithofacies assemblage in Face 1. C) The two detailed profiles drawn displaying lithology, lithofacies, grain size, and sedimentary structures.....	42
Figure 3.12: Face 1 Upper Bench orientated WNW-ESE, as seen in the plan view. A) The extent of lithological units in Face 1. B) The extent of the lithofacies assemblage in Face 1. C) The three detailed profiles drawn displaying lithology, lithofacies, grain size, and sedimentary structures.....	43
Figure 3.13: Face 2 Lower Bench orientated NNE-SSW, as seen in the plan view. A) The extent of lithological units in Face 1. B) The extent of the lithofacies assemblage in Face 1. C) The three detailed profiles drawn displaying lithology, lithofacies, grain size, and sedimentary structures.....	44
Figure 3.14: Face 2 Upper Bench orientated NNE-SSW, as seen in the plan view. A) The extent of lithological units in Face 1. B) The extent of the lithofacies assemblage in Face 1. C) The three detailed profiles drawn displaying lithology, lithofacies, grain size, and sedimentary structures.....	45
Figure 3.15: Face 3 Lower Bench orientated ESE-WNW, as seen in the plan view. A) The extent of lithological units in Face 1. B) The extent of the lithofacies assemblage in Face 1. C) The three detailed profiles drawn displaying lithology, lithofacies, grain size, and sedimentary structures.....	46
Figure 3.16: Face 3 Upper Bench orientated ESE-WNW, as seen in the plan view. A) The extent of lithological units in Face 1. B) The extent of the lithofacies assemblage	

in Face 1. C) The three detailed profiles drawn displaying lithology, lithofacies, grain size, and sedimentary structures.....	47
Figure 3.17: Face 4 Lower Bench orientated SSW-NNE, as seen in the plan view. A) The extent of lithological units in Face 1. B) The extent of the lithofacies assemblage in Face 1. C) The two detailed profiles drawn displaying lithology, lithofacies, grain size, and sedimentary structures.....	48
Figure 3.18: Face 4 Upper Bench orientated SSW-NNE, as seen in the plan view. A) The extent of lithological units in Face 1. B) The extent of the lithofacies assemblage in Face 1. C) The three detailed profiles drawn displaying lithology, lithofacies, grain size, and sedimentary structures.....	49
Figure 3.19: A) The arrow shows calcite mineralization in a joint. B) The arrows show sandstone with low-grade metamorphic halo adjacent to joint structures and calcite mineralization on a joint plane. C) The arrows show low-grade metamorphic halo between horizontally bedded sandstone layers adjacent to a joint.....	50
Figure 3.20: Face 1 Lower Bench Joints. A) Photo-panorama of Face 1, with the sandstone outline and the uppermost contact of the bench. B) The position of the joints on Face 1, with the strikes coordinated by color. Calcite veins are indicated with a blue circle. C) The number of each joint strike counted in 5 m intervals.	53
Figure 3.21: Face 2 Lower Bench Joints. A) Photo-panorama of Face 2, with the sandstone outline and the uppermost contact of the bench. B) The position of the joints on Face 2, with the strikes coordinated by color. Calcite veins are indicated with a blue circle. C) The number of each joint strike counted in 5 m intervals.	54
Figure 3.22: Face 3 Lower Bench Joints. A) Photo-panorama of Face 3, with the sandstone outline and the uppermost contact of the bench. B) The position of the joints on Face 3, with the strikes coordinated by color. Calcite veins are indicated with a blue circle. C) The number of each joint strike counted in 5 m intervals.	55
Figure 3.23: Face 4 Lower Bench Joints. A) Photo-panorama of Face 4, with the sandstone outline and the uppermost contact of the bench. B) The position of the joints on Face 4, with the strikes coordinated by color. Calcite veins are indicated with a blue circle. C) The number of each joint strike counted in 5 m intervals.	56
Figure 3.24: The uranium distribution in Face 1 Lower Bench. A) A photo-panorama of Face 1 with uranium distribution contour lines, sample collection localities, and XRF uranium results. B) A Gamma-Ray contour map of the uranium distribution in Face 1, with the highest readings to center of more than 2000 cps.	59
Figure 3.25: The uranium distribution in Face 2 Lower Bench. A) A photo-panorama of Face 2 with uranium distribution contour lines, sample collection localities, and XRF uranium results. B) A Gamma-Ray contour map of the uranium distribution in Face 2, with the two hot-spots of more than 2000 cps.	60
Figure 3.26: The uranium distribution in Face 3 Lower Bench. A) A photo-panorama of Face 3 with uranium distribution contour lines, sample collection localities, and XRF uranium results. B) A Gamma-Ray contour map of the uranium distribution in Face 3, with the a single hot-spot of more than 3000 cps.	61
Figure 3.27: The uranium distribution in Face 4 Lower Bench. A) A photo-panorama of Face 4 with uranium distribution contour lines, sample collection localities, and XRF uranium results. B) A Gamma-Ray contour map of the uranium distribution in Face 4, with multiple hot-spots to the base of the face of more than 3000 cps.	62

Figure 3.28: The 5 fractions the carbon was classified as. 1) The carbon is finely distributed throughout the sandstone. 2) The carbon is confined to laminae. 3) The carbon is confined to bedding planes. 4) The carbon is highly dispersed. 5) Carbon occurs as coaly fragments.....	63
Figure 3.29: The carbon distribution in Face 1 Lower Bench. A) A photo-panorama of Face 1 with carbon distribution, sample collection localities, and carbon concentrations measured by the LECO Analyzer. B) Carbon distribution in Face 1.....	65
Figure 3.30: The carbon distribution in Face 2 Lower Bench. A) A photo-panorama of Face 2 with carbon distribution, sample collection localities, and carbon concentrations measured by the LECO Analyzer. B) Carbon distribution in Face 2.....	66
Figure 3.31: The carbon distribution in Face 3 Lower Bench. A) A photo-panorama of Face 3 with carbon distribution, sample collection localities, and carbon concentrations measured by the LECO Analyzer. B) Carbon distribution in Face 3.....	67
Figure 3.32: The carbon distribution in Face 4 Lower Bench. A) A photo-panorama of Face 4 with carbon distribution, sample collection localities, and carbon concentrations measured by the LECO Analyzer. B) Carbon distribution in Face 4.....	68
Figure 3.33: Plain polarized light petrographic images (4X magnification). A) Typical internal grading some of the samples exhibit. B) Fractures with opaque minerals...	69
Figure 3.34: Petrology of the sandstone at Rietkuil mine. A) Minerals: Q= quartz, P-Fsp= plagioclase, Musc= muscovite and sericite. B) Vesicles in a quartz grain and sericite. C) Disseminated carbon plebs. D) Fe-ox= iron-oxide in the matrix and adjacent to grain (carbon and quartz) boundaries, siltstone clasts and deformed plant fragment. E) Lithic fragments of chert- and carbonate clasts. F) Iron-oxide and coaly seams of carbon.....	71
Figure 3.35: Ore petrography of sandstone samples from Rietkuil mine. For each slide A-D, the left image is under transmitted light and the right image under reflective light. A) Photomicrographs of ore minerals adsorbed on coal-like seams or precipitated in solution seams. B) Photomicrographs of ore minerals in the matrix and around mineral grains. C) Photomicrographs of coal-like seam with adsorbed ore minerals. D) Photomicrographs of ore mineralization around grains and in matrix.....	72
Figure 3.36: A) Sandstone classification by Dott (1964) applied to the selected sandstone samples from Rietkuil mine. B) Provenance classification by Dickenson (1983) applied to the selected sandstone samples from Rietkuil mine.....	73
Figure 3.37: Sandstone classification by Harron (1988) for the sandstone samples at Rietkuil mine.....	77
Figure 3.38: Sandstone provenance classification by Bhatai (1983) for the sandstone samples at Rietkuil mine.	78
Figure 3.39: Correlation between uranium measured by the ICP-MS Vs XRF in ppm.	81

Chapter 5

Figure 5.1: Proposed genetic uranium mineralization model for Rietkuil mine.....	92
---	----

List of Tables

Chapter 2

Table 2.1: Specifications of the microscope used at the University of the Free State. Reflected and transmitted light was used to identify different mineral phases in the samples along with a description of the relationship between the minerals.	20
Table 2.2: Specifications of the X-Ray diffraction spectrometer at the University of the Free State.	21
Table 2.3: Specifications of the X-Ray fluorescence spectrometer at the University of the Free State.	22
Table 2.4: Specifications of the induced coupled plasma mass spectrometer at the University of Cape Town.	22
Table 2.5: Specifications of the LECO analyzer at the University of the Free State, Department of Soil Science.	23
Table 2.6: Specifications of the automatic titrator and electrode at the University of the Free State, Department of Soil Science.	24

Chapter 3

Table 3.1: Lithofacies identified at Rietkuil mine. Compiled from basic principles of Ghazi and Mountney (2009), and Miall (1988) and applied to Rietkuil mine. (The table is displayed over the next three pages, pg 31-33).....	30
Table 3.2: Summary of the total number of joints in each face in the lower bench separated into 5 m intervals. The blue blocks indicated intervals with calcite vein filling.	52
Table 3.3: The estimated modal mineralogical composition for 17 sandstone samples from at Rietkuil mine.....	69
Table 3.4: The minerals that were identified during the XRD analysis of the 36 selected sandstone samples, with their chemical formulae.	74
Table 3.5: The average major element oxide (%) in sandstone samples from Rietkuil mine measured with the XRF.	76
Table 3.6: Pearson correlation coefficient matrix of the major element oxides and trace element uranium. Positive correlations are marked in green and negative correlations are marked in red. The black values were considered as weak correlations.....	76
Table 3.7: The average trace element (ppm) in sandstone samples from Rietkuil mine measured with the XRF.....	80
Table 3.8: Pearson correlation coefficient matrix of the trace elements. Positive correlations are marked in green and negative correlations are marked in red. The black values were considered as weak correlations.....	80
Table 3.9: The average total carbon (%TC) and organic carbon (%OC) in sandstone samples from Rietkuil mine measured with the LECO analyzer and the Mebius titration method, respectively.	82

Table 3.10: Pearson correlation coefficient matrix of the trace element uranium, total carbon (TC), organic carbon (OC), and major elements oxides Ca and Fe. Positive correlations are marked in green. Negative correlations are marked in red. The black values were considered as weak correlations. 82

List of Abbreviations

Analytical abbreviations

CPL	cross-polarized light
GPS	global positioning system
ICP-MS	induced coupled plasma mass spectrometry
PPL	plain polarized light
XRD	X-ray diffracted spectrometry
XRF	X-ray fluoresce spectrometry

Measurement abbreviations

c	coarse
cps	count per second
f	fine
m	medium
ppm	parts per million
vf	very fine
wt%	weight percentage

Lithofacies abbreviations

Gm	clay pellet conglomerate
St	cross-bedded sandstone
Sh	horizontally bedded sandstone
Sr	ripple cross-bedded sandstone
Sm	massive sandstone
Fl	parallel laminated siltstone and mudstone
Fm	massive mudstone
Fs	massive mudstone with ball-and-pillow structures

Mineral abbreviations

Fe-ox	iron-oxide
IC	inorganic carbon
Musc	muscovite
OC	organic carbon
P-Fsp	plagioclase feldspar
Q	quartz
TC	total carbon

Direction abbreviations

N	north
E	east
S	south
W	west

Chapter 1: Introduction

1.1 Geology of the Karoo Supergroup

The Karoo Supergroup is a 2 to 3 km thick accumulation of sediments that are capped with volcanic deposits (Lindeque, *et al.*, 2011 and Johnson, *et al.*, 2006). These deposits formed from the Late Carboniferous to Middle Jurassic (Johnson, *et al.*, 2006). The Karoo Supergroup is a series of basin deposits, of which the Main Karoo Basin is the largest. Other smaller basins include the Springbok Flats, Ellisras Basin, Tshipise Basin, Tuli Basin, Botswana Basin (Kalahari Basin), Aranos Basin, and the Karasburg Basin (Johnson, *et al.*, 2006).

The Main Karoo Basin is referred to as a retro-arc foreland basin (Johnson, *et al.*, 2006), that formed due to the northward subduction of the paleo-Pacific oceanic plate underneath the paleo-continent Gondwana (Tankard, *et al.*, 2009). The geometry of the basin is a thick, wedge-shaped successions that thins towards the north. It consists of flysch-molasse deposits (Tankard, *et al.*, 2009).

The Main Karoo Basin is subdivided into five groups (Figure 1.1), from oldest to the youngest; the Dwyka Group, Eccra Group, Beaufort Group, Stormberg Group and lastly the Drakensberg Group which mostly consists of basaltic lava deposits (Johnson, *et al.*, 2006).

1.1.1 Development of the Main Karoo Basin

It is important for this study to understand the tectonic development of the Cape-Karoo Basin (located in the southwest of Gondwana) as this may resolve questions regarding the source of the uranium and structures that occur in the study area.

Visser (1992) described the basin tectonics to the southwest of Gondwana that led to the formation of the Cape Fold Belt. Hancox & Rubidge (1997) studied the role that fossils had in interpreting the development of the Karoo Basin to enhance the paleo-environmental reconstructions. Catuneanu, Hancox, and Rubidge (1998) constructed a basin development model for the Karoo retro-arc foreland system. Tankard, *et al.* (2009) conducted an in-depth study on the Cape-Karoo basin formation and constructed a tectonic development model thereof.

In brief, as described by Visser (1992), the Cape Supergroup (Figure 1.1) was deposited in the Cape Basin, located to the southwest of Gondwana. The Cape Basin sediments were deposited on a semi-stable, passive margin trending northward. Deposition in the Cape Basin occurred from the Devonian and ended in the Middle Carboniferous. It comprises a thick accumulation of beach, shallow marine and deltaic sediments, with mud deposits on the basin floor and along the continental slope. The thick succession of sediments led to the thinning and weakening of the crust, resulting in an extensional setting of the passive margin (Visser, 1992; and Tankard *et al.*, 2009). Visser (1992) research revealed a global sea-level regression during the Middle Carboniferous that terminated the shelf deposits of the Cape Supergroup.

Simultaneously, southwest Gondwana experienced an increase in oceanic plate movement, leading to the northward subduction of the paleo-Pacific plate, underneath Gondwana (Visser, 1992). This was followed by a hiatus, with regional uplift and erosion (Visser, 1992; and Tankard, *et al.*, 2009). The Main Karoo Basin sediments were deposited over the Cape Basin deposits (Lindeque, *et al.*, 2011).

The Main Karoo Basin first started to deposit sediments with the onset of glaciation during the Late Carboniferous. The initiation of subduction of the paleo-Pacific plate led to the development of a magmatic-arc with a large back-arc basin, wherein deposition of the Main Karoo Basin occurred (Tankard, *et al.*, 2009).

Visser (1992) explains that the glacial deposits from the Dwyka Group led to an isostatic depression in the back-arc basin due to the weight of the ice sheet. This resulted in the subsidence, thinning and thermal weakening of the back-arc basin crust. In turn, this caused an unstable marine ice sheet which increased sedimentation into the back-arc basin. During the Early Permian, the Karoo Basin experienced compression, as the paleo-Pacific plate continued to subduct, causing an increase in the subsidence in the back-arc basin, along with the collapse of the final ice sheets.

The Dwyka Group style of subsidence continued with the deposition of Ecca Group deposits (Tankard, *et al.*, 2009). The main sediments are basal mud and shale deposits, turbidite fan deposits and deltaic sedimentation, at the top (Tankard, *et al.*, 2009). During the deposition of the Ecca Group, the continued pulsating subduction of the paleo-Pacific plate resulted in a rising inner-arc in the western margin of Gondwana, transforming the basin into a foreland basin (Visser, 1992). Along with the development of the inner-arc, there was an increase in metamorphism associated with intrusive and extrusive magmatic activity and the development of a second sediment source area into the Main Karoo Basin, the northern highlands (Visser, 1992; and Kingsley, 1981). At the end of the Permian, the basin was completely closed, with predominantly fluvial style depositions (Visser, 1992).

According to Tankard, *et al.* (2009), the Late Permian Beaufort Group had a change in deposition style where fluvial-lacustrine successions were deposited into the Main Karoo Basin. During the deposition of the upper Beaufort Group of Triassic, the locus of subsidence moved eastwards in the Main Karoo Basin as major uplift in the southwestern part of Gondwana occurred due to the subduction of the paleo-Pacific plate leading to the shrinking of the Main Karoo Basin (Catuneanu, *et al.*, 1998; and Vigliettie, *et al.*, 2017). This event completed the formation of the Cape Fold Belt (Cape orogeny) in the southern part of the Main Karoo Basin. This event transformed the Main Karoo Basin into a retro-arc foreland basin. It gradually transformed the upper Beaufort Groups' depositional environment from braided stream deposits to meandering stream deposits although both low and high sinuosity in both lower and upper Beaufort.

The Stormberg Group sediments were deposited during fluvial-aeolian events as the climate progressively increased to more dry and arid conditions, as Gondwana drifted away from the South Pole towards the equator (Johnson, *et al.*, 2006). The deposition center was formed by fault-controlled subsidence due to the weight of the sediments

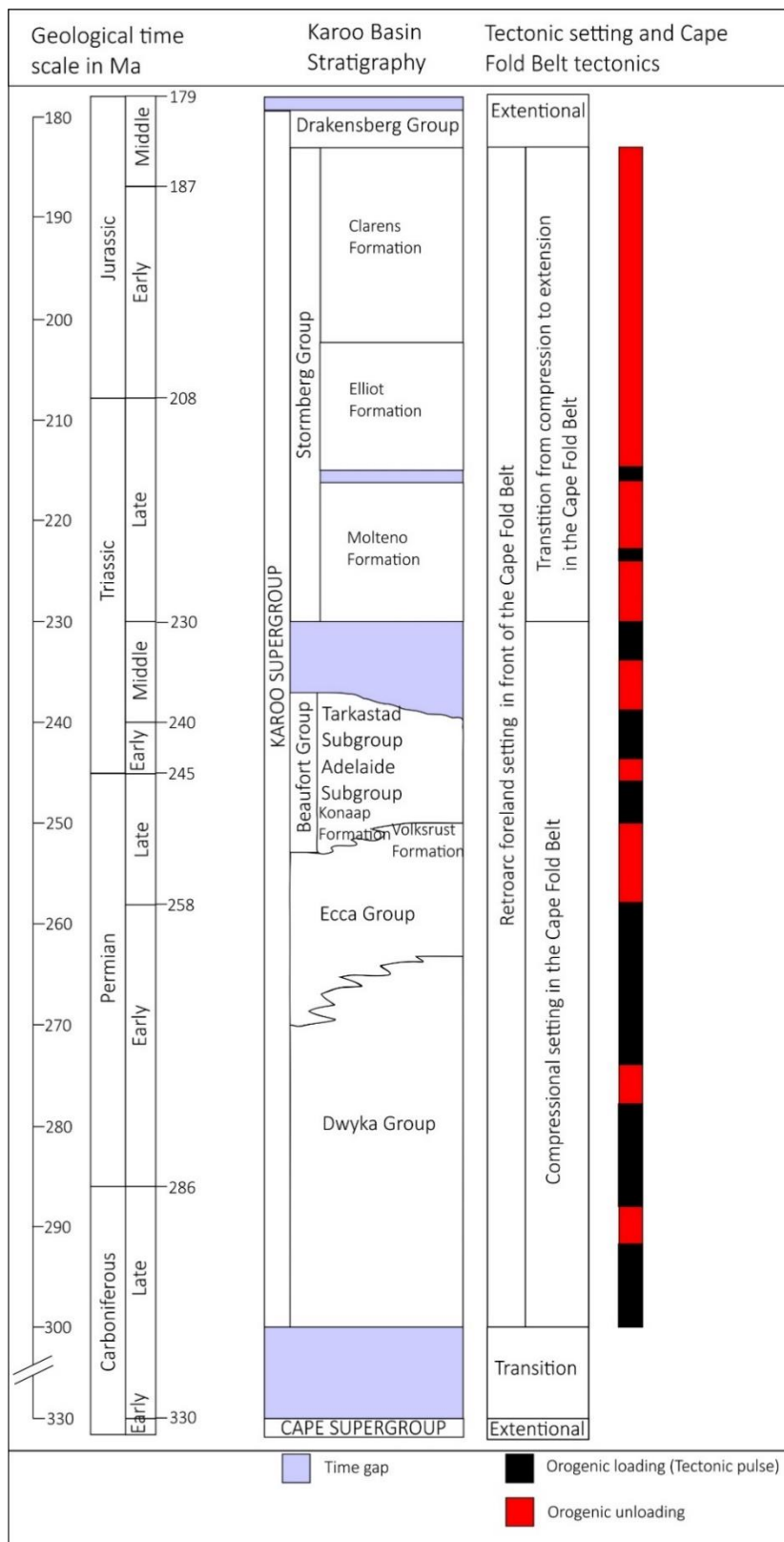


Figure 1.1: Represent the geological age of the generalized stratigraphy of the Karoo Basin (from the south to the northeast) along with time gaps in deposition. The tectonic evolution of the Karoo Basin is represented in the tectonic setting. The black and red bar represent periods of tectonic pulses (black) and crustal relaxation (red) during the formation of the Cape Fold Belt with the onset of subduction (tectonic pulse) of the paleo-Pacific plate. The image was modified after Catuneanu, *et al.* (1998).

in the shrinking basin (Tankard, *et al.*, 2009). The deposition of the Stormberg Group was terminated because of the outflow of Karoo Flood Basalts along fractures and faults caused by the breakup of Gondwana, resulting in the Drakensberg Group of Jurassic (Tankard, *et al.*, 2009).

1.1.2 Stratigraphy of the Main Karoo Basin

The study area is located in the southwest of the Main Karoo Basin and only the southwestern stratigraphy will be described.

The basement of the Main Karoo Basin is a stable floor (Johnson, *et al.*, 2006). To the south, the basement comprises Namaqua-Natal Metamorphic Belt rocks overlain by the Cape Supergroup deposits, which in turn is overlain by the Main Karoo Basin deposits of the Karoo Supergroup (Figure 1.1) (Johnson, *et al.*, 2006).

The Dwyka Group initiated the formation of the Karoo Supergroup. The Dwyka Group primarily represents dark-colored valley-fill glacial deposits (Lindeque, *et al.*, 2011). It was deposited by retreating glaciers and is thickest in the south (100 m-800 m) and thins towards the north (200 m) of the basin. The southern facies, *i.e.* the Elandsvlei Formation, is a stratified diamictite that overlies the Cape Supergroup unconformably (Johnson, *et al.*, 2006).

The Ecca Group overlies the Dwyka Group. The Ecca Group succession (maximum thickness of 3000 m in the southern part of the Main Karoo Basin and is remarkably thinner elsewhere) was deposited in a marine and deltaic environment. There are 16 different formations reflecting facies changes laterally in the Ecca Group (Tankard, *et al.*, 2009; and Johnson, *et al.*, 2006). In the western part of the basin the sequence of formations is as follows; Tierberg-, Skoorsteenberg-, Kookfontein- and Waterford Formations (Johnson, *et al.*, 2006). The Beaufort Group overlies the Ecca Group and will be discussed in more detail as the study area is located within this group.

The Beaufort Group is covered by the Stormberg Group (Molteno-, Elliot-, and Clarens Formations) succession which was deposited in a fluvial-aeolian depositional environment (Johnson, *et al.*, 2006). It comprises approximately an 1100 m thick succession (Tankard, *et al.*, 2009). The Stormberg Group is absent from the southwest of the Main Karoo Basin due to the shrinking of the Main Karoo Basin caused by a decrease in accommodation space (Catuneanu, *et al.*, 1998; and Bordy, *et al.*, 2005) (Figure 1.2). This was a result of upliftment in the southwestern margin of the Main Karoo Basin, after the deposition of the Adelaide Subgroup, shifting the locus of subsidence (*i.e.*, the depocenter for the upper Beaufort Group and the Stormberg Group) shifted towards the east (Tankard, *et al.*, 2009; and Johnson, *et al.*, 2006).

The Drakensberg Group comprises stacked lava flow deposits covering the sediments of the Main Karoo Basin and terminates deposition in the Main Karoo Basin (Tankard, *et al.*, 2009).

Beaufort Group

The geology of the Beaufort Group was first described in parts of Beaufort West, Prince Albert, and Sutherland by Rogers & Schwartz (1902). The Beaufort Group succession (Figure 1.2) is approximately 6000 m thick in the south and pinching out

& Rubidge, 2014; Cole & Wipplinger, 2001; and Le Roux, 1985). The Moordenaars Member is the most widespread unit of the Abrahamskaal Formation. Is a fine to medium grained sandstone package about 435 m thick which is arenaceous to the base and becomes argillaceous to the top (Day & Rubidge, 2014).

According to Catuneanu, *et al.* (2005), the Abrahamskraal- and Teekloof Formations, in the west of the Main Karoo Basin, is predominantly sandstone and purple mudstone units formed by large meandering streams that flowed north-east. The deposit formed a 3500 m thick upwards fining succession where upper and lower flow-regimes are preserved within channel sandstone deposits (Catuneanu, *et al.*, 2005). The Abrahamskraal Formation shows an increase thickness of the sandstone packages towards the provenance located southwest of the basin and an increase in sandstone to mudstone ratio (Cole & Wipplinger, 2001; Day & Rubidge, 2014 and Cole, *et al.*, 2016). The sandstone of the Adelaide Subgroup generally consist an average of 19% quartz, 28% feldspar, 36% lithic fragments, and 12% matrix (Johnson, *et al.*, 2006). The mudstone of the Adelaide Subgroup is usually massive with blocky weathering (Johnson, *et al.*, 2006). The boundary between the Abrahamskraal Formation and the Teekloof Formation is marked by arenaceous Poortjie Member in the base of the Teekloof Formation (Johnson, *et al.*, 2006).

Considering Catuneanu, *et al.* (1998 and 2005), it can be summarized that the Koonap- and Middleton Formations (eastern portion of the Main Karoo Basin) is a 2800 m thick sandstone, siltstone, and mudstone succession, that was deposited in fluvial-lacustrine environments. The Koonap Formation comprises upwards fining cycles of sandstone and greenish mudstone. This is overlain by the Middleton Formation which comprises upwards fining successions of sandstone, siltstone, and maroon to greenish-grey mudstone. These deposits are overlain by the Balfour Formation.

Research by Vigliettie, *et al.*, 2017 revealed that the Balfour Formation is a dominant sandstone and mudstone. The sediment was deposited by braided streams and to the top meandering streams (Catuneanu, *et al.*, 2005). The northern equivalent of the upper Balfour Formation is the Normandien Formation which consists of interbedded sandstone and mudstone that was deposited by meandering streams. Recent revision by Vigliettie, *et al.*, 2017 revealed by that the Balfour Formation rapidly thins towards the north of the Main Karoo Basin with a conformable contact in the west of the basin and unconformable towards the north because of missing Oudeberg Member stratigraphy in the northern part of the basin.

Tarkastad Subgroup

The Tarkastad Subgroup (Figure 1.2) can be subdivided into the proximal Katberg- and Burgersdorp Formations and the distal equivalents Verkykerskop- and Driekoppen Formations (Catuneanu, *et al.*, 1998). The Tarkastad Subgroup is absent in the west of the Main Karoo Basin. This may be a result of the major upliftment occurring in the southwestern margin of Gondwana causing erosion in the end of the Permian (hiatus in Figure 1.1).

The Katberg Formation conformably overlies the Balfour Formation (Stavrakis, 1980; Hiller & Stavrakis, 1984; Groenewald, 1996; and Gastaldo *et al.*, 2019). The Katberg-

and Verkykerskop Formations were deposited by braided streams and preserved various transverse- and longitudinal bars with horizontal beds and trough- and planar cross-stratification (Catuneanu, *et al.*, 1998). The sediments comprise mostly siltstone and per volume more sandstone (coarse- to medium-grained) content than the units above and below and it becomes finer towards the north of the basin (Catuneanu, *et al.*, 1998).

The Burgersdorp Formation conformably overlies the Katberg Formation (Catuneanu, *et al.*, 1998). The Burgersdorp- and the Driekoppen Formations represent deposits from meandering streams and floodplains (Catuneanu, *et al.*, 1998). They consist of fine to medium-grained sandstone bodies interlayered with maroon siltstone and mudstone (Catuneanu, *et al.*, 1998). The Stormberg Group overlies the Burgersdorp Formation unconformably throughout the basin and conformably to the north of the basin (Cole, *et al.*, 1991; Catuneanu, *et al.*, 1998; and Bordy, *et al.*, 2005).

1.2 Uranium

1.2.1 Uranium chemistry

Uranium is a lithophile element with a high affinity for oxygen, therefore it remains close to the surface (Dahlkamp, 1993). It belongs to the actinides and is located in Group 1-14 in the Periodic Table of elements (Dahlkamp, 1993). It is characterized by close chemical relationships and peculiar contraction behaviour of the ionic radii caused by poor shielding of nuclear charges, resulting in electrons that are drawn close to the nucleus, leading to a decrease in the radius, similar to the lanthanides (Dahlkamp, 1993).

According to Dahlkamp (1993) the physicochemical properties of uranium are:

- Atomic number: 92
- Atomic weight: 238
- Density: 18.9 g/cm³
- Melting point: 1405 °C
- Oxidation stages: 3, 4, 5, 6
- Decay U²³⁵: Half-life of 4.46 Ga with α -particles

1.2.2 Mobilization and deposition of uranium in aqueous systems

Considering the oxidation states of uranium, tetravalent (U⁴⁺) and hexavalent (U⁶⁺) states are mineralogically and geochemically more important (Dahlkamp, 1993; and Skirrow, *et al.*, 2009). The trivalent (U³⁺) and pentavalent (U⁵⁺) uranium states are not stable in natural environments (Dahlkamp, 1993). Skirrow, *et al.* (2009), classifies U⁴⁺ and U⁶⁺ as hard acids that tend to form complexes with hard base ligands like F⁻, OH⁻, NO₃⁻, CO₃⁻², SO₄⁻², PO₄⁻², VO₄⁻², amongst others, according to a scheme created by Pearson (1963). Other common associations with uranium are arsenic, vanadium and rare earth elements which also react as hard acids (Skirrow, *et al.*, 2009).

The tetravalent oxidation state of uranium (U⁴⁺) has an ionic radius of 0.97 Å or 1.01 Å depending on the coordination number, 6 or 8, respectively (Dahlkamp, 1993). The dominant ore minerals will form are insoluble oxides like uraninite and pitchblende. The formation of either depend strongly on the formational environment (Dahlkamp,

1993; and Bednar, *et al.*, 2007). Skirrow, *et al.* (2009), suggests that in reduced environments, which prevails in magmatic and metamorphic environments, uranium will predominantly occur in the tetravalent state.

The hexavalent oxidation state of uranium (U^{6+}) has an ionic radius of 0.80 Å and has a coordination number of 6 (Dahlkamp, 1993). Hexavalent uranium tends to form uranyl complexes (UO_2)²⁺ (Dahlkamp, 1993). The uranyl complexes have extensive complexation chemistry with organic and inorganic substances (Bednar, *et al.*, 2007). Skirrow, *et al.* (2009), suggests that in oxidizing environments, which prevails in near-surface environments, uranium will predominantly occur in the hexavalent state.

Skirrow, *et al.* (2009), suggest that favourable conditions for the enhancement of uranium solubility and transport in hydrothermal fluids (at low to moderate temperatures, <200°C), requires the following conditions:

- increased fO_2 (oxygen fugacity),
- low pH (acidic),
- increasing temperatures, and
- increasing concentration of dissolved ions like CO_3^{2-} , SO_4^{2-} , PO_4^{2-} , Cl^- , and F^- .

When the above-mentioned conditions prevail, uranium will be transported as uranyl complexes of the dissolved ions CO_3^{2-} , SO_4^{2-} , PO_4^{2-} , Cl^- , and F^- .

The major factors controlling the precipitation of uranium from solution according to Skirrow, *et al.* (2009) are:

- redox state,
- pH,
- ligand concentrations,
- temperatures, and
- adsorption

At low temperatures and oxidizing environments, fluid-rock interactions and fluid mixing are the most important controlling factor for uranium deposition (Skirrow, *et al.*, 2009). When uranyl complexes are the dominant aqueous uranium species, the reduction of the oxidized uranium-hosting fluids is necessary (Skirrow, *et al.*, 2009). Reductants may include organic matter, iron (II)-bearing minerals and reduced sulfur in sulfide minerals. The uranyl complex will form uranium minerals with distinctive mineral associations (e.g., phosphate minerals with uranyl phosphate complex, or carbonate alteration minerals with uranyl bicarbonate complexes) (Skirrow, *et al.*, 2009).

In natural environments, the mobility of uranium is controlled by its oxidation state and solubility with uranyl ions (Cumberland, *et al.*, 2018). When uranium binds with dissolved organic matter like humic and fulvic acids, the uranium will stay in solution but, when the uranium bind with solid-phase organic matter, it will be adsorbed leading to the accumulation of uranium mineralization within organic-rich sedimentary environments (Cumberland, *et al.*, 2018). The uranium mobility is strongly affected by organic matter in its dissolved and/or colloidal form (Cumberland, *et al.*, 2018).

1.2.3 Sandstone-hosted uranium deposits

Sandstone uranium ore deposits usually have uraninite and coffinite and many other alteration products as part of uranium mineralization (Robertson, *et al.*, 1978). The uranium mineralization usually occurs in a combination of lenticular arkosic sandstones along with associated organic matter (Robertson, *et al.*, 1978). These deposits usually form within confined basins where drainage is relatively closed (Robertson, *et al.*, 1978). The source for the uranium in these deposits is leached by groundwater that moves through underlying rocks like uraniferous granite or tuffaceous beds and transported by the groundwater into permeable sandstones (Robertson, *et al.*, 1978). The uranium in solution occurs in the oxidized hexavalent form and when it encounters a reducing environment, thus one where organic matter and/or sulfide minerals occur, it will precipitate out of the solution into the tetravalent state (Robertson, *et al.*, 1978).

1.2.4 Karoo Uranium Province

The Karoo Uranium Province extends southward from Bloemfontein in the Free State, as a semi-crescent through the Eastern Cape into the interior of the Western Cape (Figure 1.3). The Rietkuil study area is located approximately 40 km west of Beaufort West and lies within the Karoo Uranium Province of the Beaufort Group.

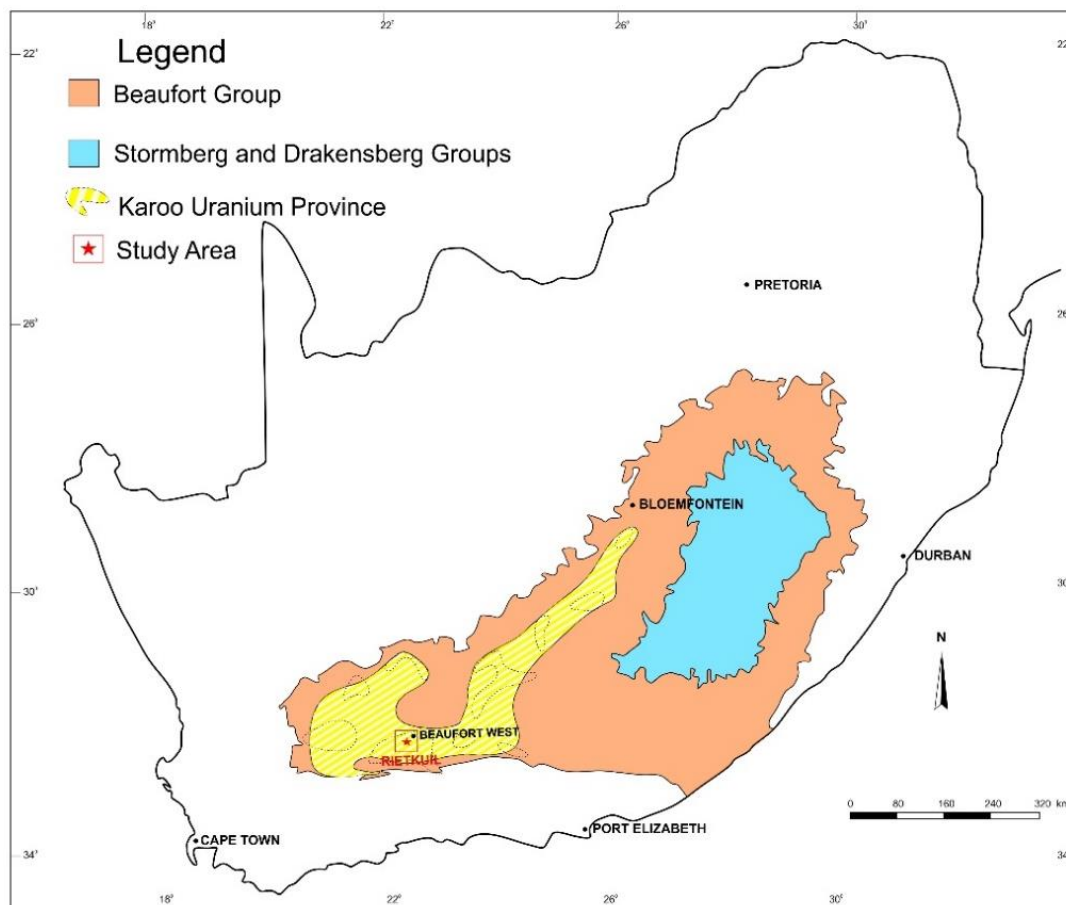


Figure 1.3: The extent of the Karoo Uranium Province and the location of Rietkuil study area in the Beaufort Group of South Africa. Within the Karoo Uranium Province known trail mining sites are also indicated in dotted-lines. The image was modified after Xu, *et al.* (2012).

Kubler (1977), conducted a detailed study on the sedimentology and uranium mineralization between Beaufort West, Fraserburg and Merweville. He described the nature of the uranium mineralization, origin, and the environment of the formation along with a detailed description of the sediments. Kubler (1977) states, “the deposits are not truly syngenetic, they are best described as epigenetic, formed by supergene ground waters”.

Uranium in the Beaufort Group

Turner (1978, 1979, and 1981) describes the stratigraphy of the Beaufort Group in the southern part of the Karoo Basin. He combined it with biozones described by Keyser & Smith (1979); and Kitching (1977) and found that important uranium mineralized zones correlated well with certain biostratigraphic zones and certain lithofacies. He proposed, that in the Beaufort West district, that the uranium mineralization is confined within the *Pristerognathus-Diictodon* assemblage zone and in high sinuosity channel facies associations.

Since the discovery of the uranium in the Main Karoo Basin many efforts have been made to identify the source of the uranium and to create an accurate mineralization model for these uranium deposits. Currently, there are two basic conceptual models considered for the uranium deposits of Karoo Uranium Province. Le Roux (1985); and Cole & Labuschagne (1985) described models for the sandstone-hosted uranium deposits of the Karoo and the geological environment related to these deposits. Both theories seem to agree that the host rock is calcareous channel sandstone bodies that is horizontally layered and contains high amounts of carbonaceous matter (Cole & Labuschagne, 1985; and Le Roux, 1985). Controversy arises when considering the source of the uranium and the way mineralization occurred. Both models agree that the emplacement of the uranium into present sandstone bodies was epigenetic in nature.

The first conceptual model by Cole & Labuschagne (1985), states that uraniferous liquids initially originated either from volcanic tuff deposited simultaneously with fluvial sediments, and/or from granitic fragments transported from a granitic source via river channels. They suggested that volcanic tuff was initially deposited with mudstone and uranium was adsorbed onto clay and organic particles. They propose that the clay minerals were sourced from a granitic source and transported into the inter-channel localities. Eventual, dewatering and leaching of these mudstones by groundwater, that were enriched in carbonates and silica, led to the uranium mineral precipitation in permeable channel sandstone bodies. The precipitation of uranium minerals occurred in the presence of carbonaceous matter. The sandstone units that were interfingering displayed higher concentrations of uranium mineralization.

The second conceptual model proposed by Le Roux (1985), considered a tectonic approach where the back-arc basin is adjacent to a calc-alkaline magmatic arc. The paraphrased model by Le Roux (1985) reads: during the formation of the Cape Fold Belt, tuffaceous layers, rich in uranium and other ore mineral elements, were deposited simultaneously with sediments, particularly when tectonic pulses reached a high in the Triassic age (Figure 1.1). During the Paleozoic and Mesozoic, land plants occurred and was trapped in place forming peats and coals (Le Roux, 1985). With upliftment

redistribution of the organic matter occurred during landscape erosion, concentrating as organic matter in sediments in certain localized channel sandstones. These organic-rich layers were protected for the atmosphere by high water table produced localized reducing environments, important for the mineralization of uranium. Furthermore, Le Roux suggests that post-depositional groundwater may have leached these uraniferous strata and deposited new ore bodies along basal contacts of the first thick impermeable horizon. He also states that fractures and fault systems may have contributed to the localization of the sandstone-hosted uranium deposits. Fractures and faults can control the groundwater flow either away from the ore deposit, protecting it from leaching or, it can concentrate a new deposit leaving behind a ghost deposit. Le Roux mentioned that uranium ore deposits are often found in close proximity or stacked in different horizons along fault and fracture zones. Based on the latter this thesis will aim to prove that the mineralization is a result of the introduction of a uranium-bearing solution along fractures and fault, and in the presence of a reductant, uranium minerals will precipitate from the solution.

Rietkuil Mine

Rietkuil mine (S32°25'15"/E022°08'10") is located on Rietkuil farm 307 RD (Province of the Western Cape). In 1970, Union Carbide discovered the Rietkuil uranium deposit with the aid of airborne radiometric techniques. In 1977, the Rietkuil mine test pit was excavated (AEC-AEK, 1994) to obtain a bulk sample for analysis of subsurface uranium mineralization.

Cole, *et al.* (1991), studied the underlying sandstone layer comprising horizontally bedded, channel bar deposits followed by ripple cross-lamination and natural levee siltstone. The uranium mineralization occurs within the base of these sandstone layers and predominantly consists of uraninite and pitchblende. This positioning of the uranium mineralization in the strata implies important permeability constraints. They also found that there is a close association with horizontally bedded sandstone from an upper-flow regime, and channel-bars containing organic material.

Cole & Wipplinger (2001) suggested that Rietkuil mine falls within the Moordenaarskraal Member of the upper part of the Abrahamskraal Formation (Figure 1.2) in the Main Karoo Basin. They stated that at Rietkuil mine, the basal sandstone units are comprised of predominantly fine-grained horizontally bedded layers that are characterized by low angle trough-cross bedding. Individual sandstone stories show upwards fining from trough cross-bedding to fine-grained ripple cross-lamination sandstones that are overlain by mudstone.

Scholtz (2003) conducted a study to determine the potential toxic influence of uranium trail mining in the Karoo Uranium Province. He found high concentrations of heavy metals at Rietkuil mine amongst other locations within the Karoo Uranium Province due to a lack of remediation.

Despite the vast research conducted on the Main Karoo Basin and the Karoo Uranium Province, there is still no clear mineralization model for the uranium mineralization. There is a discrepancy regarding the mineralization model. One side suggest a tectonic uranium mineralization model and the other side suggests primary channel deposits and later redistribution of the uranium mineralization. This study will be aimed

to create a model based on detailed field mapping considering all aspects studied by the different uranium mineralization models with the sights on proposing a revised model for the uranium mineralization of the Karoo Uranium Province.

1.3 The aim and objectives of the study

The aim of this study will be to determine the following:

- 1) The type of uranium mineralization at Rietkuil mine.
- 2) The controlling factors on the distribution of the uranium mineralization by considering; tectonic structures, lithology, and carbon (and other reductants) occurrences.
- 3) To compile a mineralization model for the uranium deposit at Rietkuil mine that considers the latter point 2.

Chapter 2: Materials and methods

2.1 Fieldwork at Rietkuil opencast mine

Fieldwork at Rietkuil opencast mine was conducted in two phases.

The first phase was a reconnaissance field visit. Throughout this period of time, five test samples were collected for preliminary geochemistry, as well as creating mosaics/lateral profiles that formed the basis on which the mapping of Rietkuil mine was constructed. The latter was constructed by capturing photographs, with a Canon *PowerShot A2200 HD* camera every two meters in a horizontal line, for each of the four faces with the upper and lower benches. These photographs were stitched together, with CorelDraw X8, to generate photo-panoramas for each face. These photo-panoramas were then used to construct the mosaics/lateral profiles that indicated major contacts.

The second phase involved the detailed mapping of the four faces with upper and lower benches at Rietkuil opencast mine, along with constructing a general geological map of the study area. The detailed mapping of the mine was constructed by compiling detailed sedimentary profiles, noting lithological and lithofacies changes, counting and mapping different joint sets, drawing gamma-ray contour maps showing the distribution of the uranium mineralization, noting the carbon distribution within layers, and collecting samples for geochemistry.

The mapping was conducted by plotting GPS coordinates (approximately every 5-20 meters) along the contacts that were followed out in the field and with the aid of aerial photographs (SPOT images). Important sedimentological and tectonic features were also noted and plotted with GPS coordinates. The map was created at a 1:10 000 scale with the aid of Arch-GIS and CorelDRAW.

The sedimentary profiles were constructed by closely examining the mine faces, taking note of different lithologies, sedimentary structures, grain-size (with the aid of a grain-size chart), sorting and colour (with the aid of a colour chart) as well as the nature of the contacts within and between lithological units.

The joints were counted and mapped by carefully counting a specific joint set at a time in 5 m intervals and noting the exact position of each on a mosaics/lateral profiles, also taking note of joints that showed calcite crystallization.

The gamma-ray contour maps were compiled using a 2 m by 2 m grid across the faces of the mine. Where two lines intersected, a gamma-ray reading was taken with a scintillator counter, *Thermo Scientific RedEye PRD*, (in counts per second, cps) by placing it directly in contact with the rock. These readings were plotted on a mosaics/lateral profiles and contoured to produce gamma-ray maps. These maps are used to illustrate the dispersion of radioactive minerals (uranium distribution) throughout the faces of the mine.

The carbon distribution maps were constructed by inspecting multiple pieces of fresh sandstone samples through a hand lens and describing how the carbon is distributed throughout the sample, the size of the carbon matter, as well as the shape thereof. This was performed at different heights, preferably in a vertical line from the bottom to the top, and at several positions along each face.

Samples were exclusively collected from the sandstone units. Samples were collected (Figure 2.1 to Figure 2.4) at points with low and high gamma-ray readings; at joints, away from joints and at joint intersections; and at places with low and high amounts of carbon. Samples were collected in this manner for mineralogical and geochemical analysis and comparison purposes so that the controlling factors of the uranium mineralization can be identified.

A general geological map was also constructed during the timeframe of stage two where the change in lithologies was noted as well as joints and other tectonic features for a better understanding of the environment.

2.2 Sample preparation

The samples that were collected were prepared in various ways for mineralogical and geochemical analysis. Thin sections were prepared for petrographic studies (using reflective and transmitted light microscopy). A portion of the samples collected were crushed and then milled to a talcum powder consistency (~particle size of $<10\text{ }\mu\text{m}$). The powders were prepared for X-Ray Diffraction spectrometry (XRD), X-Ray Fluorescence spectrometry (XRF), Induced coupled plasma mass spectrometry (ICP-MS), LECO analysis and Mebius titration method studies.

2.2.1 Thin section preparation

The petrographic studies will provide insight into how the uranium minerals are related to the rest of the minerals within the rock.

A total of 17 thin sections were prepared, from different sampling localities (marked with a red star in Figure 2.1 to Figure 2.4) for petrographic examination using transmitted and reflected light. A particular problem with polishing the thin sections is the loss of some of the minerals like quartz grains and other hard minerals, due to the matrix material being softer than some of the grains present.

2.2.2 Preparation of samples for XRD

The XRD analysis will determine the type of uranium complexations present. From the complexes, the oxidation state of the uranium can be depicted, giving information on the environment of mineralization.

Following the milling, a small sample portion was hand-pressed on an XRD sample holder and mounted onto the XRD for geochemical analysis.

2.2.3 Preparation of samples for XRF

The XRF analysis aided in giving quantitative major and trace element concentrations.

Preparation of fusion discs

Fusion discs are the preferred method to introduce oxide samples into the spectrometer for XRF, the reason being that during the fusion process, factors like

heterogeneity, particle size, and mineralogical effects are eliminated. Fusion discs were prepared at the Department of Geology at the University of the Free State.

After milling, 10 g of sample was heated to 110°C to dehydrate and devolatilize the sample. It was measured gravimetrically. Thereafter, the sample was heated to 1050°C to release the volatile content by breaking down minerals such as carbonates and sulfides. Again, the sample was measured gravimetrically. This gives rise to the total loss of ignition or the total gain on ignition. The fusion discs were prepared by weighing 0.28 g of sample and 10 g of flux. The Alfa Aesar Spectroflux consists of Li-tetraborate, Li-carbonate, and La-oxide (47:37:16 w/w%, respectively). The mixture was heated to 1000°C for approximately 5 minutes until a consistent fluid formed within a platinum crucible. The molted liquid was poured into a mold and pressed to form the fusion disc.

The certified reference material was prepared in the same way. The certified standards used to calibrate the XRF were AMIS 0095 and SARM 30/UREM 10.

Preparation of pressed pellets

Following milling, 8 g of the sample was measured. Then 3 g of Hoechst Wax ($C_6H_8O_3N_2$) was added to the measured sample. This was mixed for 20 minutes in a Turbula mixer to ensure that the sample is homogeneous. The mixture was then pressed at 395 N/m² to form the pellet.

The certified reference material was prepared in the same way. The certified standards used to calibrate the XRF were AMIS 0095 and SARM 30/UREM 10.

2.2.4 Preparation of samples for ICP-MS

The ICP-MS analysis aided in giving quantitative major and trace element concentrations.

The sample preparation for the ICP-MS was conducted at the Department of Geology at the University of Cape Town for samples marked with a yellow star in Figure 2.1 to Figure 2.4.

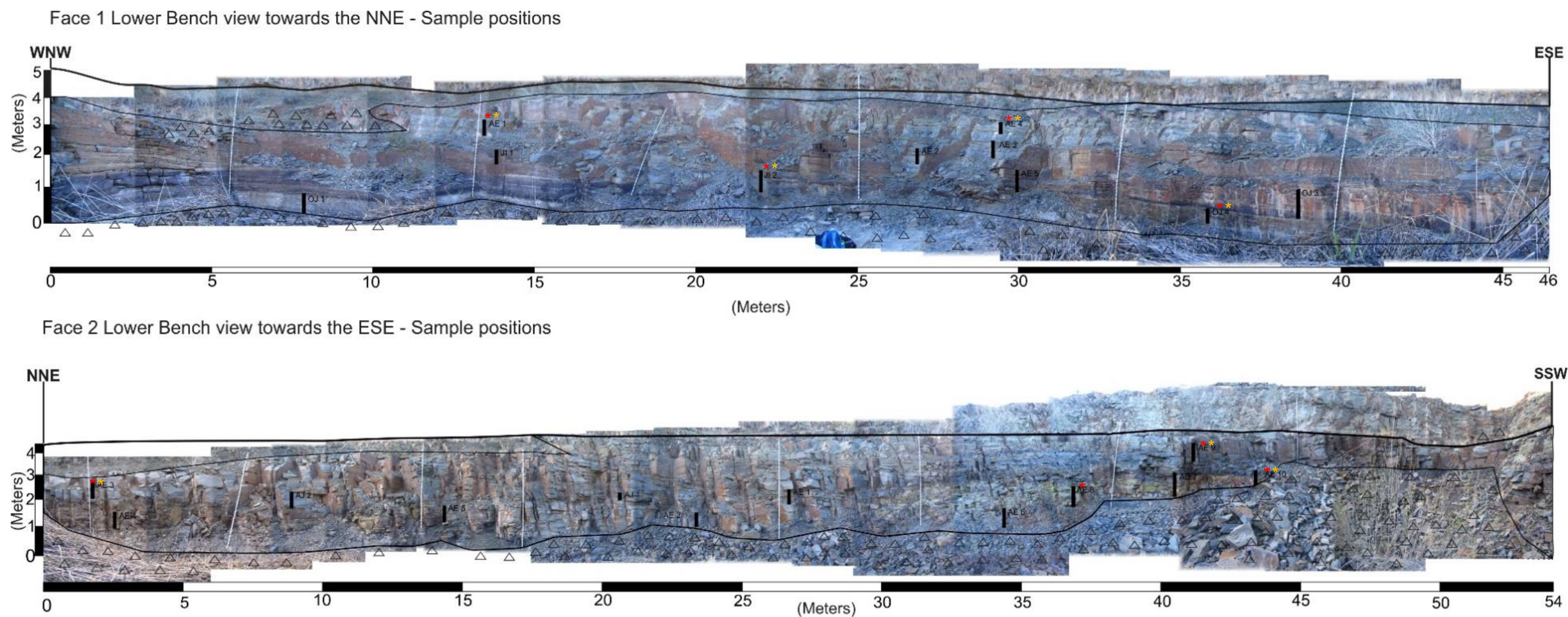
Following milling, 50 mg of sample powder were dissolved in a 4:1 HF/HNO₃ acid mixture in sealed Savilex beakers on a hotplate for 48 hours. Followed by evaporation to incipient dryness and two treatments of 2 mL concentrated HNO₃. The final dried product was then taken up in a 5% HNO₃ solution containing 10 ppb Re, Rh, In, and Bi, used as internal standards.

The certified reference materials and blanks were prepared in the same way. The certified standards used to calibrate the ICP-MS were AMIS 0095 and SARM 30/UREM 10. Calibration curves were obtained using artificial multi-element standards, from which standard solutions were made.

2.2.5 Preparation of samples for LECO analyzer

The LECO analysis was performed on 53 samples to gain information on the total carbon within the sandstones.

After milling, 0,2 g of the sample was weighed off and placed in a special tin foil, capsulated and placed into the LECO analyzer sample holder.



LEGEND		LEGEND	
Symbol	Discription	Carbon Samples	
—	Sandstone contacts	Sample number	
—	Upper most contact of bench		
△	Rubble		

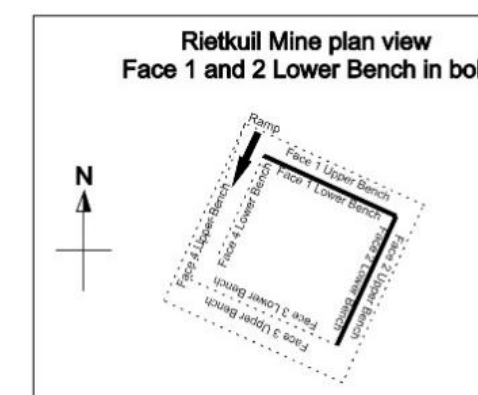
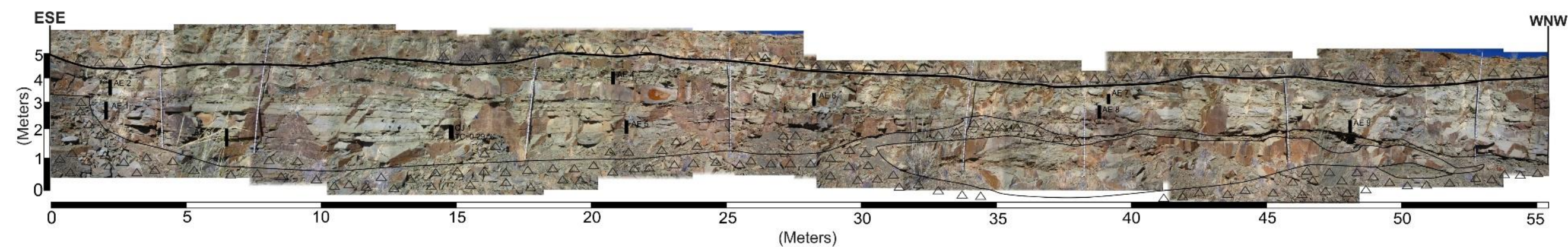
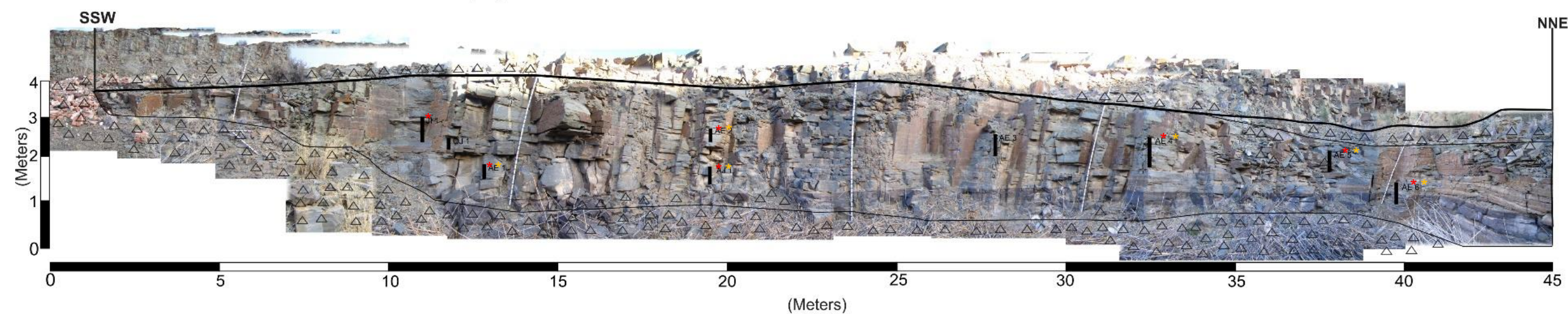


Figure 2.1: Represents the sample collection of Face 1 and 2 of the lower bench at Rietkuil mine. The sample number is displayed along with its positions. The red stars represent samples used for petrography and the yellow stars represents samples used for ICP-MS analysis.

Face 3 Lower Bench view towards the SSW - Sample positions



Face 4 Lower Bench view towards the WNW - Sample positions



LEGEND	
Symbol	Discription
	Sandstone contacts
	Upper most contact of bench
	Rubble

LEGEND	
Carbon Samples	
	Sample number

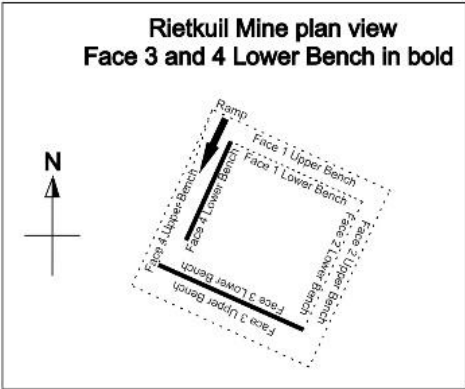
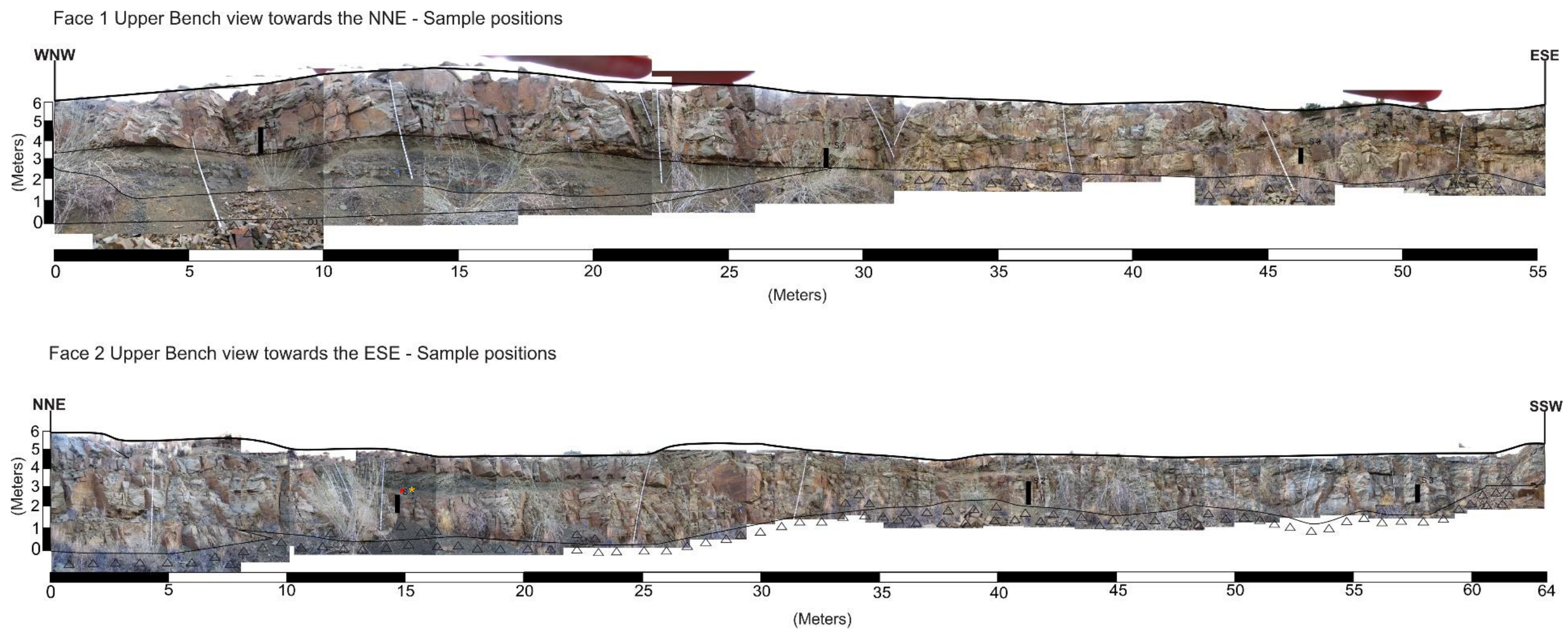


Figure 2.2: Represents the sample collection of Face 3 and 4 of the lower bench at Rietkuil mine. The sample number is displayed along with its positions. The red stars represent samples used for petrography and the yellow stars represents samples used for ICP-MS analysis.



LEGEND	
Symbol	Description
	Contact
	Upper most contact of a bench
	Rubble

LEGEND	
Carbon Samples	
	Sample number

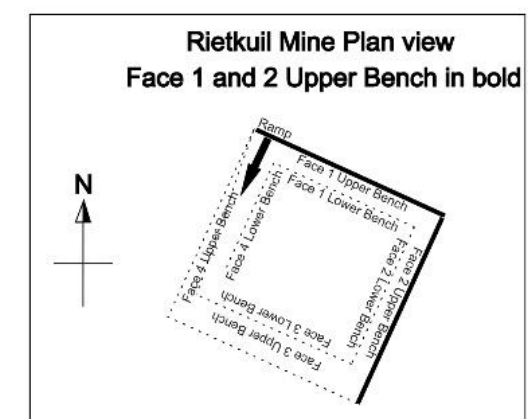
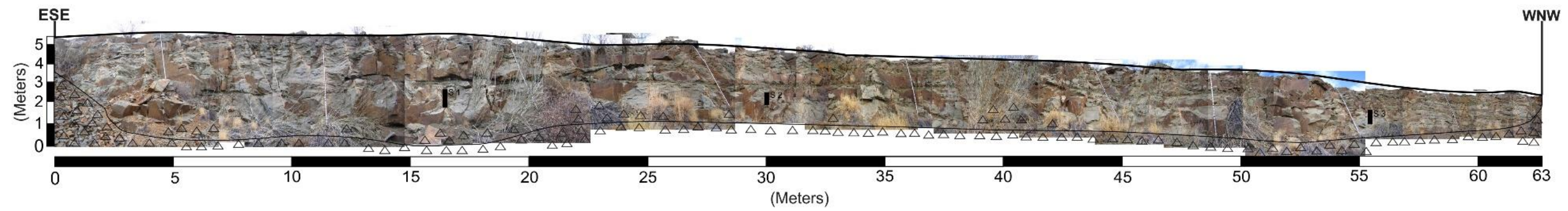
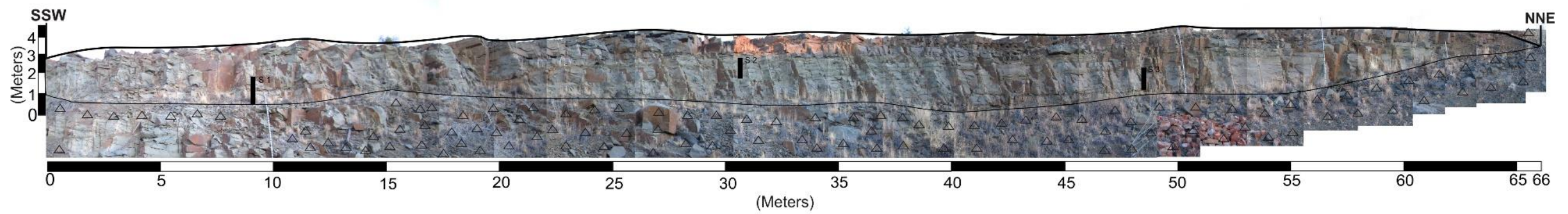


Figure 2.3: Represents the sample collection of Face 1 and 2 of the upper bench at Rietkuil mine. The sample number is displayed along with its positions. The red stars represent samples used for petrography and the yellow stars represents samples used for ICP-MS analysis.

Face 3 Upper Bench view towards the SSW - Sample positions



Face 4 Upper Bench view towards the WNW - Sample positions



LEGEND	
Symbol	Discription
	Contact
	Upper most contact of bench
	Rubble

LEGEND	
Carbon Samples	
	Sample number

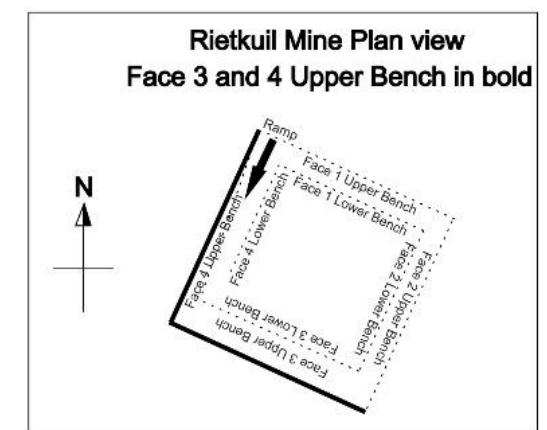


Figure 2.4: Represents the sample collection of Face 3 and 4 of the upper bench at Rietkuil mine. The sample number is displayed along with its positions. No petrography or ICP-MS analysis was conducted on these faces.

The internal certified reference material was prepared in the same way. The certified standard used to calibrate the LECO analyzer was NCS DC 73025 Soil.

2.3 Analytical procedures

2.3.1 Petrography

Petrographic examination was conducted with transmitted and reflected light microscopy referred to in Table 2.1. This allowed the study to determine how the ore (uranium minerals) were intergrown in relation to gangue minerals. It also aided in describing the minerals and determining a modal mineralogical concentration of the mineralogy within the rock. The modal mineralogy was determined by estimation.

Table 2.1: Specifications of the microscope used at the University of the Free State. Reflected and transmitted light was used to identify different mineral phases in the samples along with a description of the relationship between the minerals.

Model	Reflective and transmitted light microscope: Olympus BX51 Camera used for pictures: Altra 20 soft imaging system Software: Analysis imager
Analyze	To identify and describe the mineralogy of the ore in relation to the gangue minerals
Sample preparation	Polished thin sections
Magnification	2x, 4x, 10x, 20x magnification objective lenses

2.3.2 XRD

The specifications of the XRD are indicated in Table 2.2. The XRD was used to gain the quantitative mineralogical data for samples collected from the sites of study.

The X-ray source produces a $\text{CuK}\alpha_1$ X-ray beam with a Bragg-Brentano geometry focus position along the Theta-Theta goniometer configuration. The primary X-ray produced is directed to the crystalline mineral powder in the sample holder at various angles. The grains in the sample are orientated randomly and other grains will favor a certain orientation, this causes diffraction of the primary X-ray according to Bragg's law. The diffracted ray passes through a series of slits. First, the diffracted ray will pass through the anti-scatter slits which reduce background radiation, ensuring the x-rays measured were only from the sample area. Thereafter the X-rays pass through Soller slits, defining the width of the beam admitted to the detector. This beam then hit the W-filament in the tube to amplify the signal and was then measured as counts by the detector (Suryanarayana & Norton, 1998). Data Collector V.3.0c is used for data

collection and Highscore V.3.0e is equipped with the ICDD PDF-2 database for the evaluation of diffractograms.

Table 2.2: Specifications of the X-Ray diffraction spectrometer at the University of the Free State.

Model	PANanalytical Empyrean XRD
Analyze	Whole-rock mineralogy
Analyzers	Theta-Theta Goniometer (CuK α 1 X-ray beam) (Scans between 3.5° and 70°)
Software	Data Collector V.3.0c and Highscore V.3.0e
Acc. voltage	45 kV
Probe current	40 mA
Tube	Cu-side window tube (Anode-Cu and Cathode-W filament)
Detectors	X-Celerator detector

2.3.3 XRF

The parameters of the XRF are indicated in Table 2.3. The XRF was used to determine the bulk composition of the samples.

The XRF aids in the identification and determination of the bulk chemistry of a rock sample. XRF is a non-destructive method, but it removes all spatial information. Analysis of elements by XRF is made possible by the behavior of atoms when they interact with high energy primary X-ray photons. Electrons are expelled in the form of photoelectrons causing a hole in the orbital, making it unstable. This hole is filled with electrons from outer orbitals to create a stable state. During the excitation or replacement, energy is released because of a decrease in the binding energy of the electron, known as fluorescence. The energy of the emitted fluorescence photons is determined by the difference in energies between the individual and final orbitals for the individual transitions. Wavelength is inversely proportional to the energies and is characteristic for each element, making it possible to identify different concentrations of a certain element (Willis, *et al.*, 2011).

2.3.4 ICP-MS

The ICP-MS is a multi-elemental technique that uses a plasma with a high ion density and temperature that is ideal for element ionization (Ammann, 2007). It is a highly accurate and sensitive machine and provide values for elements in the parts-per-

trillion range. Due to its low detection limits, it is ideal for elements such as uranium (U) and thorium (Th).

Table 2.3: Specifications of the X-Ray fluorescence spectrometer at the University of the Free State.

Model	Axios PANanalytical W-D XRF spectrometer
Analyze	Whole-rock major and trace elements
Analyzers	Wavelength dispersive (WD) spectrometer
Software	Super Q software V.4.
Acc. voltage	60 kV (changes with the element 4 kV system)
Current	66 mA (changes with the element 4 kV system)
Tube	Rh-tube
Power level	4 kV
Detection limit	1 ppm (changes with element)
Detectors	Flow count and duplex detectors, scintillator detector

After the sample enters the plasma (5500°C) it undergoes atomization or element ionization. The ions are then extracted and separated based on their atomic-mass/charge ratio, with the aid of a quadrupole or magnetic sector analyzer. The specifications of the ICP-MS are indicated in Table 2.4 below.

Table 2.4: Specifications of the induced coupled plasma mass spectrometer at the University of Cape Town.

Model	Xseries2 Thermo Fisher
Analyze	Whole-rock trace elements
Measurement	Peak-hopping mode
Number of sweeps (per reading)	100
Carrier gas	Argon gas
Number of readings (per analysis)	3
Dwell time	10 ms

2.3.5 LECO analyzer

The LECO TruSpec CN Analyzer, refer to Table 2.5, was used to analyze the total carbon in the samples by dry combustion (Nelson & Sommers, 1982). The capsulated samples were placed in the loading chamber where they are dropped into the first furnace, individually. The first furnace is held at 950°C and for complete and rapid combustion it is flushed with oxygen gas. The combustion gases were then passed through to the secondary furnace held at 850°C so that further oxidation can occur before entering the collection vessel. In the collection vessel, oxygen was injected and mixed with the combustion gases, and removed through a CO₂ infrared detector, that measures C and CO₂.

Table 2.5: Specifications of the LECO analyzer at the University of the Free State, Department of Soil Science.

Model	TruSpec LECO
Analyses	C, N
Furnace 1	950°C
Combustion gas	Oxygen gas
Furnace 2	850°C
Detector	C, CO ₂ infrared detectors

2.3.6 Mebius method for titration of organic carbon

For the determination of the organic carbon content in 53 samples, the Mebius titration method (Nelson & Sommers, 1982; Prinsloo, 1988; and Wiltshire, 1987) was used. This experiment was conducted at the Department of Soil Science at the University of the Free State.

0.6 g of each milled sample was washed with 3 mL of a 2 N H₂SO₄ to get rid of inorganic carbon and dried in an oven, set to 50°C, to minimize volatile loss until they were completely dry. For these analyses, 0.5 g of the washed, dried, and re-crushed (with quartz mortar-and-pestle) sample were weighed off gravimetrically into a glass beaker. Exactly 10 mL of 0.5 N K₂Cr₂O₇ standard solution and 15 mL of concentrated H₂SO₄ was added to the beakers, including two blanks, one was boiled and the other was left unboiled. Thereafter the samples were placed on a sand bath that was preheated to 130°C, to react for 10 minutes, without letting the acid mixture boil; this minimizes volatile loss. Afterward, the beakers were removed from the sand bath and 35 mL of cold distilled water was added to them to stop all reactions. The excess chromate was then titrated with 0.2 N Fe(NH₄)₂(SO₄)₂•6H₂O until the endpoint is reached. An automatic titrator was used with an electrode to identify the endpoint (Table 2.6). The amount of carbon was calculated indirectly (Walkey & Black, 1934) by the amount of K₂Cr₂O₇ that reacted, with a series of calculations as seen in Appendix E-E2.

Table 2.6: Specifications of the automatic titrator and electrode at the University of the Free State, Department of Soil Science.

Model	Crison Micro TT 2050
Plunger	Crison Micro BLI 2030
Magnetic stir stage	Crison Micro ST 2039
Electrode	ACC SEN EL300, mV +/-2000, 0-80°C
Electrolyte	3 M KCl

Chapter 3: Results

3.1 Rietkuil opencast mine

3.1.1 Geological map of Rietkuil area

Rietkuil mine (S32°25'15"/E022°08'10") is located on Rietkuil farm 307 RD (Province of the Western Cape). Figure 3.1 shows the geology of the area surrounding Rietkuil mine. The area was mapped about 1 km to the north, south and west and approximately 2 km to the east. Rietkuil mine is situated within the Moordenaarskraal Member of the upper Abrahamskraal Formation consisting of argillaceous sandstones and mudstone units.

The local geology of the mapped area consists of sandstone, siltstone and mudstone units. The sandstone units are predominantly multi-layered channel deposits with greenish-grey to light badge color. The grey sandstone units, which host the uranium mineralization, is enriched in carbonaceous matter. Carbonate-rich sandstones (locally known as, '*koffieklip*'), are also present and indicated on the geological map at coordinates S32°25'30"/E022°08'0", where surficial uranium mineralization occurs. The sandstone units have dips that varies between 0° to 10° in predominantly the NW as well as NE dip direction in places. Paleocurrents were measured using parting or primary current lineation, along with ripple cross-bedding where present. The average flow direction is NE to ENE and marked with black arrows on the map in Figure 3.1. The siltstone and mudstone units are interlayered. Rip-up clasts consisting of clay and mud drape the basal contact of sandstones with underlying siltstone and mudstone units. The sandstone represents large channel-fills sequences deposited across the area, where a few of these channel fills are exposed at Rietkuil mine.

The tectonic structures mapped include joints and lineaments with slickensides in some instances. There are three major joint directions noted across the mapped area. The three sets are joints that strike 88° (E), 133° (SE), and 168° (SSE). The joints that occur on the map (Figure 3.1) were placed exactly where they were encountered. Thus, the joints marked on the map represents the strikes of the joints present and do not attest to the lateral extent or the number of joints at the specific location. The linear features strike in a NE direction as marked on the geological map in Figure 3.1. The lineaments that were encountered in the field are marked with a solid line and most of them had slickenside features. The dotted lineaments were mapped from an aerial photograph, with the surety that there are no fences in this vicinity. The lineament closest to Rietkuil mine was studied in more detail. It was noted that the sandstone on either side of the lineament dips in opposite directions (~10°), possibly indicating an open-anticline. There are also slickenside present showing a movement direction in an NNW direction.

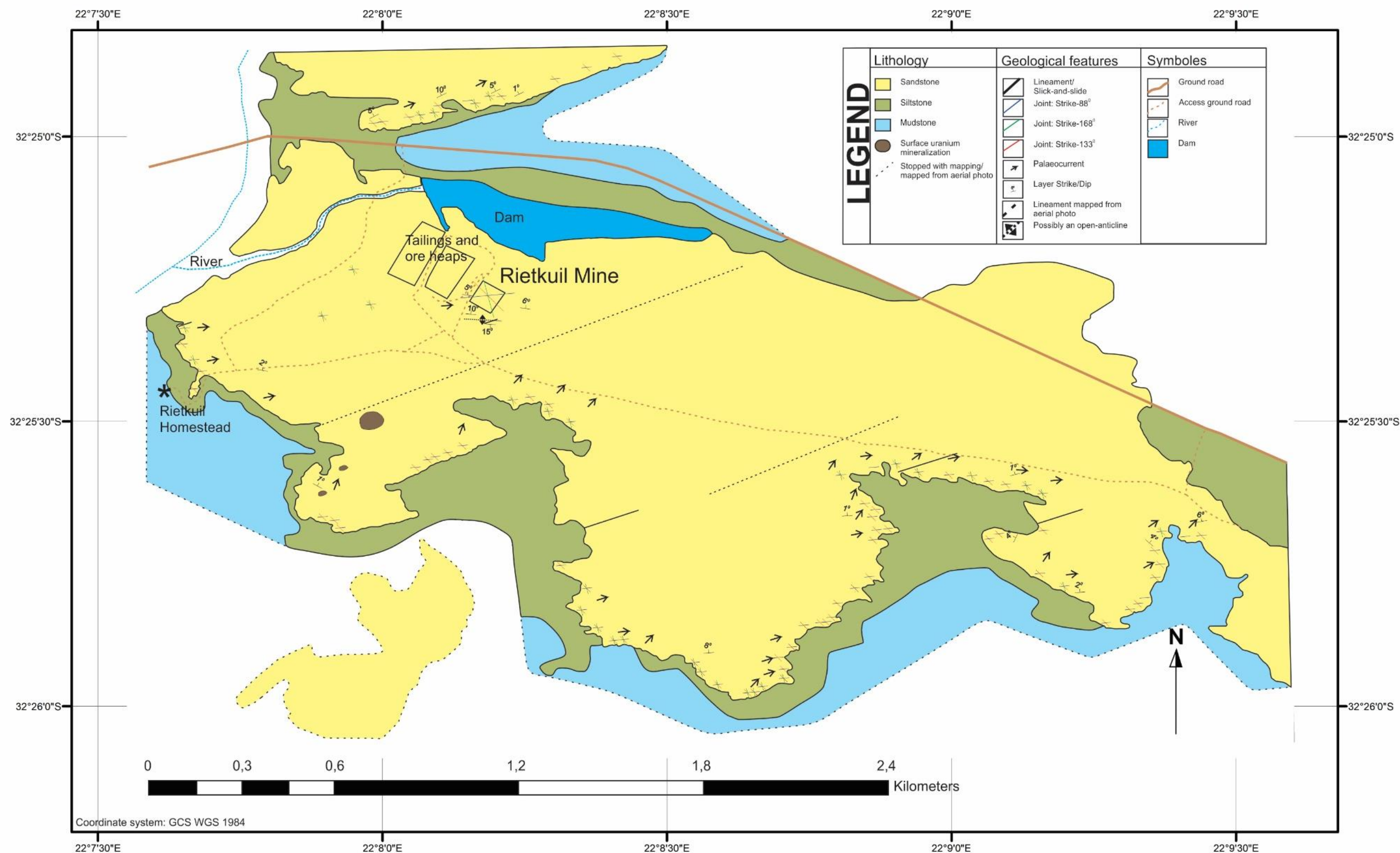


Figure 3.1: Mapped lithologies, tectonic structures, measured dips and flow directions at Rietkuil mine.

3.1.2 Rietkuil mine

Rietkuil mine (S32°25'15"/E022°08'10") showed in plan view in Figure 3.2, are composed of sandstone and mudstone units excavated in two benches. These benches and faces will be referred to as the upper bench and lower bench, and the four faces were numbered Face 1 to Face 4, throughout this thesis.

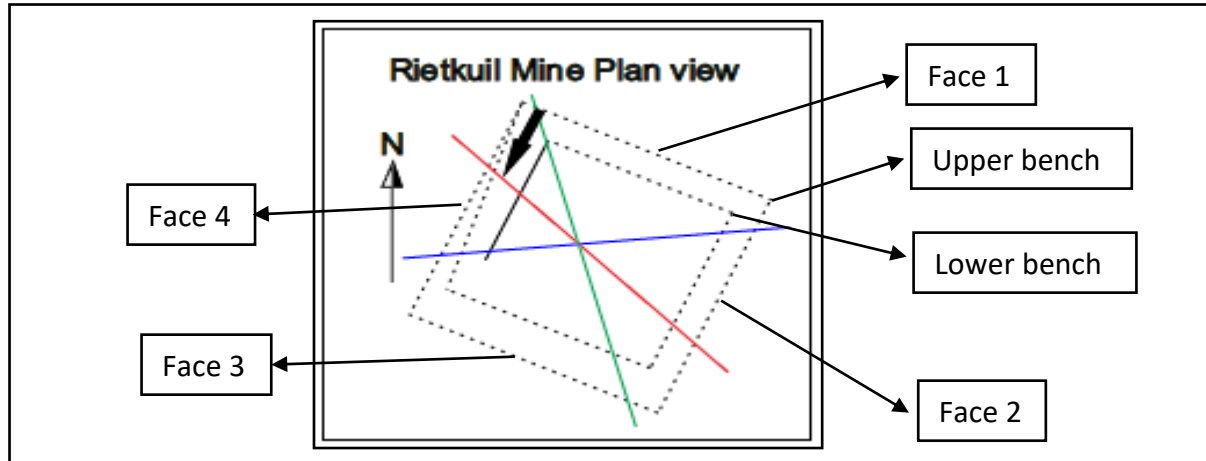


Figure 3.2: Plan view of Rietkuil mine identifying the main faces and benches used in this thesis. The blue, green and red lines is a schematic representation of the major strikes of joints present in the area. The blue joints strike 88°; the green joints strike 168°; and the red joints strike 133°. The black arrow indicates the ramp into the mine.

In the text, detailed sections, profiles, and figures will illustrate the results of data that were obtained from Rietkuil mine.

The sections were composed and primarily used to indicate the detailed fieldwork. The sections firstly show the sandstone that was considered during the mapping and the uppermost contact of that particular face along with the orientation of the face. Rubble was indicated with triangles. It is important to note for the upper and lower benches, that the bottom contact is not necessarily the lowest contact of the sandstone unit, as the sandstone continues beneath the surface or covered with rubble.

3.1.3 Lithology and lithofacies

The lithologies in Figure 3.11 to Figure 3.18 were assigned a particular color and the lithofacies are illustrated as shades of that color, corresponding to its lithology. The profiles illustrate sedimentary structures and the nature of the contacts.

There are eight lithofacies identified at Rietkuil mine (summarized in Table 3.1). The lithofacies were identified and noted in vertical profiles that were compiled (Figure 3.11 to Figure 3.18). The lithofacies herein are described based on the classification techniques by Ghazi & Mountney (2009); and Miall (1988) and applied to Rietkuil mine. No depositional environment interpretations were described due to a lack of sufficient data. The eight lithofacies of Rietkuil mine are described below and in Table 3.1:

1) *Clay pellet conglomerate (Gm)*

Lithofacies Gm are massive mudstone and siltstone pellets set in a mixed coarse grained sandstone-mudstone matrix. The pellets are rounded and oblate with a pellet

size of up to 5 cm. The pellets are green and/or red in color. No preferred pellet orientation was observed.

Lithofacies Gm occurs within sandstone beds. The contact with the overlying sandstone is sharp.

2) Cross-bedded sandstone (St)

Lithofacies St are cross-bedded sandstone that varies in grain size from 1/8 mm to 1/4 mm *i.e.* fine sandstones.

Lithofacies St dominates the upper bench sandstone units and in the upper portion of certain lower bench sandstone units. Lithofacies St contains little carbonaceous material. There are localized clay pellet conglomerate layers contained in some of the cross-bedded units with a coarse-grained matrix material.

3) Horizontally bedded sandstone (Sh)

Lithofacies Sh are horizontally bedded sandstone that varies in grain size from 1/16 mm to 1/4 mm *i.e.* very fine sandstones.

Lithofacies Sh is most abundant in the lower bench. Within Lithofacies Sh the lamination is horizontal to wavy. Individual laminae varied from about 1 mm to 1 cm. These laminae are rich in fine-grained carbonaceous material. To the base of the lower bench, the beds are gently-inclined horizontally bedded. This may be due to the unequal loading of the sediments during diagenesis or subtle internal erosional surfaces. At the top of the horizontal beds occurs parting lineations.

4) Ripple cross-laminated sandstone (Sr)

Lithofacies Sr is ripple cross-laminated sandstone that varies in grain size from 1/16 mm to 1/8 mm *i.e.* predominantly fine grained.

Lithofacies Sr is associated with Lithofacies Sh and St units as localized layers of a few cm and/or at the top of thick sandstone bed. Lithofacies Sr is generally not well preserved.

5) Massive sandstone (Sm)

Lithofacies Sm is massive sandstone units that vary in grain size from 1/8 mm to 1/2 mm *i.e.* fine to medium-grained sandstones. Due to weathering and fracturing, sedimentary structures could not be identified.

6) Parallel laminated siltstone and mudstone (FI)

Lithofacies FI is parallel laminated mudstone, siltstone or in some cases a 1/16 mm grain size sandstone.

Lithofacies FI occurs where a sandstone unit grades into siltstone. Where Lithofacies FI occurs as lenses within Lithofacies Fm, it has gradational upper and lower contacts. Lithofacies FI shows fine lamination and very small ripple cross-lamination within the sandstone and siltstone units. The contact between Lithofacies FI with sandstone units is erosional at the base of the sandstone. Lithofacies FI is predominantly mudstone with 30-80 cm thick lenses of siltstone that in some instances grade into a fine-grained sandstone.

7) Massive mudstone (Fm)




Lithofacies Fm is massive mudstone or siltstone and desiccation cracks occur occasionally.

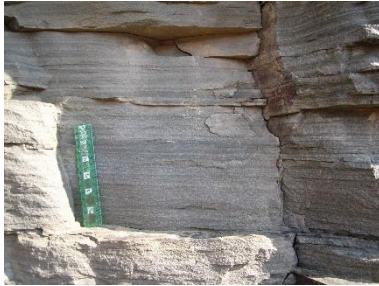




Lithofacies Fm occurs as layer deposits between the upper and the lower bench and as lenses between sandstone units in the upper bench. The contact between Lithofacies Fm with sandstone units are erosional at the base of the sandstone. Lithofacies Fs occurs in the top portion of Lithofacies Fm close to the overlying sandstone unit.




8) Massive mudstone with ball-and-pillow structures (Fs)

Lithofacies Fs are massive mudstone with slump-structures of sandstone *i.e.* ball-and-pillow structures at the top.

Table 3.1: Lithofacies identified at Rietkuil mine. Compiled from basic principles of Ghazi and Mountney (2009), and Miall (1988) and applied to Rietkiul mine. (The table is displayed over the next three pages, pg 31-33)

Lithofacies code	Facies description	Sedimentary structures	Figure of the facies
Gm	Clay pellet conglomerate	Massive	
St	Sandstone, (1/8 mm) fine to (1/4 mm) medium grained with localized clay pellet conglomerates (few mm to 5cm clasts)	Cross-bedded	 

Sh	Sandstone, (1/16 mm) very fine to (1/4 mm) medium-grained	Horizontal to wavy lamination, parting or primary current lineation	 
Sr	Sandstone, (1/16 mm) very fine to (1/8 mm) fine-grained	Ripple cross-lamination	 
Sm	Sandstone, (1/8 mm) fine to (1/2 mm) coarse-grained	Massive	

Fl	Mudstone, siltstone, very fine-grained (1/16 mm) sandstone	Finely laminated to small ripple cross-laminated	
Fm	Mudstone, siltstone	Massive, desiccation cracks	
Fs	Mudstone	Massive with ball-and-pillow structures	

Face 1

Face 1, views towards the NNE with the face orientated WNW-ESE and is highlighted in the plan view in bold in Figures 3.11 and 3.12.

The lower bench in Figure 3.11 is approximately 46 m long and 5 m in height. The basal sandstone unit in the lower bench (Figure 3.11) consists of a very fine to fine-grained sandstone with moderate sorting. The sandstone comprises quartz, feldspar, lithic fragments, mica, carbonaceous matter, and heavy minerals. In Figure 3.3 (Profile 1 in Figure 3.11), was applied to represent the lithological features such as sedimentary structures and lithofacies assemblage for Face 1 of the lower bench. The sandstone unit is overlain by a thick, massive mudstone layer.

The upper bench in Figure 3.12 is approximately 55 m long and 6 m in height. The base of the upper bench (Figure 3.12) is a thick mudstone layer that occasionally contains siltstone and very fine-grained sandstone lenses which grades upwards into mudstone again. This top portion of the basal mudstone layer contains ball-and-pillow structures (refer, Figure 3.4). The upper bench sandstone unit comprises stacked sandstone lenses. The sandstone is coarse-grained at the base of the unit and grades upwards into a medium-grained sandstone both with moderate sorting. The sandstone mainly contain quartz, feldspar, lithic fragments with minor mica, carbonaceous matter and heavy minerals. In Figure 3.4 (Profile 1 in Figure 3.12), indicates the lithological features such as sedimentary structures and lithofacies assemblage for Face 1 of the upper bench.

Meters	Lithofacies assemblage	Lithology	Contacts	Sedimentary structure	Notes
5					
	Fm	Mudstone	Sharp	Massive	
4					
3					
2			Sharp	Horizontally bedded	
			Irregular	Gently-inclined HB	
	Sr			Ripple cross-bedded	Thin layer of
			Sharp		Lithofacies Sr
1					
0	Sh	Sandstone	Contact is covered by rubble	Horizontally bedded	

Figure 3.3: Summary of the lithological features and lithofacies assemblage in the lower bench on Face 1, Profile 1 (see, Figure 3.11). HB = horizontally bedded; Sh = horizontally bedded sandstone; Sr = ripple cross-laminated sandstone; Fm = massive mudstone.

Meters	Lithofacies Assemblage	Lithology	Contact	Sedimentary structure	Notes
7					
6			Erosional		Isolated clay pellets
			Sharp		
5			Sharp		
			Sharp		
			Sharp		
4					
3			Sharp		Isolated clay pellets
			Erosional		
	St	Sandstone	Gradational		Isolated clay pellets
	Fs	Mudstone	Erosional	Cross-bedded	
2			Gradational	Ball-and-pillow	Sandstone pillows
	vf sandstone		Gradational		
	FI	Siltstone	Sharp	Fine internal layering	
1					
0	Fm	Mudstone	Sharp	Massive	

Figure 3.4: Summary of the lithological features and lithofacies assemblage in the upper bench on Face 1, Profile 1 (refer, Figure 3.12). St = cross-bedded sandstone; Fs = massive mudstone with ball-and-pillow structures; FI = parallel laminated siltstone and mudstone; Fm = massive mudstone.

Face 2

Face 2, views towards the ESE with the face orientated NNE-SSW and is highlighted in the plan view in bold in Figures 3.13 and 3.14.

The lower bench in Figure 3.13 is approximately 54 m long and 4,2 m in height. Towards the SSW (Figure 3.13 B), where the base is exposed, a massive mudstone with ball-and-pillow structures occur. The sandstone consists of a very fine to fine-

grained sandstone with moderate sorting. The sandstone comprises quartz, feldspar, lithic fragments, mica, carbonaceous matter, and heavy minerals. In Figure 3.5 (Profile 3 in Figure 3.13) indicates the lithological features such as sedimentary structures and lithofacies assemblage for Face 2 of the lower bench. Towards the NNE the sandstone grades upward into a very fine-grained sandstone, then a siltstone unit which is overlain by mudstone.

The upper bench in Figure 3.14 is approximately 64 m long and 6 m in height. The base of the sandstone unit, in the upper bench (Figure 3.14), is a thin mudstone unit towards the NNE-side of the face and the sandstone continuous with the lower bench towards the SSW-side of the face. The sandstone unit is mostly medium-grained sandstone with moderate sorting. The major constituents are quartz, feldspar, lithic fragments with minor mica, carbonaceous matter and heavy minerals. In Figure 3.6 (Profile 1 in Figure 3.14) indicates the lithological features such as sedimentary structures and lithofacies assemblage for Face 2 of the upper bench. The base comprises sandstone with gently-inclined horizontally bedded units, attributing to an appearance of thin stacked lenses. In Face 2 numerous lenses (Figure 3.14 – Profiles) consisting of either massive clay pellet conglomerate with variable clast sizes or mudstone lenses (Figure 3.14) of variable thicknesses occur. Within the certain mudstone lenses, ball-and-pillow structures are readily observed.

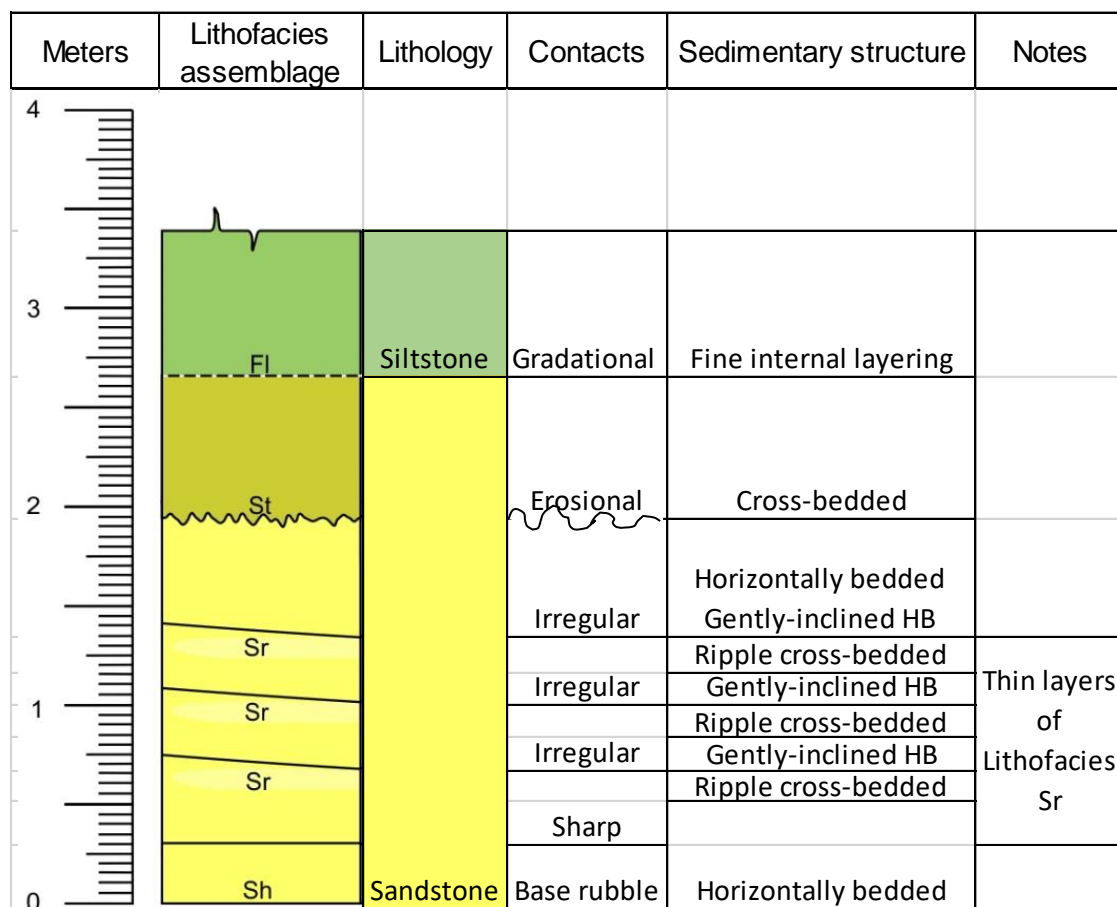


Figure 3.5: Summary of the lithological features and lithofacies assemblage in the lower bench on Face 2, Profile 3 (refer, Figure 3.13). HB = horizontally bedded; Sh = horizontally bedded sandstone; Sr = ripple cross-laminated sandstone; St = cross-bedded sandstone; Fl = parallel laminated siltstone and mudstone.

Meters	Lithofacies assemblage	Lithology	Contacts	Sedimentary structure	Notes
4	Sh	Sandstone	Erosional	Horizontally bedded	Isolated clay pellets
	Fm	Mudstone		Massive	
3	Sh		Erosional	Horizontally bedded	
			Erosional		
2			Sharp		
1			Erosional		Isolated clay pellets
0	St	Sandstone	Covered by rubble	Cross-bedded	

Figure 3.6: Summary of the lithological features and lithofacies assemblage in the upper bench on Face 2, Profile 1 (refer, Figure 3.14). Sh = horizontally bedded sandstone; St = cross-bedded sandstone; Fm = massive mudstone.

Face 3

Face 3, views towards the SSW with the face orientated ESE-WNW and is highlighted in the plan view in bold in Figures 3.15 and 3.16.

The lower bench in Figure 3.15 is approximately 55 m long and 5 m in height. At the base of Face 3 (Figure 3.15 B), towards the ESE-side, is a mudstone unit with ball-and-pillow structures. The sandstone unit is mostly fine to medium-grained sandstone with moderate sorting. The major constituents are quartz, feldspar, lithic fragments with minor mica, carbonaceous matter and heavy minerals. In Figure 3.7 (Profile 1 in Figure 3.15) indicates the lithological features such as sedimentary structures and lithofacies assemblage for Face 3 of the lower bench. In Face 3 numerous lenses (Figure 3.15 – Profiles) consisting of either massive clay pellet conglomerate with variable clast sizes or mudstone lenses. Where Lithofacies Sm (Figure 3.15 – Profile 2 & 3) is indicated, the sandstone units had a lack of sedimentary structures or it was obscured by rock breakage.

The upper bench in Figure 3.16 is approximately 63 m long and 5,5 m in height. The base of the sandstone, in the upper benches (Figure 3.16), is presumed to be a thin mudstone unit. The sandstone unit is mostly medium-grained with moderate sorting. The major constituents are quartz, feldspar, lithic fragments with minor mica, carbonaceous matter and heavy minerals. In Figure 3.8 (Profile 1 in Figure 3.16) indicates the lithological features and lithofacies assemblage for Face 3 of the upper bench. Thin mudstone lenses also occur locally between the sandstone unit elsewhere in Face 3 (Figure 3.16).

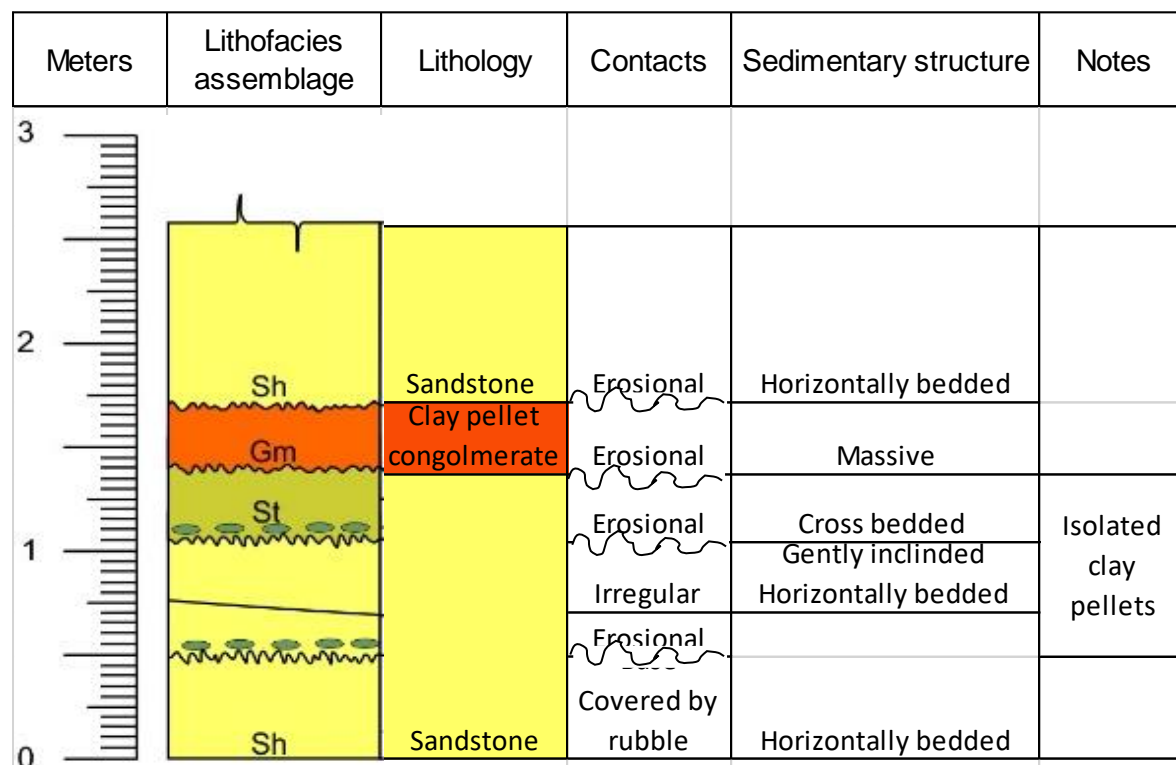


Figure 3.7: Summary of the lithological features and lithofacies assemblage in the lower bench on Face 3, Profile 1 (refer, Figure 3.15). HB = horizontally bedded; Gm = clay pellet conglomerate; Sh = horizontally bedded sandstone; St = cross-bedded sandstone.

Meters	Lithofacies assemblage	Lithology	Contacts	Sedimentary structure	Notes
5					
4	Sr		Erosional	Cross bedded	Thin layer of Lithofacies Sr
				Ripple cross-bedded	
3	St		Sharp	Cross-bedded	
			Sharp		
2	Sh		Irregular	Horizontally bedded Gently-inclined HB	
1	St		Erosional		Isolated clay pellets
			Erosional		
0	St	Sandstone	Covered by rubble	Cross-bedded	

Figure 3.8: Summary of the lithological features and lithofacies assemblage in the upper bench on Face 3, Profile 1 (refer, Figure 3.16). HB = Horizontally Bedded.

Face 4

Face 4, views towards the WNW with the face orientated SSW-NNE and is highlighted in the plan view in bold in Figures 3.17 and 3.18.

The lower bench in Figure 3.17 is approximately 45 m long and 4 m in height. The sandstone unit in the lower bench (Figure 3.17) consists of a fine-grained sandstone with moderate sorting. The sandstone comprises quartz, feldspar, lithic fragments, mica, carbonaceous matter, and heavy minerals. In Figure 3.9 (Profile 1 in Figure 3.17) indicates the lithological features such as sedimentary structures and lithofacies assemblage for Face 4 of the lower bench. The base comprises sandstone that is gently-inclined horizontally bedded units, attributing to an appearance of thin stacked lenses (Figure 3.17). The sandstone unit is overlain by a thick mudstone layer (about 2 m mudstone drape).

The upper bench in Figure 3.18 is approximately 66 m long and 5 m in height. The sandstone unit of the upper bench in Face 4 is medium-grained with moderate sorting. The major constituents are quartz, feldspar, lithic fragments with minor mica, carbonaceous matter and heavy minerals. In Figure 3.10 (Profile 1 in Figure 3.18) indicates the lithological features such as sedimentary structures and lithofacies assemblage for Face 4 of the lower bench. The contacts are sharp or erosional in cross-bedded sandstones. The base of the sandstone unit is cross-bedded with thin clay pellet conglomerates layers at the base with variable clast sizes (1mm to 50 mm).

Meters	Lithofacies assemblage	Lithology	Contacts	Sedimentary structure	Notes
3	St	Sandstone	Sharp	Cross-bedded	Isolated clay pellets
2			Sharp		
1	Sr		Sharp	Horizontally bedded	
				Ripple cross-bedded	Thin layers of Lithofacies Sr
	Sr		Irregular	Gently-inclined HB	
				Ripple cross-bedded	
0	Sh		Base rubble	Horizontally bedded	

Figure 3.9: Summary of the lithological features and lithofacies assemblage in the lower bench on Face 4, Profile 1 (refer, Figure 3.17). HB = horizontally bedded. Sh = horizontally bedded sandstone; Sr = ripple cross-laminated sandstone; St = cross-bedded sandstone.

Meters	Lithofacies assemblage	Lithology	Contacts	Sedimentary structure	Notes
5					
4	St	Sandstone	Irregular	Cross-bedded	
3	Sh		Sharp	Horizontally bedded	
2					
1			Erosional		Isolated clay pellets
0	St		Covered by rubble	Cross-bedded	

Figure 3.10: Summary of the lithological features and lithofacies assemblage in the upper bench on Face 4, Profile 1 (refer, Figure 3.18). Sh = horizontally bedded sandstone; St = cross-bedded sandstone.

It is clear from the fieldwork data that the upper and lower benches represent separate channel-fill systems. The lithologies mostly consist of sandstone and mudstone with minor siltstone and conglomerates. The sandstone units are composed of quartz, feldspar, lithic fragments, carbonaceous matter, and heavy minerals. The mudstone, siltstone, and conglomerate units occur as lenses and sheets between the sandstone units. The main differences between the upper and lower benches are: 1) the grain size of the lower bench is finer-grained compared to the upper bench, 2) the lower bench sandstone contains more carbonaceous material compared to the upper bench, and 3) the sedimentary structures in the lower bench is predominantly horizontally bedded compared to the predominantly cross-bedded upper bench.

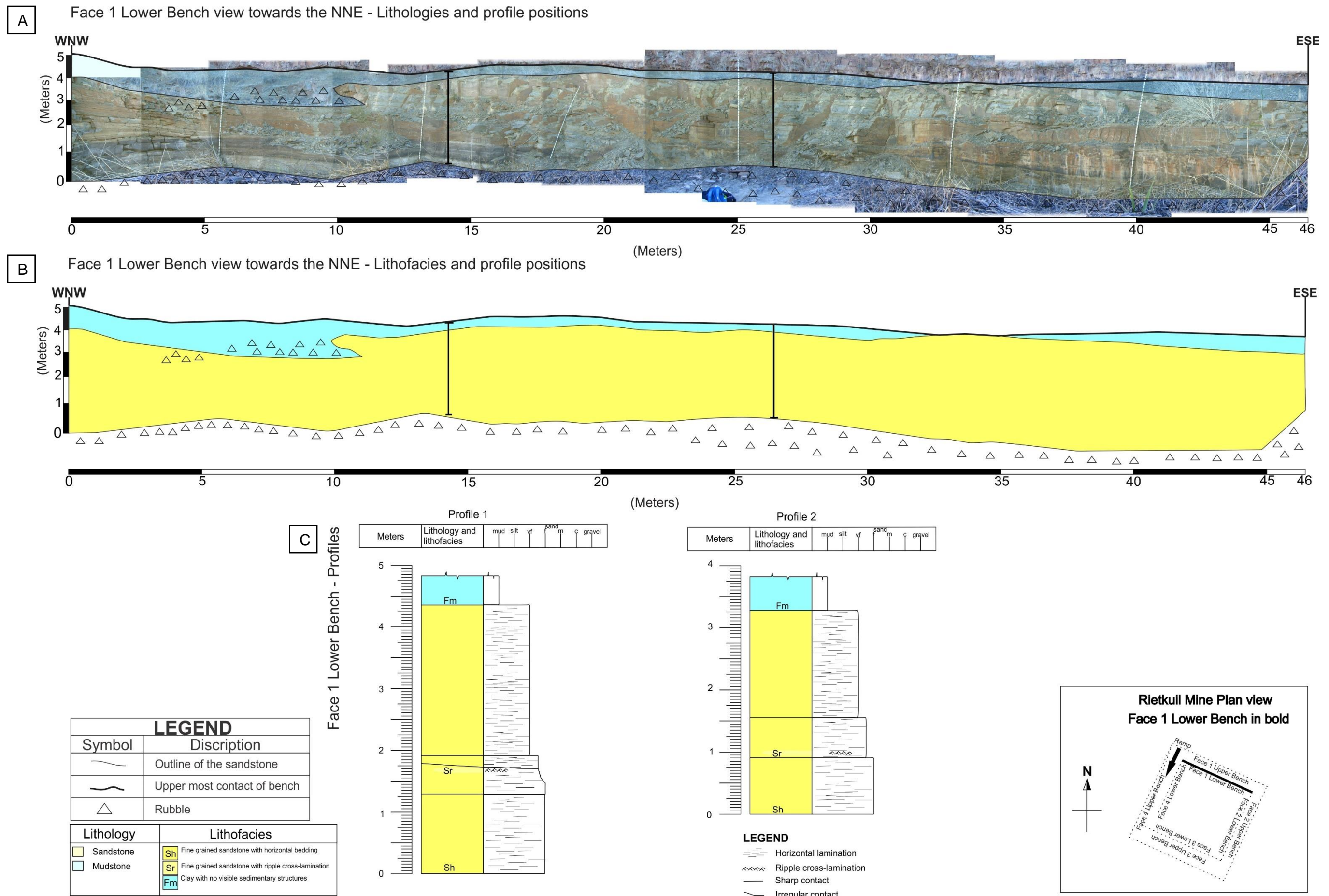


Figure 3.11: Face 1 Lower Bench orientated WNW-ESE, as seen in the plan view. A) The extent of lithological units in Face 1. B) The extent of the lithofacies assemblage in Face 1. C) The two detailed profiles drawn displaying lithology, lithofacies, grain size, and sedimentary structures.

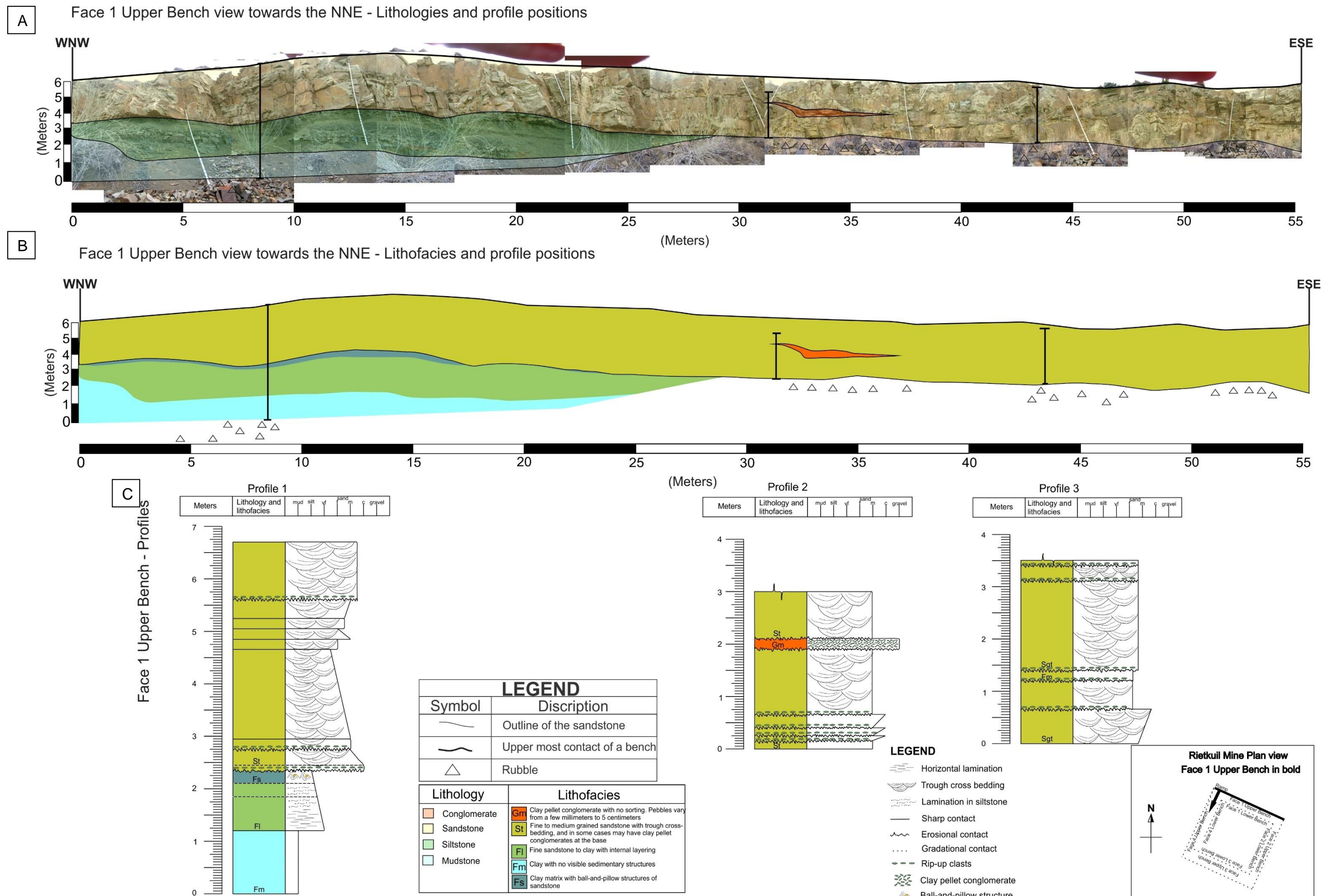


Figure 3.12: Face 1 Upper Bench orientated WNW-ESE, as seen in the plan view. A) The extent of lithological units in Face 1. B) The extent of the lithofacies assemblage in Face 1. C) The three detailed profiles drawn displaying lithology, lithofacies, grain size, and sedimentary structures.

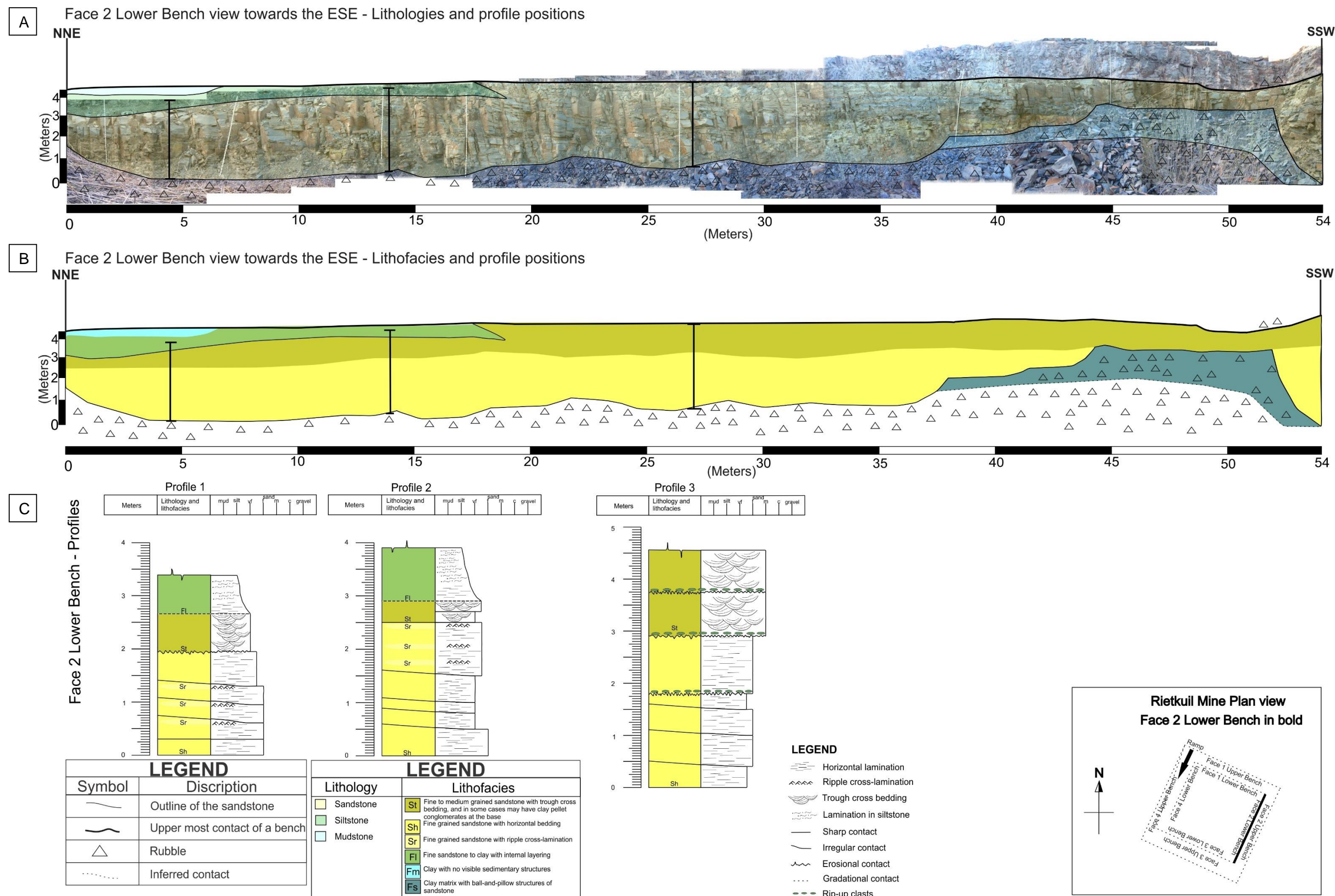


Figure 3.13: Face 2 Lower Bench orientated NNE-SSW, as seen in the plan view. A) The extent of lithological units in Face 1. B) The extent of the lithofacies assemblage in Face 1. C) The three detailed profiles drawn displaying lithology, lithofacies, grain size, and sedimentary structures.

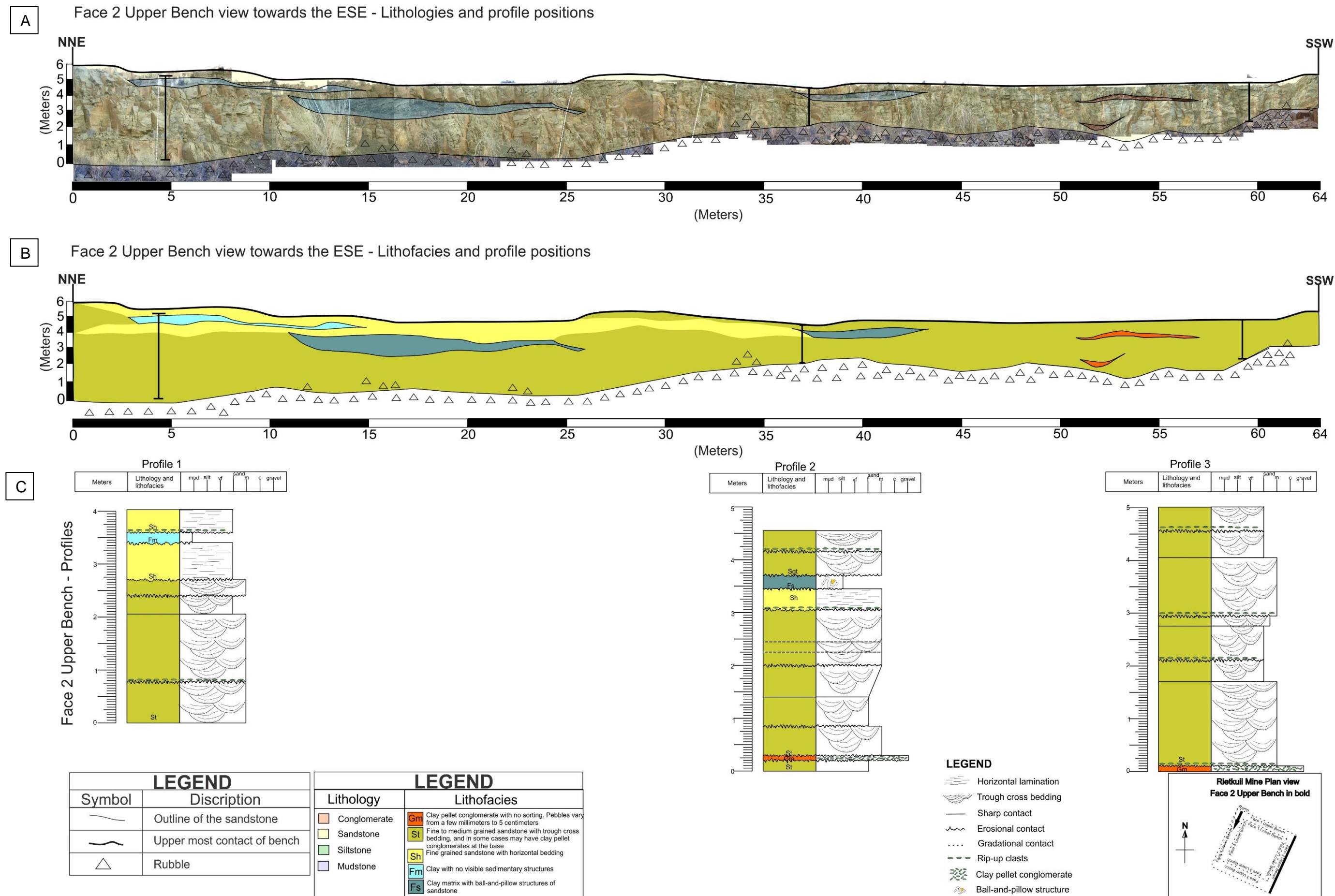
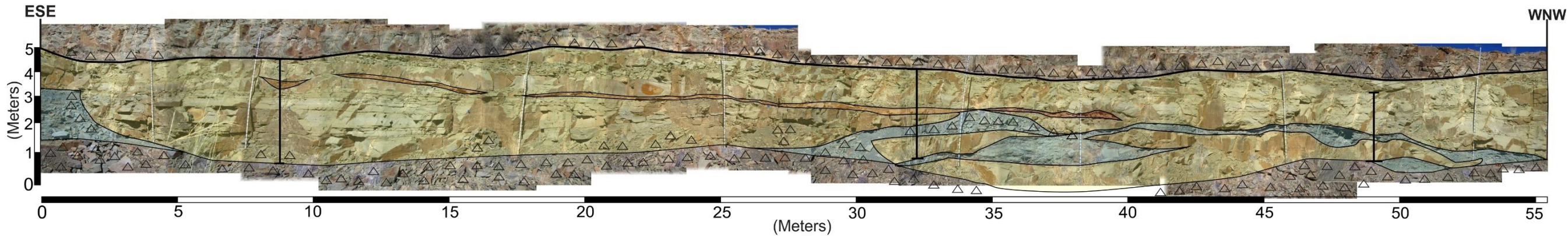
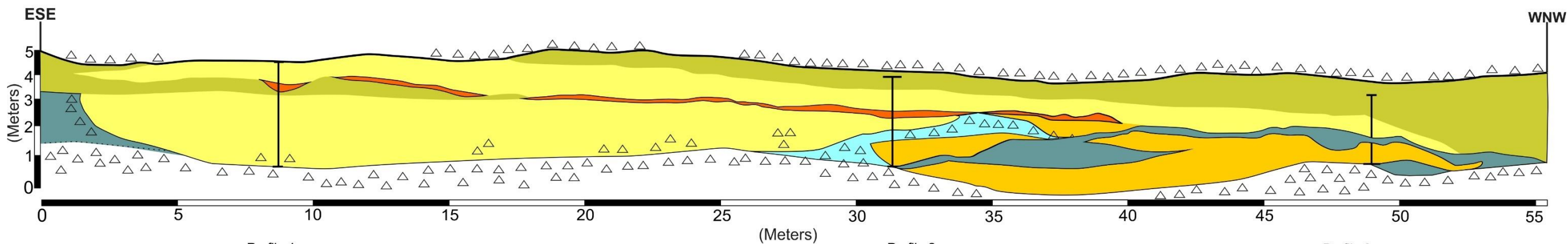


Figure 3.14: Face 2 Upper Bench orientated NNE-SSW, as seen in the plan view. A) The extent of lithological units in Face 1. B) The extent of the lithofacies assemblage in Face 1. C) The three detailed profiles drawn displaying lithology, lithofacies, grain size, and sedimentary structures.

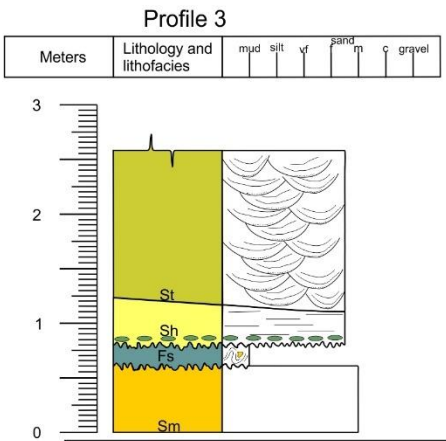
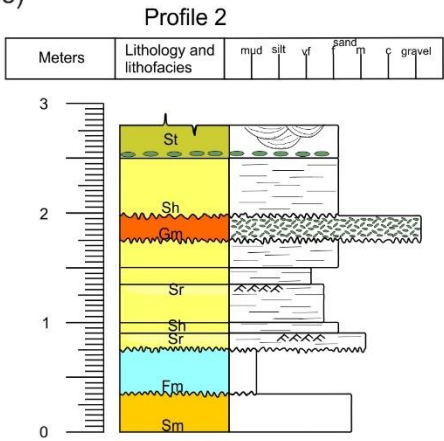
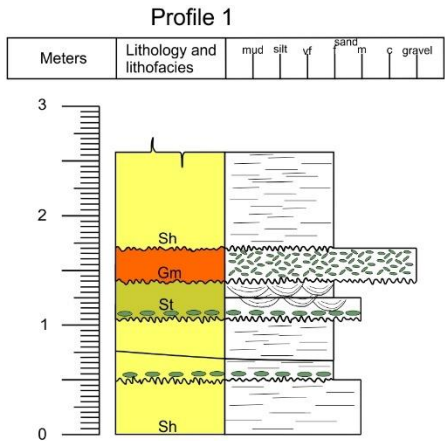
A Face 3 Lower Bench view towards the SSW - Lithologies and profile positions



B Face 3 Lower Bench view towards the SSW - Lithofacies and profile positions



C Face 3 Lower Bench - Profiles



LEGEND	
Symbol	Discription
	Outline of the sandstone
	Upper most contact of a bench
	Rubble
	Inferred contact

LEGEND	
Lithology	Lithofacies
Conglomerate	Clay pellet conglomerate with no sorting. Pebbles vary from a few millimeters to 5 centimeters
Sandstone	Fine to coarse grained sandstone with no visible sedimentary structures
Siltstone	Fine to medium grained sandstone with trough cross bedding, and in some cases may have clay pellet conglomerates at the base
Mudstone	Fine grained sandstone with horizontal bedding
	Fine grained sandstone with ripple cross-lamination
	Clay with no visible sedimentary structures
	Clay matrix with ball-and-pillow structures of sandstone

LEGEND	
	Horizontal lamination
	Ripple cross-lamination
	Trough cross bedding
	Sharp contact
	Irregular contact
	Erosional contact
	Rip-up clasts
	Clay pellet conglomerate
	Ball-and-pillow structure

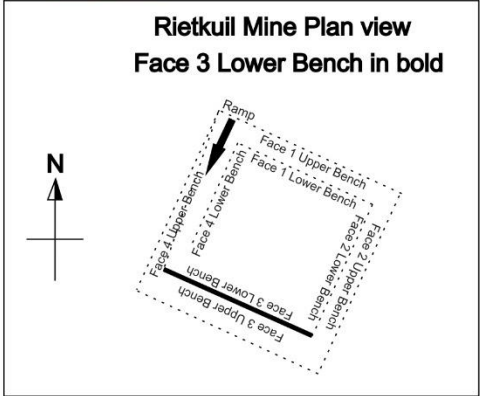


Figure 3.15: Face 3 Lower Bench orientated ESE-WNW, as seen in the plan view. A) The extent of lithological units in Face 1. B) The extent of the lithofacies assemblage in Face 1. C) The three detailed profiles drawn displaying lithology, lithofacies, grain size, and sedimentary structures.

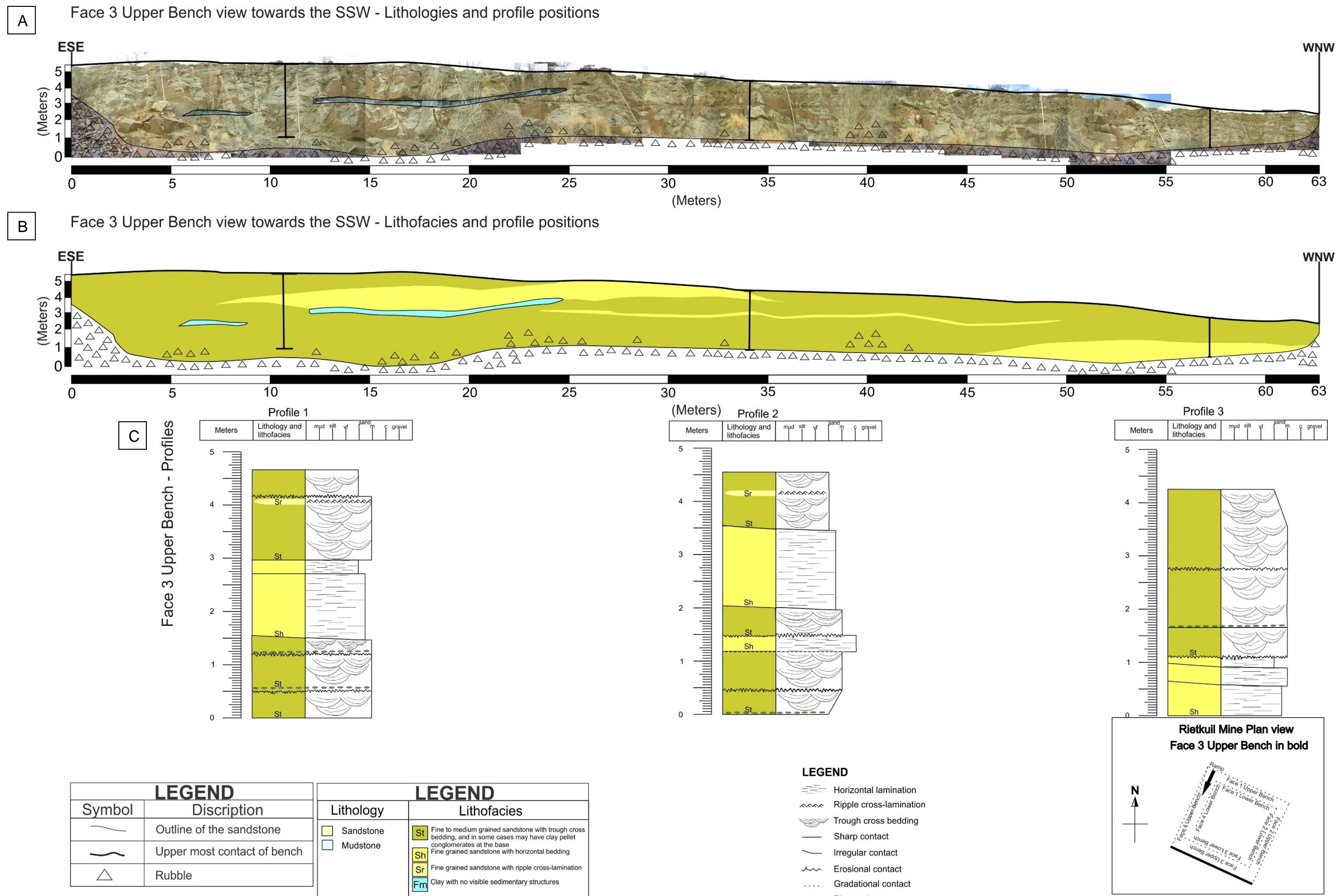


Figure 3.16: Face 3 Upper Bench orientated ESE-WNW, as seen in the plan view. A) The extent of lithological units in Face 1. B) The extent of the lithofacies assemblage in Face 1. C) The three detailed profiles drawn displaying lithology, lithofacies, grain size, and sedimentary structures.

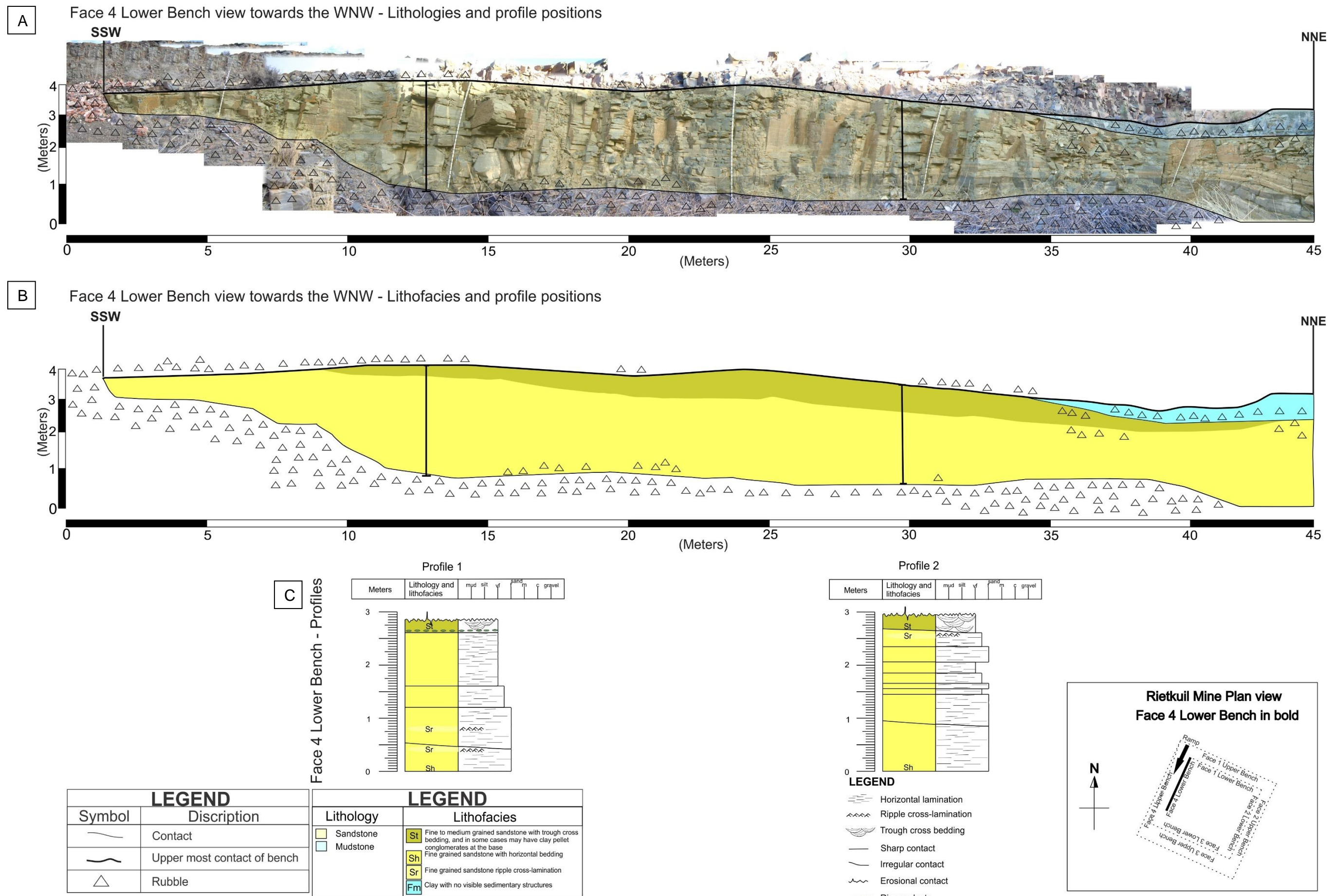


Figure 3.17: Face 4 Lower Bench orientated SSW-NNE, as seen in the plan view. A) The extent of lithological units in Face 1. B) The extent of the lithofacies assemblage in Face 1. C) The two detailed profiles drawn displaying lithology, lithofacies, grain size, and sedimentary structures.

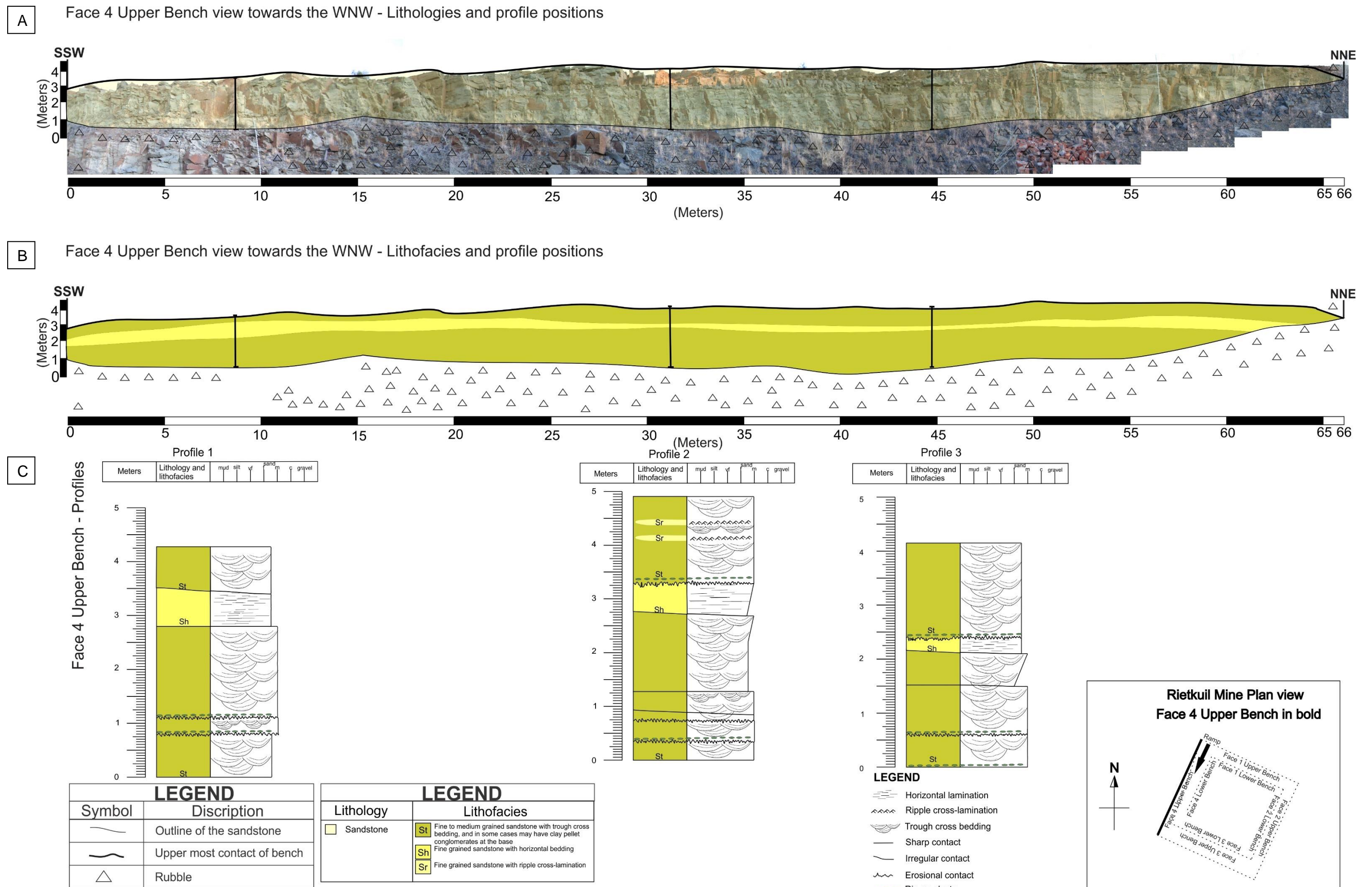


Figure 3.18: Face 4 Upper Bench orientated SSW-NNE, as seen in the plan view. A) The extent of lithological units in Face 1. B) The extent of the lithofacies assemblage in Face 1. C) The three detailed profiles drawn displaying lithology, lithofacies, grain size, and sedimentary structures.

3.1.4 Tectonic features

According to research conducted by Jordaan (1990), joints in the Main Karoo Basin occur as conjugated sets trending north-south, east, and northeast. Furthermore, these joints are readily filled with quartz or calcite. Jordaan (1990) also described the folds in the western Main Karoo Basin and found the fold axes to trend east-west. Jordaan (1990) furthermore describes the faults in the western Main Karoo Basin as strike-slip faults with lateral displacement and little vertical displacement. Furthermore, Jordaan (1990) suggested that the faults are associated with the breaking of fold hinges and the sense of movement is shown by slickensides on vein quartz filling. Jordaan (1990) suggested that these tectonic features formed as a result of the formation of the Cape Fold Belt.

At Rietkuil mine three major joint structures are present (Figure 3.20 to Figure 3.23). The blue lines represent joints that strike 88° (easterly); the green lines are joints that strike 168° (south-southeasterly) and; the red lines are joints that strike 133° (southeasterly). Overall, the dip of the joints is practically vertical (85° to 88°). The joints that strike in the eastern direction are occasionally filled with calcite (Figure 3.19-A & B) that effervesces when acid was poured onto it. Furthermore, adjacent to the joint structures, there are thin halos of very low-grade metamorphosed sandstone (Figure 3.19-B & C).

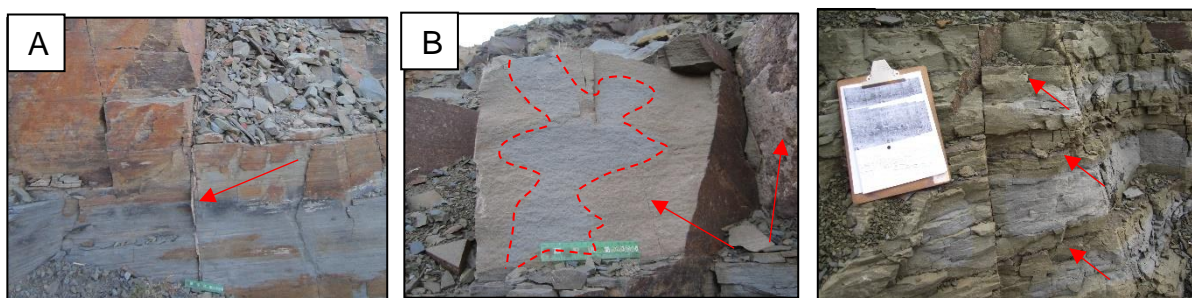


Figure 3.19: A) The arrow shows calcite mineralization in a joint. B) The arrows show sandstone with a low-grade metamorphic halo adjacent to joint structures and calcite mineralization on a joint plane. C) The arrows show low-grade metamorphic halo between horizontally bedded sandstone layers adjacent to a joint.

The joints were only counted in the lower bench. The joints were counted, plotted on a mosaics/lateral profiles and where calcite occurs in the joints, a little blue circle was drawn above the corresponding joint. The cross section was then divided into 5 m intervals and within those, the joints were counted and histograms were constructed. This aided the identification of areas with a higher intensity of joints, for later correlations. The Rietkuil mine plan view schematic in Figure 3.20 to Figure 3.23, represents the joint strikes as measured.

As described in section 3.1.1 (see, Figure 3.1) other tectonic features in close vicinity to Rietkuil mine are an open-anticline and a lineament with slickensides.

Face 1

Face 1, views towards the NNE with the face orientated WNW-ESE and is highlighted in the plan view in bold (Figure 3.20).

The easterly joints are by far the most dominant joint set present. On occasion, the joints are filled with calcite. Calcite veins (Figure 3.20B) were encountered at approximately; 9, 16, 22 and 33 m. A total of 50 easterly joints were counted and their positions indicated in Figure 3.20B. There is a marked increase in the density of the easterly joints as indicated in the histograms (Figure 3.20C) between 5 to 10 m and particularly between 15 to 35 m.

The south-southeasterly joints are few and relatively dispersed. A total of 11 south-southeasterly joints were counted and their positions on the face is indicated in Figure 3.20B. There is a marked increase (Figure 3.20C) in the 20 to 25 m interval.

The southeasterly joints are also very few. A total of 6 southeasterly joints were counted and their positions on the face is indicated in Figure 3.20B. The highest number occurs between 20 to 25 m.

Considering all three joint strikes, the highest number of joints occurs between 15 to 25 m (Table 3.2).

Face 2

Face 2, views towards the ESE with the face orientated NNE-SSW and is highlighted in the plan view in bold (Figure 3.21).

The easterly joints are the most dominant joint set present. On occasion, the joints are filled with calcite. Calcite veins (Figure 3.21B) were encountered at approximately; 3, 18, 34, 39 and 44 m. A total of 89 easterly joints were counted and their position on the face is indicated in Figure 3.21B. The easterly joints are fairly evenly dispersed across the face with a slight increase in density of the joints as indicated in the histograms (Figure 3.21C) between 0 to 5 m and 10 to 20 m.

The south-southeasterly joints are also very prominent in this face. A total of 36 South-southeasterly joints were counted and their positions indicated in Figure 3.21B. There are clear intervals (Figure 3.21C) with a marked increase in south-southeasterly joints between; 0 to 5 m, 20 to 25 m, 35 to 40 m, and 45 to 50 m.

The southeasterly joints are few and dispersed across the face. A total of 20 southeasterly joints were counted and their positions indicated in Figure 3.21B. There are two intervals (Figure 3.21C) with an increased number of joints. They occurred between 5 to 10 m and 35 to 40 m.

Considering all three joint strikes, the highest number of joints occurs between 35 to 40 m and 45 to 50 m (Table 3.2).

Face 3

Face 3, views towards the SSW with the face orientated ESE-WNW and is highlighted in the plan view in bold (Figure 3.22).

The easterly joints are the most dominant joint set in this face. On occasion, the joints are filled with calcite. Calcite veins (Figure 3.22B) were encountered at approximately; 4, 22, 33 and 47 m. A total of 49 easterly joints were counted and their positions indicated in Figure 3.22B. There is a marked increase in the density of the easterly joints as displayed in the histograms (Figure 3.22C) between 15 to 35 m.

The south-southeasterly joints are also prominent in this face and evenly dispersed across the face. A total of 21 south-southeasterly joints were counted and their positions indicated in Figure 3.22B. There is an increase (Figure 3.22C) in the number of joints between 35 to 50 m intervals.

The southeasterly joints are less prominent in Face 3. A total of 7 southeasterly joints were counted and their positions indicated in Figure 3.22B. The highest number (Figure 3.22C) of joints is counted between 5 and 10 m.

Considering all three joint strikes, the highest number of joints occurs between 15 to 20 m and 25 to 35 m (Table 3.2).

Face 4

Face 4, views towards the WNW with the face orientated SSW-NNE and is highlighted in the plan view in bold (Figure 3.23).

The easterly joints are the dominant joint set present in Face 4. On occasion, the joints are filled with calcite. Calcite veins (Figure 3.23B) were encountered at approximately; 9, 19, 22, 27, 29, 32 and 41 m. A total of 46 easterly joints were counted and their position indicated in Figure 3.23B. There is a marked increase in the density of the easterly joints as indicated in the histograms (Figure 3.23C) between 5 to 10 m and particularly between 15 to 30 m and 35 to 40 m.

The south-southeasterly joints are also prominent in Face 4. A total of 23 south-southeasterly joints were counted and their position indicated in Figure 3.23B. There is an increase (Figure 3.23C) in the 0 to 5 m-, 20 to 25 m- and 30 to 35 m intervals.

The southeasterly joints are few and widely dispersed over the face. A total of 8 southeasterly joints were counted and their positions are indicated in Figure 3.23B. The highest number (Figure 3.23C) of southeasterly joints occurs between 15 to 20 m.

Considering all three joint strikes, the highest number of joints occurs between 15 to 25 m (Table 3.2).

Table 3.2: Summary of the total number of joints in each face in the lower bench separated into 5 m intervals. The blue blocks indicated intervals with calcite vein filling.

	0-5 m	5-10 m	10-15 m	15-20 m	20-25 m	25-30 m	30-35 m	35-40 m	40-45 m	45-50 m	50-55 m
Face 1	1	6	5	13	15	8	9	4	2	2	
Face 2	15	15	14	15	15	14	9	16	12	16	3
Face 3	6	4	6	9	8	9	9	6	7	8	5
Face 4	9	10	7	13	12	11	11	10	3		

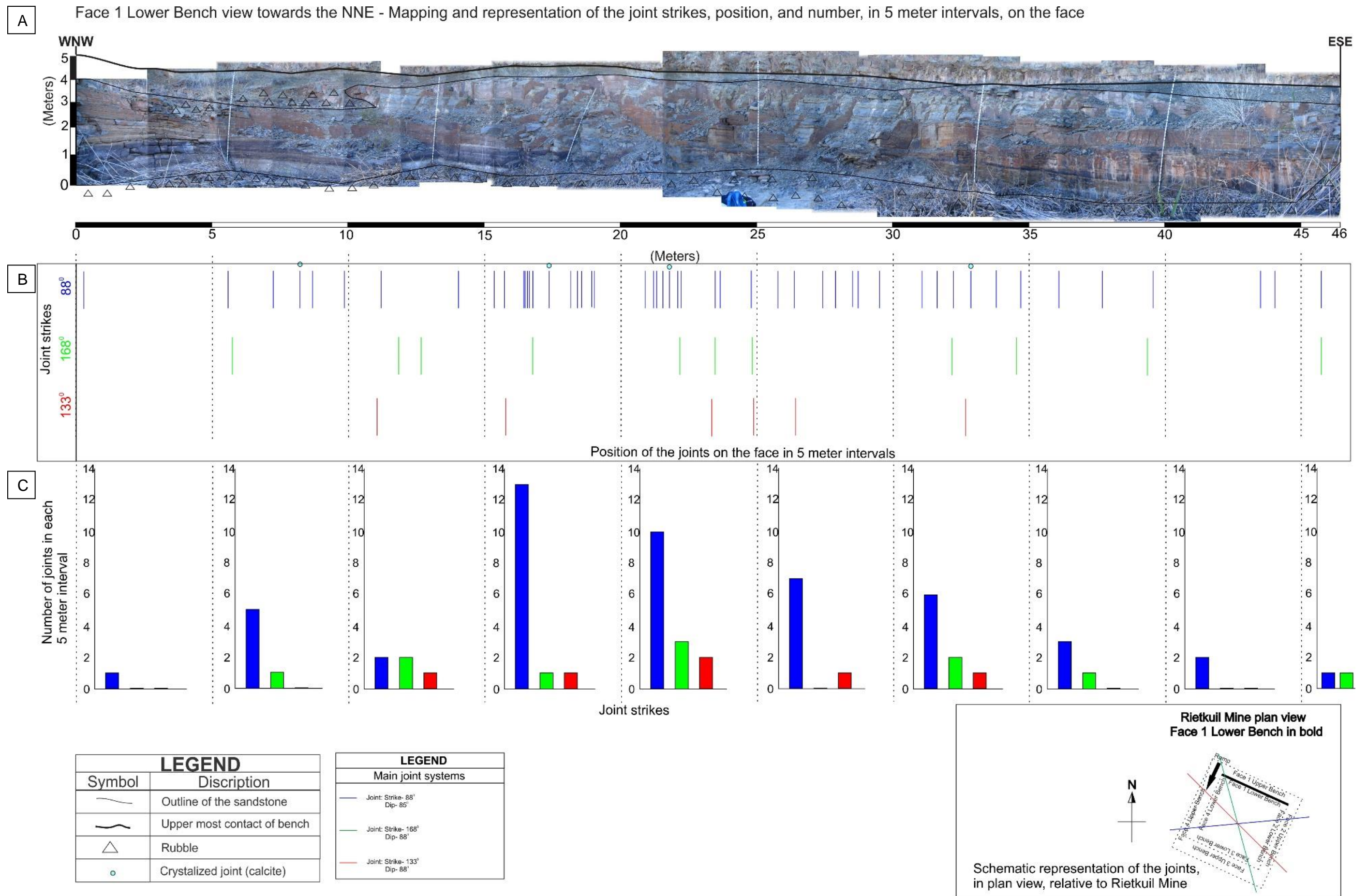


Figure 3.20: Face 1 Lower Bench Joints. A) Photo-panorama of Face 1, with the sandstone outline and the uppermost contact of the bench. B) The position of the joints on Face 1, with the strikes coordinated by color. Calcite veins are indicated with a blue circle. C) The number of each joint strike counted in 5 m intervals.

A Face 2 Lower Bench view towards the ESE - Mapping and representation of the joint strikes, position, and number, in 5 meter intervals, on the face

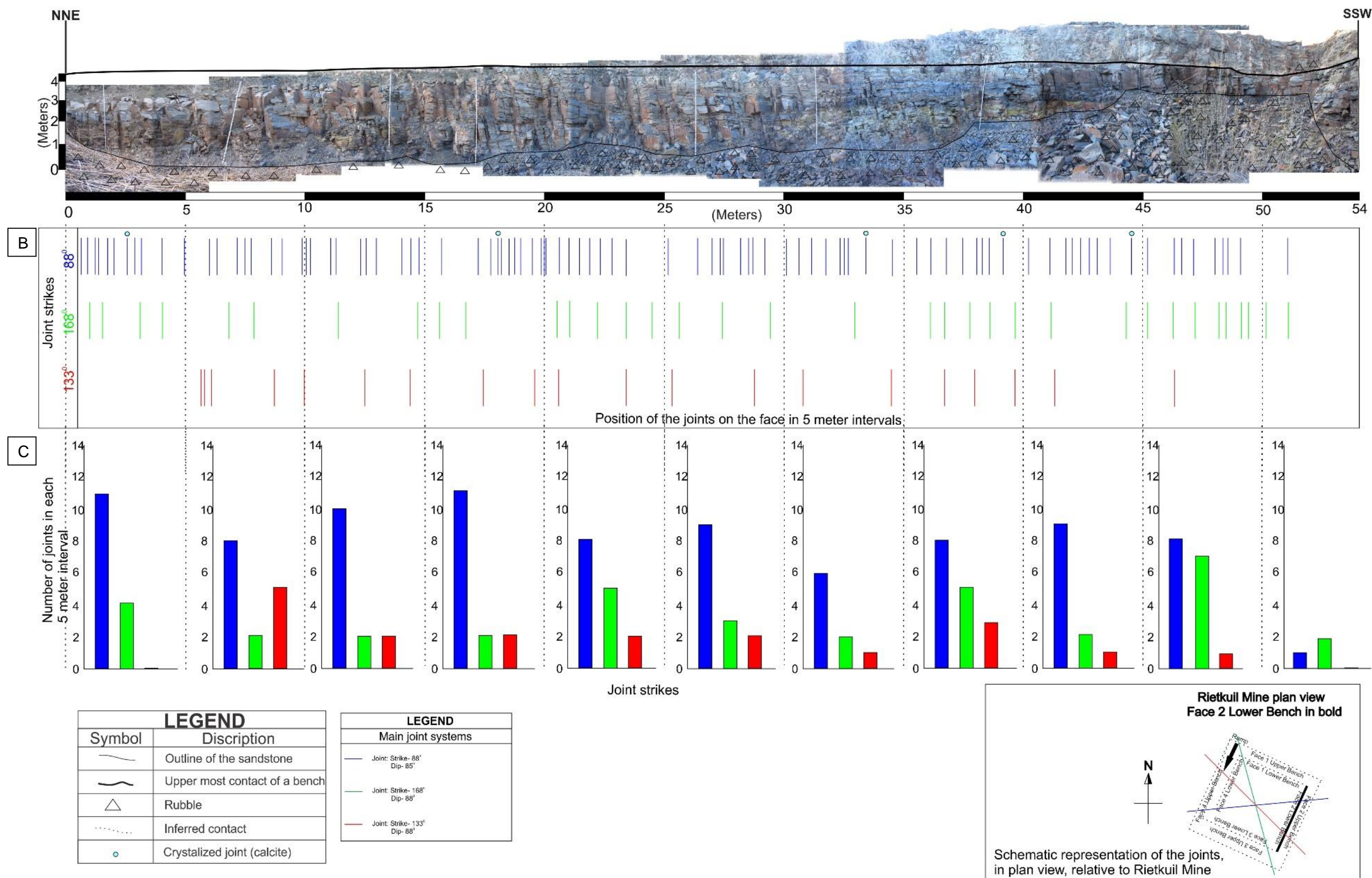


Figure 3.21: Face 2 Lower Bench Joints. A) Photo-panorama of Face 2, with the sandstone outline and the uppermost contact of the bench. B) The position of the joints on Face 2, with the strikes coordinated by color. Calcite veins are indicated with a blue circle. C) The number of each joint strike counted in 5 m intervals.

A Face 3 Lower Bench view towards the SSW - Mapping and representation of the joint strikes, position, and number, in 5 meter intervals, on the face

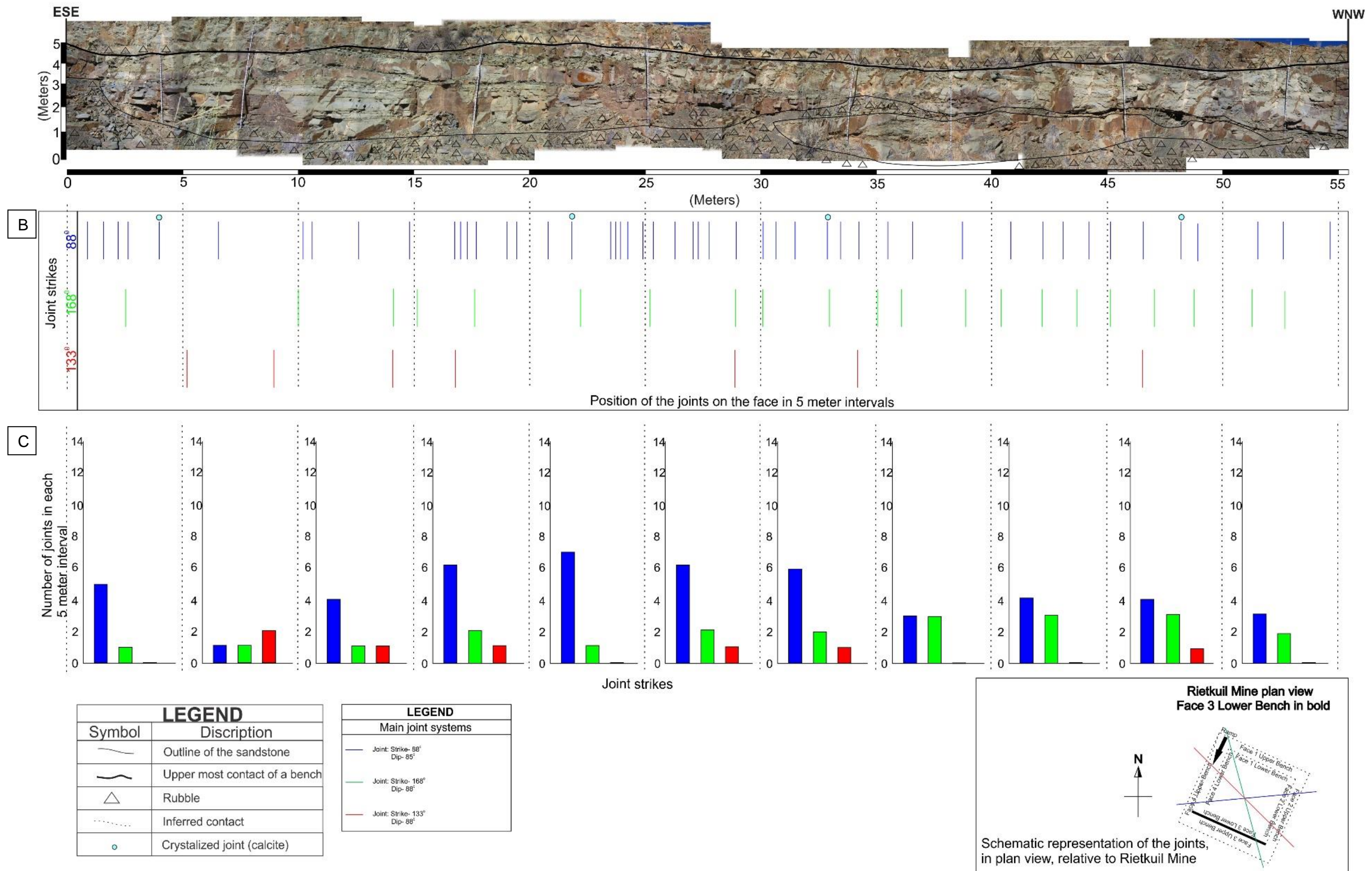


Figure 3.22: Face 3 Lower Bench Joints. A) Photo-panorama of Face 3, with the sandstone outline and the uppermost contact of the bench. B) The position of the joints on Face 3, with the strikes coordinated by color. Calcite veins are indicated with a blue circle. C) The number of each joint strike counted in 5 m intervals.

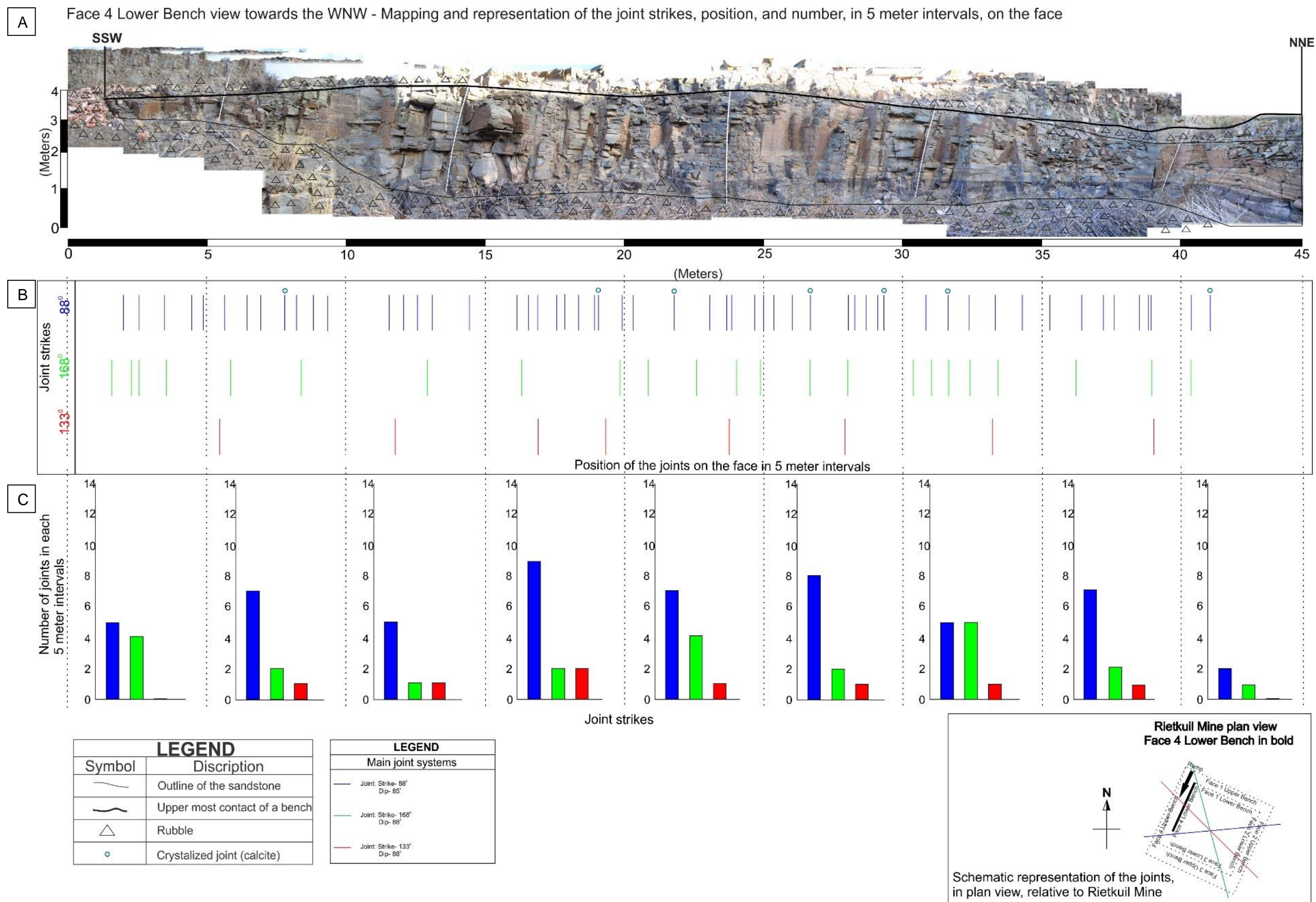


Figure 3.23: Face 4 Lower Bench Joints. A) Photo-panorama of Face 4, with the sandstone outline and the uppermost contact of the bench. B) The position of the joints on Face 4, with the strikes coordinated by color. Calcite veins are indicated with a blue circle. C) The number of each joint strike counted in 5 m intervals.

3.1.5 Uranium distribution (Gamma-Ray)

The gamma-ray contour maps were constructed to illustrate the dispersion of radioactive mineralization (uranium distribution) across the faces of the lower bench in Rietkuil mine. Contour lines were drawn at 0, 500, 1000, 1500, 2000, and 3000 cps (counts per second), measured with the scintillometer.

The upper bench (Appendix G-Figure 1G to 4G) showed low cps readings, between 40 to 250 cps indicating no 'hot-spots' as all the values fall within the 0 to 500 cps contour field. For this reason, there were no gamma-ray contour maps created for the upper faces.

The lower bench, however, showed a significant increase in cps readings that varied from smaller than 500 to more than 3000 cps on some of the faces. The contours were compiled on mosaics/lateral profiles displayed in Figure 3.24 to Figure 3.27. For the purpose of this study values above 1000 cps were considered to be potentially mineralized as from this value there is a sharp increase in the cps reading. Localities where samples were collected for geochemical analysis were numbered along with the values obtained from the XRF in parts per million (ppm). This was prepared so that the uranium concentrations (XRF) could be compared with the radioactive mineralization (cps). It could be noted that overall, the cps readings decrease from the base to the top of the sandstone units as seen in Figure 3.24 to Figure 3.27. The uranium mineralization presented as sporadic hot-spots along the faces, from which the concentrations decrease upwards and to the sides (*i.e.* circular or half-moon shaped). This may indicate a fluid intrusion along weak zones into the sandstone.

Face 1

Face 1, views towards the NNE with the face orientated WNW-ESE (highlighted in the plan view in bold in Figure 3.24).

The shape of the contours is elliptical. There are two zones of mineralization with readings higher than 1000 cps, from 0 to 13 m and 14 to 33 m. The highest readings were measured between 15 to 26 m with values higher than 2000 cps but lower than 3000 cps.

Face 2

Face 2, views towards the ESE with the face orientated NNE-SSW (highlighted in the plan view in bold in Figure 3.25).

The shape of the contours is circular to semi-elliptical. There are three zones of mineralization with readings higher than 1000 cps, from approximately 3 to 8 m, 13 to 28 m, and 28 to 49 m. The highest readings were measured between 18 to 22 m and between 38 to 47 m with values higher than 2000 cps but lower than 3000 cps.

Face 3

Face 3, views towards the SSW with the face orientated ESE-WNW (highlighted in the plan view in bold in Figure 3.26).

The shape of the contours is elliptical and circular. There are two zones of mineralization with readings higher than 500 cps but lower than 1000 cps, from approximately 3 to 9 m. The highest readings were measured at 40 m with a single

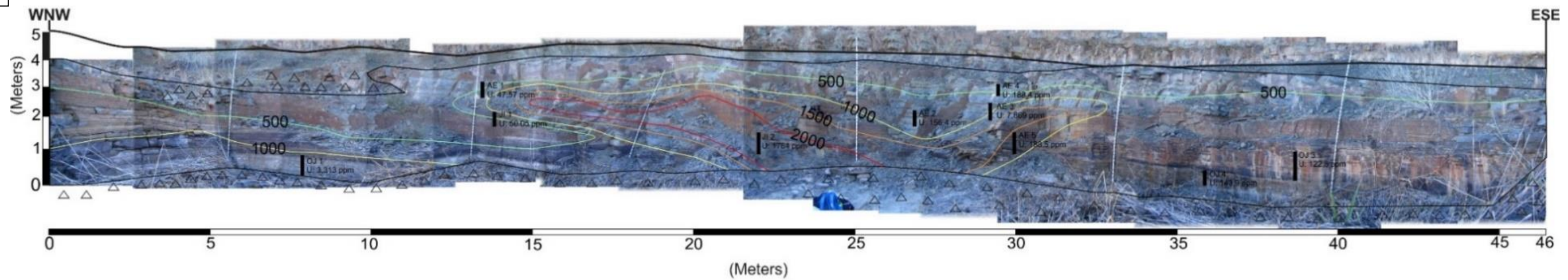
hot-spot with values higher than 3000 cps. The rest of this face had measurements lower than 500 cps.

Face 4

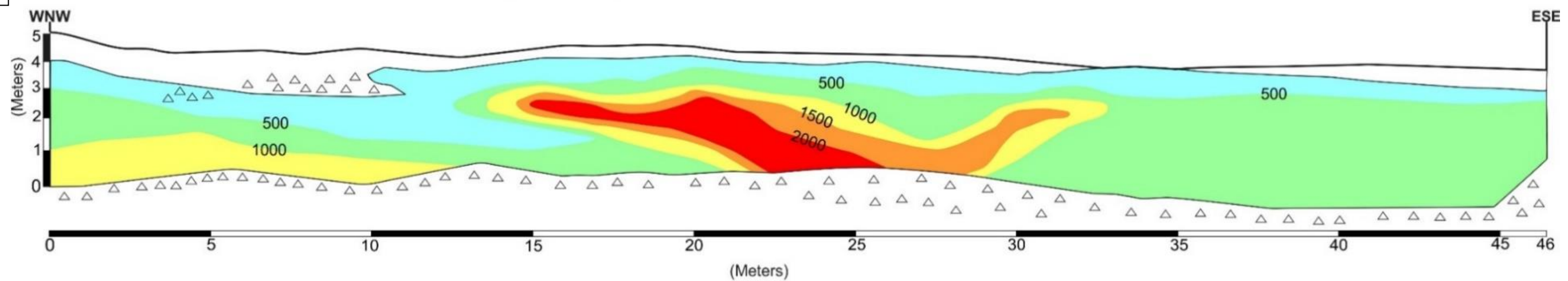
Face 4, views towards the WNW with the face orientated SSW-NNE (highlighted in the plan view in bold in Figure 3.27).

The shape of the contours is circular. There is one continuous zone of mineralization with readings higher than 1000 cps, from 8 to 45 m. The highest readings were measured between 10 to 12 m, 14 to 18 m, and 33 to 37 m with values higher than 3000 cps.

A Face 1 Lower Bench view towards the NNE - Gamma-ray contour map, along with sample positions and uranium concentration



B Face 1 Lower Bench view towards the NNE - Gamma-ray contour map



LEGEND	
Symbol	Description
	Outline of the sandstone
	Upper most contact of bench
	Rubble

LEGEND	
Gamma-ray contour map in counts per second (cps)	
	0-499 cps
	500-999 cps
	1000-1499 cps
	1500-1999 cps
	2000-2999 cps

LEGEND	
Uranium Samples	
	Sample number
	Uranium concentration in ppm, measured with the XRF

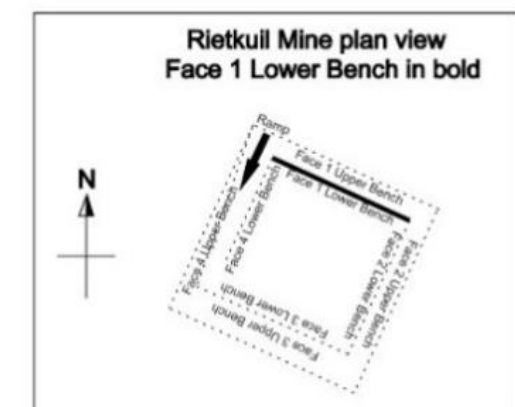
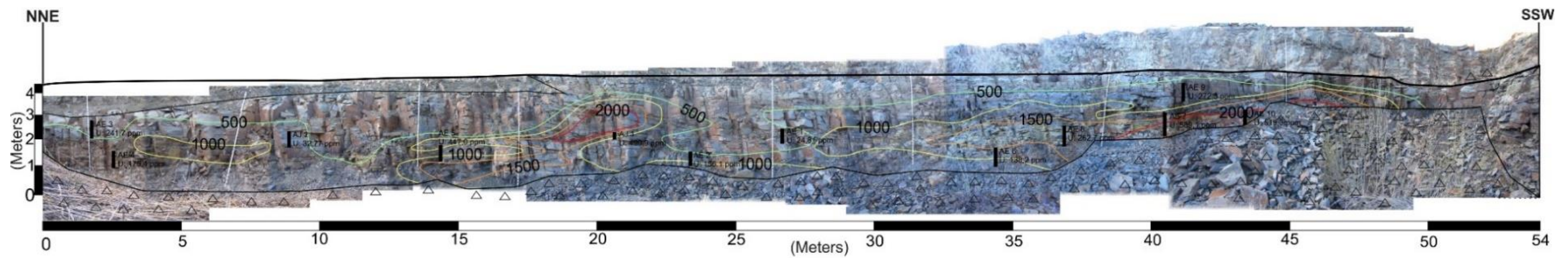
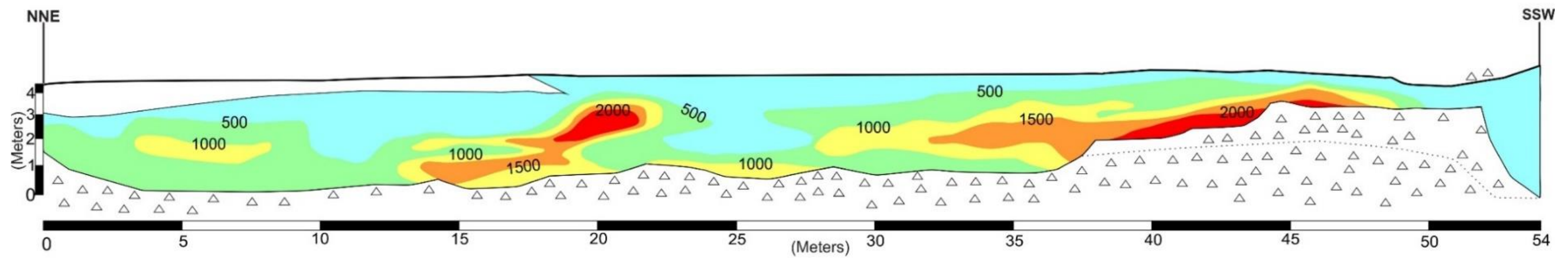


Figure 3.24: The uranium distribution in Face 1 Lower Bench. A) A photo-panorama of Face 1 with uranium distribution contour lines, sample collection localities, and XRF uranium results. B) A Gamma-Ray contour map of the uranium distribution in Face 1, with the highest readings to center of more than 2000 cps.

A Face 2 Lower Bench view towards the ESE - Gamma-ray contour map, along with sample positions and uranium concentrations



B Face 2 Lower Bench view towards the ESE - Gamma-ray contour map



LEGEND	
Symbol	Description
	Outline of the sandstone
	Upper most contact of a bench
	Rubble
	Inferred contact

LEGEND	
Gamma-ray contour map in counts per second (cps)	
	0-499 cps
	500-999 cps
	1000-1499 cps
	1500-1999 cps
	2000-2999 cps

LEGEND	
Uranium Samples	
	Sample number
	U: Uranium concentration in ppm, measured with the XRF

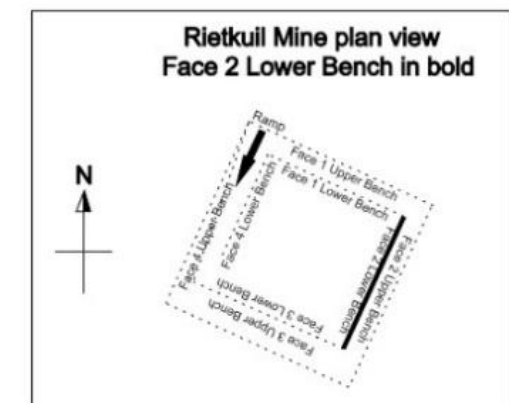
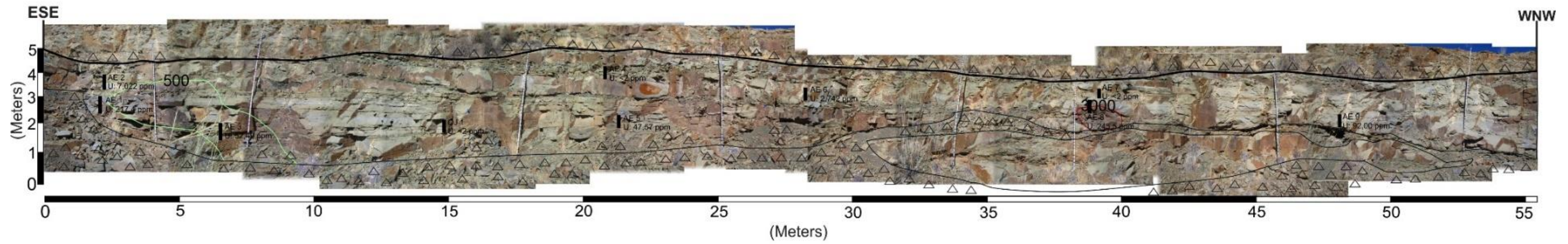
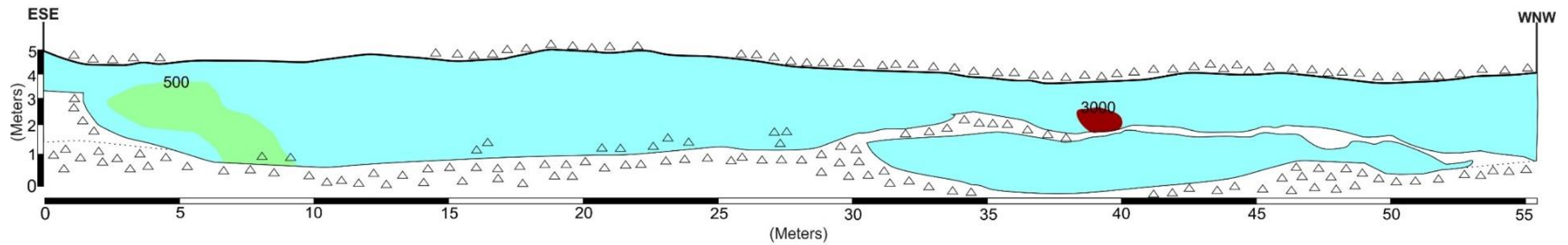


Figure 3.25: The uranium distribution in Face 2 Lower Bench. A) A photo-panorama of Face 2 with uranium distribution contour lines, sample collection localities, and XRF uranium results. B) A Gamma-Ray contour map of the uranium distribution in Face 2, with the two hot-spots of more than 2000 cps.

A Face 3 Lower Bench view towards the SSW - Gamma-ray contour map, along with sample positions and uranium concentrations



B Face 3 Lower Bench view towards the SSW - Gamma-ray contour map



LEGEND	
Symbol	Description
	Outline of the sandstone
	Upper most contact of a bench
	Rubble
	Inferred contact

LEGEND	
Gamma-ray contour map in counts per second (cps)	
	0-499 cps
	500-999 cps
	> 3000 cps

LEGEND	
Uranium Samples	
	Sample number
	U: Uranium concentration in ppm, measured with the XRF

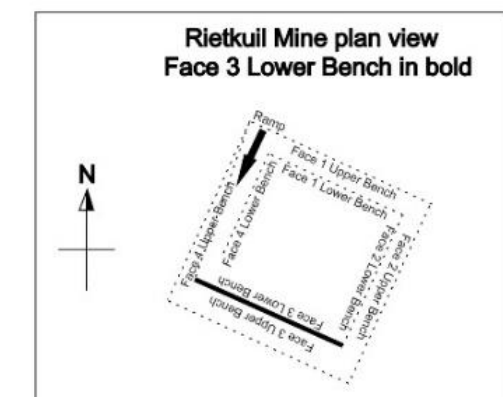
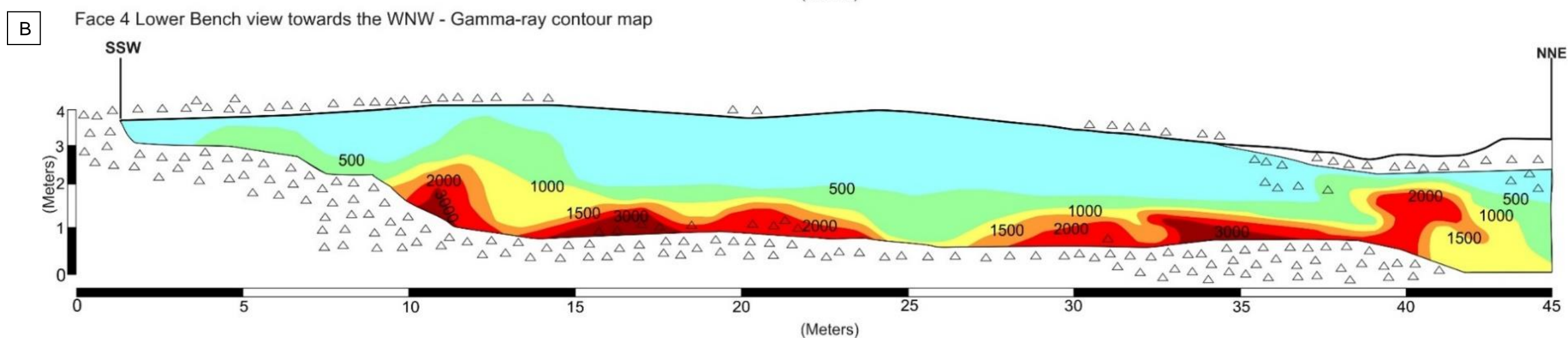
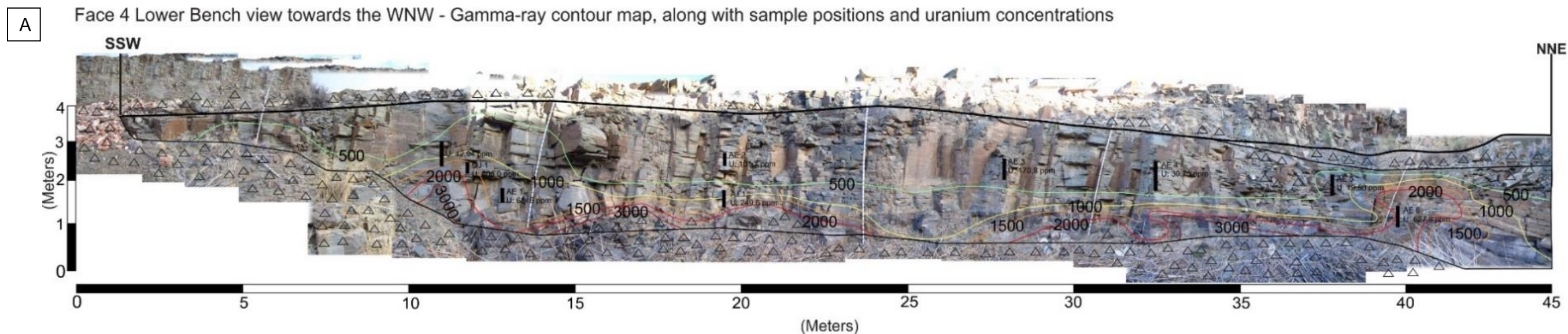


Figure 3.26: The uranium distribution in Face 3 Lower Bench. A) A photo-panorama of Face 3 with uranium distribution contour lines, sample collection localities, and XRF uranium results. B) A Gamma-Ray contour map of the uranium distribution in Face 3, with the a single hot-spot of more than 3000 cps.



LEGEND	
Symbol	Description
	Outline of the sandstone
	Upper most contact of bench
	Rubble

LEGEND	
Gamma-ray contour map in counts per second (cps)	
	0-499 cps
	500-999 cps
	1000-1499 cps
	1500-1999 cps
	2000-2999 cps
	> 3000 cps

LEGEND	
Uranium Samples	
	Sample number
	U: Uranium concentration in ppm, measured with the XRF

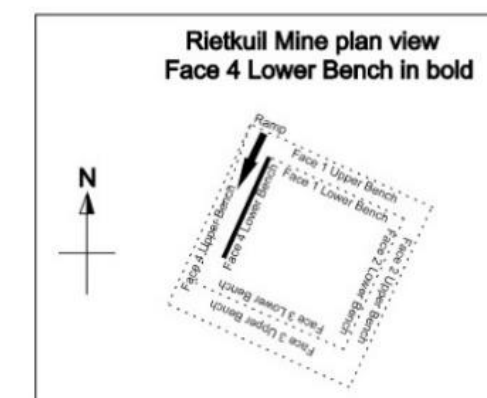


Figure 3.27: The uranium distribution in Face 4 Lower Bench. A) A photo-panorama of Face 4 with uranium distribution contour lines, sample collection localities, and XRF uranium results. B) A Gamma-Ray contour map of the uranium distribution in Face 4, with multiple hot-spots to the base of the face of more than 3000 cps.

3.1.6 Carbon distribution

The carbon that occurs in the lower bench can be classified in 5 different fractions (Figure 3.28):

- (1) carbon (<1 mm) that is finely distributed throughout the sandstone units. On the sandstone bedding plains, the carbon is elongated and flat, wood-like and is 1 to 2 cm in size;
- (2) carbon that is confined to sandstone laminations. Carbon (<1 mm) confined to lamina surfaces are finely distributed along these sandstone laminae. On the sandstone bedding plains, the carbon is rounded and flat, wood-like and is 1 to 2 mm in size;
- (3) carbon that is confined to the sandstone bedding plains. The carbon is rounded and flat, wood-like and is about 1 mm in size;
- (4) carbon that is highly dispersed; and
- (5) carbon that occurs as fragments are coal-like in nature, with various sizes and are confined to certain bedding planes or locally as single clasts. Carbon fragments are often associated with clay pellet rip-up clasts and leached pyrite (now iron-oxide).

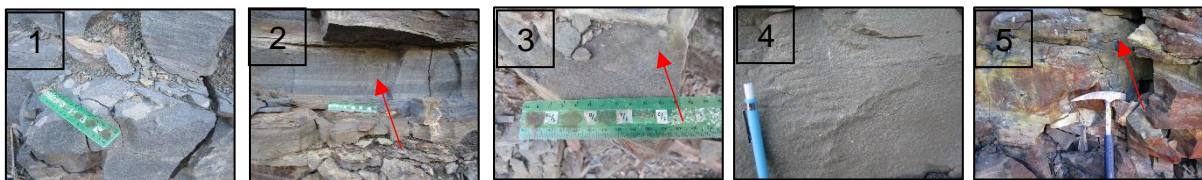


Figure 3.28: The 5 fractions the carbon was classified as. 1) The carbon is finely distributed throughout the sandstone. 2) The carbon is confined to laminae. 3) The carbon is confined to bedding planes. 4) The carbon is highly dispersed. 5) Carbon occurs as coaly fragments.

In the upper bench (Appendix G-Figure 1G to 4G) carbon was highly dispersed. For this reason, there were no carbon dispersion maps created for these faces.

The lower benches, however, showed a significant increase in carbon content (refer to the channel-like sandstone bodies that were mapped and indicated in Figure 3.29 to Figure 3.32). The 5 described fractions were assigned a color to present them on the mosaics/lateral profiles. Localities where samples were collected for geochemical analysis were numbered along with the concentration values (%) obtained from the LECO analyzer. The LECO analyzer uses a very small amount of sample (0,2 g sample) and thus the smallest grain of carbon can make a significant impact on the results, for this reason visual estimations were used to describe the dispersion of the carbon within the sandstones. This was done so that the carbon concentrations (LECO) can be compared with the dispersion of carbon described.

Face 1

Face 1, views towards the NNE with the face orientated WNW-ESE and is highlighted in the plan view in bold in Figure 3.29.

The carbon content is the highest at the base of the sandstone unit in Face 1. At the base, the carbon is finely distributed throughout sheet-like sandstone bodies. Within the finely distributed carbon zone, there are carbon fragments that are mainly confined to specific horizons between 31 to 46 m, although single carbon fragments occur

throughout the sandstone at this location. The carbon fragments occur associated with iron-oxide. Upwards the carbon content decreases and becomes highly dispersed.

Face 2

Face 2, views towards the ESE with the face orientated NNE-SSW and is highlighted in the plan view in bold in Figure 3.30.

The carbon content in Face 2, is the highest at the base of the sandstone unit. At the base, the carbon is finely distributed throughout channel-like sandstone bodies. Within these finely distributed carbon zones between 0 to 5 m and 37 to 43 m. The carbon fragments are mainly confined to specific horizons possibly representing a palaeosol horizon or a confinement where larger amounts of organic material could be deposited. Single carbon fragments occur throughout the sandstone in these locations. The carbon fragments occur associated with iron-oxide and clay pellet rip-up clasts. Upwards the carbon content decreases and becomes highly dispersed.

Face 3

Face 3, views towards the SSW with the face orientated ESE-WNW and is highlighted in the plan view in bold in Figure 3.31.

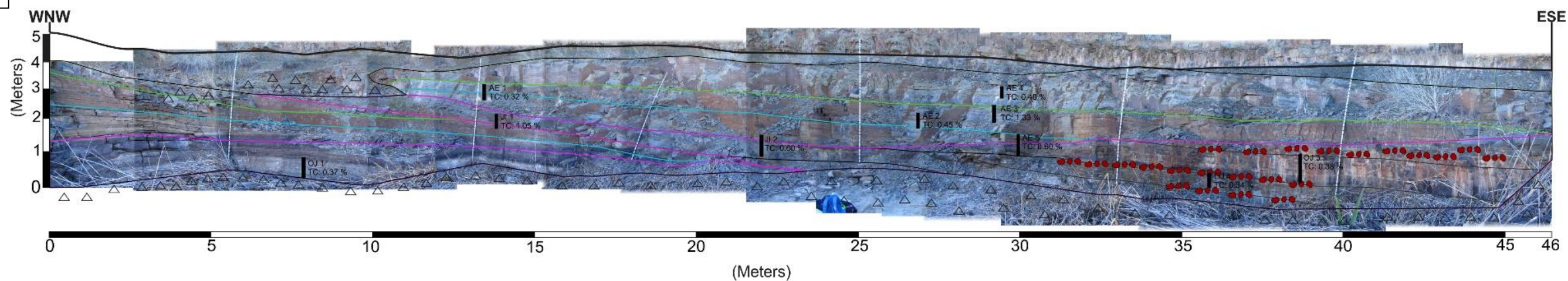
The carbon content in Face 3, decrease upwards throughout the sandstone unit. The carbon content in this face is generally highly dispersed but where the carbon content is higher, it is confined to laminae or bedding planes in the sandstone. There is a single confined area at 40 m where the carbon is finely distributed throughout the sandstone unit.

Face 4

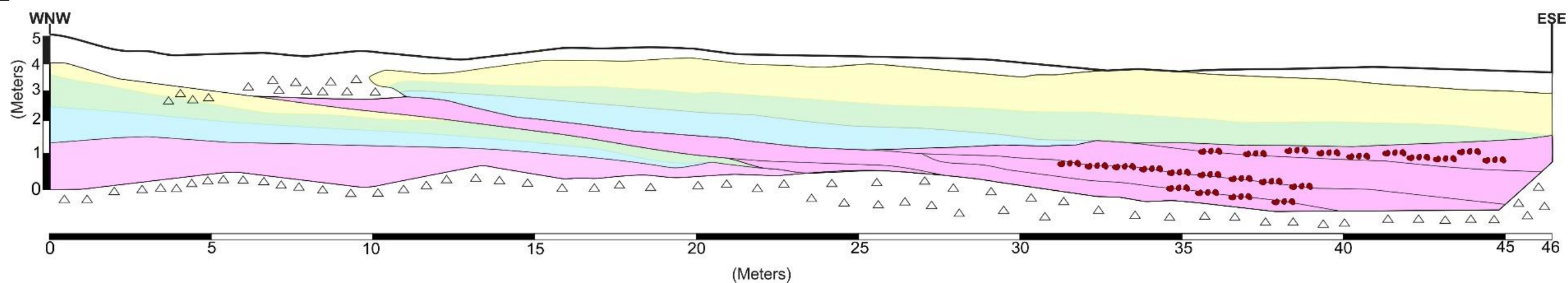
Face 4, views towards the WNW with the face orientated SSW-NNE and is highlighted in the plan view in bold in Figure 3.32.

The carbon content is the highest at the base of the sandstone unit, in Face 4. At the base, the carbon is finely distributed throughout channel-like sandstone bodies. Single carbon fragments occur throughout the sandstone. Upwards the carbon content decreases, firstly in confined to thin laminae in the sandstone, then bedding planes until finally, it becomes highly dispersed.

A Face 1 Lower Bench view towards the NNE - Carbon distribution, along with sample positions and carbon concentrations



B Face 1 Lower Bench view towards the NNE - Carbon distribution



LEGEND	
Symbol	Description
	Sandstone outline
	Upper most contact of bench
	Rubble

LEGEND	
Carbon distribution description	
	Carbon is finely (< 1 mm) distributed throughout the entire confined area. On sandstone bedding plains, elongated and flat, woody carbon occur between 1-2 cm
	Carbon is confined to sandstone laminae. The carbon is finely (< 1 mm) distributed within laminae. On sandstone bedding plains, rounded and flat, woody carbon occur between 1-2 mm
	Carbon is confined to sandstone bedding plains. On sandstone bedding plains, rounded and flat, woody carbon occur 1 mm
	Very little to no carbon occurs
	Carbon fragments

LEGEND	
Carbon Samples	
	Sample number
	TC: Total carbon (%), measured with the LECO

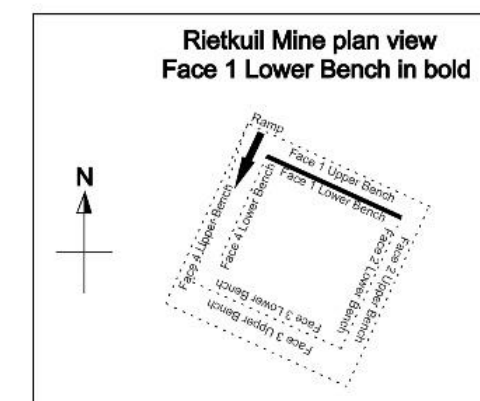
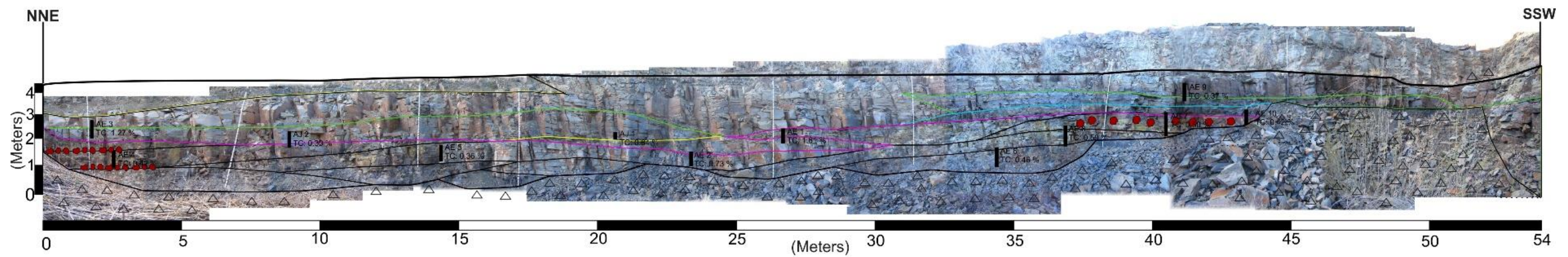
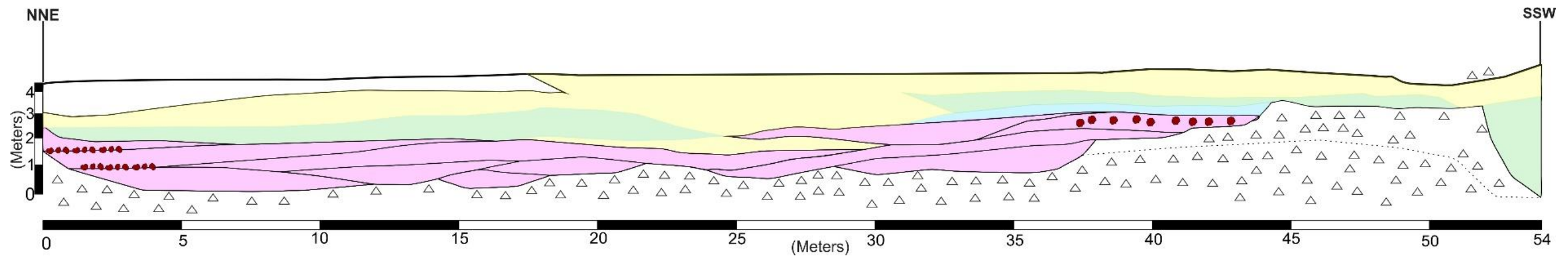


Figure 3.29: The carbon distribution in Face 1 Lower Bench. A) A photo-panorama of Face 1 with carbon distribution, sample collection localities, and carbon concentrations measured by the LECO Analyzer. B) Carbon distribution in Face 1.

A Face 2 Lower Bench view towards the ESE - Carbon distribution, along with sample positions and carbon concentrations



B Face 2 Lower Bench view towards the ESE - Carbon distribution



LEGEND	
Symbol	Description
	Sandstone outline
	Upper most contact of a bench
	Rubble
	Inferred contact

LEGEND	
Carbon distribution description	
	Carbon is finely (< 1 mm) distributed throughout the entire confined area. On sandstone bedding plains, elongated and flat, woody carbon occur between 1-2 cm
	Carbon is confined to sandstone laminae. The carbon is finely (< 1 mm) distributed within laminae. On sandstone bedding plains, rounded and flat, woody carbon occur between 1-2 mm
	Carbon is confined to sandstone bedding plains. On sandstone bedding plains, rounded and flat, woody carbon occur 1 mm
	Very little to no carbon occurs
	Carbon fragments

LEGEND	
Carbon Samples	
	Sample number
	TC: Total carbon (%), measured with the LECO

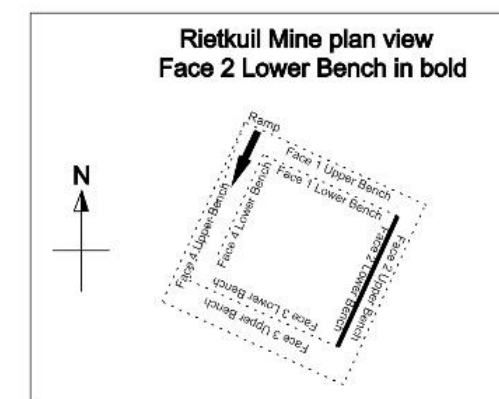
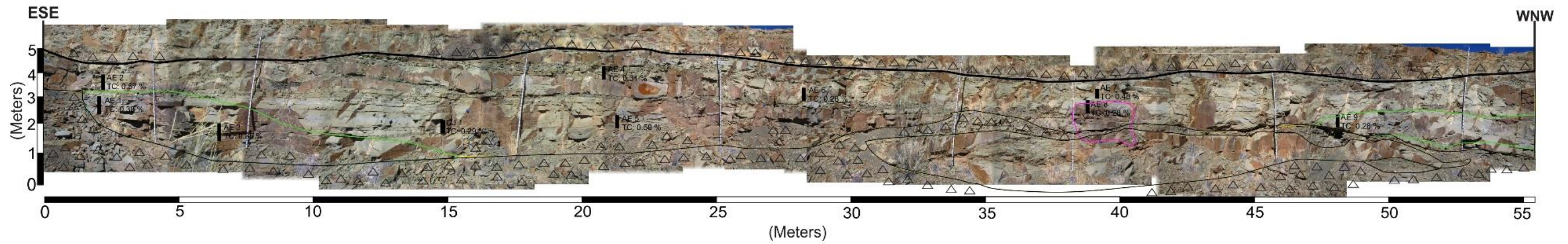
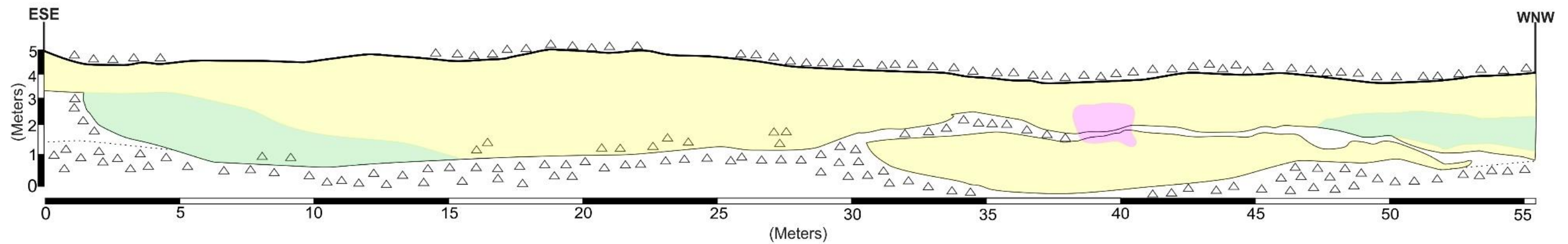


Figure 3.30: The carbon distribution in Face 2 Lower Bench. A) A photo-panorama of Face 2 with carbon distribution, sample collection localities, and carbon concentrations measured by the LECO Analyzer. B) Carbon distribution in Face 2.

A Face 3 Lower Bench view towards the SSW - Carbon distribution, along with sample positions and carbon concentrations



B Face 3 Lower Bench view towards the SSW - Carbon distribution



LEGEND	
Symbol	Description
	Sandstone outline
	Upper most contact of a bench
	Rubble
	Inferred contact

LEGEND	
Carbon distribution description	
	Carbon is finely (< 1 mm) distributed throughout the entire confined area. On sandstone bedding plains, elongated and flat, woody carbon occur between 1-2 cm
	Carbon is confined to sandstone bedding plains. On sandstone bedding plains, rounded and flat, woody carbon occur 1 mm
	Very little to no carbon occurs

LEGEND	
Carbon Samples	
	Sample number
	TC: Total carbon (%), measured with the LECO

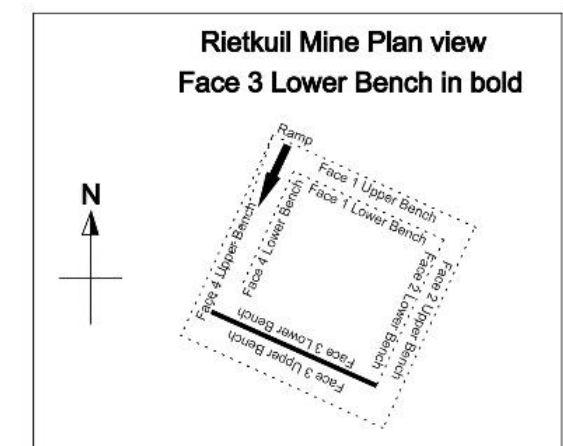
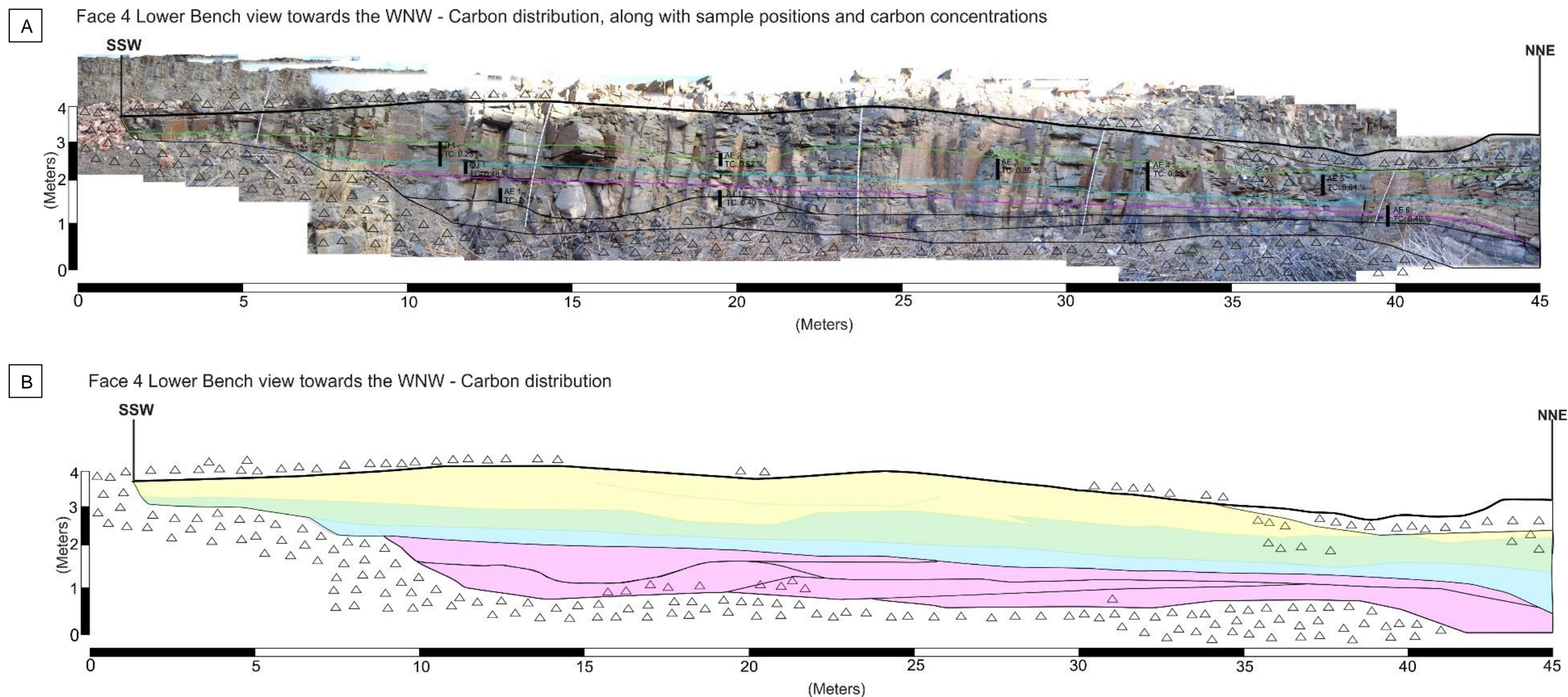


Figure 3.31: The carbon distribution in Face 3 Lower Bench. A) A photo-panorama of Face 3 with carbon distribution, sample collection localities, and carbon concentrations measured by the LECO Analyzer. B) Carbon distribution in Face 3.



LEGEND	
Symbol	Discription
	Sandstone outline
	Upper most contact of bench
	Rubble

LEGEND	
Carbon distribution description	
	Carbon is finely (< 1 mm) distributed throughout the entire confined area. On sandstone bedding plains, elongated and flat, woody carbon occur between 1-2 cm
	Carbon is confined to sandstone laminae. The carbon is finely (< 1 mm) distributed within laminae. On sandstone bedding plains, rounded and flat, woody carbon occur between 1-2 mm
	Carbon is confined to sandstone bedding plains. On sandstone bedding plains, rounded and flat, woody carbon occur 1 mm
	Very little to no carbon occurs
	Carbon fragments

LEGEND	
Carbon Samples	
	Sample number
	TC: Total carbon (%), measured with the LECO

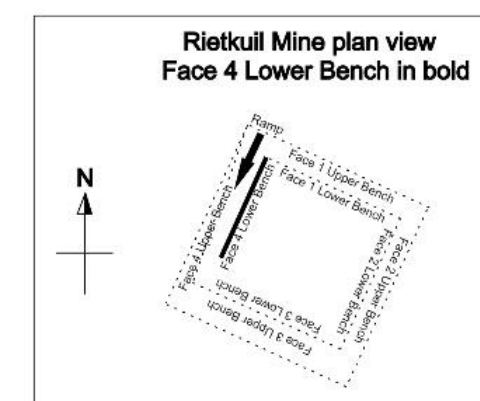


Figure 3.32: The carbon distribution in Face 4 Lower Bench. A) A photo-panorama of Face 4 with carbon distribution, sample collection localities, and carbon concentrations measured by the LECO Analyzer. B) Carbon distribution in Face 4.

3.2 Petrography

The samples that were collected are indicated in the sections of the mine (Figure 2.1 to Figure 2.4). Fieldwork identified the lower bench as the main mineralized zone.

3.2.1 Petrographic description

For the microscopy (Appendix A-A2), 17 randomly selected samples (Figure 2.1 to Figure 2.4, refer to the red stars) were analyzed for its modal mineralogy (Table 3.3). This was applied to determine the source of the sediments, classify the sandstone, and to analyze how the ore minerals are associated with the gangue minerals.

Table 3.3: The estimated modal mineralogical composition for 17 sandstone samples from at Rietkuil mine.

Detrital minerals	% Abundance	Autogenic minerals	% Abundance
Quartz	42-66	Opaque	2-10
Feldspar	3-6	Alteration minerals:	
Chert	3-7	Sericite	1-8
Siltstone clasts	0-2	Iron-oxide	2-7
Carbonate	3-10		
Muscovite	2-5		
Zircon	<1		
Carbonaceous material	1-2	Matrix	6-15

Textures

The texture of the samples was described according to the sorting, roundness, and grain orientation along with other visible features. All samples demonstrated moderate sorting. Larger grains appeared to be subangular to subrounded and the smaller grains were rounded. All the different minerals present generally had the same grain size characteristics. Typically, the minerals were distributed randomly. Some samples displayed grading (Figure 3.33A) or distinct layers with coarser and finer grains, this feature is the result of internal lamination of the sandstone. Within matrix dominated areas within the sandstone, but not restricted to it, there sometimes occur fractures (Figure 3.33B) which may have been caused by a fluid intrusion as ore minerals are located within and in close proximity to these fractures (Figure 3.35).

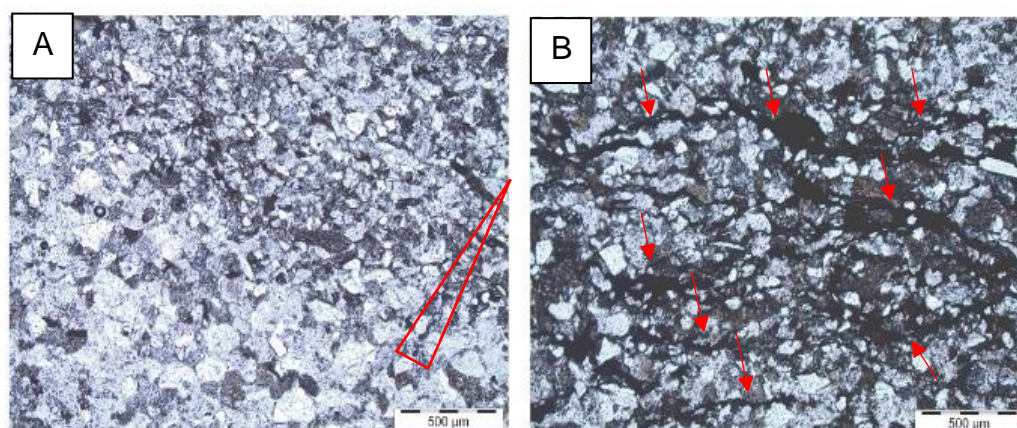


Figure 3.33: Plain polarized light petrographic images (4X magnification). A) Typical internal grading some of the samples exhibit. B) Fractures with opaque minerals.

Detrital mineral grains

Detrital mineral grains are derived from a source rock, due to weathering (Figure 3.36B), and deposited by sedimentary processes. These minerals in Table 3.3 and Figure 3.34 make out the bulk of the mineralogical composition of the sandstone.

Quartz

The quartz grains (Figure 3.34A) comprise on average 57% of the modal mineralogy. The quartz grains displayed low birefringence under plane-polarized light (PPL) and had no cleavage. Under cross-polarized light (CPL) the grains generally show uniform extinction, with single grains having undulatory extinction. The grains are generally anhedral and subrounded to rounded with moderate sorting. Singular grains may be euhedral and they typically contain inclusions like zircon, muscovite and vesicles (Figure 3.34B). The dominant portion of the grains are monocrystalline, but polycrystalline grains also occurs. The polycrystalline grains or microcrystalline quartz were classified with the lithic fragments as chert. Around some quartz grain boundaries, iron-oxide is concentrated in the matrix, which is brown-orange in color (Figure 3.34D).

Feldspar

Plagioclase-feldspar (Figure 3.34A) is the only feldspar grains identified microscopically and occupies on average 4% of the modal mineralogy. The grains show relatively low birefringence under PPL. Under CPL, albite twinning was identified with no zoning. The grains are semi-euhedral, subrounded and are randomly orientated and some highly altered. Typical alteration is vacuolization (holes that form due to weathering) on the surface of the grains and sericitization (Figure 3.26A) on grain surfaces and boundaries.

Lithic fragments

The lithic fragments (Figure 3.26D & E) that were identified include siltstone, polycrystalline calcite grains and chert clasts and they occupy on average 1%, 5%, and 6%, respectively, of the modal mineralogy. The siltstone clasts have a brownish color under PPL and CPL. The calcite and chert could only be identified under CPL. The calcite clasts are very colorful (pink and blue) and the chert shades of white, grey, and black. The clasts are well rounded with micro-polycrystalline grains. They are typically elliptical and randomly orientated. These grains are larger than most other minerals that were identified.

Mica

Muscovite (Figure 3.26A) is the only mica mineral identified during the microscopic analysis and represents on average 3% of the modal mineralogy. The muscovite minerals show relatively high birefringence under PPL. Under CPL it typically appears blue. They commonly occur on grain boundaries, within the matrix or as small inclusions in quartz grains.

Carbon

The carbonaceous material (carbon) (Figure 3.34C, D, & F) occupies on average, about 1% of the modal mineralogy. The carbon occurred in three forms: (1) the carbon

occurred as deformed plant fragments where the carbon is pressed between mineral grains in the matrix (Figure 3.34D) with reddish-brown color (under PPL and CPL), and they usually have iron-oxide on the boundaries (2) the carbon occurring as disseminated blebs (Figure 3.34C) between mineral grains in the matrix, that appeared dark-brown to black under PPL and CPL (3) the carbon occurring as coal-like strings (Figure 3.34F) that most likely represent a horizontal layer that appeared black under

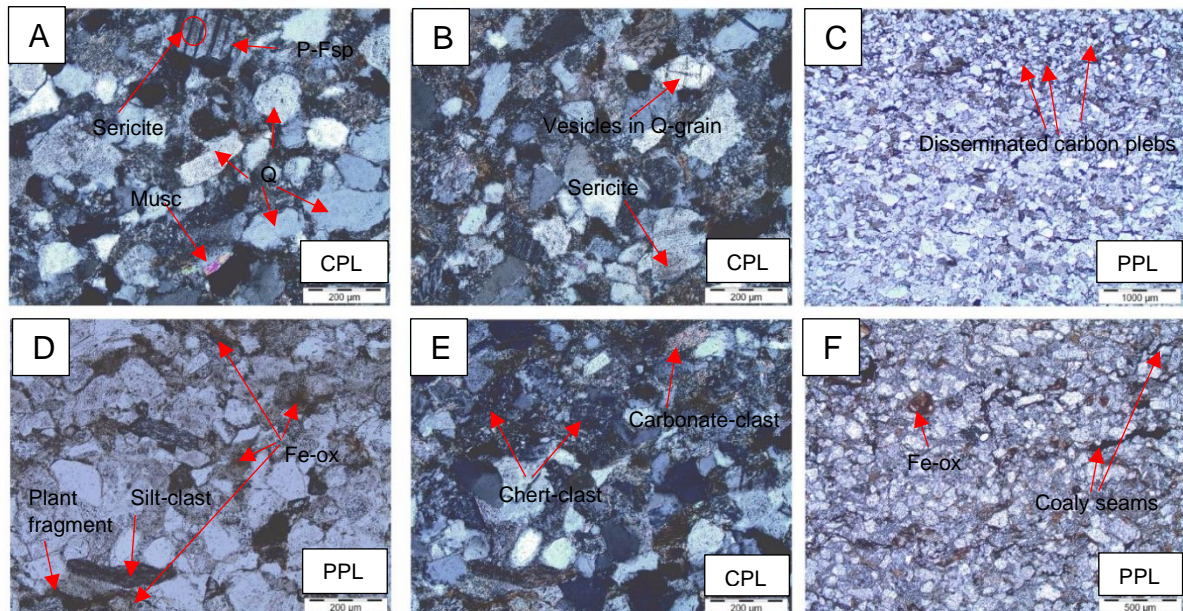


Figure 3.34: Petrology of the sandstone at Rietkuil mine. A) Minerals: Q= quartz, P-Fsp= plagioclase, Musc= muscovite and sericite. B) Vesicles in a quartz grain and sericite. C) Disseminated carbon blebs. D) Fe-ox= iron-oxide in the matrix and adjacent to grain (carbon and quartz) boundaries, siltstone clasts and deformed plant fragment. E) Lithic fragments of chert- and carbonate clasts. F) Iron-oxide and coaly strings of carbon.

PPL and CPL.

Autogenic mineral grains

The autogenic mineral content formed through in situ precipitation after or during diagenesis as a result of fluid intrusion or expulsion. These minerals (Table 3.3) are usually replacing a mineral or occur in open spaces between minerals.

Ore minerals

The ore minerals (Figure 3.35) occupy on average 5% of the modal mineralogy. The ore minerals usually are opaque under PPL and CPL. When the ore minerals (*cf.* Section 3.3.1 and 3.3.2 for ore mineralogical composition) are considered under reflective light they appear to be adsorbed mineralization on carbon fragments; disseminated mineralization in calcite minerals and; mineralization around grain boundaries and in close proximity to carbon fragments in the matrix.

Alteration minerals

The alteration minerals (Figure 3.34A, B, D, & F) are typically clay minerals like sericite and leaching products like iron-oxide. The sericite forms due to the weathering of minerals like feldspar and mica and consists on average 4% of the modal mineralogy.

The iron-oxide occupies about 4% of the modal mineralogy and most likely formed due to leaching of Fe-rich minerals like pyrite in an oxidized environment with fluctuating water table or high rainfall. The alteration minerals typically occur on mineral grain boundaries or on the surface of the grains.

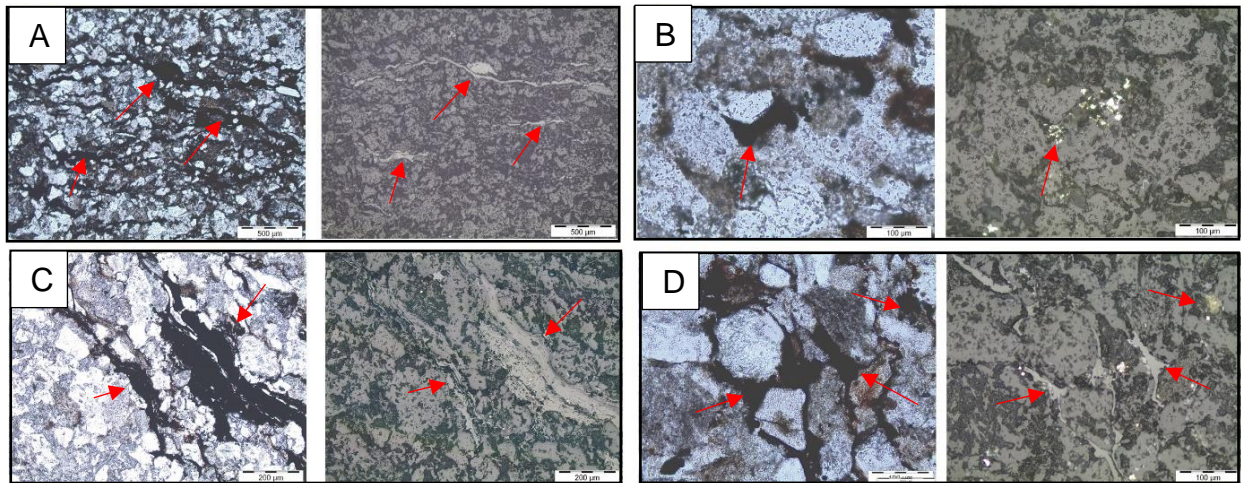


Figure 3.35: Ore petrography of sandstone samples from Rietkuil mine. For each slide A-D, the left image is under transmitted light and the right image under reflective light. A) Photomicrographs of ore minerals adsorbed on coal-like seams or precipitated in solution seams. B) Photomicrographs of ore minerals in the matrix and around mineral grains. C) Photomicrographs of coal-like strings with adsorbed ore minerals. D) Photomicrographs of ore mineralization around grains and in matrix.

Matrix

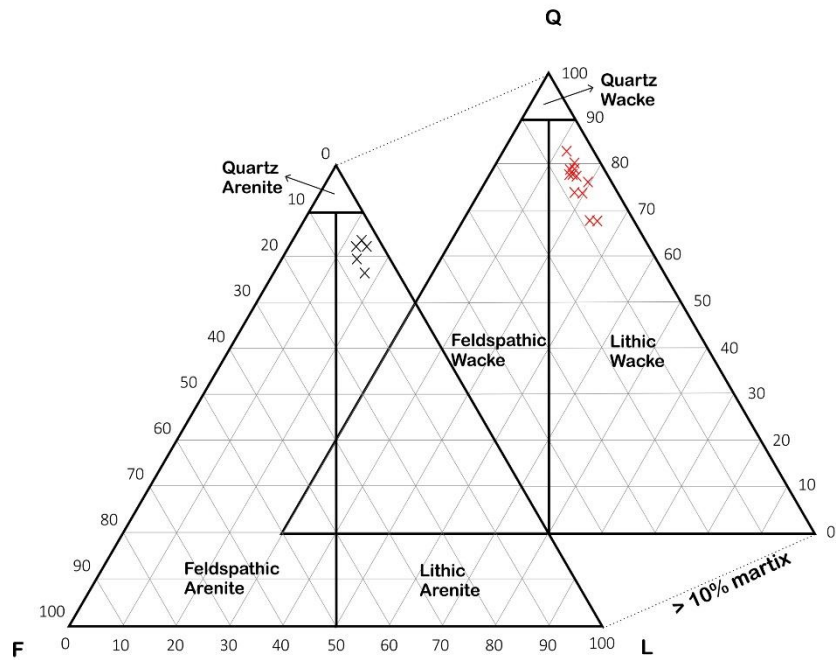
The matrix is clay-size and consists illite (and/or other clay minerals), as well as possible very fine non-clay minerals like quartz, iron oxide, organic material. The matrix occupies about 6 to 15% of the modal mineralogy. The matrix filled voids between mineral grains, gave it a very low porosity. The matrix was determined using optical microscopy

Sandstone classification and source

These minerals were used to classified based on the ternary plot developed by Dott (1964), which considers the mineralogy of the framework grains, based primarily on the relative abundance, specifically quartz, feldspar and lithic fragments (Figure 3.36A). Due to the high percentage of matrix (6-15%), the majority of samples were classified as wacke that plotted within the lithic field in the ternary diagram, *i.e.* a lithic wacke. A small number of samples classified within the lithic arenite field.

The Dickenson (1983) ternary diagram in Figure 3.36B, also uses the major constituents of sandstones to identify provenance. The sandstone samples were plotted on the provenance plot that identified a recycled orogeny as the source for the sediments.

A) Sandstone Classification (Dott, 1964)



B) Source/Provenance (Dickenson, 1983)

LEGEND

- × Wacke sandstone
- × Arenite sandstone

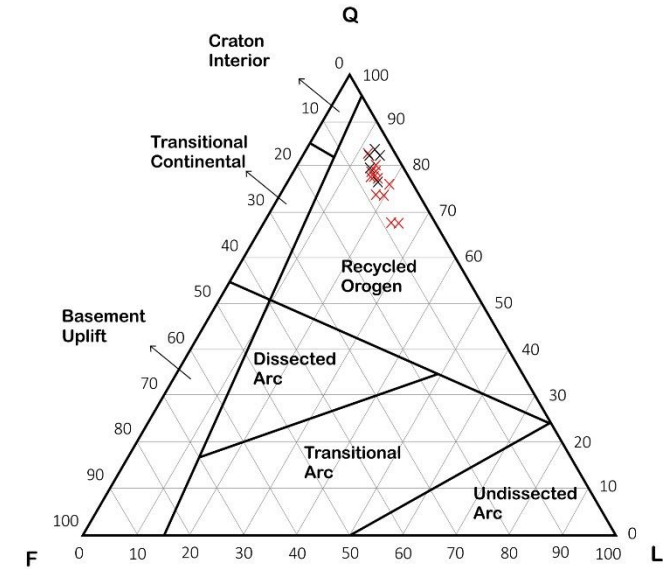


Figure 3.36: A) Sandstone classification by Dott (1964) applied to the selected sandstone samples from Rietkuil mine. B) Provenance classification by Dickenson (1983) applied to the selected sandstone samples from Rietkuil mine.

3.3 Geochemical analysis

3.3.1 XRD analysis

The XRD mineral data were used to correlate the minerals identified during the petrographic study and to identify the ore mineral complexes present. The latter was particularly important in the case of the uranium minerals because it revealed information on the redox-state of the uranium. This was conducted on 36 samples that can be viewed in Appendix B.

The mineral population identified through XRD analysis (Table 3.4) overlap with mineral population identified through the petrographic study, with the additional identification of minerals like alkali-feldspar and apatite. Also, the XRD analysis also revealed that the ore minerals (the opaque minerals from the petrographic study) can be assigned to either sulphide or uranium minerals.

Sulfide minerals

The sulfide minerals, chalcopyrite, and pyrite were identified. Chalcopyrite and calcite share the same main peak (XRD graphs in Appendix B) thus amplifying the peak. Pyrite, however, has an identifiable main peak.

Uranium minerals

The uranium minerals that were identified include autunite, novacekite, umohoite, zippeite, and carnotite. When considering the XRD graphs in Appendix B, regarding the uranium minerals, it was clear that there is overlap with some framework mineral peaks and the major peaks of some ore minerals. This phenomenon especially occurs between muscovite, novacekite, and autunite as well as plagioclase, umohoite, and carnotite. Zippeite, however, has an identifiable main peak. Uranium minerals like monazite also occur.

It is clear from the chemical formulae (Table 3.4) of the minerals that the uranium occurs in the U^{6+} oxidation state as UO_2^{2+} (uranyl ion).

Table 3.4: The minerals that were identified during the XRD analysis of the 36 selected sandstone samples, with their chemical formulae.

SAMPLE NAME	
MINERALS	CHEMICAL FORMULAS
Quartz	SiO_2
Plagioclase	$NaAlSi_3O_8$
Muscovite	$KAl_3Si_3O_{10}(OH)_2$
Smectite	$(Mg, Fe^{2+})_5Al_2Si_3O_{10}(OH)_8$
Feldspar	$(Na, K)AlSi_3O_8$
Calcite	$CaCO_3$
Apatite	$Ca_5(PO_4)_3(OH, F, Cl)$
SULPHIDE MINERALS	
Chalcopyrite	$CuFeS_2$
Pyrite	FeS_2
URANIUM MINERALS	
Autunite	$Ca(UO_2)_2(PO_4)_2 \cdot 10-12(H_2O)$
Novacekite	$Mg(UO_2)_2(AsO_4)_2 \cdot 12(H_2O)$
Umohoite	$(UO_2)MoO_4 \cdot 4(H_2O)$
Zippeite	$K_4(UO_2)_6(SO_4)_3(OH)_{10} \cdot 4(H_2O)$
Carnotite	$K_2(UO_2)_2(VO_4) \cdot 3(H_2O)$

3.3.2 XRF analysis

The XRF data (Appendix C) was used to analyze the whole-rock major and trace elements for the sandstone samples. It was also used to determine the distribution of uranium within the faces of the lower bench. The major elements were also used to classify the sandstone and to determine the tectonic setting.

The XRF uranium values of each sample were plotted on the faces in Figure 3.24 to Figure 3.27 for the lower bench and Appendix G for the upper bench. In the lower bench, the uranium values range from 20 ppm to upwards of 6000 ppm in some samples.

Major element oxide analysis

The major elements were measured as oxides their sum numbered to approximately 100 wt% for each of the 41 samples analyzed. The complete dataset can be viewed in Appendix C-Table C1.

Pearson correlation coefficient matrix

The selected samples, (Appendix F-Table F1) with complete data sets for all the geochemical analyses, were used to calculate Pearson correlation coefficient matrixes to assess the linear relationships of all the elements with each other (Table 3.6). The correlation matrix (Appendix F-Table F2) was calculated with the aid of the 'Data analysis' package in Excel, calculating values between +1 and -1. It enabled the study to identify strong associations between different elements (Cox and Clifford, 1982), and in particular the associations with uranium for the present study. The correlation matrix was calculated for major element oxides, trace elements, and carbon. The correlations were considered positive when the values were 0,5 and above (green) and negative when the values were -0,5 and below (red). Any values between the range of 0,5 and -0,5 (black) were considered a weak correlation.

The following assumptions were made regarding the Pearson's correlation coefficient matrixes: (1) elements with positive relationship have the same origin (source) and (2) that these elements are hosted in the minerals identified during petrographic description and XRD analysis.

Major element correlations

At Rietkuil mine (average major element oxide percentages in Table 3.5) the sandstone samples consist of 60-76 wt% of SiO₂ as the major constituent, followed by Al₂O₃ with concentrations of 12-28 wt%. Other major element oxides that occur in significantly lower concentrations, in order of relative abundance, are Fe, Na, K, Ca, Mg, Ti, P, and Mn. For the correlation matrix of the major elements see Table 3.6.

The average SiO₂ content was 70,70 wt% (Table 3.5), with a maximum of 75,88 wt%. SiO₂ has such high concentrations because it is a major constituent in many different minerals like quartz, feldspar, muscovite, and alteration minerals. The major elements (Mn, Ca, and P) and trace element (U) indicate a strong negative correlation with SiO₂. SiO₂ and Na₂O however, exhibits a positive relationship with a regression of 0,6128, probably due to their co-existence in albite and alkali-feldspar. The rest of the major elements show weak positive correlations with SiO₂ (Table 3.6).

Al₂O₃ have an average of 13,66 wt% in the analysis (Table 3.5). In the correlation matrix, Al₂O₃ have a strong positive relationship with major element oxides Fe, Ti, and K (Table 3.6). These are the typical constituents in the feldspar-group minerals and the alteration minerals like sericite and smectite.

The average Fe₂O₃ was calculated to be 3,12 wt% (Table 3.5). This can be attributed to the sulfide minerals, pyrite and chalcopyrite, found during XRD analysis. Minor amount can be allocated to alteration minerals smectite and iron-oxide, due to the strong positive correlations of Fe₂O₃ with major element oxides Al, Ti, and K (Table 3.6).

The K₂O is a minor constituent with an average of 1,78 wt% (Table 3.5). The K₂O can be contained in minerals like muscovite, alkali-feldspar, and also some uranium minerals can have minor amounts of potassium as part of their chemistry.

MgO occurs in low amounts (average 0,90 wt%) (Table 3.5) and has no significant correlations with any of the major elements, positive or negative (Table 3.6). The MgO can be attributed to the alteration mineral smectite.

CaO, MnO, and P₂O₅ had averages of 1,64; 0,08; and 0,14 wt%, respectively (Table 3.5). The CaO and P₂O₅ have a positive correlation that can be attributed by apatite. Calcite also contains CaO in its chemistry. The MnO, and P₂O₅ have strong positive correlations with U and can be attributed to monazite. It is remarkably interesting to note that these major elements have a strong negative relationship with SiO₂ but have a strong positive relationship with U (Table 3.6). The strong negative correlation might indicate a separate source for the uranium and the above-mentioned major elements, as they all have strong positive correlations with each other (Table 3.6). CaO, MnO, and P₂O₅ readily form mineral complexes with uranium as is listed in the XRD results (Table 3.4).

Table 3.5: The average major element oxide (%) in sandstone samples from Rietkuil mine measured with the XRF.

Sample name	SiO ₂ (%)	TiO ₂ (%)	Al ₂ O ₃ (%)	Fe ₂ O ₃ (%)	MgO(%)	MnO(%)	CaO(%)	K ₂ O(%)	P ₂ O ₅ (%)	Na ₂ O(%)
Average values:	70.70	0.54	13.66	3.12	0.90	0.08	1.64	1.78	0.14	2.58

Table 3.6: Pearson correlation coefficient matrix of the major element oxides and trace element uranium. Positive correlations are marked in green and negative correlations are marked in red. The black values were considered as weak correlations.

	SiO ₂	TiO ₂	Al ₂ O ₃	Fe ₂ O ₃	MgO	MnO	CaO	K ₂ O	P ₂ O ₅	Na ₂ O	U
SiO ₂	1	0,0933	0,0520	0,2811	0,0706	-0,9349	-0,9396	0,3074	-0,9488	0,6128	-0,9446
TiO ₂	0,0933	1	0,8773	0,7665	0,4738	-0,3190	-0,3644	0,8288	-0,3215	-0,5356	-0,3417
Al ₂ O ₃	0,0520	0,8773	1	0,7156	0,4942	-0,2664	-0,3345	0,8279	-0,3335	-0,5502	-0,3457
Fe ₂ O ₃	0,2811	0,7665	0,7156	1	0,0691	-0,4804	-0,5297	0,6696	-0,4523	-0,3960	-0,4571
MgO	0,0706	0,4738	0,4942	0,0691	1	-0,0082	-0,1180	0,4426	-0,1989	-0,1565	-0,2087
MnO	-0,9349	-0,3190	-0,2664	-0,4804	-0,0082	1	0,9834	-0,5251	0,9502	-0,4139	0,9473
CaO	-0,9396	-0,3644	-0,3345	-0,5297	-0,1180	0,9834	1	-0,5419	0,9780	-0,3931	0,9746
K ₂ O	0,3074	0,8288	0,8279	0,6696	0,4426	-0,5251	-0,5419	1	-0,5191	-0,3936	-0,5229
P ₂ O ₅	-0,9488	-0,3215	-0,3335	-0,4523	-0,1989	0,9502	0,9780	-0,5191	1	-0,4342	0,9987
Na ₂ O	0,6128	-0,5356	-0,5502	-0,3960	-0,1565	-0,4139	-0,3931	-0,3936	-0,4342	1	-0,4201
U	-0,9446	-0,3417	-0,3457	-0,4571	-0,2087	0,9473	0,9746	-0,5229	0,9987	-0,4201	1

Sandstone classification and tectonic setting

The Harron (1988) sandstone classification scheme uses the ratios of the major constituents found in sandstone and plots it on a diagram on the x-axes ($\log \text{SiO}_2/\text{Al}_2\text{O}_3$) against the y-axes ($\log \text{Fe}_2\text{O}_3/\text{K}_2\text{O}$). The Rietkuil sandstone samples (Figure 3.37) were plotted in the sandstone classification plot and classified as predominantly wacke and in some instances a lithic-arenite, mirroring the results of the petrographic analysis.

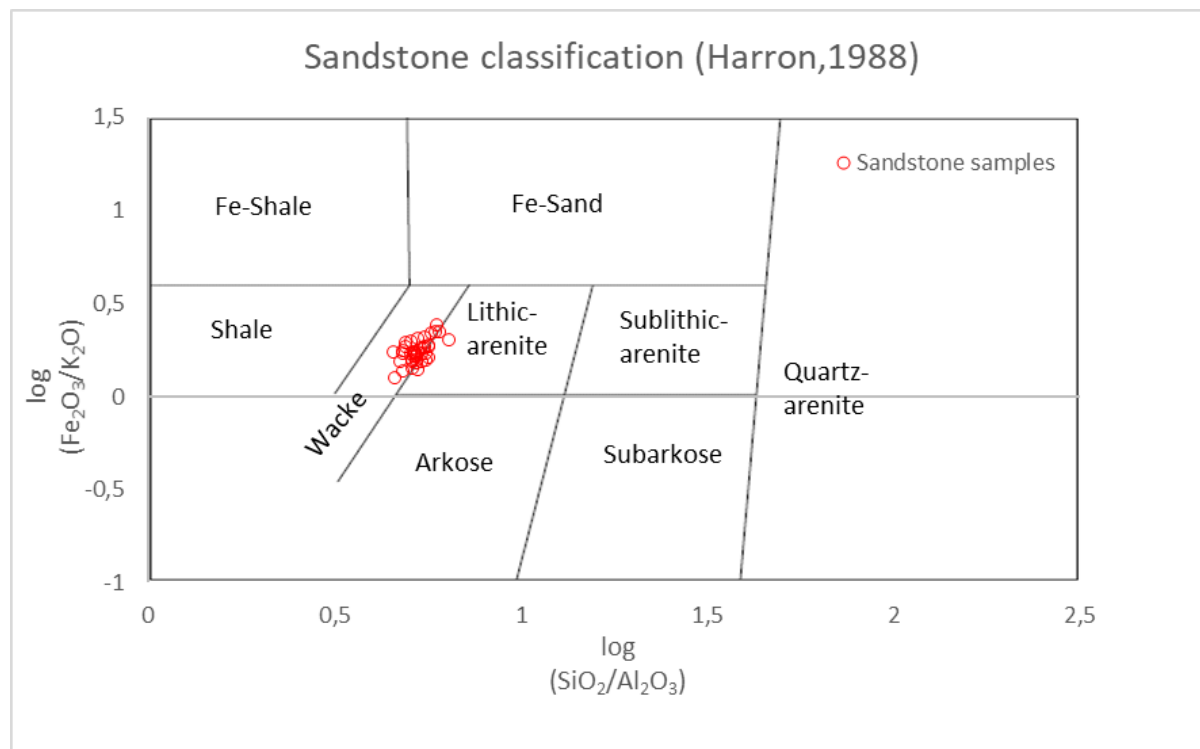


Figure 3.37: Sandstone classification by Harron (1988) for the sandstone samples at Rietkuil mine.

The discrimination plot by Bhatai, 1983 was used to determine the tectonic setting (provenance) of sandstones, plotting on the x-axes ($\text{Fe}_2\text{O}_3+\text{MgO}$) against the y-axes ($\text{Al}_2\text{O}_3/\text{SiO}_2$). The provenance plot suggests the Rietkuil sandstone samples (Figure 3.38) were deposited in an active continental margin setting as most of the sandstone samples plotted close to or within this field. The petrographic samples suggested a recycled orogen as the provenance of the sandstone.

Johnson (1991) had the same discrepancy and attributed it to the fact that the Karoo sequence was deposited in a retro-arc foreland basin with the Cape Fold Belt as the primary provenance for the upper Karoo sequences.

Trace element analysis

The trace element data (averages in Table 3.7) were primarily used to support ore mineralogical findings, presented by the petrography and XRD analysis. Therefore, this section will be described in two sections. The sulfide minerals and uranium complexes which might be present in the sandstone samples from Rietkuil mine. In most instances, the trace elements substitute major elements in minerals and rarely

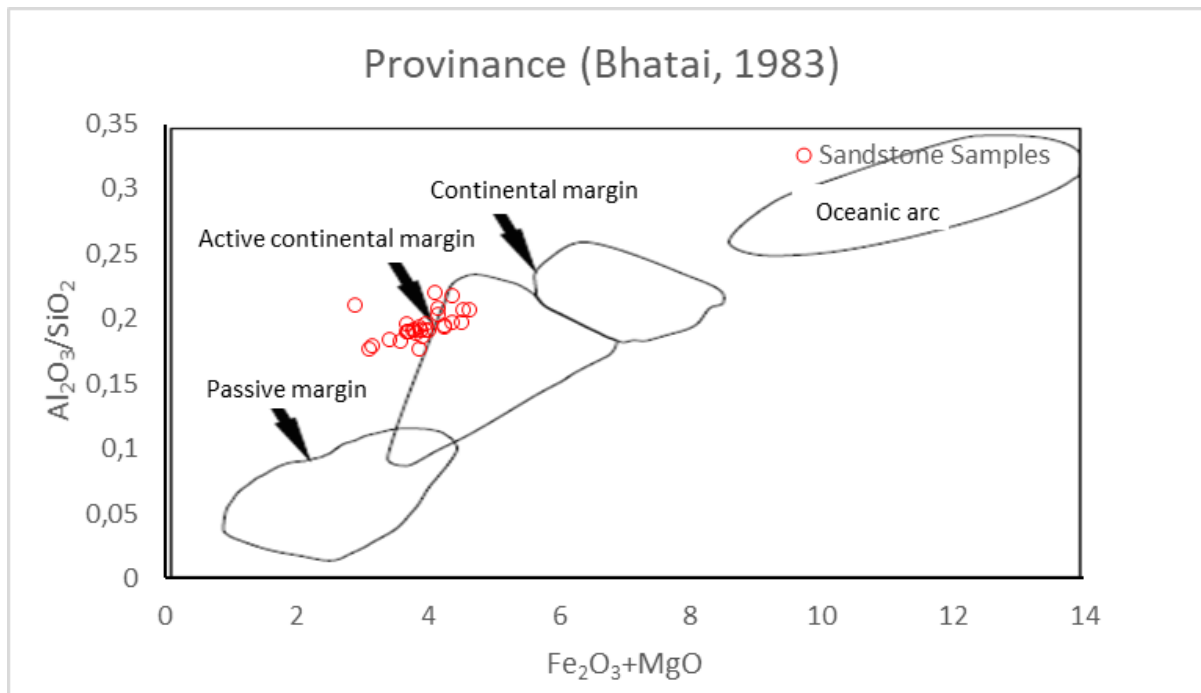


Figure 3.38: Sandstone provenance classification by Bhatai (1983) for the sandstone samples at Rietkuil mine.

form minerals of their own. Appendix C-Table C2 contains the trace element data for the 53 sandstone samples that were analyzed.

Sulfide minerals

The most abundant cations found in sulfide minerals are Fe, Cu, Co, Ni, As, Sb, Zn, Mo, and Pb (Vaughan and Corkhill, 2017). The work by Vaughan and Corkhill (2017) was used to deduce which of the current studies trace elements data could be attributed to specific sulphide minerals that were identified with the XRD and petrography. This aided to assess the possible sulfide mineralization in the Rietkuil sandstone samples. From XRD analysis pyrite and chalcopyrite are identified and major element Fe_2O_3 and trace element Cu are allocated to these minerals. Based on the trace element data (Table 3.7) it is likely/possible that other sulfide minerals are also present. From the trace element data minor amounts of As and Mo occurred within the samples and were assigned to arsenopyrite and molybdenite possibly occur. The positive correlation between most elements, except for Cu and Fe, suggest a common source for these sulfide minerals. The Cu and Fe are attributed to pyrite and chalcopyrite and is likely to be closely related to organic material, whereas other sulfides like arsenopyrite and molybdenite where deposited simultaneously with ore minerals (proof the these statements will be discussed in more detail later in this thesis).

Uranium minerals

The uranium concentration has an average of 414,46 ppm with values ranging from below detection limits (< 2 ppm) to 6816,01 ppm. XRD analysis (Table 3.4), indicated that uranium formed ligand complexes with phosphate, arsenate, molybdate, sulfate, and vanadate. The strong positive correlation between U and P_2O_5 (Table 3.6), from the major element data, showed a strong positive correlation, indicating the mineral

autunite. A strong positive relationship also occurs between U and elements As and V can be attributed to the minerals novacekite and carnotite, respectively (Table 3.8). A weak positive relationship, with a correlation of 0,3961, between U and Mo may suggest minor amounts of umohoite, but Mo would rather be considered to form molybdenite (sulfide mineral). Zippeite which hosts the sulfate variety in the U-ligand complexes cannot be supported with trace element data due to a lack of sulfur information, but it can be considered as zippeite because it has a very identifiable peak in the XRD analysis. It can also be noted from the correlation matrix (Table 3.8) for the trace element data that the U and the sulfide mineral elements (Co, Ni, As, Sb, Zn, Mo, and Pb) have strong positive relationships which could suggest a common origin for all these elements.

Table 3.7: The average trace element (ppm) in sandstone samples from Rietkuil mine measured with the XRF.

Sample name	Sc	V	Cr	Co	Ni	Cu	Zn	As	Rb	Sr	Y	Zr	Nb	Mo	Sn	Sb	Ba	Pb	Th	U
Average Values:	24.24	93.47	111.26	71.20	44.45	70.12	95.94	87.20	79.90	183.14	29.28	279.14	7.96	44.08	1.74	42.50	718.91	44.52	11.43	404.88

Table 3.8: Pearson correlation coefficient matrix of the trace elements. Positive correlations are marked in green and negative correlations are marked in red. The black values were considered as weak correlations.

	Sc	V	Cr	Co	Ni	Cu	Zn	As	Rb	Sr	Y	Zr	Nb	Mo	Sn	Sb	Ba	Pb	Th	U
Sc	1	0,8578	0,8421	0,9605	0,9815	0,0170	0,9606	0,9599	0,9749	0,4209	0,0839	0,7833	0,9313	0,5504	-0,0760	0,7726	-0,1022	0,9794	-0,6236	0,9721
V	0,8578	1	0,9498	0,8630	0,8276	0,0451	0,8818	0,7765	0,8368	0,4515	0,1655	0,7511	0,7282	0,6624	0,0480	0,7462	-0,1655	0,7910	-0,2589	0,7891
Cr	0,8421	0,9498	1	0,8410	0,8236	0,0758	0,8842	0,7851	0,8471	0,3902	0,1233	0,7546	0,7508	0,5644	0,0466	0,6853	-0,2413	0,7976	-0,2707	0,7931
Co	0,9605	0,8630	0,8410	1	0,9736	0,0823	0,9115	0,9062	0,9152	0,3304	0,1640	0,7524	0,8387	0,7064	-0,0708	0,7571	-0,2780	0,9375	-0,5376	0,9122
Ni	0,9815	0,8276	0,8236	0,9736	1	0,1363	0,9510	0,9739	0,9724	0,2896	0,0796	0,7942	0,9358	0,5384	-0,1151	0,7573	-0,2138	0,9847	-0,6748	0,9770
Cu	0,0170	0,0451	0,0758	0,0823	0,1363	1	0,1434	0,1326	0,0942	-0,5969	0,0528	0,3231	0,1364	-0,1203	0,0481	0,0895	-0,4580	0,1151	-0,1339	0,1147
Zn	0,9606	0,8818	0,8842	0,9115	0,9510	0,1434	1	0,9414	0,9696	0,3771	0,1861	0,7583	0,9356	0,4547	-0,0153	0,7242	-0,1237	0,9588	-0,6229	0,9578
As	0,9599	0,7765	0,7851	0,9062	0,9739	0,1326	0,9414	1	0,9852	0,2870	0,0068	0,8195	0,9837	0,3890	-0,1293	0,7231	-0,1708	0,9842	-0,7563	0,9959
Rb	0,9749	0,8368	0,8471	0,9152	0,9724	0,0942	0,9696	0,9852	1	0,3188	0,0483	0,7993	0,9774	0,4158	-0,0839	0,7208	-0,1472	0,9822	-0,6897	0,9922
Sr	0,4209	0,4515	0,3902	0,3304	0,2896	-0,5969	0,3771	0,2870	0,3188	1	0,0432	0,2631	0,2772	0,3778	0,2010	0,3609	0,3917	0,3388	-0,0069	0,3130
Y	0,0839	0,1655	0,1233	0,1640	0,0796	0,0528	0,1861	0,0068	0,0483	0,0432	1	-0,1743	-0,0022	0,2437	0,4160	0,0101	-0,2160	0,1014	-0,0575	0,0386
Zr	0,7833	0,7511	0,7546	0,7524	0,7942	0,3231	0,7583	0,8195	0,7993	0,2631	-0,1743	1	0,7788	0,3931	-0,0817	0,6844	-0,3014	0,7909	-0,3991	0,7951
Nb	0,9313	0,7282	0,7508	0,8387	0,9358	0,1364	0,9356	0,9837	0,9774	0,2772	-0,0022	0,7788	1	0,2446	-0,1081	0,6820	-0,0755	0,9648	-0,7952	0,9868
Mo	0,5504	0,6624	0,5644	0,7064	0,5384	-0,1203	0,4547	0,3890	0,4158	0,3778	0,2437	0,3931	0,2446	1	0,0726	0,4661	-0,3833	0,4618	0,0698	0,3961
Sn	-0,0760	0,0480	0,0466	-0,0708	-0,1151	0,0481	-0,0153	-0,1293	-0,0839	0,2010	0,4160	-0,0817	-0,1081	0,0726	1	-0,0491	-0,0518	-0,0503	0,1534	-0,0987
Sb	0,7726	0,7462	0,6853	0,7571	0,7573	0,0895	0,7242	0,7231	0,7208	0,3609	0,0101	0,6844	0,6820	0,4661	-0,0491	1	0,1671	0,7218	-0,3995	0,7237
Ba	-0,1022	-0,1655	-0,2413	-0,2780	-0,2138	-0,4580	-0,1237	-0,1708	-0,1472	0,3917	-0,2160	-0,3014	-0,0755	-0,3833	-0,0518	0,1671	1	-0,1750	-0,0290	-0,1331
Pb	0,9794	0,7910	0,7976	0,9375	0,9847	0,1151	0,9588	0,9842	0,9822	0,3388	0,1014	0,7909	0,9648	0,4618	-0,0503	0,7218	-0,1750	1	-0,7254	0,9910
Th	-0,6236	-0,2589	-0,2707	-0,5376	-0,6748	-0,1339	-0,6229	-0,7563	-0,6897	-0,0069	-0,0575	-0,3991	-0,7952	0,0698	0,1534	-0,3995	-0,0290	-0,7254	1	-0,7525
U	0,9721	0,7891	0,7931	0,9122	0,9770	0,1147	0,9578	0,9959	0,9922	0,3130	0,0386	0,7951	0,9868	0,3961	-0,0987	0,7237	-0,1331	0,9910	-0,7525	1

3.3.3 ICP-MS analysis

The ICP-MS analysis was only conducted on some of the samples and they were randomly picked (Figure 2.1 to Figure 2.4, refer to the yellow stars).

The ICP-MS was used, due to the low detection limits, to assess the accuracy of the XRF trace element data, especially the uranium values (Figure 3.39). The values correlated well, with a regression of 0.9999 and therefore XRF trace element data could be used (see Appendix D for ICP-MS data and correlation with the XRF data).

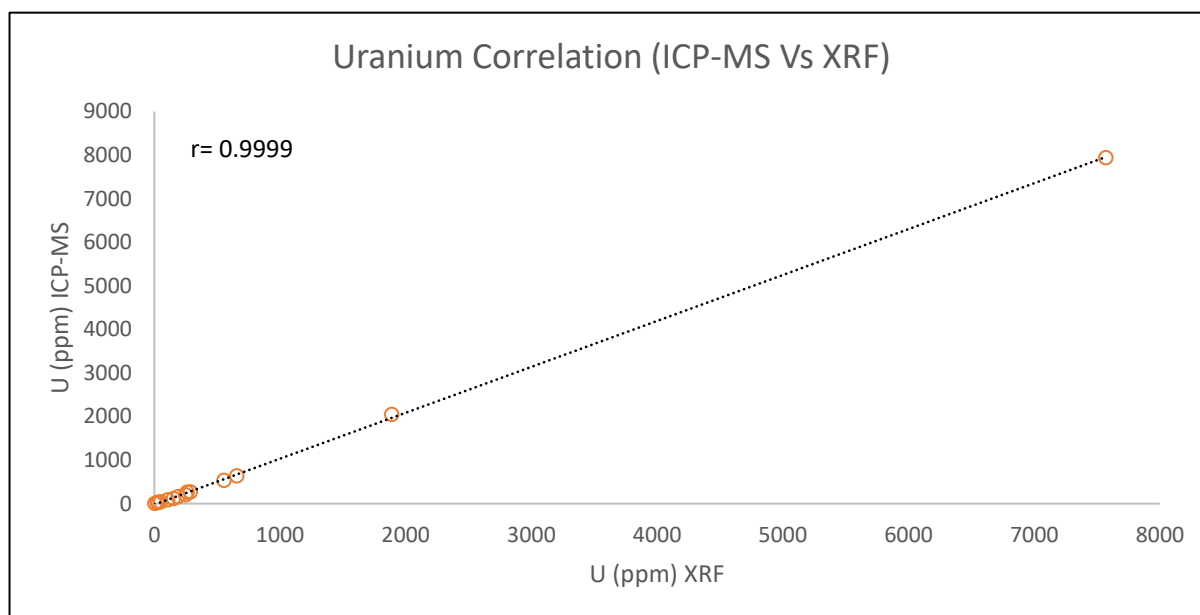


Figure 3.39: Correlation between uranium measured by the ICP-MS Vs XRF in ppm.

3.3.4 Carbon analysis

The organic carbon was measured to form an idea of the amount of carbon within the sandstones which in turn aided in the dispersion of the carbon. It was also used to understand the relationship, if any, with U, Fe_2O_3 , and CaO. The data can be viewed in Appendix E.

LECO analysis

The LECO analysis was conducted to analyze the total carbon (TC) % from exposed outcrop faces and the values were plotted on the faces where the samples were collected (Figure 3.29 to Figure 3.32 for the lower bench and Appendix G for the upper bench)

An average of 0,60 wt% (Table 3.9) is measured for the TC content in the samples, with the maximum amount being 2,17 wt%. Due to the small amount of sample used during analyzing the TC, the values may vary a lot, because a tiny fragment of carbon can make a significant difference in the final wt%. There is no clear relationship between TC and the elements U, OC, CaO, and Fe_2O_3 .

Mebius titration method

This method was used to identify the organic carbon (OC) % within the faces of the mine. The results of this experiment are inconclusive as in a few cases, the TC wt% measured by the LECO analyzer is less than the amount of OC obtained by the

Mebius titration method. It could also not be said with certainty that the acids used to flush out the inorganic carbon (IC-CaCO₃) did not alter the OC. Nonetheless, the data was used to make assumptions regarding the mineralisation environment by considering the OC content of the sandstone samples and the relationship thereof with TC, U, CaO, and Fe₂O₃ in the correlation matrix (Table 3.10). CaO is considered the IC component because it is a major constituent is calcite (CaCO₃).

The average OC is 0,26 wt% (Table 3.9) with the highest concentrations at 0,57 wt%. There is no significant relationship between OC and the U, TC, and CaO. The OC has a strong positive relationship with Fe₂O₃, which reflects the association commonly found between sulfide minerals (particularly, pyrite and chalcopyrite) and OC.

It is clear from Table 3.10 that the TC on its own cannot be used to make assumptions on the environment. Once the data is separated into the OC and IC fractions it becomes visible that U has a strong correlation with the IC and the sulfide minerals pyrite and chalcopyrite has a strong relationship with the OC.

Table 3.9: The average total carbon (%TC) and organic carbon (%OC) in sandstone samples from Rietkuil mine measured with the LECO analyzer and the Mebius titration method, respectively.

Sample	%OC	%TC
Average values:	0,26	0,60

Table 3.10: Pearson correlation coefficient matrix of the trace element uranium, total carbon (TC), organic carbon (OC), and major elements oxides Ca and Fe. Positive correlations are marked in green. Negative correlations are marked in red. The black values were considered as weak correlations.

Elements	U	OC	TC	CaO	Fe ₂ O ₃
U	1	-0,0489	-0,1598	0,9746	-0,4571
OC	-0,0489	1	-0,2724	-0,1560	0,7390
TC	-0,1598	-0,2724	1	-0,0976	-0,0995
CaO	0,9746	-0,1560	-0,0976	1	-0,5297
Fe ₂ O ₃	-0,4571	0,7390	-0,0995	-0,5297	1

Chapter 4: Discussion

The present study dealt with describing the distribution of the uranium mineralization by means of detailed mapping of the study area. This was ensured by considering the influences that joints, lithology, and reductants had on the uranium mineralization. Furthermore, the type of uranium mineralization at Rietkuil mine was identified by studying the mineralogy and geochemistry of 53 sandstone samples.

In this chapter, the results are summarized, discussed and compared to enable the compilation of a uranium mineralization model for Rietkuil mine.

4.1 Mineralogy and whole-rock geochemistry

The mineralogy of the wacke was revealed by petrography and XRD analysis (Table 3.3 and Table 3.4, respectively) and it was recognized that there are detrital and autogenic minerals. The detrital minerals grains comprise quartz, feldspar, lithic fragments, mica, carbonaceous matter, pyrite, and chalcopyrite. The autogenic minerals present in the wacke were formed post-deposition of the detrital minerals and comprises alteration minerals (smectite and sericite), sulfide minerals arsenopyrite and molybdenite, and uranium minerals.

The major and trace element data were used to describe the deposition style of the wacke and ore minerals. Pearson's correlation coefficient matrix in Appendix F-Table F2 indicates that there are separate deposition styles for the detrital and autogenic minerals. This statement is being made because (1) it was established in Chapter 3 that the source of the sediments was a recycled Cape orogeny. This implicates the deposition of the detrital minerals and alteration minerals found in the sediments at Rietkuil Mine were via sedimentary processes. This however does not explain the deposition of the ore minerals; (2) The ore minerals might have been from the same source as the detrital minerals primarily but deposited in a lower stratigraphic horizon. Later hydrothermal events possibly remobilised the ore minerals and deposited it in the present sediments at Rietkuil Mine. The nature of the ore minerals (uranium, and sulfide minerals arsenopyrite and molybdenite) within the sediment, as revealed by petrography (*c.f.* Section 3.2), supports a hydrothermal remobilisation as the ore minerals are found in fractures and adsorbed onto the surfaces of certain minerals. This parallels the findings of Duane, *et al.* (1989) who used U-Pb to determine the age and genesis of the uranium mineralisation in the Karoo. They concluded that the rise of the Cape Fold Belt and increased hydrothermal gradients at 258-278 Ma led to the dewatering of the Karoo Basin facilitating low temperature U-bearing fluids.

Considering the geochemical relationships between pairs of elements. The detrital and ore elements, hosted in respective minerals, appear to have strong negative correlations (*c.f.* Section 3.3.2). For this reason, two depositional styles are suspected for the present whole-rock geochemistry. The elements that are hosted in the detrital minerals displayed a high degree of correlation (*c.f.* Section 3.3.2) and is likely governed by sedimentary processes due to it recycled orogeny orogen. The ore

elements related to autogenic minerals showed a high degree of correlation and were likely controlled by post-depositional hydrothermal and alteration processes (*c.f.* Section 3.3.2). Sulfide minerals like pyrite and chalcopyrite had a negative correlation with uranium and other sulfide minerals such as arsenopyrite and molybdenite. This indicates that pyrite and chalcopyrite formed differently than arsenopyrite and chalcopyrite. The geochemistry suggests that pyrite and chalcopyrite formed shortly after deposition of the sediments replacing organic matter where as arsenopyrite and molybdenite is precipitated with the uranium-hydrothermal mineralization in fractures, matrix, and absorbed onto and in close proximity to organic matter and mineral grains.

Major element data revealed that quartz is a main component of the source rock for the detrital minerals, reflected in relatively high $\text{SiO}_2/\text{Al}_2\text{O}_3$ ratios. Elements with a positive correlation with SiO_2 (detrital minerals) were Na_2O , K_2O , C, Fe_2O_3 , and Cu. These elements are hosted in feldspar, muscovite, carbonaceous matter, pyrite, and chalcopyrite, respectively. According to Tankard, *et al.* (2009) the major source rock was the Cape orogeny (Cape Supergroup) which is granitic and sedimentary in nature. Quartz, feldspar and muscovite are the major constituents in granites and sedimentary rocks. The pyrite and chalcopyrite may have formed shortly after deposition of the sediments due to the presence of organic matter and anoxic conditions due to a slightly reduced environment created by the organic matter, promoting the formation of these minerals. Le Roux (1985) suggested a similar scenario when he describes that organic material was eroded and deposited locally with channel sediments creating a reduced environment suitable for the precipitation of uranium mineralisation. Al_2O_3 and MgO shows a weak positive relationship with SiO_2 and might be represented in alteration minerals like sericite, smectite, and iron-oxide. These minerals are alteration minerals of the detrital minerals like quartz, feldspar, mica, and pyrite.

Petrography (Figure 3.35A to D) revealed that the ore minerals are typically found in the matrix, around grain boundaries, and/or adsorbed onto carbon. The sandstones were classified as a wacke which consist of more than 10% matrix (mud/clay) material. The hydrothermal fluids were absorbed by the muddy matrix material and crystallized on the grain boundaries of impermeable crystals like quartz or it adsorbed onto carbon. Mineralization of the ore minerals (uranium, arsenopyrite and molybdenite) occurred in fractures, matrix, and absorbed onto/and in close proximity to organic matter and mineral grains.

4.2 Controls on the uranium distribution

Wacke sandstones are known as hard rocks with low porosity. The pivotal question was what influenced the distribution of the uranium mineralization in a sandstone with low porosity?

The distribution of the uranium mineralization in the lower bench at Rietkuil presented as sporadic mineralized zones along the faces of the mine, as illustrated by the gamma-ray contours in Figure 3.24B to Figure 3.27B. The concentrations of the uranium decrease upwards and to the sides of the mineralized zones. This is revealed by the gamma-ray contours and supported by the uranium concentrations from the XRF in Figure 3.24A to Figure 3.27A.

All the data to this point indicated a secondary uranium mineralization transported by hydrothermal fluids into the current host wacke. This statement is supported by Cole & Labuschagne (1985); and Le Roux (1985) who suggests that the uranium mineralization in the Karoo Uranium Province is epigenetic in nature.

4.2.1 Host sandstone

At Rietkuil mine, the sandstone which hosts the uranium mineralization is confined to the lower bench.

The main differences between the upper and lower benches are: 1) the grain size of the lower bench is finer-grained compared to the upper bench, 2) the lower bench sandstone contains more carbonaceous material compared to the upper bench, and 3) the sedimentary structures in the lower bench is predominantly horizontally bedded compared to the predominantly cross-bedded upper bench.

The sandstone from the lower bench (Figure 3.11, 3.13, 3.15, and 3.17) is a very fine to fine-grained wacke, with a moderate sorting. The petrography reveals variable grain sizes. Larger grains appear subangular and smaller grains subrounded to rounded. This may imply a slight distance from the source area. The wacke is horizontally bedded, with thin horizontal laminations, suggesting deposition in the upper-flow regime. The lower portion of the lower bench appear to be gently-inclined horizontally bedded units presenting as stacked sandstone lenses (see, Table 3.1 Lithofacies Sh and Figure 3.13). This can be imputed to mutually eroding and offset barforms (also see Figure 3.30).

The host sandstone was classified with the aid of petrographic and whole-rock geochemistry. The petrographic study conducted on sandstone samples from Rietkuil reveals that the sandstone is predominantly a lithic-wacke with a few samples classifying as a lithic arenite on the Dott (1964) classification scheme (Figure 3.36A). These results are supported by whole-rock geochemistry plotted on a Harron (1988) classification diagram (Figure 3.37) as predominantly wacke and some samples in the lithic-arenite field.

The tectonic setting was evaluated with the use of petrographic and whole-rock geochemistry. The Dickenson (1983) (Figure 3.36B) and Bhatai (1983) plots (Figure 3.38), respectively, was used to identify the provenance and tectonic setting during sedimentation. The Bhatai (1983) diagram in Figure 3.30 proposes that an active continental margin can be ascribed to the Rietkuil mine sediments supporting the Dickenson (1983) diagram in Figure 2.36B which indicates a recycled orogen, involving the upliftment and erosion of the source area. Johnson (1991) describes a nonorogenic and the recycled orogeny field and attributed it to the fact that the Karoo sequence was deposited in a retro-arc foreland basin with the Cape Fold Belt as the primary provenance for the upper Karoo sequences. This parallels the findings by De Wit & Ransome (1992); and Cole (1992) who suggested major upliftment in the southwestern part of Gondwana as a result of the subduction of the paleo-Pacific plate in the Permian age *i.e.*, the Cape orogeny which is a granitic source. Mineralogically the sediments correspond with the typical mineral assemblage of a granite which can further prove the Cape orogeny as the source for the sediments, as proposed by Tankard, *et al.* (2009).

4.2.2 Porosity and hydrothermal fluid intrusion

For the fluids to have been able to penetrate the wacke in the fashion that it did, the porosity of the wacke had to be increased. The factors that essentially contributed to increasing the porosity of the wacke were the joints and the manner in which the wacke was bedded.

Rietkuil mine showed many features of tectonic activity. This was indicated by three joint sets (Figure 3.20 to Figure 3.23), faults and folding (Figure 3.1). These tectonic features formed as a result of the formation of the Cape Fold Belt (Jordaan, 1990). Some of these features may have formed due to the break-up of Gondwana. It became apparent when comparing the joint sets (Figure 3.20 to Figure 3.23) with the uranium distribution sections (Figure 3.24 to Figure 3.27) that the joints were the major controlling factor for the distribution of the uranium mineralization. Where there is an increase in the number of joints, and particularly where these joints are filled with calcite, the concentration of the uranium also increases. The joints are suspected to be the feeder of the uranium-bearing hydrothermal fluid. Le Roux (1985) and Jordaan (1990) suggested that uranium fluids were transported via joints and faults.

Considering the sedimentology of the lower bench (Figure 3.11, 3.13, 3.15, and 3.17) and the uranium distribution sections (Figure 3.24 to Figure 3.27) it was clear that the lithology had very little impact on the distribution of the uranium mineralization. If the uranium were controlled or deposited with the sediments it would have appeared to be confined in horizons in the wacke, which was not the case at Rietkuil mine.

The manner in which the lithology is deposited however, contributed to increasing the porosity of the wacke. The wacke was horizontally bedded and finely laminated. These observations were also made by Cole & Labuschagne (1985). Due to suspected unequal loading of the sediment during diagenesis, the base of the wacke underwent soft-sediment deformation. This resulted in the appearance of stacked interfingering sandstone lenses. When the fluid passed through the joints into the sandstone, these contacts in the sandstone acted as access routes into the sandstone via thin laminations and the interfingered lenses, increasing permeability.

Reflected light petrography in Figure 3.35 revealed that the ore minerals are also found within the matrix at and around impermeable mineral grain boundaries. This indicated that the hydrothermal fluid was absorbed by the matrix and furthered the distributed of the uranium-bearing fluid into the sandstone.

The Pearson correlation coefficient matrix in Appendix F-Table F2 indicates a strong negative relationship between detrital and the ore minerals (autogenic minerals). In Section 4.1 it was seen that the detrital and the ore minerals possibly have two separate depositional styles. There were various indications from the petrographic and geochemical results that the uranium and other elements hosted in ore minerals were possibly transported by means of a uranium-bearing hydrothermal solution or alternatively it displays the alteration of primary uranium mineralisation.

Field observations revealed that on occasion the easterly joints are filled with calcite (Figure 3.20 to Figure 3.23). Where there was calcite present in the joints, there was a higher concentration of uranium mineralisation (Figure 3.24 to Figure 3.27) illustrated

by the dispersion of uranium around these localities. The wacke exhibited low-grade metamorphic halos associated with calcite filled joints, adjacent to the joints, and between horizontally bedded wacke contacts (Figure 3.19 A to C). Petrography also revealed evidence of fluid intrusion shown by fractures filled with ore minerals (Figure 3.33B). The correlation matrix (Appendix F-Table F2) revealed that the U had a strong positive correlation with CaO (inorganic carbon). The observations indicate a Ca-rich uranium-bearing hydrothermal solution with relatively low temperatures. Le Roux (1993) also suggested that a calcite rich mineralised solution was produced by carbonate rich groundwater and dewatering of tuffaceous lake sediments which he based on the widespread association of the uranium ore deposits with calcite gangue material. The possible chemistry of the hydrothermal fluid is shown by strong positive correlations between CaO, MnO, P₂O₅, Co, Ni, As, Sb, Zn, Mo, Pb, V and U.

4.2.3 Reductants

Carbon is confined within lower bench sandstone unit. This suggests that the distribution of carbon in the wacke was controlled by the deposition of the lithology (Figure 3.29 to Figure 3.32). Le Roux (1985) suggests that the organic material was eroded from a source area and deposited locally with channel sediments and covered rapidly to produce a reduced environment suitable for uranium mineralisation.

Fieldwork revealed that the carbon is finely distributed lower in the lithology, whereas higher up in the unit the carbon is confined to laminations in the sandstone. Further up in the lithology it is confined to layer plains until finally the carbon only occurs as highly dispersed in the wacke. In some instances, carbon fragments are concentrated on horizons (Figure 3.29). This was also evident in the petrology and geochemistry. The petrology (Figure 3.34C, D, and F) revealed that the carbon occurred as deformed plant fragments, disseminated blebs and coal-like seams between the mineral grains. The Pearson correlation coefficient matrix (Appendix F-Table F2) revealed a weak positive relationship between the total carbon and the SiO₂ (detrital minerals). The elements hosted in the detrital minerals showed no significant correlation with organic carbon. It is uncertain why there was no significant correlation, but possible explanations are that C and SiO₂ are completely different compounds and/or that they were sourced from different sources (*i.e.* organic plant and rock). The organic carbon and detrital minerals are still considered to have been deposited simultaneously from the petrographic evidence. The organic matter was sourced by the erosion of plant material and consented locally along with the detrital minerals. Since oxidation destroys plant material, the preservation of organic carbon on its own would be indicative of at least a mildly reducing environment after deposition Gastaldo & Demko (2012).

The organic carbon and sulfide minerals (pyrite and chalcopyrite) showed strong positive correlations in Appendix F-Table F2. This may indicate that the carbon was deposited in a mildly reduced environment promoting the replacement carbon with pyrite and chalcopyrite. Nonetheless, the carbon, pyrite, and chalcopyrite had negative correlations with uranium. This indicated that the carbon and sulfide anoxic reducing environment produced a suitable environment for the precipitation of uranium minerals. Le Roux (1985) also suggests this to produce the reduced environment needed to mineralise uranium. The uranium was associated with the inorganic carbon

revealed by a strong positive correlation between CaO and U in Appendix F-Table F2 supporting theories made by Le Roux (1993).

4.3 Uranium mineralogy and geochemistry

XRD analysis (Table 3.4) revealed that the uranium was in the U^{6+} valence state. Thus, in this valence state, the U will be transported as uranyl complexes of dissolved ions as stated by Skirrow, *et al.* (2009). In the presence of reductants like carbon and Fe(II)-bearing minerals, the uranium precipitated out of the solution to form stable uranium minerals (Robertson, *et al.*, 1978). These minerals are typically uraninite and pitchblende according to vast research conducted on Beaufort Group Uranium Provinces however no primary mineralisation was observed at Rietkuil mine.

The major and trace element composition of the hydrothermal fluid was reflected by the chemistry as CaO, MnO, P_2O_5 , Co, Ni, As, Sb, Zn, Mo, Pb, V, and U (*c.f.* Section 4.2.2). These elements formed the minerals hosted in the wacke. These elements were hosted in the calcite, apatite, sulfide, monazite and uranium minerals. The sulfide minerals were identified with the aid of interpretations from trace element data as arsenopyrite, and molybdenite. The uranium mineralization at Rietkuil mine was identified with the aid of XRD analysis and supported by trace element data. The uranium minerals include autunite, novacekite, carnotite, umohoite, zippeite. These minerals are typical secondary and alteration minerals of uraninite and pitchblende which a vast number of researchers revealed to be the main uranium minerals in the Karoo Uranium Province.

Alexandre & Kyser (2005) suggested that uraninite is a chemically active mineral that readily exchanges elements or recrystallize during fluid-circulation events. Calcium is the most common element to replace uranium in the uraninite structure during oxidized fluid-circulation events. Calcium has an ionic radius closest to that of uranium and thus they can easily substitute during fluid-circulation. Other substituents like iron and silica has a smaller ionic radius and will thus not readily alter uraninite but rather form discrete uranium-bearing alteration phases such as coffinite during oxidized fluid-circulation events.

4.4 Genetic uranium mineralization model for Rietkuil mine

This section will summarize the findings at Rietkuil mine incorporating the results with the geological and tectonic development of the Karoo Basin to construct a uranium mineralization model applicable to Rietkuil mine. The two models proposed by Cole & Labuschagne (1985); and Le Roux (1985), respectively, describing the uranium mineralization of the Karoo Basin will also be considered when describing the uranium mineralization model for Rietkuil mine.

During the marine and deltaic deposition of Ecca Group in the Permian (Figure 5.1A), southwestern Gondwana experienced tectonic activity. This was due to the pulsating subduction of the paleo-Pacific plate leading to the development of a calc alkaline magmatic-arc. This caused an increase in intrusive and extrusive magmatic and volcanic activity also producing tuff deposits in the basin. The tuff could be transported for hundreds of kilometers in the downwind direction (Visser, 1992; Kingsley, 1981; and Le Roux, 1985). Thin tuff layers were deposited simultaneously as part of the

sedimentological sequence of the Eccra Group and also parts of the Beaufort Group rocks.

The southern magmatic-arc (highlands) was the main source of sedimentation for the western Beaufort Group deposits. The sediments of the Adelaide Subgroup were deposited by upper delta plane and fluvial sand and mud in the Late Permian (Johnson, *et al.*, 2009). Le Roux (1985) suggested that vegetation was eroded and deposited locally with sediments. This is a possible explanation for the horizontally bedded lithic-wacke at Rietkuil mine, enriched in carbon (Figure 5.1B). Due to the nature of deposition, it was assumed that the organic material was covered quickly by new sediments, creating an anoxic environment ideal for the formation of sulfide minerals like pyrite. The mineralogy of the wacke comprises quartz, feldspar, lithic fragments, carbon, pyrite, and chalcopyrite similar to those described by Cole & Labuschagne (1985). Unequal loading of the sediments may have caused soft sediment deformation shortly after burial (on geological terms) in water-logged sediments leading to mutually eroding and offset barforms as was seen in Figure 3.30 (Owen & Moretti, 2011). Cole & Labuschagne (1985) made a similar statement. In these interfingering wacke lenses the carbon appeared to be finely distributed throughout the lenses. Possibly due to compaction. The thinly horizontally bedded and the interfingering basal wacke units caused an increase in the overall porosity of the wacke.

Major upliftment in southwestern Gondwana followed in the Triassic age (Figure 5.1C), completing the formation of the Cape orogeny (Tankard, *et al.*, 2009). The active continental margin (or recycled orogeny) tectonic setting described for Rietkuil mine supports the theory of Tankard, *et al.* (2009). The formation of the Cape orogeny led to the development of joint sets, faults, and folds in the Karoo Basin (Jordaan, 1990). Faults and some joint sets may also be related to the later breakup of Gondwana. Nonetheless, these tectonic activities led to an increase in the porosity of the wacke. The results from Rietkuil mine suggests that the joints were the feeders of uranium-bearing hydrothermal fluid into the sandstone. This was supported by many of the results from Rietkuil including the vertical nature of the joints, the distribution of the uranium mineralization, calcite-filled joints, the evidence of low-grade metamorphic halos, and mineralized fractures observed in the petrography.

The primary uranium mineralization was deposited by either erosional debris from the magmatic-arc or volcanic tuff layers (Figure 5.1D) between the sediments (Cole & Labuschagne 1985; and Le Roux, 1985). Both Cole & Labuschagne (1985) and Le Roux (1985) suggest that post-depositional circulating groundwater was responsible for the redistributions of the uranium. The results from Rietkuil mine (indicates) uranium was most likely transported in by Ca-rich fluid agent and is supported by the findings of Le Roux (1993). As the fluid circulated through the underlying sediments the temperature increased and started to dissolve ions like Cl^- , F^- , CO_3^{2-} , SO_4^{2-} , PO_4^{3-} , VO_4^{2-} , and AsO_4^{2-} . These ions are typically found associated with the Karoo uranium deposits according to Le Roux (1985). The uranium at Rietkuil mine was in the U^{+6} oxidation state as revealed by XRD results. According to research compiled by Skirrow, *et al.* (2009) when uranium occurs in this state it will form uranyl complexes with dissolved ions. As the hydrothermal fluid passed through the primary uranium

deposits, it remobilized the uranium as uranyl complexes. This was evident in the mineral geochemistry from Rietkuil mine revealed by the XRD.

A final tectonic event (most likely due to the break-up of Gondwana) caused joints to form along which these uranium-bearing fluids migrated upwards (Figure 5.1D). This was explained by the joints found at Rietkuil. Only certain joints at Rietkuil mine are filled with calcite veins and associated with these joints (Figure 3.20 to Figure 3.23) were higher concentrations of uranium mineralization (Figure 3.24 to Figure 3.27) as shown by corresponding sections. Likewise, where joint sets cross each other, where joints are closely spaced and/or where the sandstone seems to be interfingered, an increased concentration of uranium could be observed and Le Roux (1985) had similar observations. The effects of basin dewatering cannot be neglected. As the basin dewateres, fluids will migrate upwards along weak zones. When these fluids encounter the primary uranium deposits it will also be capable of dissolving and transporting the uranium to suitable locations for precipitation (Robertson, *et al.*, 1978).

As the hydrothermal fluid passed through the wacke, the uranium and possibly other sulfides like arsenopyrite and molybdenite precipitated from the fluid when it encountered the reductants (the organic carbon and pyrite and chalcopyrite) (Figure 5.1D). Similar models were proposed by Cole & Labuschagne (1985) and Le Roux (1985). At Rietkuil the reduced environment was produced by carbon and pyrite in the sediments. The uranium mineralization at Rietkuil was not the typical mineralization described by many authors as uraninite and pitchblende, but rather the secondary and alteration minerals of uraninite as suggested by Alexandre & Kyser (2005) (*c.f. Section 4.3*). Petrography revealed that the uranium and sulfide minerals occur disseminated in the matrix material where it crystalized on impermeable mineral grain boundaries, in close proximity to carbon, and/or adsorbed unto carbon fragments.

With all the above-mentioned information, it was concluded that the uranium mineralization at Rietkuil mine is epigenetic in nature, *i.e.* a secondary deposit. It can also be said, when the uranium mineralization models proposed by Cole & Labuschagne (1985) and Le Roux (1985) are combined, it may provide a more accurate model of the uranium mineralization of the Karoo Uranium Province.

Chapter 5: Conclusions

5.1 Conclusions

Rietkuil mine is a known uranium deposit of the Karoo Uranium Province in South Africa. From the results obtained by fieldwork, mineralogy, and geochemistry the following conclusions can be constituted about the sedimentology and the geochemistry of the uranium mineralization at Rietkuil mine.

The sandstone from Rietkuil mine hosting the uranium mineralization is a horizontally bedded lithic-wacke deposited in a high flow regime indicated by the dominant Lithofacies assemblage Sh with minor Sr. The tectonic setting for these sediments was slightly at odds as recycled orogeny and an active continental margin. This was attributed to the fact that the Karoo sequence was deposited in a retro-arc foreland basin with the Cape Fold Belt as the primary provenance (which was in an active continental margin setting) for the upper Karoo sequences.

Elements hosted by detrital minerals display a high degree of correlation. The detrital minerals consisted of quartz, feldspar, mica, and lithic fragments. These minerals were altered to sericite and smectite. Carbonaceous matter also formed part of the detrital minerals. The preservation of organic matter suggests a slightly reduced environment as an oxidised environment would have destroyed the carbon. This led to the formation of sulfide minerals pyrite and chalcopyrite. Fe₂O₃ and Cu hosted in pyrite and chalcopyrite, have a high degree of correlation with organic carbon but a strong negative correlation with the other ore minerals (uranium, arsenopyrite, molybdenite), indicating its cogenesis with the carbonaceous matter rather than with the ore minerals. The pyrite and chalcopyrite were altered to form iron oxides.

The carbon distribution was controlled by lithology. The basal portion of the lower bench have higher concentrations of carbon that were finely distributed throughout the wacke and higher in the lithology the carbon concentrations decreased until it appears highly dispersed.

Fieldwork, petrography and geochemistry suggested that uranium, arsenopyrite and molybdenite intruded into the wacke sandstone with a low-grade uranium-bearing hydrothermal fluid. A low-temperature hydrothermal fluid intrusion was proved by calcite-filled joints, low-grade metamorphic halos, the distribution of uranium mineralization around calcite-filled joints, and fractures in petrography.

Elements hosted in the hydrothermal minerals also show a high degree of correlation. The uranium has strong positive correlations with CaO indicating that the uranium content was possibly hosted by a Ca-rich hydrothermal fluid. The sulfide minerals associated with hydrothermal fluid was arsenopyrite, and molybdenite. The composition of the hydrothermal fluid possibly was CaO, MnO, P₂O₅, Co, Ni, As, Sb, Zn, Mo, Pb, V, and U. The hydrothermal fluid originates from circulating groundwater and/or basin dewatering fluids (Figure 5.1D).

The permeability of the wacke sandstone was increased as joints and faults formed as a result of the formation of the Cape orogen and/or the break-up of Gondwana. Other factors controlling the permeability of the sandstone was firstly the joints along with mutually eroding and offset barforms forming horizontally bedded sandstone lenses, and small fractures revealed with petrography. The uranium-bearing hydrothermal fluid was transported via joint systems into the host sandstone where it was further distributed throughout the sandstone units.

The uranium mineralization was restricted by locally deposited carbonaceous matter, presenting a sporadic appearance of uranium mineralization in the Karoo Uranium Province (Figure 5.1). Where the carbon was finely distributed throughout the sandstone more reaction space was available resulting in higher concentrations of uranium in the basal portion of the sediments. The carbon and coexisting sulfide minerals produced a reduced environment promoting the precipitation of uranium and other sulfide minerals (arsenopyrite and molybdenite) from solution.

The uranium mineralization at Rietkuil mine is secondary uranium mineralization *i.e.* epigenetic. The primary uranium was presumed to be sourced from either eroded detrital granitic fragments and/or tuff deposits and dissolved by hydrothermal fluids. XRD revealed the uranium mineral assemblage comprises autunite, novacekite, umohoite, zippeite, and carnotite. All secondary mineral phases of uraninite.

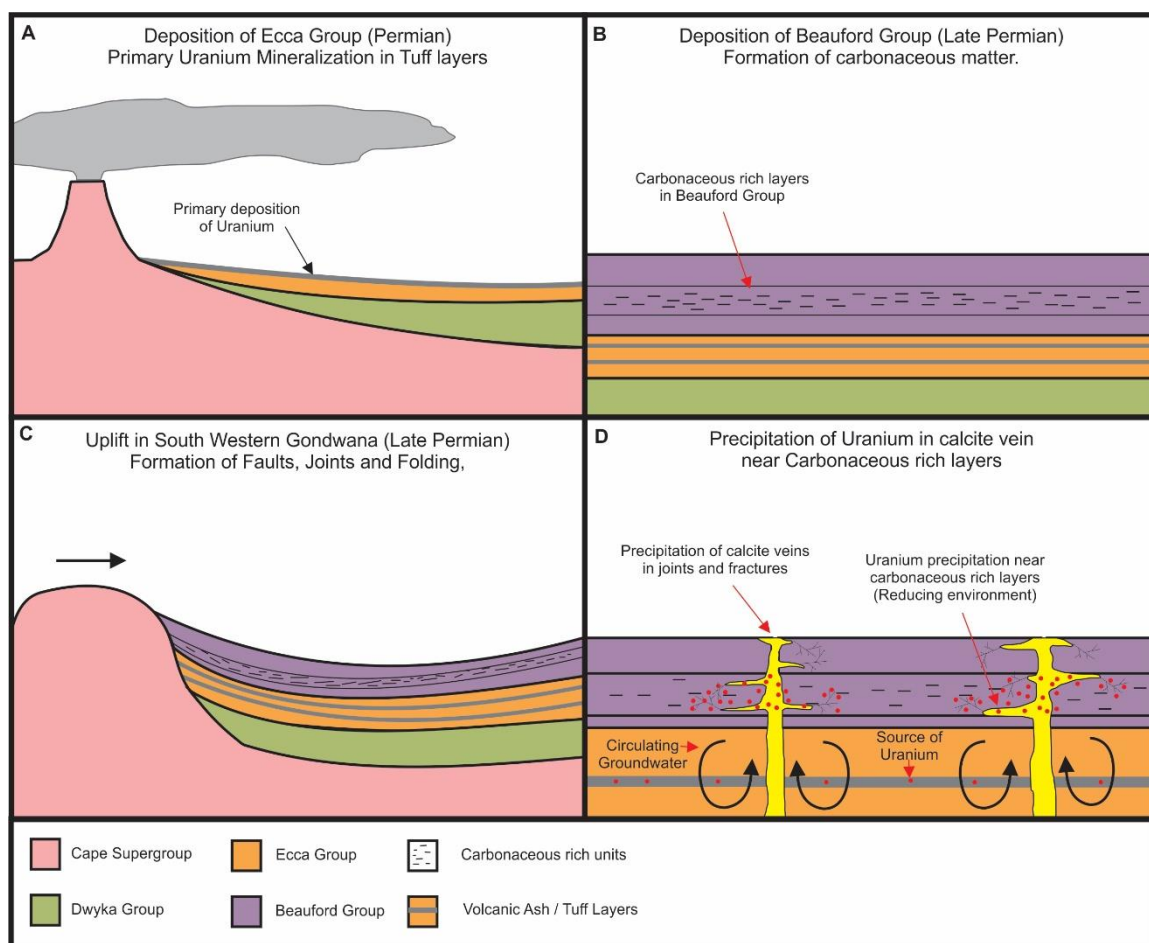


Figure 5.2: Proposed genetic uranium mineralization model for Rietkuil mine.

5.2 Suggestions for further study

1. Ore paragenesis studies will reveal information about the different ore mineral phases and relationships. This will add further proof for the theory proposed by this study.
2. The uranium mineralization model proposed by this study can be applied to other known deposits in the Karoo Uranium Province to see if similar conclusions can be made.
3. Detailed structural mapping of the Rietkuil mine area and other known deposits in the Karoo Uranium Province might reveal possible locations of significant uranium mineralization.

References

- AEC-AEK, 1994. Karoo Uranium Project Report, Pretoria, RSA: Atomic Energy Corporation of South Africa.
- Alexandre, P., & Kyser, T.K., 2005. Effects of cation substitutions and alteration in uraninite, and implications for the dating of uranium deposits. *The Canadian Mineralogist*, **43**, pp. 1005-1017.
- Ammann, A., 2007. Inductively coupled plasma mass spectrometry. *Journal of Mass Spectrometry*, **42**, pp. 419-427.
- Bednar, A.J., Medina, V.F., Ulmer-Scholle, D.S., Frey, B.A.; Johnson, B.L., Brostoff, W.N., Larson, S.L., 2007. Effects of Organic Matter on the Distribution of Uranium in Soil and Plant Matrices. *Chemosphere*, **70**, pp. 237-247.
- Bhatai, M., 1983. Plate tectonics and geochemical composition of sandstones. *J. of Geol.*, **91**, pp. 611-627.
- Bordy, E.M., Hancox, P.J., Rubidge B.S., 2005. The contact of the Molteno and Elliot formations through the main Karoo Basin, South Africa: a second-order sequence boundary. *South African Journal of Geology*, **108**, pp. 351-364.
- Catuneanu, O., Hancox, P. J., & Rubidge, B. S., 1998. Reciprocal flexural behaviour and contrasting stratigraphies: a new basin development model for the Karoo retroarc foreland system, South Africa. *Basin Research*, **10**, pp. 417-439.
- Catuneanu, O., Wopfner, H., Eriksson, P., & Cairncross, B., 2005. The Karoo Basins of South-Central Africa. *The Journal of African Earth Science*, **43**, pp. 211-253.
- Cole, D.I., 1992. Evolution and development of the Karoo Basin. **In:** De Wit, M.J. & Ransome, I.G.D. (Eds), *Inversion Tectonics of the Cape Fold Belt, Karoo and Cretaceous Basins of Southern Africa*, Rotterdam: Balkema, pp. 87-99.
- Cole, D.I., Johnson, M.R., Day, M.O., 2016. Lithostratigraphy of the Abrahamskraal Formation (Karoo Supergroup), South Africa. *South African Journal of Geology*, **119**(2), pp. 415-424.
- Cole, D.I., & Labuschagne, L., 1985. Geological environment of uranium deposits in the Beaufort Group, South Africa. *Geological Environments of the sandstone-type uranium deposits*, IAEA, Vienna, IAEA-TEDDOC-328, pp. 265-278.
- Cole, D., Labuschagne, L.S., Sohnge, A.P.G., Stettler, E.H., Schneider, G.I.C., 1991. Aeoradiometric Survey for Uranium and Ground Follow-up in the Main Karoo Basin. 1st ed. Pretoria, South Africa: Department of Mineral and Energy Affairs. *Memoir of the Geological Survey* **76**, pp.

- Cole, D., & Wipplinger, P., 2001. Sedimentology and Molybdenum Potential of the Beaufort Group in the Main Karoo Basin, South Africa. 1st ed. Pretoria, South Africa: *Council for Geoscience Memoir* **80**, pp. 225.
- Cox, K., & Clifford, P., 1982. Correlation coefficient patterns and their interpretation in three basaltic suites. *Contribution to Mineralogy and Petrology*, **79**, pp. 268-278.
- Cumberland, S.A., Etschmann, B., Brugger, J., Douglas, G., Evans, K., Fisher, L., Kappen, P., Moreau, J.W., 2018. Characterization of Uranium Redox State in Organic-Rich Eocene Sediments. *Chemosphere*, **194**, pp. 602-613.
- Dahlkamp, F. J., 1993. Uranium Ore Deposits. 1st ed. Berlin Heidelberg, Germany: Springer-Verlag.
- Day, M.O., & Rubidge, B.S., 2014. A brief lithostratigraphic review of the Abrahamskraal and Koonap Formation of the Beaufort Group, South Africa: Towards a basin-wide stratigraphic scheme for the Middle Permian Karoo. *Journal of African Earth Sciences*, **100**, pp. 227-242.
- De Wit, M.J., & Ransome, I.G.D., 1992. Regional inversion tectonics along the southern margin of Gondwana. In: De Wit, M.J. & Ransome, I.G.D. (Eds), *Inversion Tectonics of the Cape Fold Belt, Karoo and Cretaceous Basins of Southern Africa*, Rotterdam: Balkema, pp. 15-21.
- Dickenson, W.R., Beard, L.S., Brakenridge, G.R., 1983. Provenance of North American Phanerozoic sandstones in relation to tectonic setting. *Geol. Soc. Am. Bull.*, **94**, pp. 222-235.
- Dott, R., 1964. Wacke, graywacke and matrix-What approach to immature sandstone classification?. *Journal of Sedimentary Petrology*, **34**(3), pp. 625-632.
- Duane, M., Welke, H., Allsopp, H. & Wilsher, W., 1989. U-Pb isotope systematics, ages and genesis of Karoo uranium deposits, South Africa. *South African Journal of Geology*, **92**(1), pp. 49-64.
- Gastaldo, R.A., & Demko, T.M., 2012. The Relationship between Continental Landscape Evolution and the Plant-Fossil Record: Long Term Hydrologic Controls on Preservation. In: P.A. Allison and D.J. Bottjer (eds.), *Taphonomy: Process and Bias Through Time*, Topics in Geobiology 32, pp. 249-285.
- Gastaldo, R.A., Neveling, J., Geissman, J.W. and Looy, C.V. 2019. Testing the Daptocephalus and Lystrosaurus Assemblage Zones in a Lithostratigraphic, Magnetostratigraphic, and Palynological Framework in the Free State, South Africa: *Palaios*, **34**(11), pp. 542-561.
- Ghazi, S. & Mountney, N. P., 2009. Facies and Architectural Element Analysis of a Meandering Fluvial Succession: The Permian Warchha Sandstone, Salt Range, Pakistan. *Sedimentary Geology*, **221**, pp. 99-126.
- Hancox, P. & Rubidge, B., 1997. The role of fossils in interpreting the development of the Karoo Basin. *Palaeont. afr.*, **33**, pp. 41-54.

Hancox, P. & Rubidge, B., 2001. Breakthrough in the biodiversity, biogeography, biostratigraphy, and basin analysis of the Beaufort Group. *African Earth Sciences*, **33**, pp. 563-577.

Harron, M., 1988. Geochemical classification of terrigenous sands and shales from core or log data. *J. of Sed. Petrology*, **58**, pp. 820-829.

HILLER, N. & STAVRAKIS, N. 1984. Permo-Triassic fluvial systems in the southeastern Karoo Basin, South Africa. *Palaeogeography, Palaeoclimatology, Palaeoecology*, **34**, pp. 1-21.

Johnson, M.R., 1991. Sandstone petrography, provenance and plate tectonic setting in Gondwana context of the southeastern Cape-Karoo Basin. *South African Journal of Geology*, **94**(2/3), pp. 137-154.

Johnson, M.R., van Vuuren, C.J., Cole, D.I., Wickens, H.de V., Christie, A.D.M., Roberts, D.L., Brandl, G., 2006. Sedimentary Rocks of the Karoo Supergroup. In: M. Johnson, C. Anhaeusser & R. Thomas, eds. *The Geology of South Africa*. Johannesburg and Pretoria, South Africa: Published jointly by the Geological Society of South Africa, Johannesburg, and the Council for Geoscience, Pretoria, pp. 461-499. 691 pg.

Jordaan, M., 1990. Basin analysis of the Beaufort Group in the western part of the Karoo Basin. Bloemfontein: Unpublished Ph.D. at the University of the Free State.

Keyser, A., & Smith, R., 1979. Vertebrate biozonation of the Beaufort Group with special reference to the western Karoo Basin. *Ann. Geol. Surv. S. Afr.*, **12**, pp. 1-35.

Kingsley, C., 1981. A composite submarine fan-delta-fluvial model for the Ecca and lower Beaufort Groups of Permian age in the Eastern Cape Province, South Africa. *Trans. Geol. Soc. S. Afr.*, **84**, pp. 27-40.

Kitching, J., 1977. The distribution of the Karoo vertebrate fauna. *Bernard Price Inst. Palaeont. Res., Univ Witwatersrand, Memoir I*, p. 131

Kubler, M., 1977. The sedimentology and uranium mineralization of the Beaufort Group in the Beaufort West-Fraserburg-Mearweville area, Cape Province. Johannesburg: Unpublished MSc. thesis at the University of the Witwatersrand.

Le Roux, J., 1985. Tectonic and sedimentological environments of sandstone-hosted uranium-hosted uranium deposits, with special reference to the Karoo Basin of South Africa. Geological Environments of sandstone-type uranium deposits, IAEA, Vienna, IAEA-TEDDOC-328, pp. 279-290.

Le Roux, J., 1993. Genesis of stratiform U-Mo deposits in the Karoo Basin of South Africa. *Ore Geology Reviews*, **7**, pp. 485-509.

Lindeque, A., De Wit, M.J., Ryberg, T., Weber, M., Chevallier, L., 2011. Deep crustal profile across the southern Karoo Basin and Beattie Magnetic Anomaly, South Africa:

An integrated interpretation with tectonic implications. *South African Journal of Geology*, **114**(3-4), pp. 265-292.

Miall, A. D., 1988. Reservoir Heterogeneities in Fluvial Sandstones: Lesson from Outcrop Studies. *The American Association of Petroleum Geologists Bulletin*, **72**(6), pp. 682-697.

Nelson, D., & Sommers, L., 1982. Total carbon, organic carbon, and organic matter. In: A. Page, R. Miller & D. Keeney, eds. *Methods of soil analysis. Part 2 Chemical and Microbial Properties*, pp. 539-579.

Owen & Moretti, 2011. Identifying triggers for liquefaction-induced soft-sediment deformation in sands. *Sedimentary Geology*, **235**, pp. 141–147.

Pearson, R., 1963. Hard and soft acids and bases. *Journal of the American Chemical Society*, **85**, pp. 3533-3539.

Prinsloo, M., 1988. Effects of cultivation on the content and availability of nitrogen in selected Orange Free State soils. Bloemfontein: Unpublished MSc. thesis, Department of Soil Science, University of the Free State.

Robertson, D., Tilsley, J., & Hogg, G., 1978. The Time-Bound Character of Uranium Deposits. *Economic Geology*, **73**, pp. 1409-1419.

Rogers, A., & Schwartz, E., 1902. Report on a survey of parts of Beaufort West, Prince Albert and Sutherland divisions: 7th Annual Report of the Geological Commission of the Cape of Good Hope, pp 99-129

Scholtz, N., 2003. Assessment of potential toxic influence of uranium trail mining in the Karoo Uranium Province. Bloemfontein: Unpublished MSc. thesis from the University of the Free State.

Skirrow, R.G., Jaireth, S., Huston, D.L., Bastrakov, E.N., Schofield, A, Van Der Wielen, S.E., Barnicoat, A.C., 2009. Uranium mineral system: Processes, exploration criteria and a new deposit framework. Canberra, ACT: Geoscience Australia.

STAVRAKIS, N. 1980. Sedimentation of the Katberg Sandstone and adjacent formations in the southeastern Karoo Basin. *Transactions of the Geological Society of South Africa*, **83**, pp. 361-374.

Suryanarayana, C., & Norton, M., 1998. X-Ray Diffraction: A practical approach. 1st ed. New York: Springer Science+Business media.

Tankard, A., Welsink, H., Aukes, P., Newton, R., Stettler, E., 2009. Tectonic Evolution of the Cape and Karoo Basins of South Africa. *Marine and Petroleum Geology*, **26**, pp. 1379-1412.

Turner, B., 1978. Sedimentary patterns of uranium mineralization in the Beaufort Group of the southern Karoo (Gondwana) Basin, South Africa. In: A. Maill, ed. *Fluvial Sedimentology. Can. Soc. Petrol. Geol. Memoir* **5**, pp. 831-848.

- Turner, B., 1979. Geology of the uraniferous Beaufort Group near Beaufort West.. Excursion Guide Book, *Geol. Soc. S. Afr.*, **79**, p. 72 pp.
- Turner, B., 1981. Revised stratigraphy of the Beaufort Group in the Southern Karoo Basin. *Palaeont. afr.*, **24**, pp. 87-98.
- Vaughan, D., & Corkhill, C., 2017. Mineralogy of sulfides. *Elements*, **13**(2), pp. 81-87.
- Viglietti, P.A., Rubidge, B.S., Smith, R.M.H., 2017. Revised lithostratigraphy of the Upper Permian Balfour and Teekloof Formations of the main Karoo Basin, South Africa. *South African Journal of Geology*, **120**(1), pp. 45-66.
- Visser, J.N., 1992. Basin Tectonics in Southwestern Gondwana During the Carboniferous and Permian. In: A. Balkema, ed. Inversion Tectonics of the Cape Fold Belt, Karoo and Cretaceous Basins of Southern Africa. Rotterdam, Brookfield: Maarten J. De Wit and Ian G.D. Ransome, pp. 109-115.
- Walkley, A., & Black, I.A., 1934. An examination of the Degtjareff method for determining soil organic matter and a proposed modification of the chromic acid titration method. *Soil Science*, **37**, pp. 29-38.
- Willis, J., Turner, K., & Pritchard, G., 2011. XRF in the workplace: A guide to practical XRF spectrometry, South Africa: Milla Litho (Pty) Ltd.
- Wiltshire, G., 1987. Laboratory notebook 5. Unpublished document at the Department of Soil Sciences, University of the Free State.
- Xu, Y., Mahed, G., Van Wyk, Y., Lin, L., Sun, X., Xiao, L., Talma, S., 2012. Towards a sampling and monitoring protocol of radioactive elements in fractured rock aquifers for groundwater resource security in Beaufort West, Cape Town, RSA: Water Research Commission. Department of Earth Science, University of the Western Cape, Water Division of the Council of Geoscience.

Appendix A

A1 Analysis conducted on samples

Table A1: The sample names collected at Rietkuil mine and the mineralogical and geochemical analyses performed on them. Y=yes and N=no.

Bench	Face	Short name	Geochemical sample name	Petrography	XRD	XRF- MAJOR ELEMENTS	XRF- TRACE ELEMENTS	ICP-MS	LECO	Mebium titration method
Lower bench	1	AE1	F1B1AE1	N	N	Y	Y	Y	Y	Y
	1	AE2	F1B1AE2	Y	N	N	Y	N	Y	Y
	1	AE3	F1B1AE3	N	Y	Y	Y	N	Y	Y
	1	AE4	F1B1AE4	Y	N	N	Y	Y	Y	Y
	1	AE5	F1B1AE5	N	Y	Y	Y	N	Y	Y
	1	JI1	F1B1JI1	N	Y	Y	Y	N	Y	Y
	1	JI2	F1B1JI2	Y	N	Y	Y	Y	Y	Y
	1	OJ1	F1B1OJ1	N	Y	Y	Y	N	Y	Y
	1	OJ3	F1B1OJ3	N	Y	Y	Y	N	Y	Y
	1	OJ4	F1B1OJ4	Y	Y	Y	Y	Y	Y	Y
	2	AE1	F2B1AE1	N	Y	Y	Y	N	Y	Y
	2	AE2	F2B1AE2	N	N	N	Y	N	Y	Y
	2	AE3	F2B1AE3	Y	N	Y	Y	Y	Y	Y
	2	AE4	F2B1AE4	N	N	Y	Y	N	Y	Y
	2	AE5	F2B1AE5	N	Y	Y	Y	N	Y	Y
	2	AE6	F2B1AE6	N	Y	Y	Y	N	Y	Y
	2	AE7	F2B1AE7	N	Y	Y	Y	N	Y	Y
	2	AE8	F2B1AE8	Y	Y	Y	Y	N	Y	Y
	2	AE9	F2B1AE9	Y	Y	Y	Y	Y	Y	Y
	2	AE10	F2B1AE10	Y	Y	Y	Y	Y	Y	Y
	2	AJ1	F2B1AJ1	N	N	N	Y	N	Y	Y
	2	AJ2	F2B1AJ2	N	Y	Y	Y	N	Y	Y
	3	AE1	F3B1AE1	N	N	N	Y	N	Y	Y
	3	AE2	F3B1AE2	N	N	N	Y	N	Y	Y
	3	AE3	F3B1AE3	N	Y	Y	Y	N	Y	Y
	3	AE4	F3B1AE4	N	Y	Y	Y	N	Y	Y
	3	AE5	F3B1AE5	N	Y	Y	Y	N	Y	Y
	3	AE6	F3B1AE6	N	N	N	Y	N	Y	Y
	3	AE7	F3B1AE7	N	Y	Y	Y	N	Y	Y
	3	AE8	F3B1AE8	N	N	N	Y	N	Y	Y
	3	AE9	F3B1AE9	N	N	N	Y	N	Y	Y
	3	OJ1	F3B1OJ1	N	Y	Y	Y	N	Y	Y
	4	AE1	F4B1AE1	Y	Y	Y	Y	Y	Y	Y
	4	AE2	F4B1AE2	Y	N	Y	Y	Y	Y	Y
	4	AE3	F4B1AE3	N	N	N	Y	N	Y	Y
	4	AE4	F4B1AE4	Y	N	Y	Y	Y	Y	Y
	4	AE5	F4B1AE5	Y	Y	Y	Y	Y	Y	Y
	4	AE6	F4B1AE6	Y	Y	Y	Y	Y	Y	Y
	4	AJ1	F4B1AJ1	Y	Y	Y	Y	Y	Y	Y
	4	OJ1	F4B1OJ1	N	Y	Y	Y	N	Y	Y
	4	JI1	F4B1JI1	Y	N	N	Y	N	Y	Y
Upper bench	1	S1	F1B2S1	N	Y	Y	Y	N	Y	Y
	1	S2	F1B2S2	N	Y	Y	Y	N	Y	Y
	1	S3	F1B2S3	N	Y	Y	Y	N	Y	Y
	2	S1	F2B2S1	Y	Y	Y	Y	Y	Y	Y
	2	S2	F2B2S2	N	Y	Y	Y	N	Y	Y
	2	S3	F2B2S3	N	Y	Y	Y	N	Y	Y
	3	S1	F3B2S1	N	Y	Y	Y	N	Y	Y
	3	S2	F3B2S2	N	Y	Y	Y	N	Y	Y
	3	S3	F3B2S3	N	Y	Y	Y	N	Y	Y
	4	S1	F4B2S1	N	Y	Y	Y	N	Y	Y
	4	S2	F4B2S2	N	Y	Y	Y	N	Y	Y
	4	S3	F4B2S3	N	Y	Y	Y	N	Y	Y

A2 Petrography

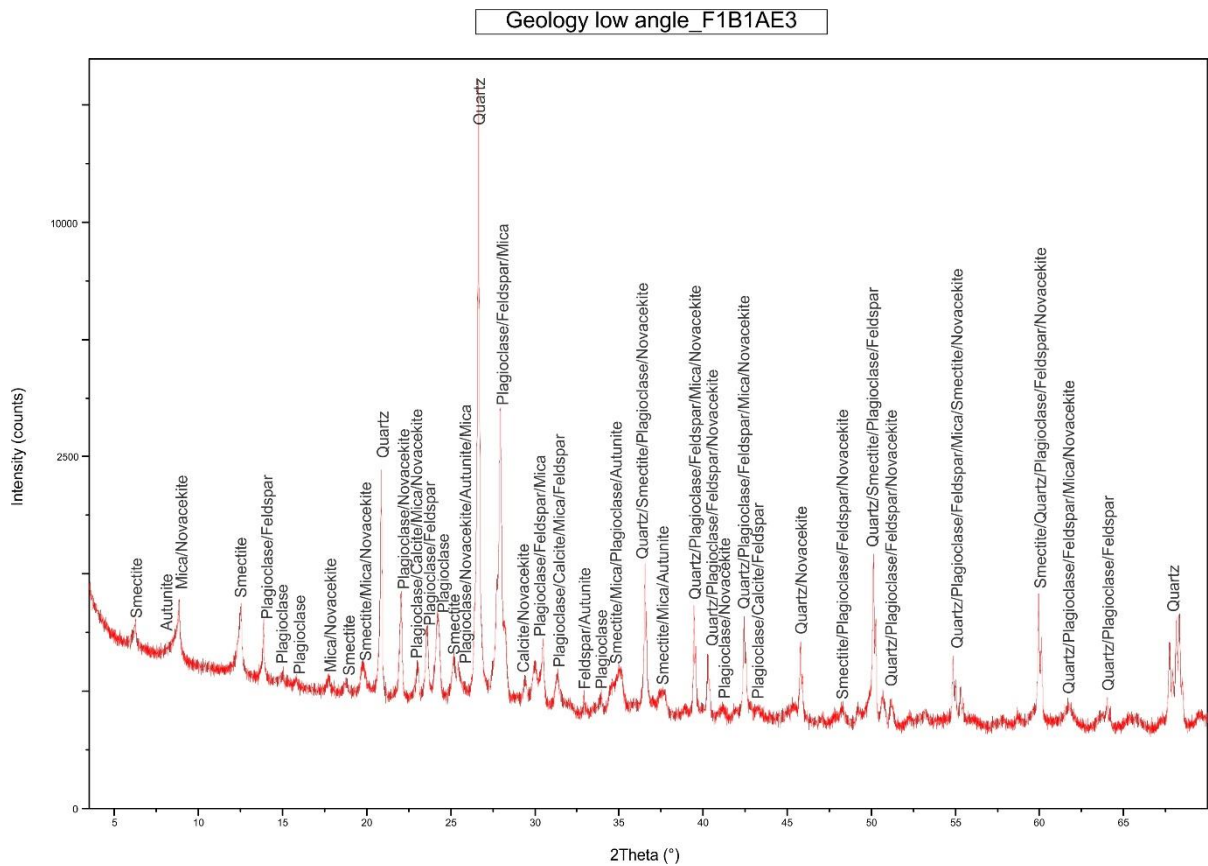
Table A2: Petrographic results obtained from sandstone samples collected at Rietkuil mine, summarized.

Sample	Quartz	Muscovite	Feldspar	Carbonate clasts	Chert Clast	Silt Clast	Zircon	Carbon	Dark Minerals	Sericite	Iron-oxide	Matrix
F1B1AE4	42	5	5	10	4		<1	2	5	5	5	15
F4B1AE1	56	4	4	7	3	1		1	3	6	3	12
F4B1AE5	59	4	5	5	5	2	<1	1	4	1	2	10
F2B1AE10B	46	3	4	10	6	1		1	6	6	7	10
F4B1AJ1	57	5	5	5	6			1	4	5	2	10
F1B1JI2	54	2	3	5	3			2	10	8	3	10
F1B1AE1	54	4	4	5	6	1		2	5	5	5	9
F1B1OJ4	56	4	3	5	5			1	5	5	7	9
F2B1AE3	54	3	4	6	7	1		2	5	5	3	10
F2B1AE8	52	4	3	5	5	1		2	7	5	4	12
F2B1AE9	56	3	4	3	5	1		1	6	6	6	8
F2B1AE10A	55	4	3	7	7			2	10	5	6	11
F2B2S1	54	2	5	6	4	1		1	2	2	5	11
F4B1AE2	64	4	4	3	5	2		2	5	2	3	6
F4B1AE4	66	3	4	5	6	1		1	3	3	3	10
F4B1AE6	55	3	6	6	5	2	<1	2	3	5	2	10
F4B1JI1	61	3	5	4	7			1	3	5	2	9

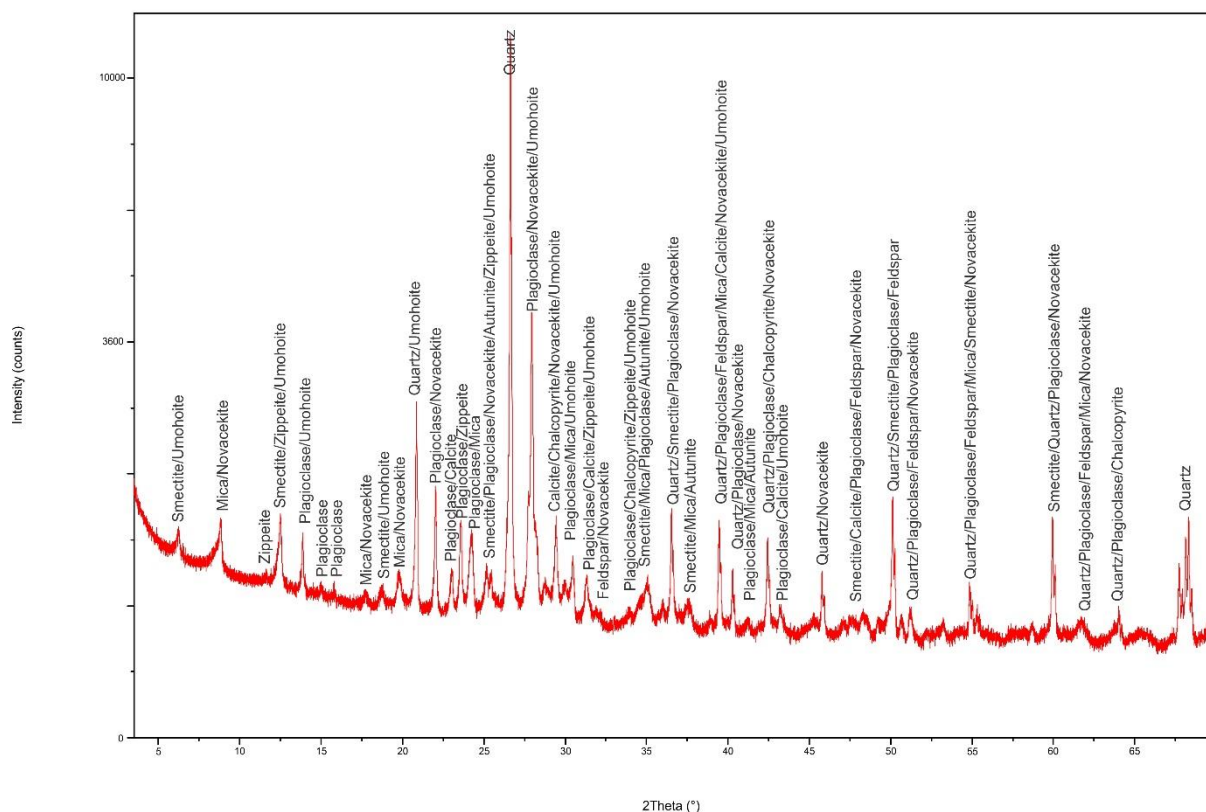
Appendix B

B1 XRD

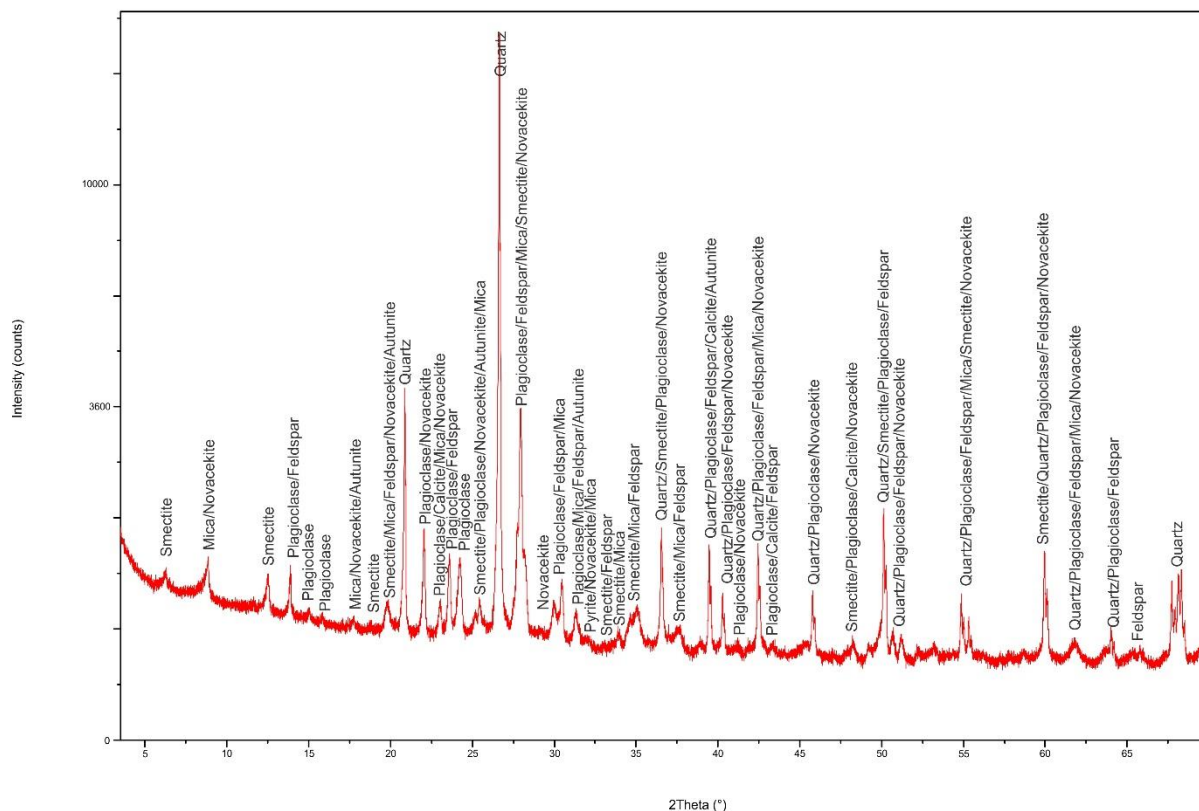
In the next few pages are the XRD spectrum data indicating the identified minerals, indicated on the peaks. The peaks are measured in counts per second (cps). The results from rietkuil mine are summarized in Table B1.



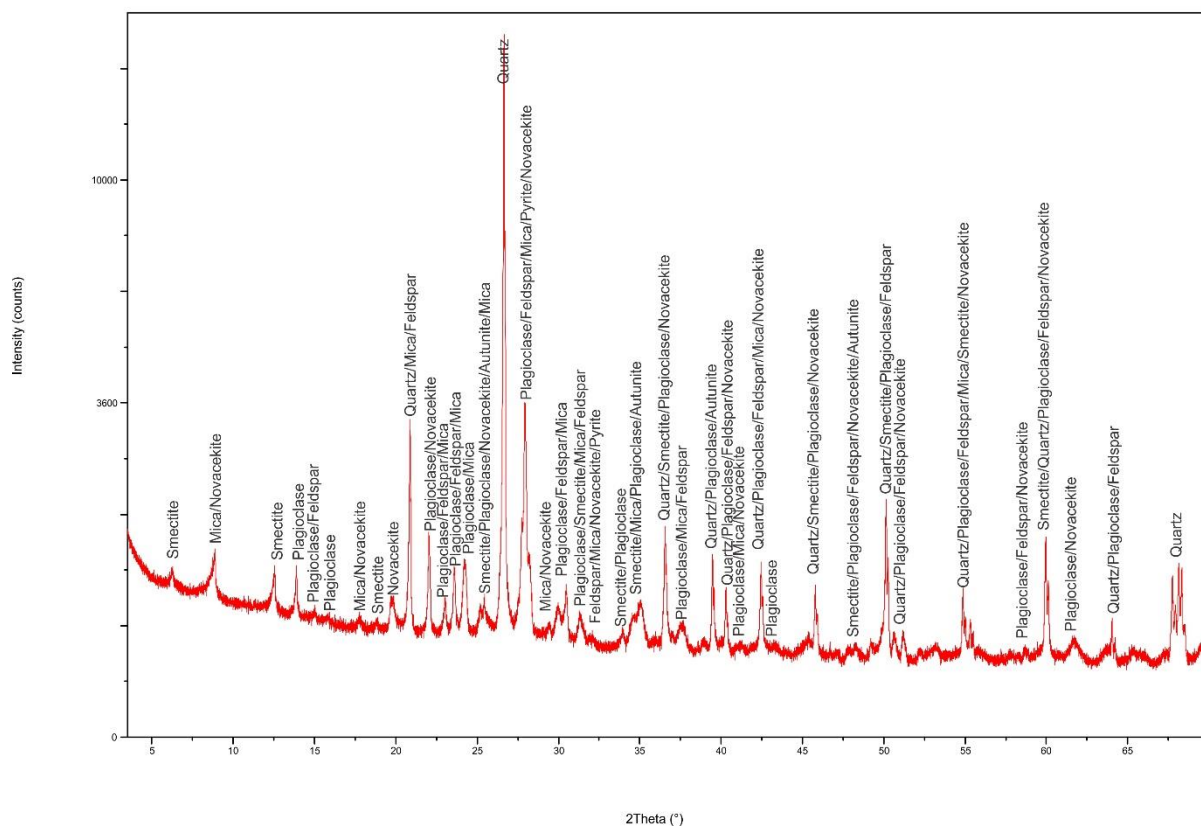
Geology low angle_F1B1J12



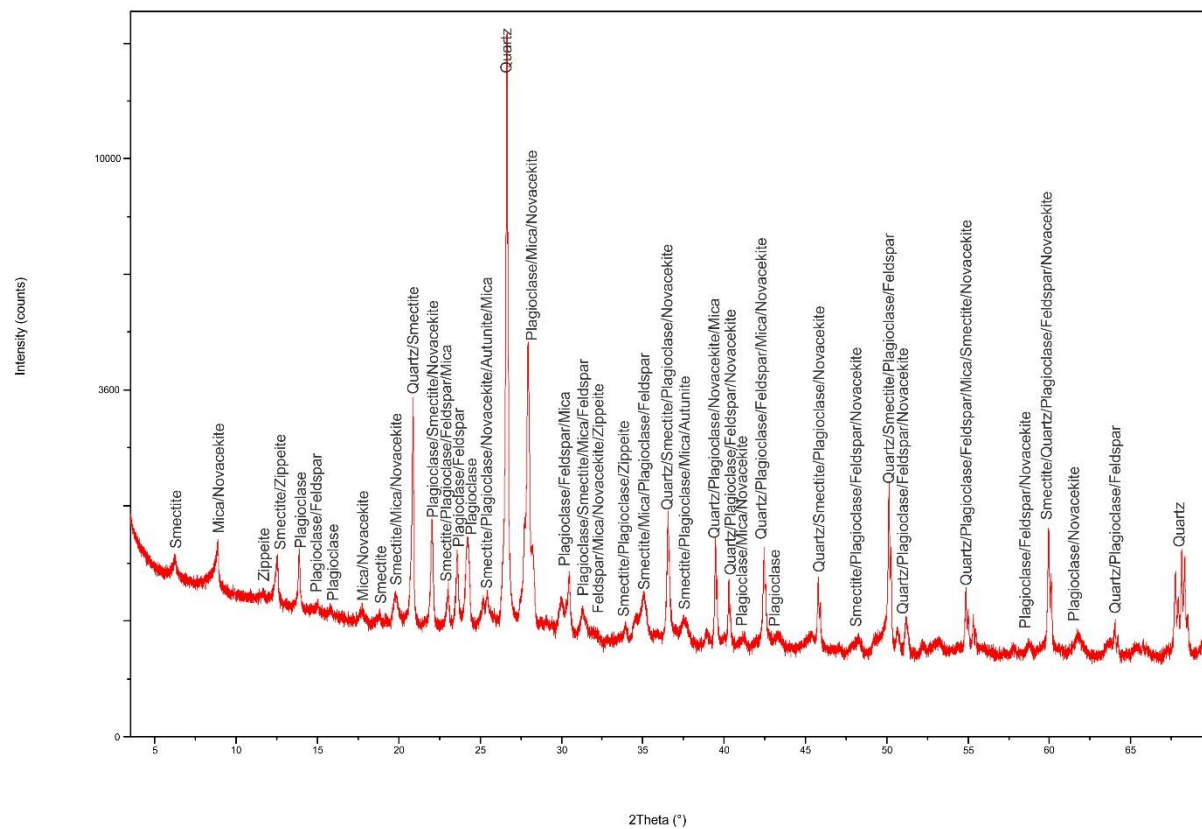
Geology low angle_F1B1AE5



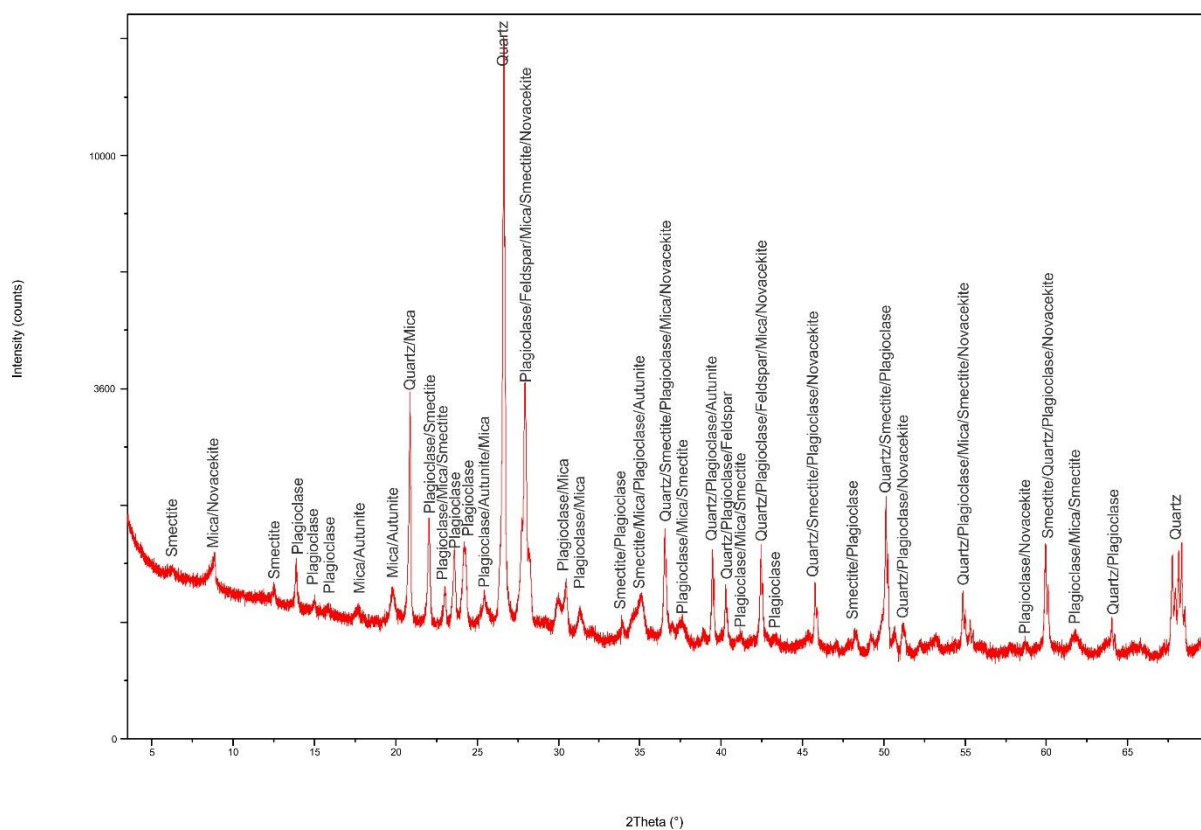
Geology low angle_F1B1OJ1



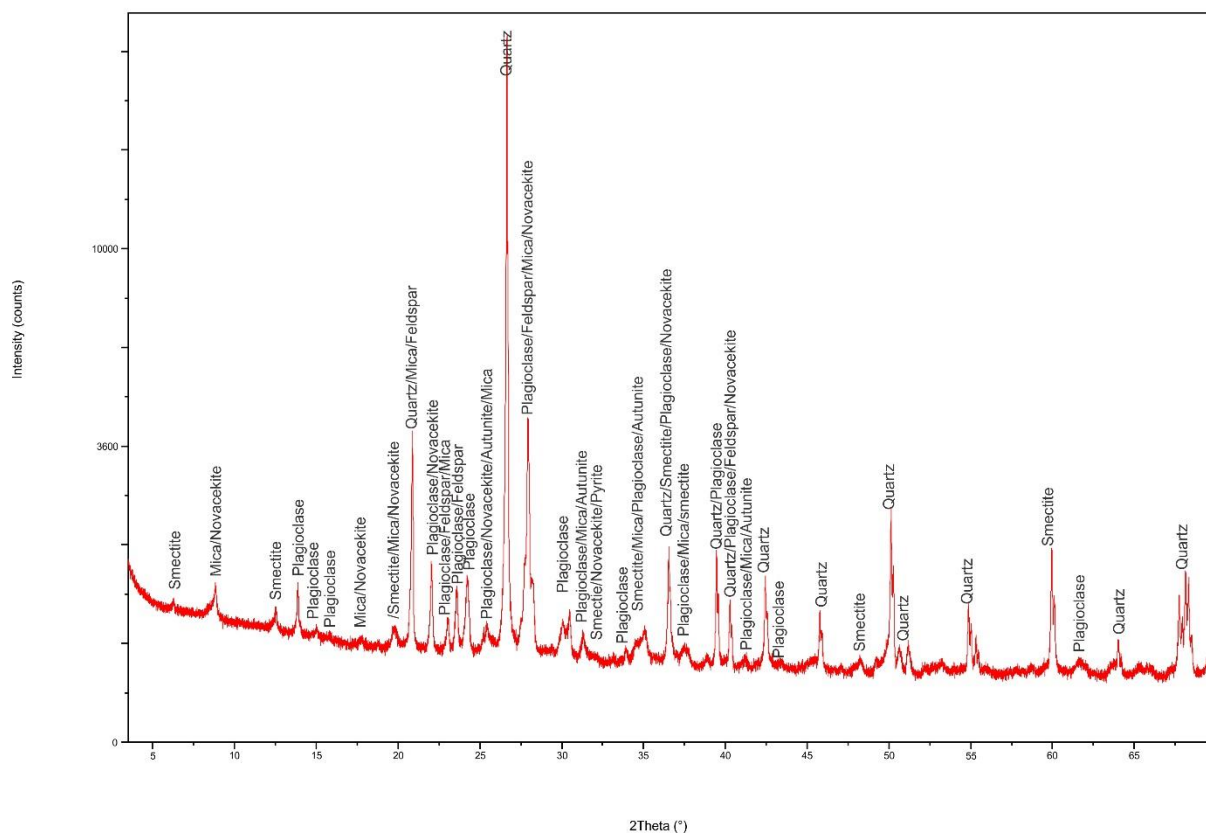
Geology low angle_F1B1OJ3



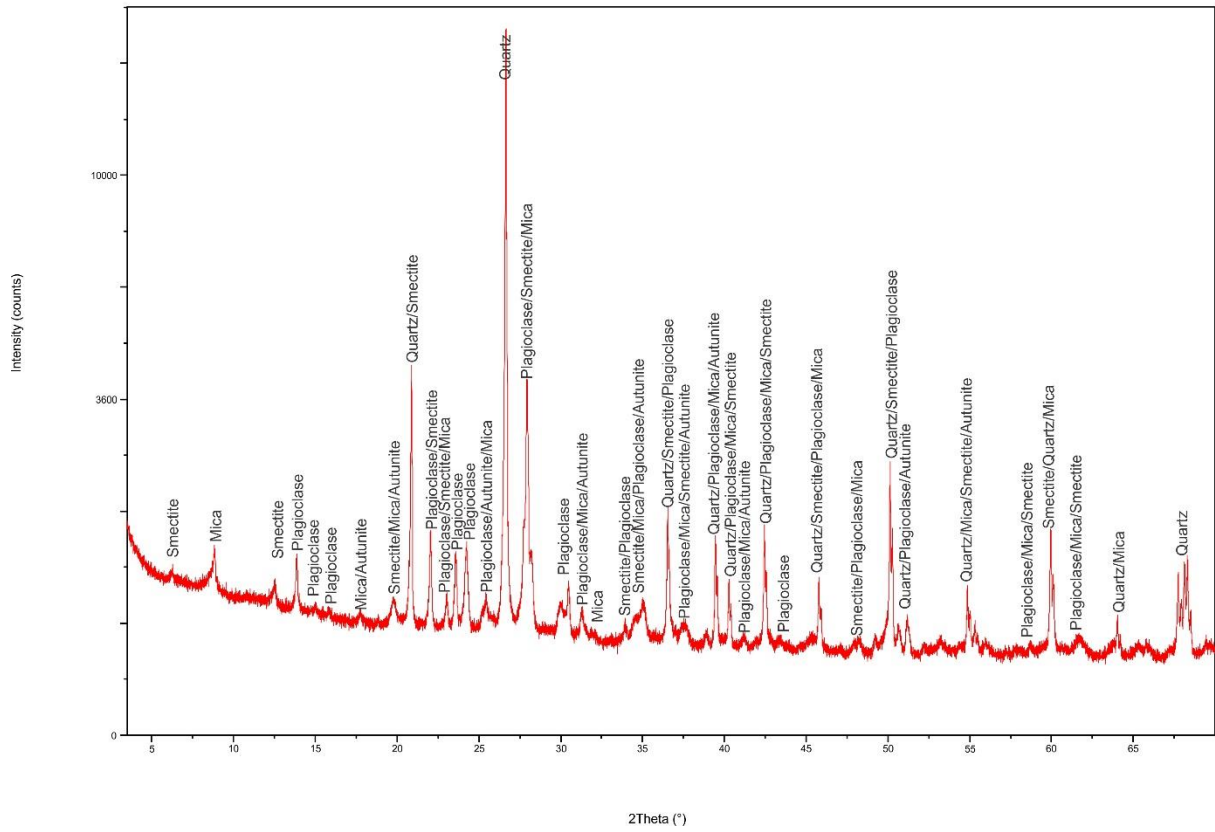
Geology low angle_F1B1OJ4



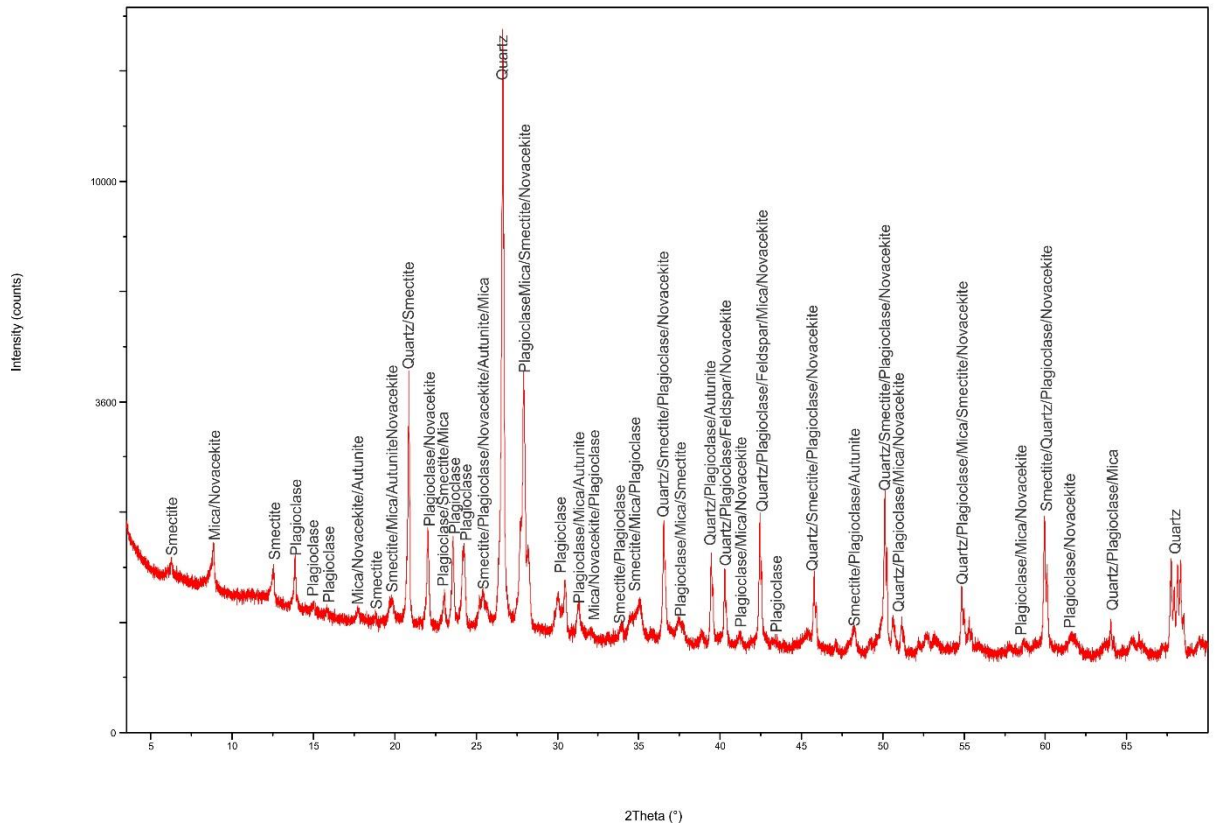
Geology low angle_F1B2S1



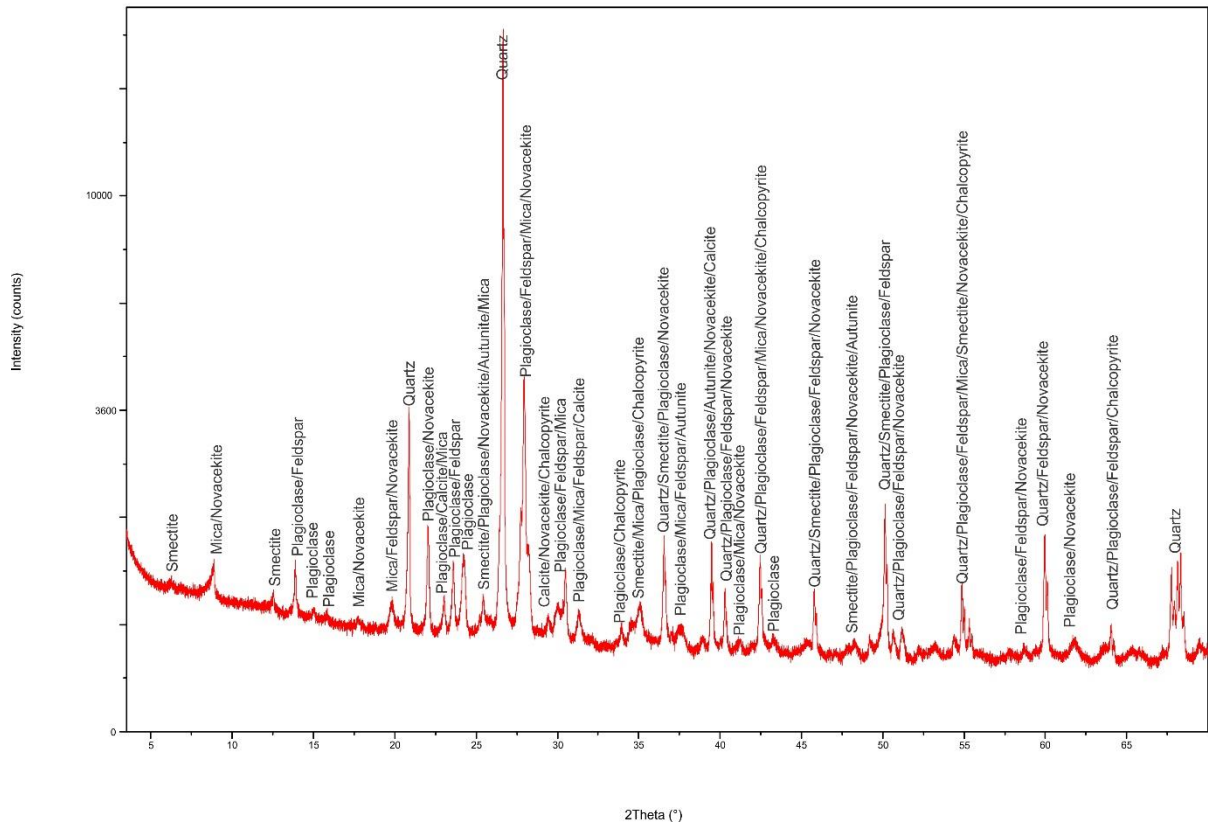
Geology low angle_F1B2S2



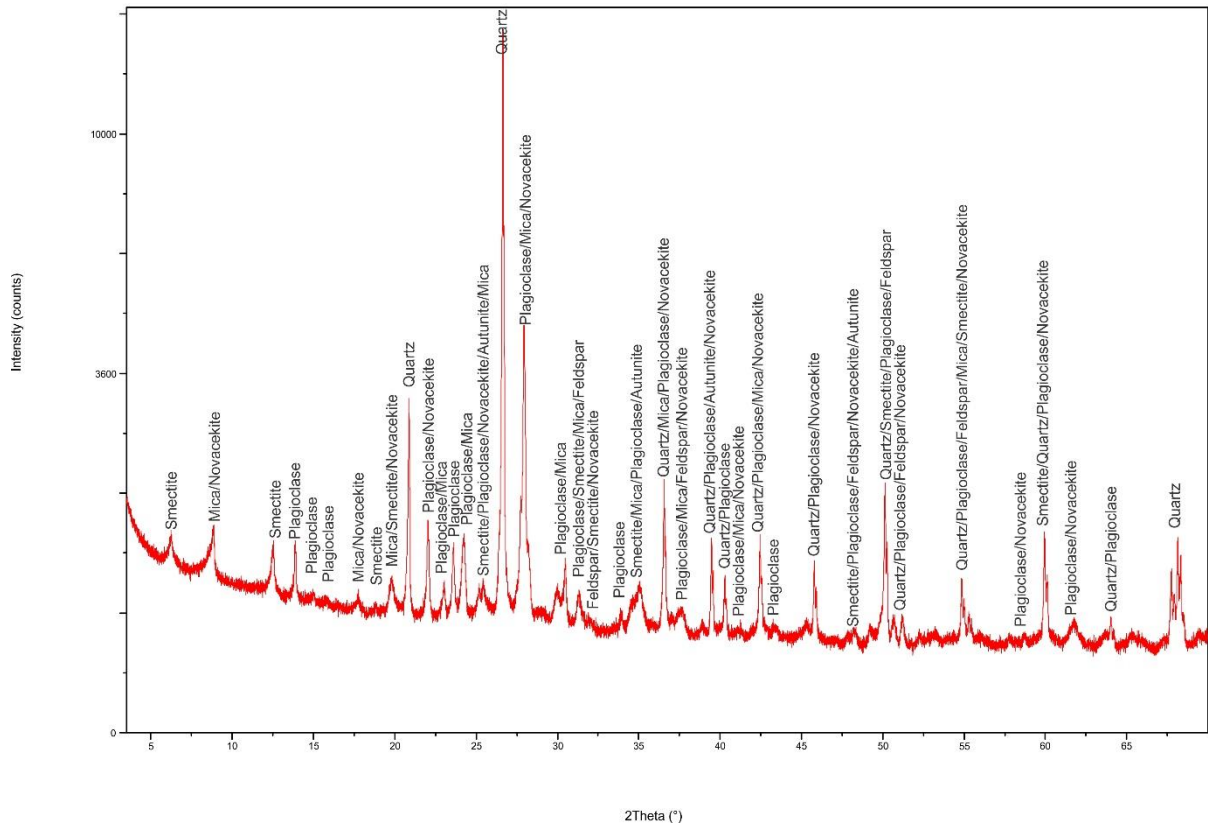
Geology low angle_F1B2S3



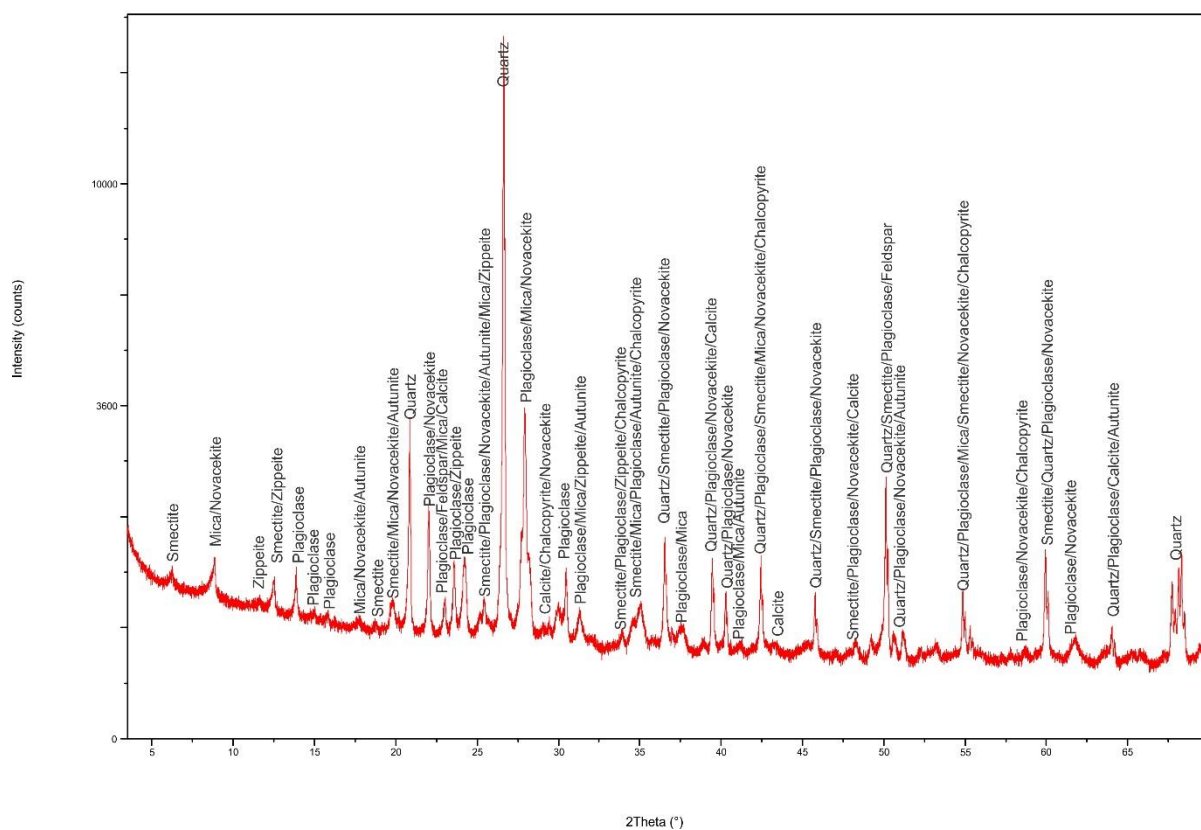
Geology low angle_F2B1AE1



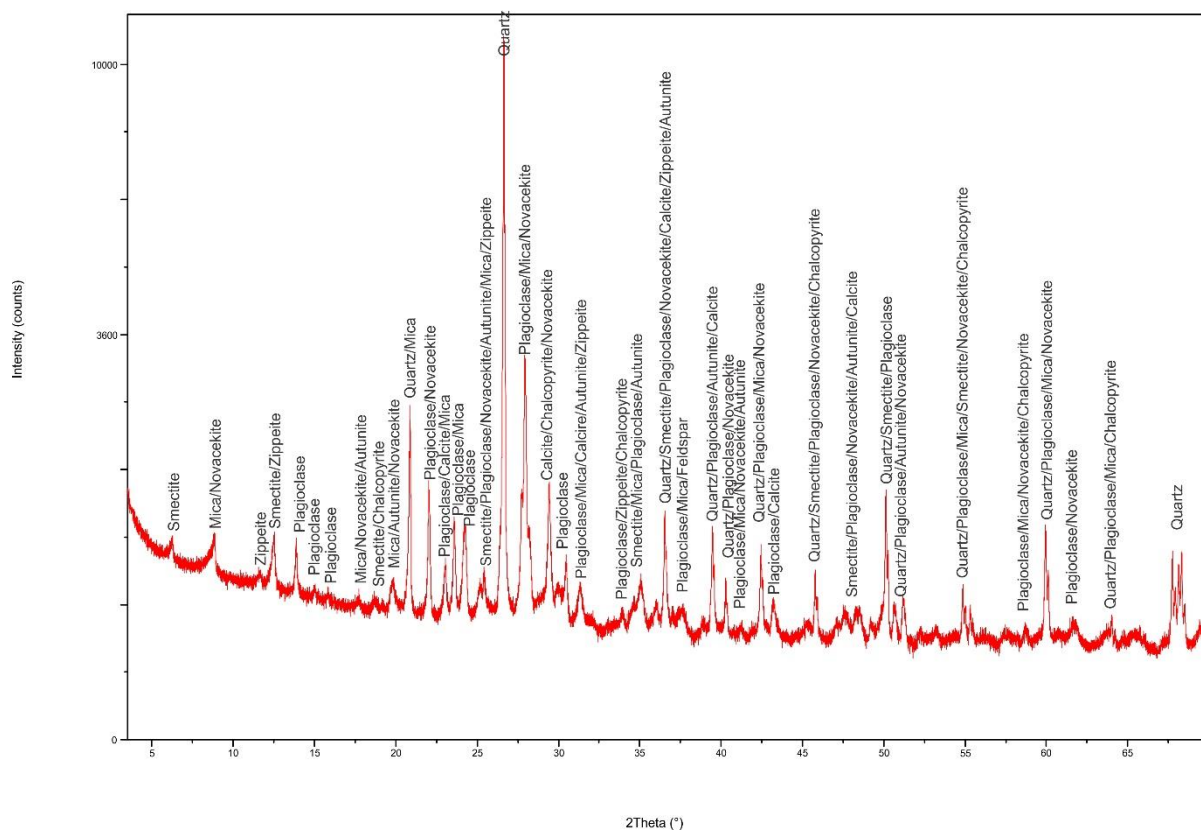
Geology low angle_F2B1AE5



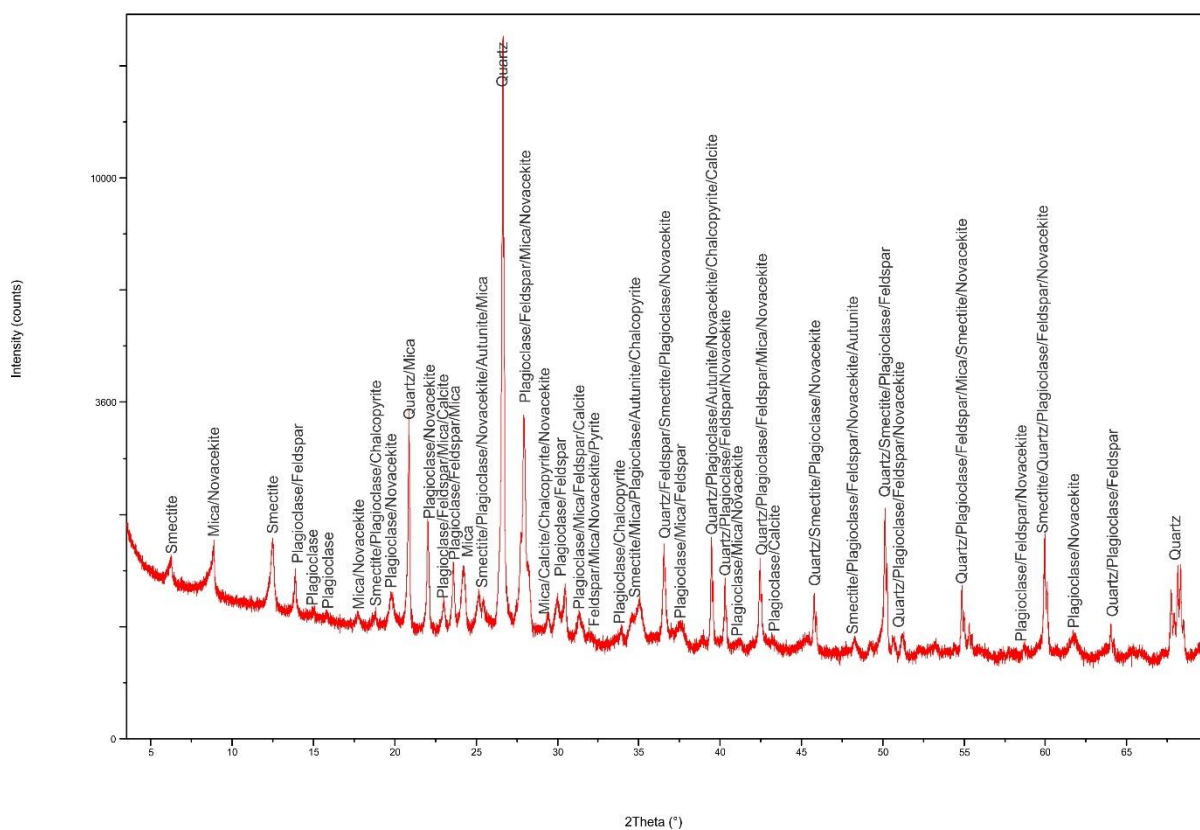
Geology low angle_F2B1AE6



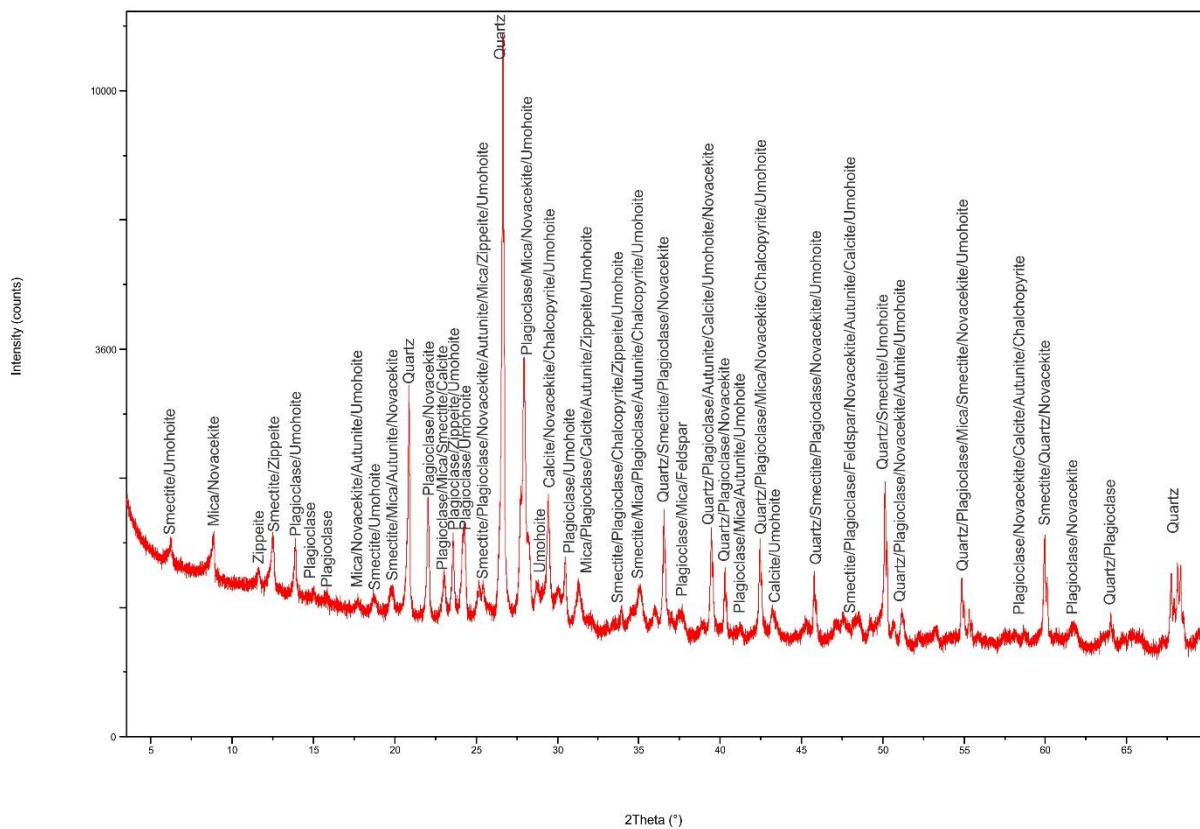
Geology low angle_F2B1AE7



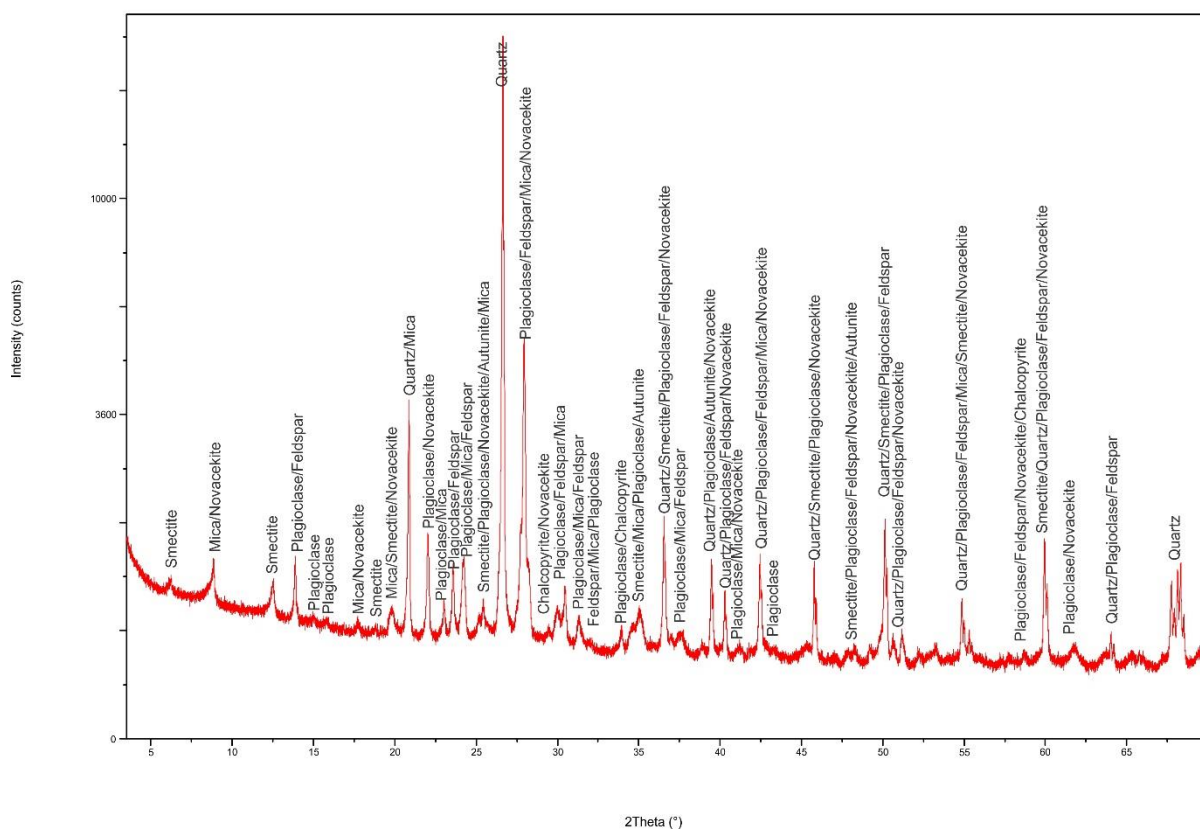
Geology low angle_F2B1AE9



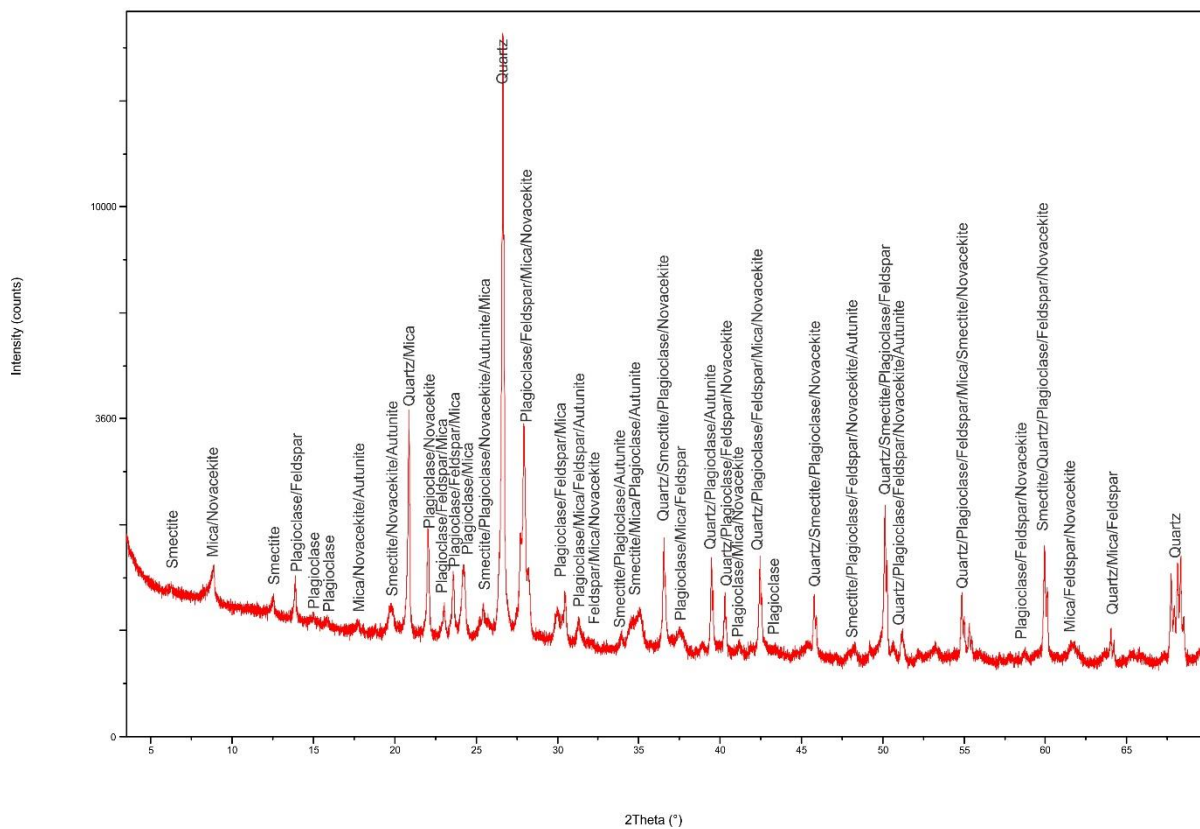
Geology low angle_F2B1AE10



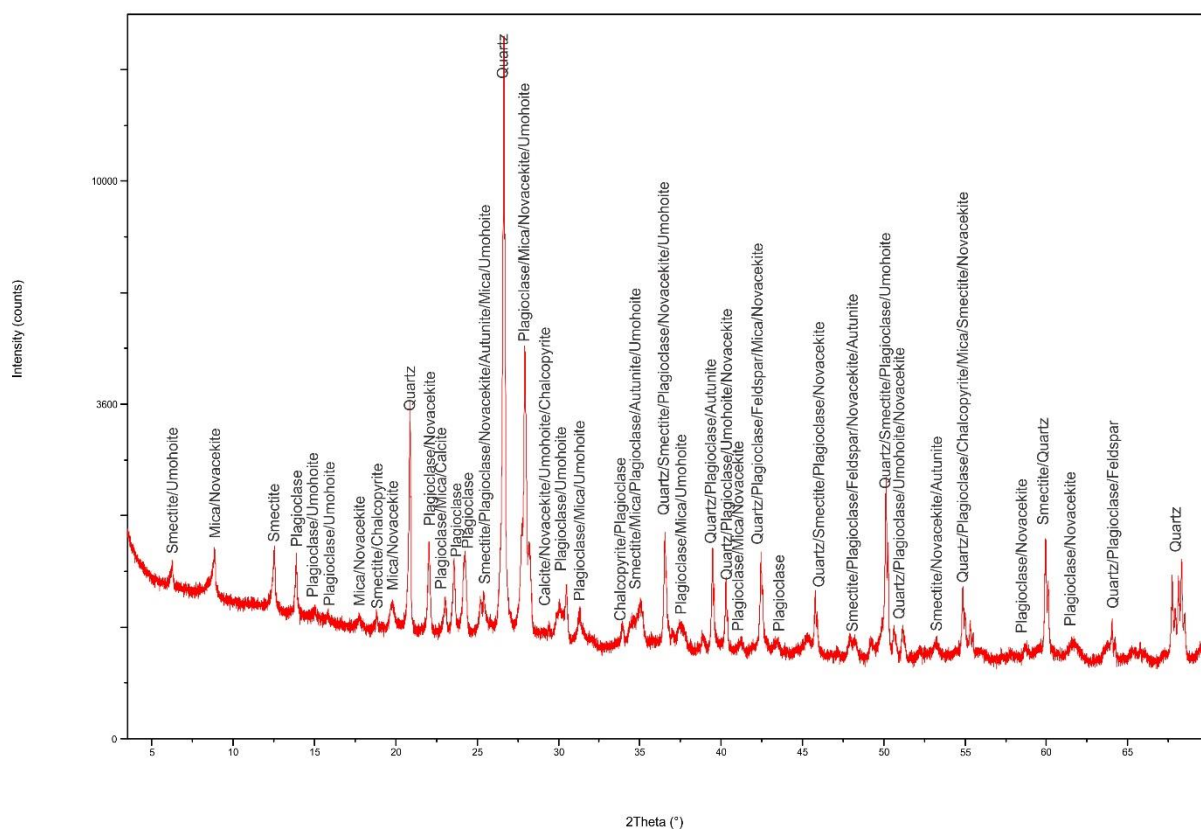
Geology low angle_F2B1AJ2



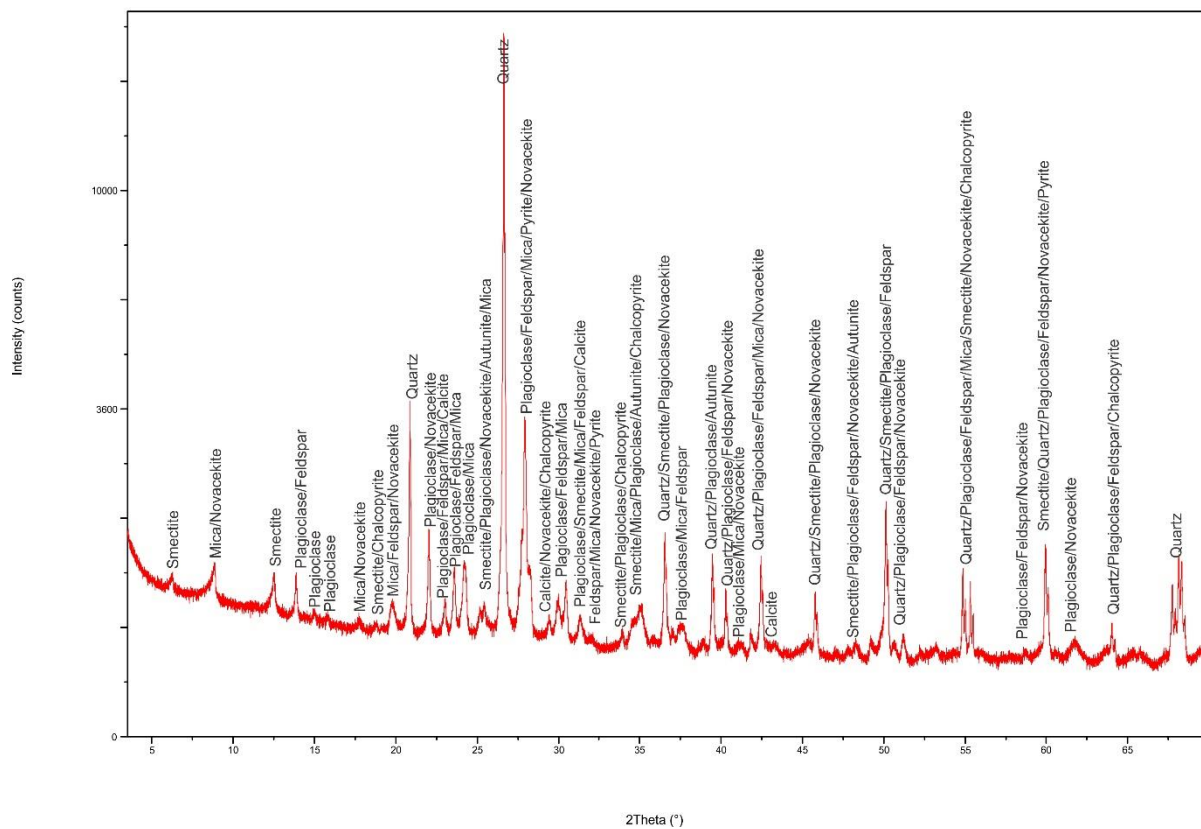
Geology low angle_F2B2S2



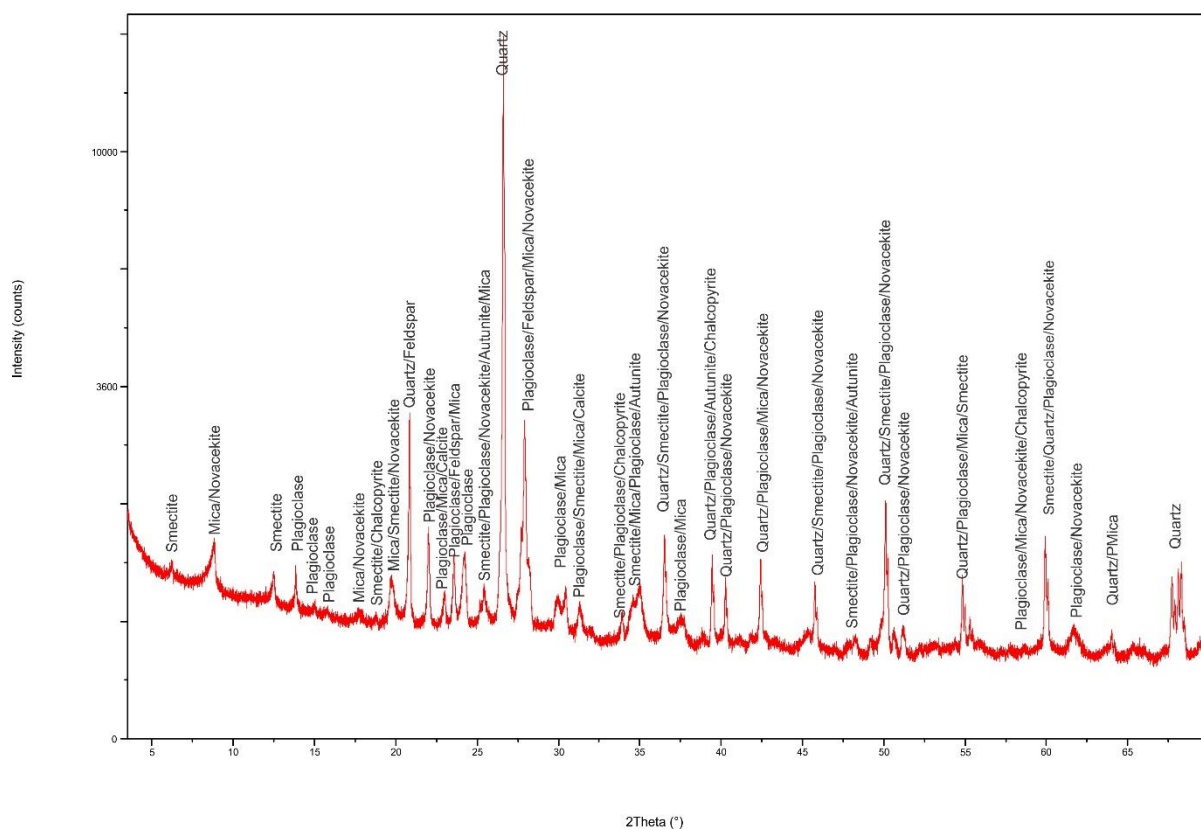
Geology low angle_F2B2S3



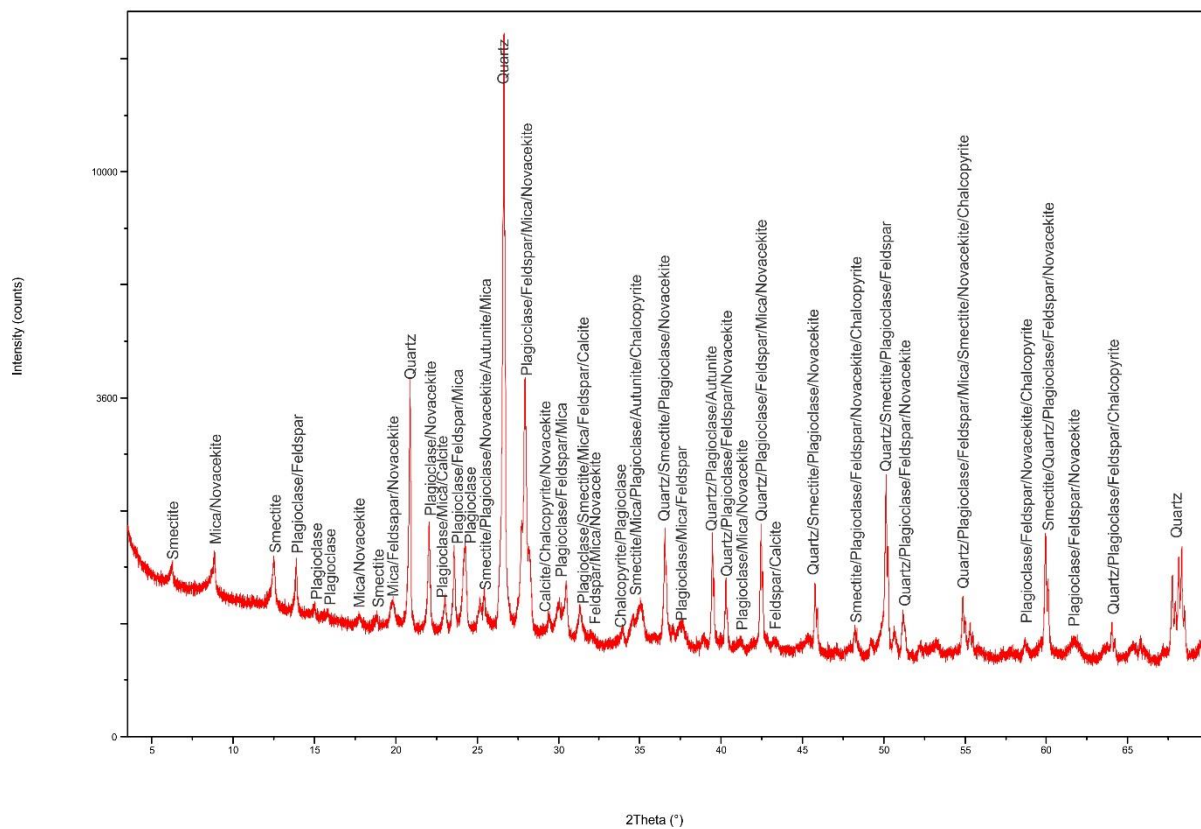
Geology low angle_F3B1AE3



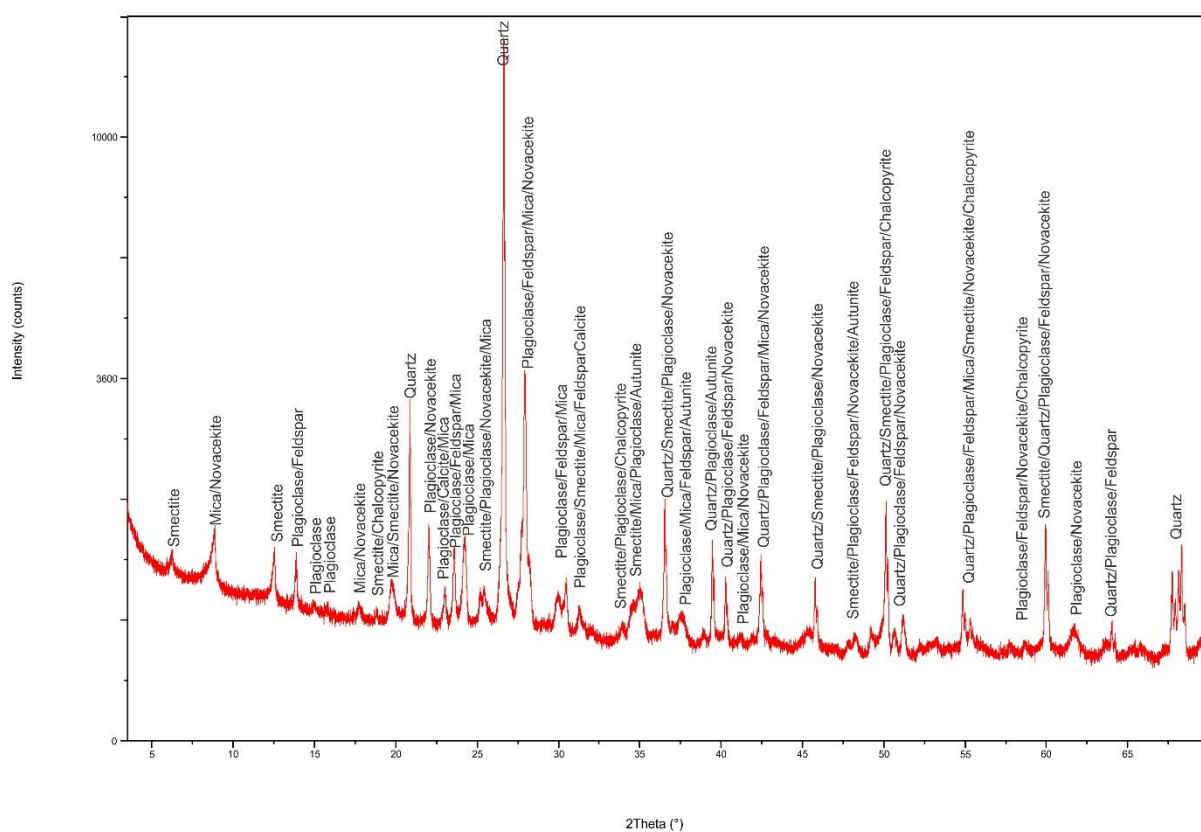
Geology low angle_F3B1AE4



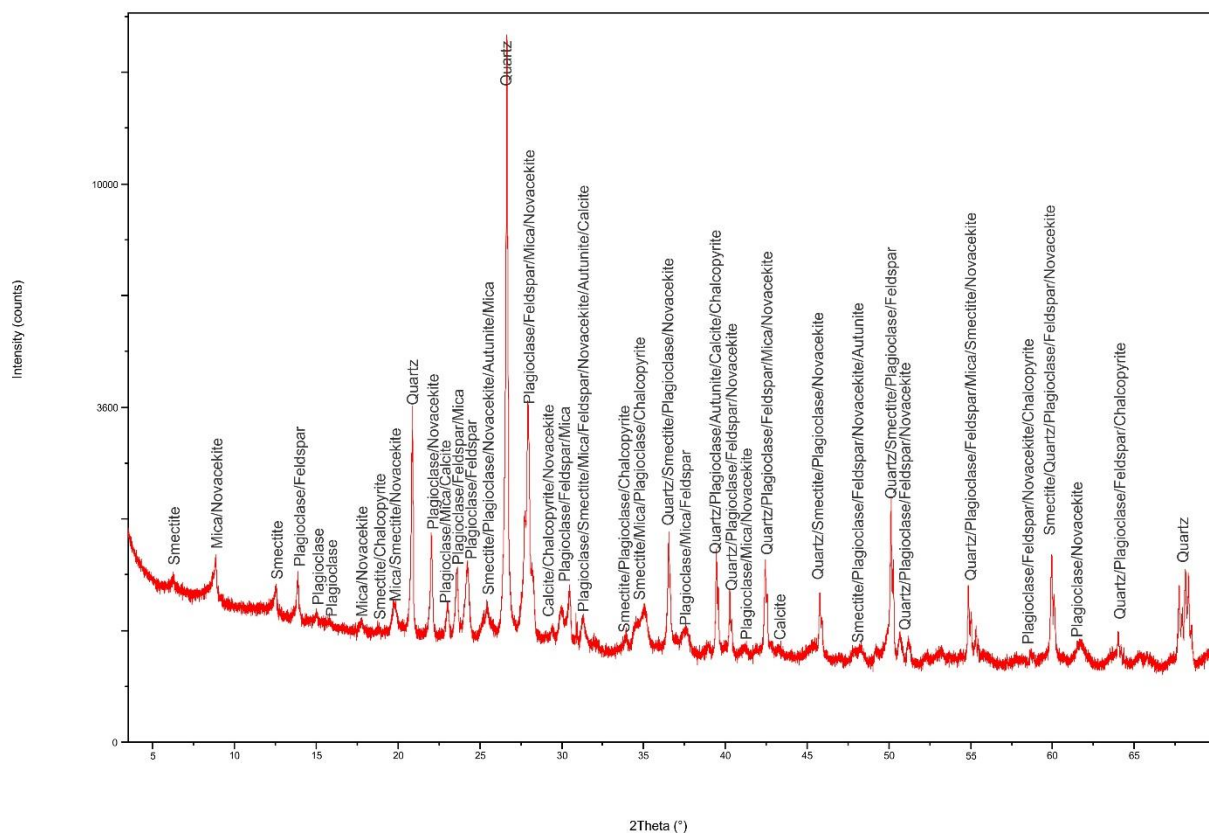
Geology low angle_F3B1AE5



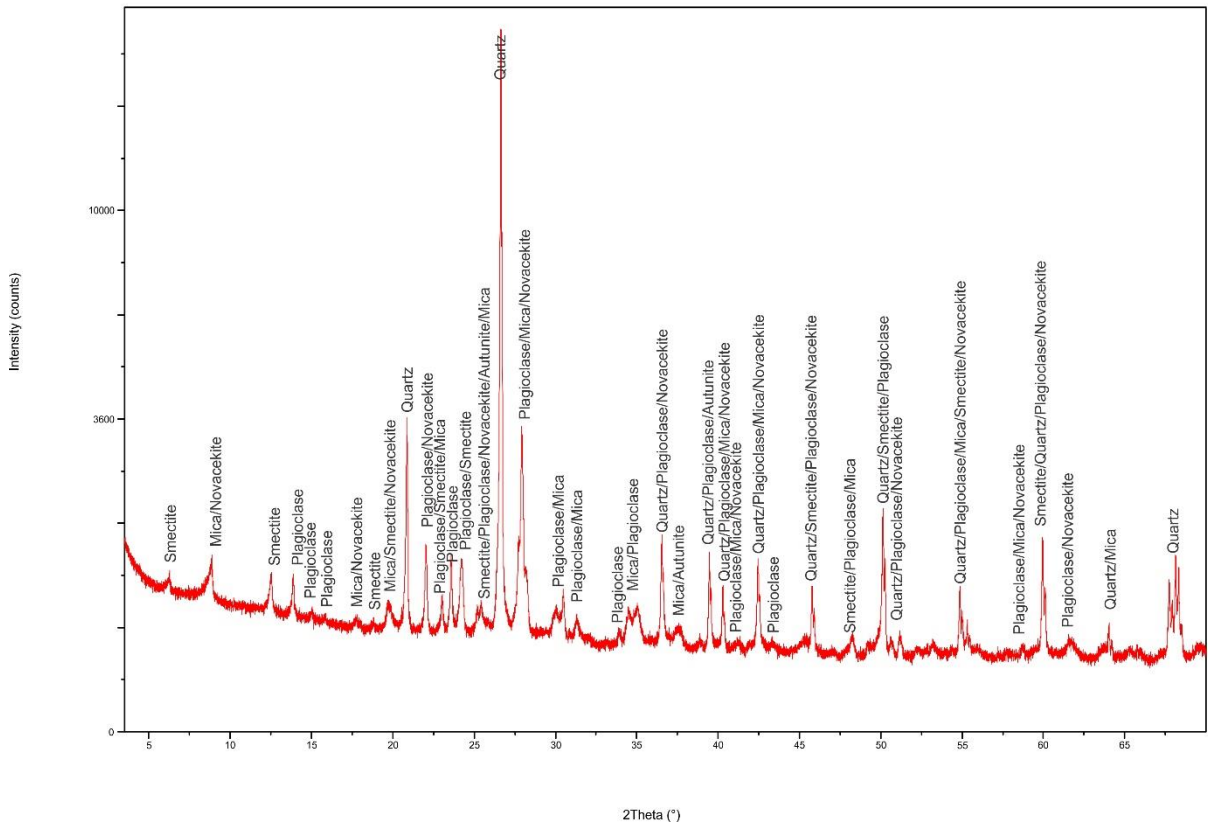
Geology low angle_F3B1AE7



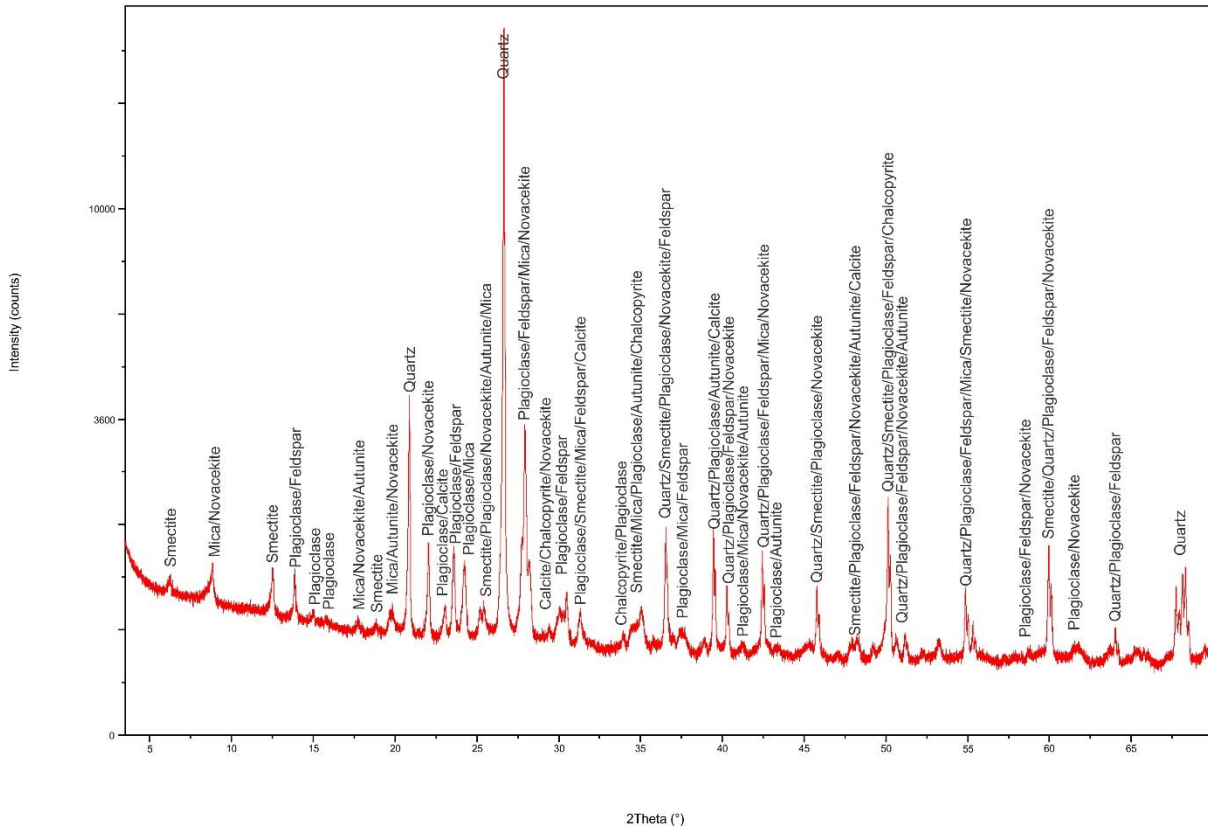
Geology low angle_F3B1OJ1



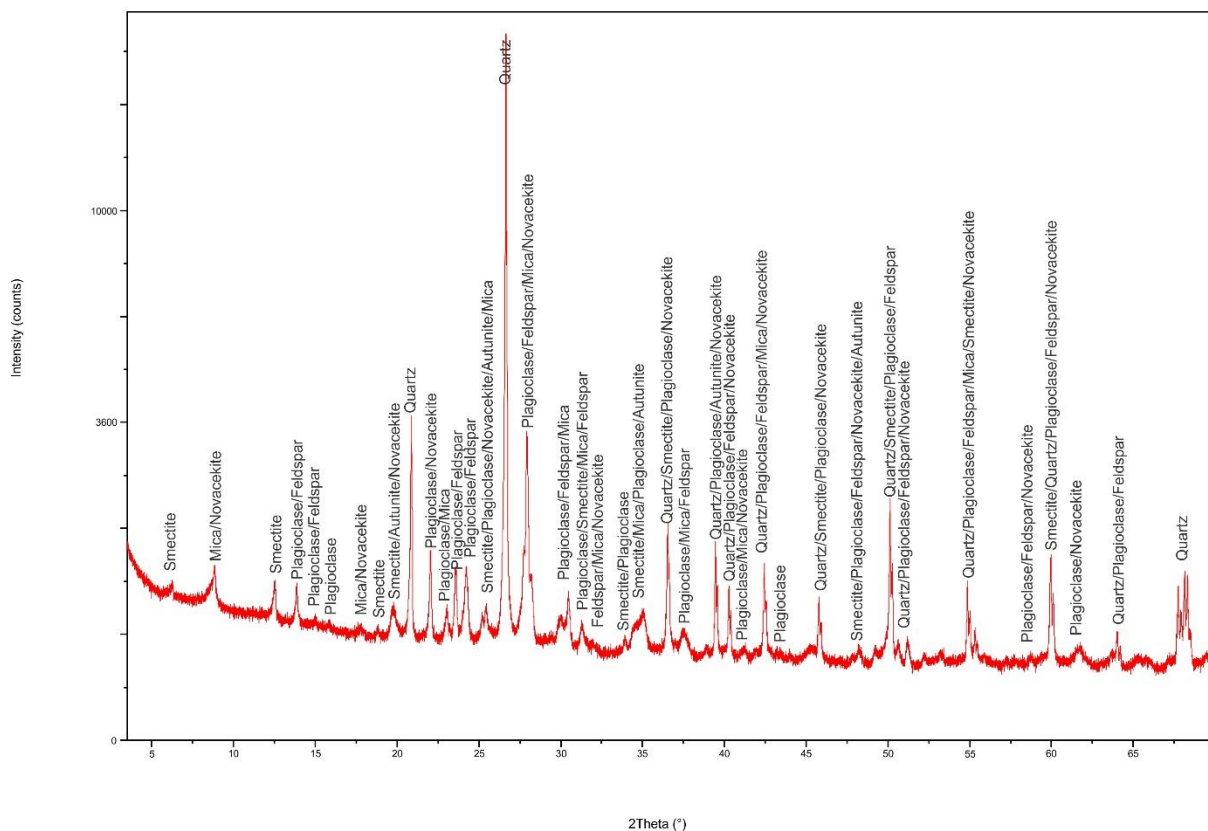
Geology low angle_F3B2S1



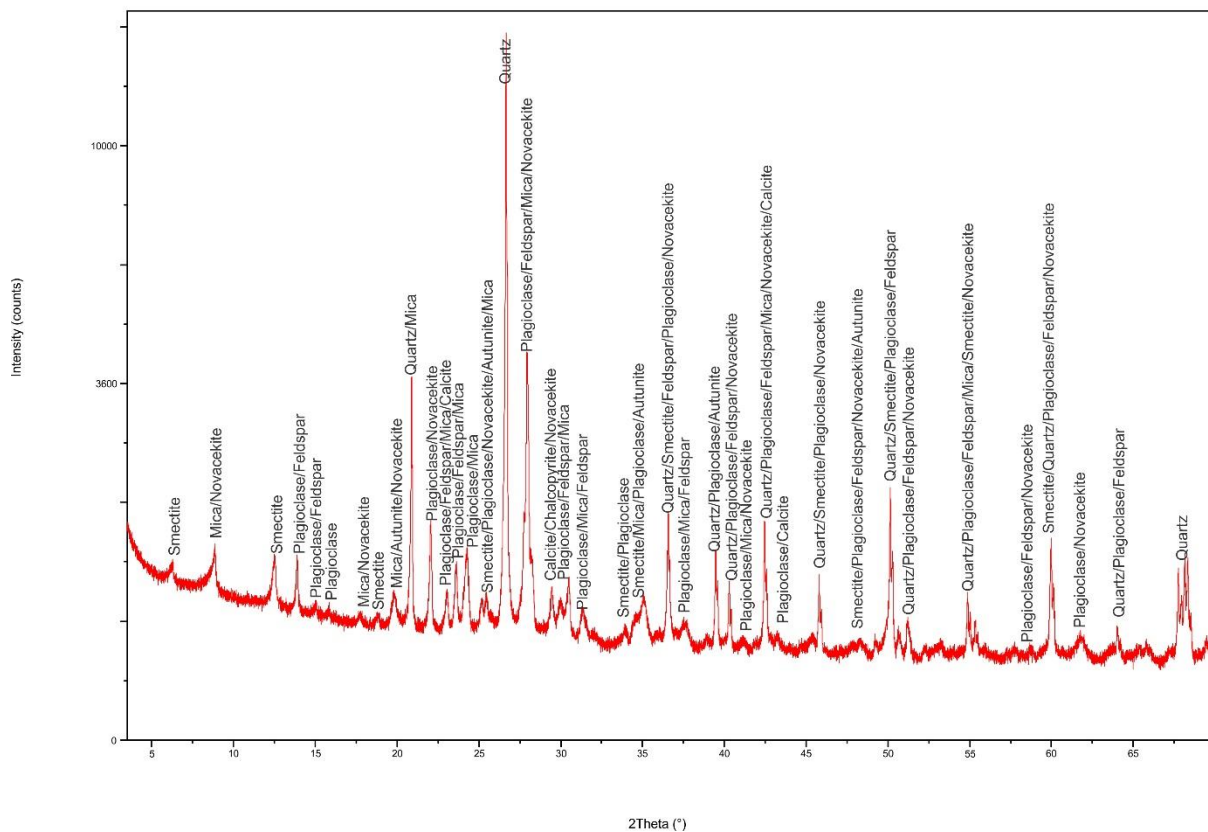
Geology low angle_F3B2S2



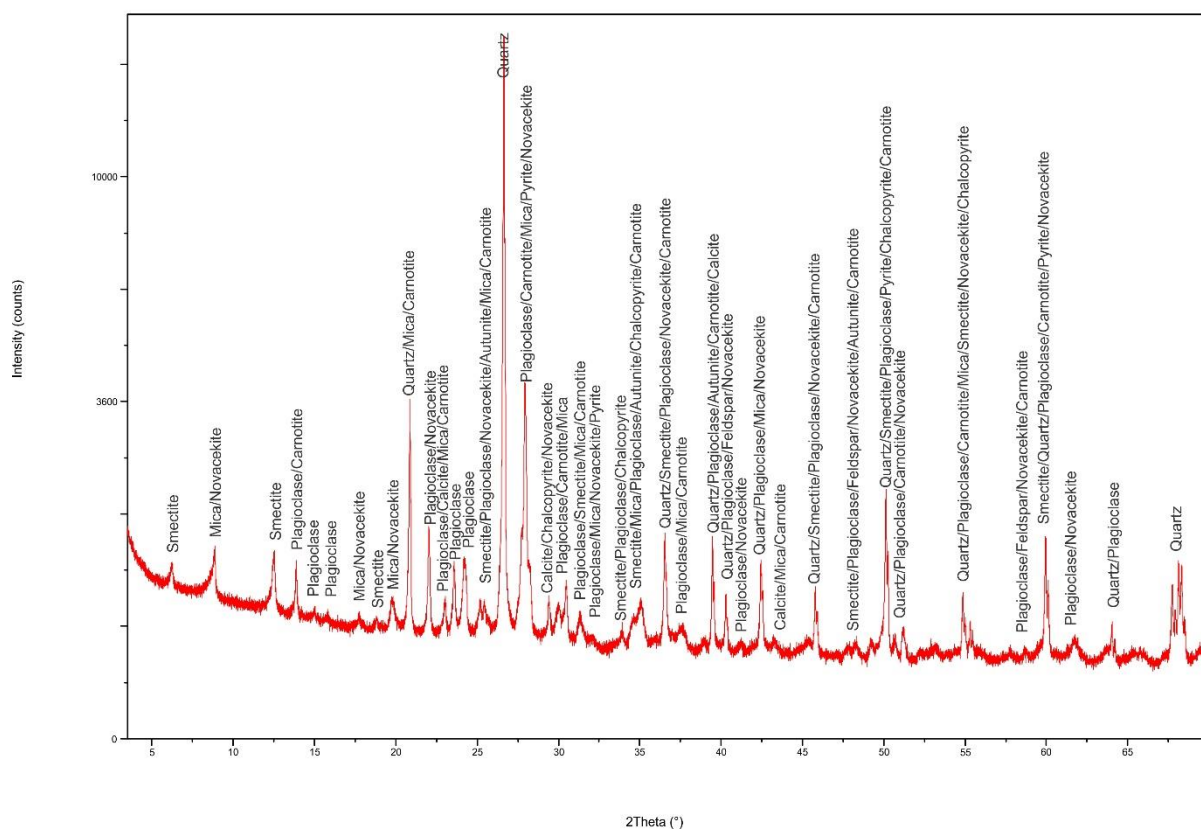
Geology low angle_F3B2S3



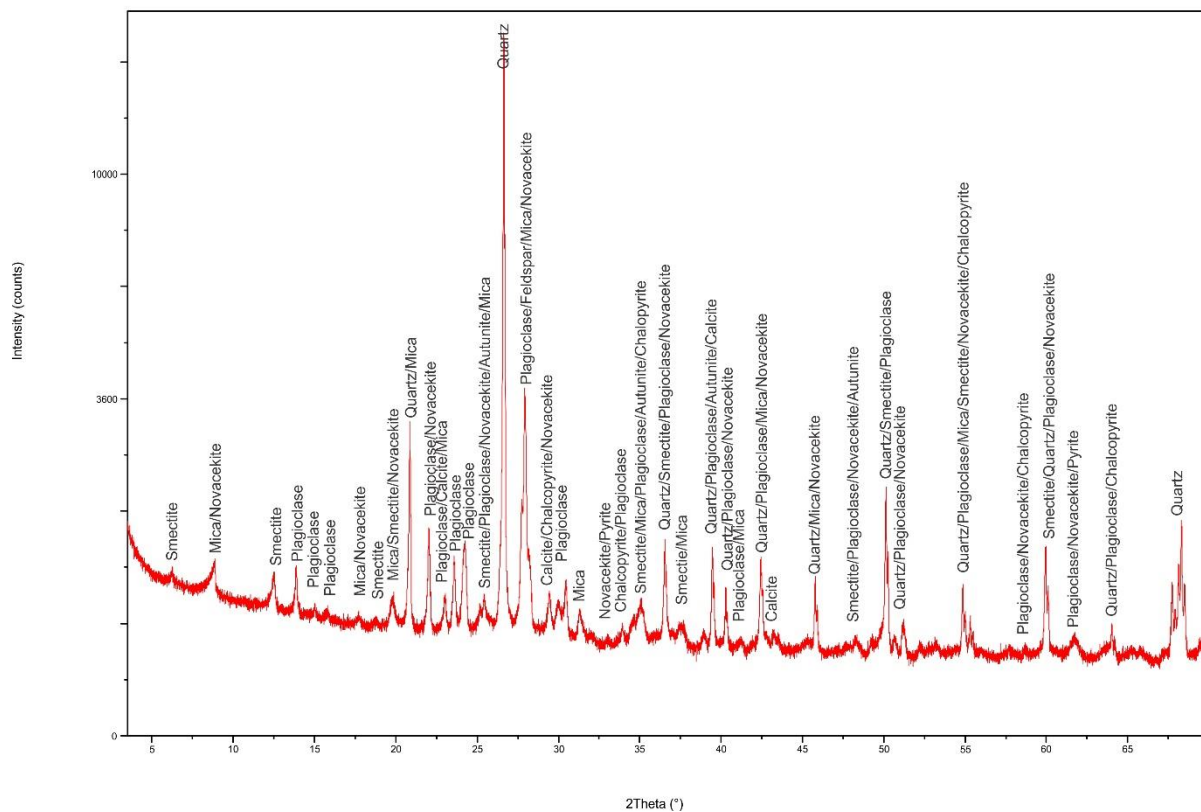
Geology low angle_F4B1AE1



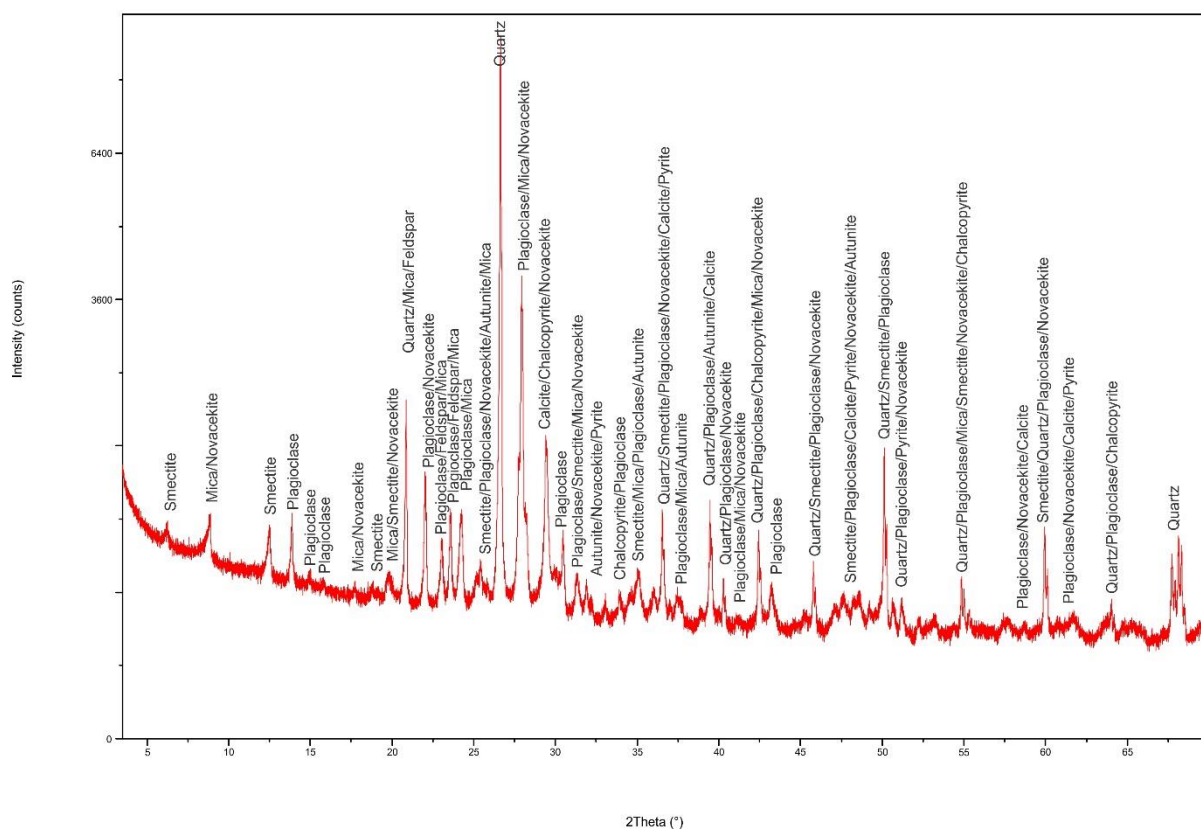
Geology low angle_F4B1AE5



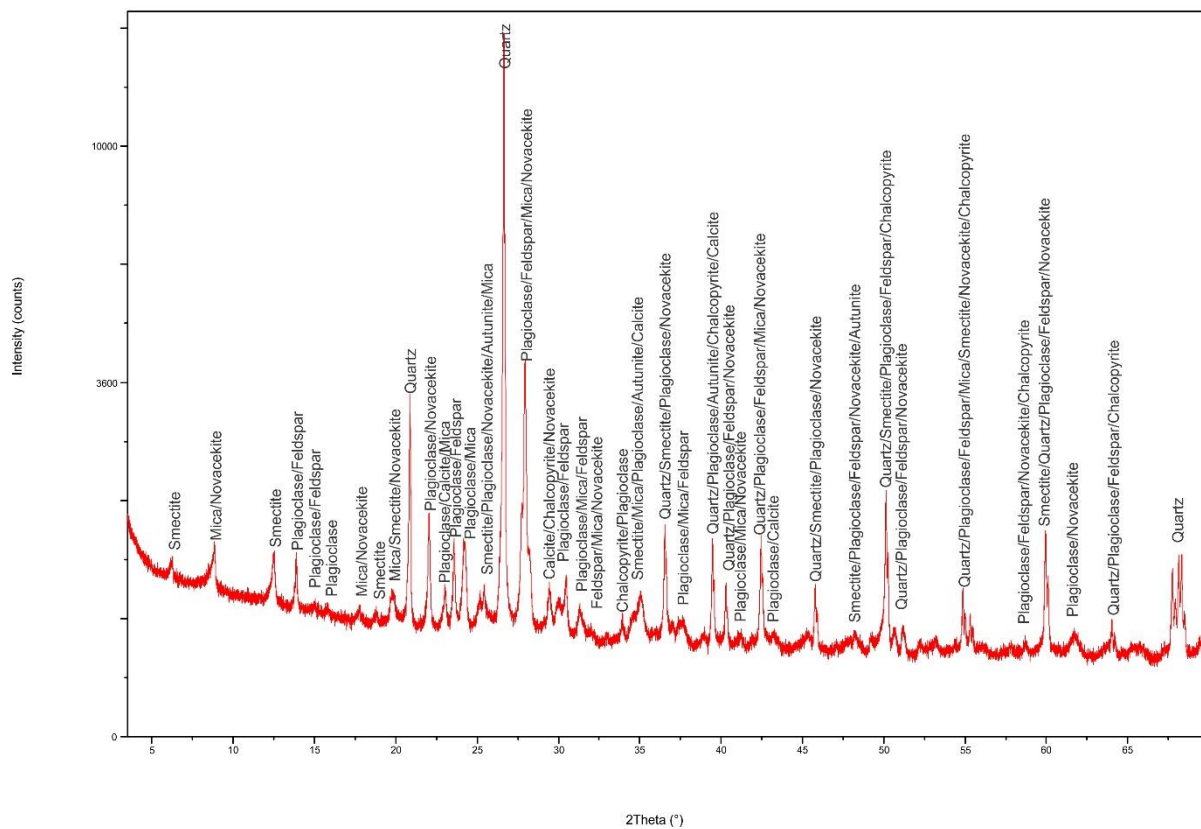
Geology low angle_F4B1AE6



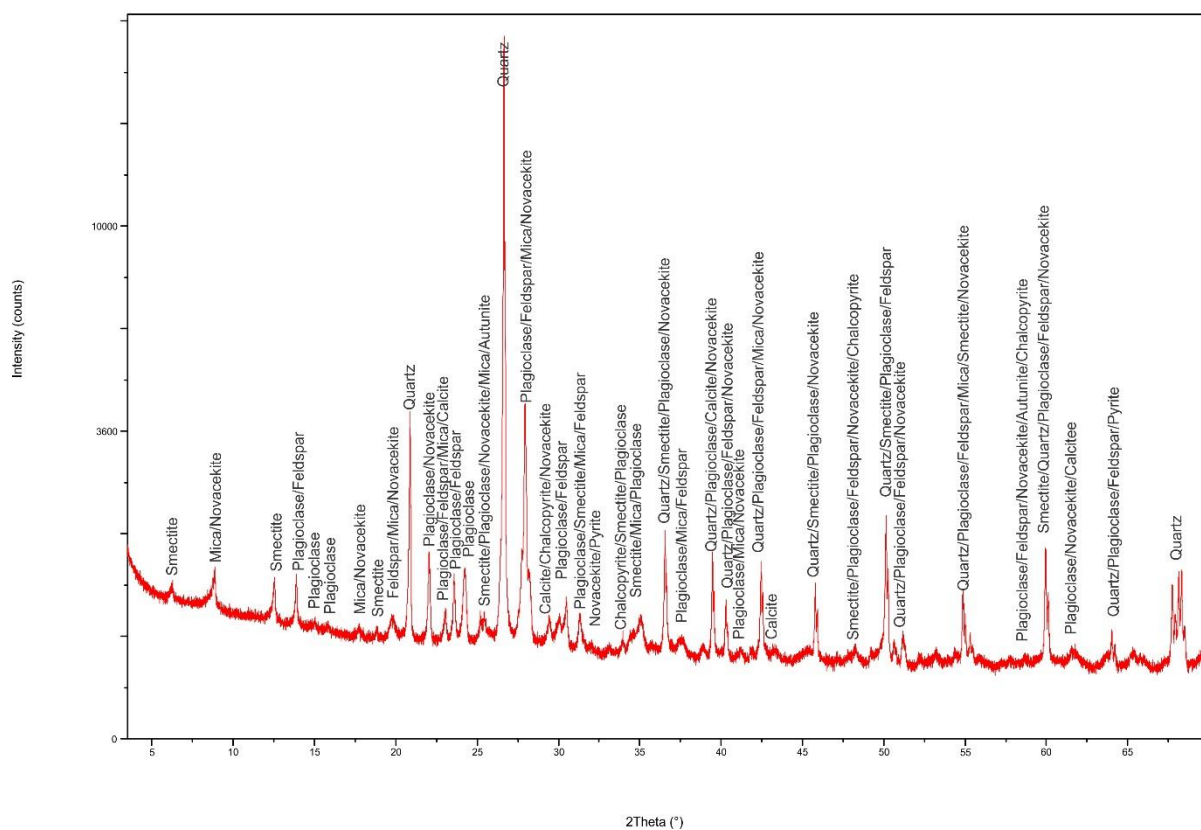
Geology low angle_F4B1AJ1



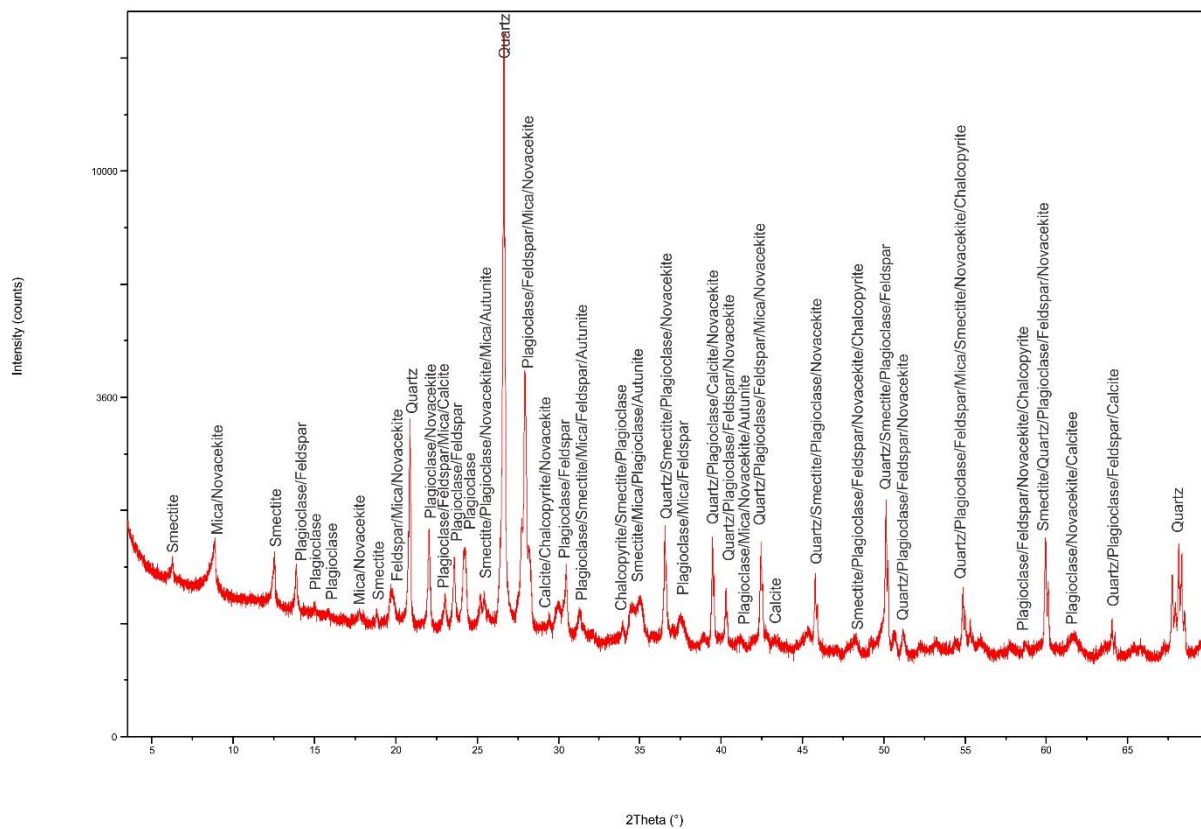
Geology low angle_F4B1OJ1



Geology low angle_F4B2S1



Geology low angle_F4B2S2



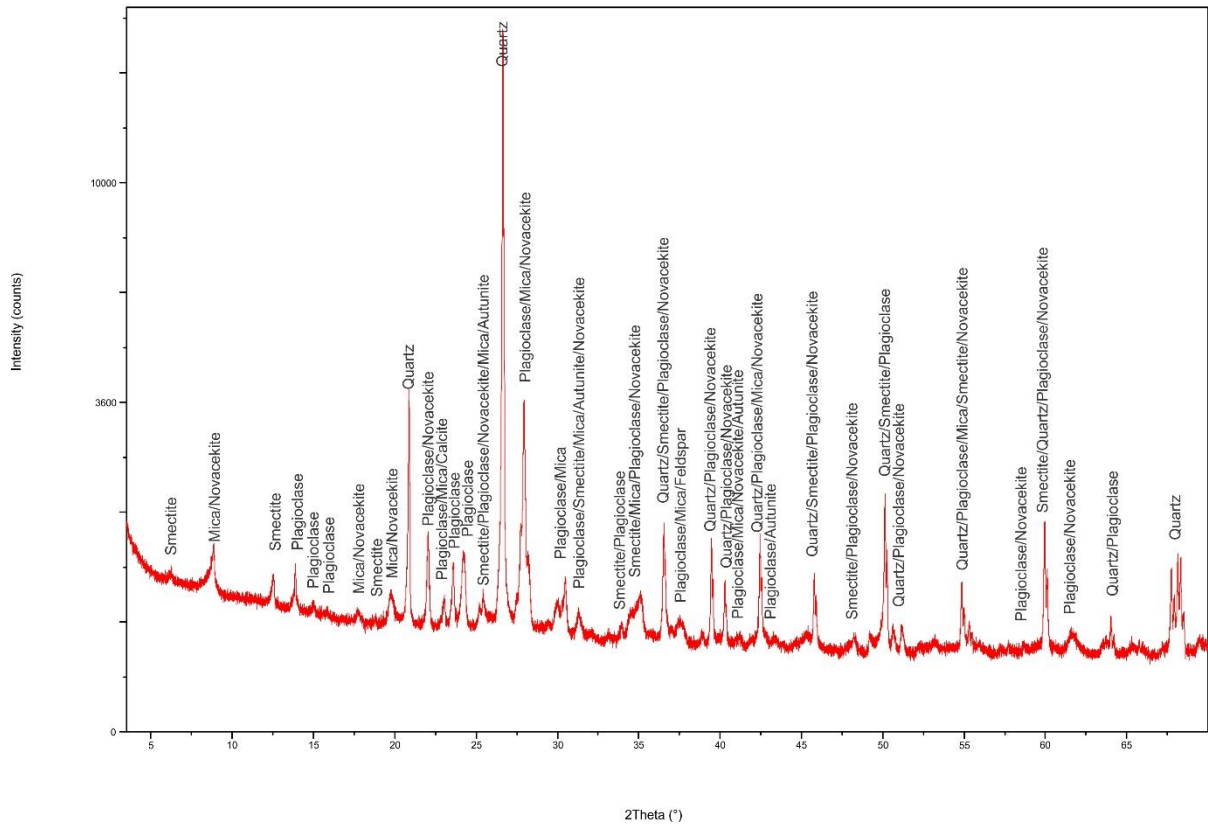


Table B1: Displays the minerals identified along with their chemical formulas in each sandstone sample at Rietkuil mine. Y=yes and N=no.

SAMPLE NAME		F1B1-OJ1	F1B1-J12	F1B1-AE3	F1B1-AE5	F1B1-OJ3	F1B1-OJ4	F2B1-AJ2	F2B1-AE5	F2B1-AE1	F2B1-AE6	F2B1-AE7	F2B1-AE8	F2B1-AE9	F2B1-AE10	F3B1-AE3	F3B1-OJ1	F3B1-AE4	F3B1-AE5	F3B1-AE7	F4B1-AE1	F4B1-OJ1	F4B1-AJ1	F4B1-AE5	F4B1-AE6	F1B2-S1	F1B2-S2	F1B2-S3	F2B2-S1	F2B2-S2	F2B2-S3	F3B2-S1	F3B2-S2	F3B2-S3	F4B2-S1	F4B2-S2	F4B2-S3	
MINERALS	CHEMICAL FORMULAS																																					
Quartz	SiO ₂	Y	Y	Y	Y	Y	Y	Y	Y	Y	Y	Y	Y	Y	Y	Y	Y	Y	Y	Y	Y	Y	Y	Y	Y	Y	Y	Y	Y	Y	Y	Y	Y	Y	Y	Y	Y	
Plagioclase	NaAlSi ₃ O ₈	Y	Y	Y	Y	Y	Y	Y	Y	Y	Y	Y	Y	Y	Y	Y	Y	Y	Y	Y	Y	Y	Y	Y	Y	Y	Y	Y	Y	Y	Y	Y	Y	Y	Y	Y	Y	
Muscovite	KAl ₂ Si ₂ O ₁₀ (OH) ₂	Y	Y	Y	Y	Y	Y	Y	Y	Y	Y	Y	Y	Y	Y	Y	Y	Y	Y	Y	Y	Y	Y	Y	Y	Y	Y	Y	Y	Y	Y	Y	Y	Y	Y	Y	Y	
Smectite	(Mg,Fe ²⁺) ₂ Al ₂ Si ₂ O ₁₀ (OH) ₂	Y	Y	Y	Y	Y	Y	Y	Y	Y	Y	Y	Y	Y	Y	Y	Y	Y	Y	Y	Y	Y	Y	Y	Y	Y	Y	Y	Y	Y	Y	Y	Y	Y	Y	Y	Y	
Feldspar	(Na,K)AlSi ₃ O ₈	Y	N	Y	Y	Y	N	N	N	Y	N	N	N	N	Y	N	Y	Y	Y	Y	Y	Y	N	N	N	N	N	N	Y	N	N	Y	N	Y	Y	Y	Y	Y
Calcite	CaCO ₃	N	Y	Y	N	N	N	N	Y	N	Y	Y	Y	Y	Y	Y	Y	Y	Y	Y	Y	Y	Y	Y	Y	N	N	N	N	N	Y	N	Y	N	Y	Y	N	
Apatite	Ca ₅ (PO ₄) ₃ (OH,F,Cl)	N	N	N	N	N	N	Y	N	N	N	N	N	N	N	N	N	N	N	N	N	N	N	N	N	N	N	N	N	N	N	N	N	N	N	N	N	N
SULPHIDE MINERALS																																						
Chalcopyrite	CuFeS ₂	N	Y	Y	N	N	N	Y	N	Y	Y	Y	Y	Y	Y	Y	Y	Y	Y	Y	Y	Y	Y	Y	Y	N	N	N	N	N	Y	N	Y	N	Y	Y	N	
Pyrite	FeS ₂	Y	N	N	Y	N	N	N	N	N	N	N	N	N	N	N	Y	N	N	N	N	N	N	Y	Y	Y	Y	N	N	N	N	N	N	N	N	Y	N	N
URANIUM MINERALS																																						
Uraninite	UO ₂	N	N	N	N	N	N	N	N	N	N	N	N	N	N	N	N	N	N	N	N	N	N	N	N	N	N	N	N	N	N	N	N	N	N	N	N	
Coffinite	U(SiO ₃) ₂ (OH) ₄	N	N	N	N	N	N	N	N	N	N	N	N	N	N	N	N	N	N	N	N	N	N	N	N	N	N	N	N	N	N	N	N	N	N	N	N	
Autunite	Ca(UO ₂) ₂ (PO ₄) ₂ •10-12(H ₂ O)	Y	Y	Y	Y	Y	Y	Y	Y	Y	Y	Y	Y	Y	Y	Y	Y	Y	Y	Y	Y	Y	Y	Y	Y	Y	Y	Y	Y	Y	Y	Y	Y	Y	Y	Y		
Novacekite	Mg(UO ₂) ₂ (AsO ₄) ₂ •12(H ₂ O)	Y	Y	Y	Y	Y	Y	Y	Y	Y	Y	Y	Y	Y	Y	Y	Y	Y	Y	Y	Y	Y	Y	Y	Y	Y	Y	Y	Y	Y	Y	Y	Y	Y	Y	Y		
Umohite	(UO ₂)MoO ₄ •4(H ₂ O)	N	Y	N	N	N	N	N	N	N	N	N	Y	N	Y	N	N	N	N	N	N	N	N	N	N	N	N	N	N	Y	N	N	N	N	N	N	N	
Zippeite	K ₂ (UO ₂) ₂ (SO ₄) ₂ (OH) ₁₀ •4(H ₂ O)	N	Y	N	N	Y	N	N	N	N	Y	Y	Y	N	Y	N	N	N	N	N	N	N	N	N	N	N	N	N	N	N	N	N	N	N	N	N	N	
Carnotite	K ₂ (UO ₂) ₂ (VO ₄)•3(H ₂ O)	N	N	N	N	N	N	N	N	N	N	N	N	N	N	N	N	N	N	N	N	N	N	Y	N	N	N	N	N	Y	N	N	N	N	N	N	N	N

Appendix C

C1 XRF

Major (Table C1) and trace (Table C2) element data obtained by the XRF from sandstone samples at Rietkuil mine.

Table C1: Whole-rock geochemistry obtained from the XRF. Major element oxide concentrations are measured as % in sandstone samples from Rietkuil mine.

Sample name	LOI (%)	Sum of conc. + LOI (%)	SiO ₂ (%)	TiO ₂ (%)	Al ₂ O ₃ (%)	Fe ₂ O ₃ (%)	MgO(%)	MnO(%)	CaO(%)	K ₂ O(%)	P ₂ O ₅ (%)	Na ₂ O(%)
F1B1 AE1	2.89	98.26	71.72	0.53	13.65	2.97	0.84	0.07	1.43	1.81	0.12	2.22
F1B1 AE2												
F1B1 AE3	2.76	98.11	71.29	0.54	13.62	3.16	0.87	0.07	1.21	1.88	0.11	2.60
F1B1 AE4												
F1B1 AE5	3.51	97.99	71.13	0.53	13.37	3.05	0.78	0.06	0.86	1.78	0.12	2.79
F1B1 J1												
F1B1 J2	5.66	98.86	65.49	0.57	14.37	3.16	0.97	0.16	4.08	1.84	0.30	2.25
F1B1 OJ1	2.64	97.91	71.72	0.53	13.55	2.86	0.85	0.05	0.97	2.05	0.11	2.57
F1B1 OJ3	3.31	97.81	71.15	0.53	13.22	3.08	0.84	0.07	1.03	1.70	0.13	2.74
F1B1 OJ4	3.97	99.13	70.82	0.55	13.92	3.76	0.76	0.07	0.71	1.90	0.12	2.55
F2B1 AE1	2.82	97.94	72.36	0.47	12.96	2.42	0.75	0.08	1.32	1.55	0.11	3.11
F2B1 AE2												
F2B1 AE3	2.51	98.02	71.96	0.54	13.89	2.94	0.95	0.07	0.95	1.70	0.12	2.38
F2B1 AE4	2.69	98.55	72.26	0.53	13.78	2.93	0.85	0.06	1.00	1.77	0.13	2.55
F2B1 AE5	3.87	98.41	69.62	0.59	14.34	3.46	1.09	0.07	0.71	2.04	0.15	2.47
F2B1 AE6	3.70	99.54	71.22	0.56	13.71	2.96	1.30	0.09	1.37	1.81	0.13	2.68
F2B1 AE7	6.36	98.88	64.40	0.51	13.07	3.06	1.10	0.18	6.10	1.57	0.19	2.33
F2B1 AE8	4.50	98.39	69.10	0.55	13.58	3.11	1.27	0.08	1.71	1.85	0.15	2.48
F2B1 AE9	4.13	98.59	69.10	0.57	14.29	3.56	1.09	0.09	1.28	2.04	0.13	2.31
F2B1 AE10	5.47	97.36	65.55	0.48	12.38	2.77	0.93	0.14	5.49	1.35	0.20	2.60
F2B1 AJ1												
F2B1 AJ2	2.72	97.71	71.89	0.53	13.21	2.64	0.79	0.07	1.09	1.72	0.12	2.93
F3B1 AE1												
F3B1 AE2												
F3B1 AE3	2.89	96.97	70.53	0.54	13.37	2.86	0.85	0.07	1.25	1.89	0.12	2.62
F3B1 AE4	3.28	98.98	69.79	0.62	15.17	3.42	0.96	0.06	0.92	2.75	0.11	1.90
F3B1 AE5	2.60	98.54	72.82	0.51	12.82	3.05	0.84	0.09	1.26	1.63	0.12	2.81
F3B1 AE6												
F3B1 AE7	2.86	98.18	70.29	0.57	14.58	3.27	0.90	0.05	0.87	2.41	0.11	2.27
F3B1 AE8												
F3B1 AE9												
F3B1 OJ1	2.80	97.63	70.98	0.54	13.50	3.10	0.81	0.07	1.08	1.97	0.11	2.67
F4B1 AE1	7.83	97.28	59.78	0.48	12.54	2.20	0.69	0.29	8.84	1.44	0.76	2.41
F4B1 AE2	2.44	95.66	71.29	0.47	12.59	2.44	0.67	0.07	1.20	1.51	0.11	2.87
F4B1 AE3												
F4B1 AE4	2.77	97.88	72.10	0.49	13.10	2.85	0.73	0.09	1.35	1.57	0.11	2.71
F4B1 AE5	2.75	98.01	70.81	0.54	13.50	3.04	0.94	0.08	1.40	1.85	0.11	2.97
F4B1 AE6	3.73	98.61	69.90	0.53	13.63	2.72	1.26	0.12	2.15	1.76	0.18	2.63
F4B1 AJ1	3.64	99.67	70.53	0.55	13.73	2.70	1.57	0.12	2.05	1.91	0.14	2.74
F4B1 OJ1	3.37	97.61	69.58	0.50	13.58	2.77	0.93	0.12	2.06	1.79	0.15	2.76
F4B1 J1												
F1B2S1	2.05	97.68	74.66	0.44	11.56	3.05	0.54	0.05	0.77	1.52	0.11	2.93
F1B2S2	2.48	97.84	72.46	0.55	12.57	3.65	0.65	0.06	0.89	1.68	0.13	2.72
F1B2S3	2.14	97.80	73.55	0.45	12.36	3.51	0.76	0.06	0.61	1.45	0.10	2.83
F2B2S1	2.92	98.73	69.76	0.53	14.14	4.16	1.87	0.05	0.73	2.25	0.12	2.20
F2B2S2	2.44	98.39	72.82	0.57	12.79	3.45	0.85	0.06	0.75	1.89	0.12	2.65
F2B2S3	2.32	97.92	71.89	0.50	12.99	3.50	0.93	0.04	0.91	1.68	0.11	3.04
F3B2S1	2.43	98.85	72.94	0.49	13.14	3.60	0.72	0.04	0.82	1.96	0.13	2.59
F3B2S2	2.29	98.68	73.85	0.51	12.16	3.33	0.76	0.04	1.05	1.51	0.11	3.09
F3B2S3	2.48	96.60	71.21	0.53	12.81	3.34	0.73	0.03	0.87	1.97	0.12	2.51
F4B2S1	3.04	98.41	71.89	0.46	12.20	3.64	0.99	0.06	1.67	1.64	0.10	2.72
F4B2S2	2.65	98.11	71.00	0.55	13.65	3.80	0.83	0.04	0.98	2.20	0.11	2.29
F4B2S3	2.63	97.77	71.48	0.51	13.17	3.49	0.82	0.04	0.89	2.06	0.10	2.58

Table C2: Whole-rock geochemistry obtained from XRF analysis. Trace element concentrations in ppm measured in sandstone samples from Rietkuil mine. d.l.= below detection limits of the XRF.

Sample name	Sc (ppm)	V (ppm)	Cr (ppm)	Co (ppm)	Ni (ppm)	Cu (ppm)	Zn (ppm)	As (ppm)	Rb (ppm)	Sr (ppm)	Y (ppm)	Zr (ppm)	Nb (ppm)	Mo (ppm)	Sn (ppm)	Sb (ppm)	Ba (ppm)	Pb (ppm)	Th (ppm)	U (ppm)
F1B1 AE1									81.40	203.23	28.22	254.50	13.15	2.74				32.70	12.86	47.51
F1B1AE2									73.88	208.54	30.85	287.02	15.15	266.20				28.38	9.67	175.42
F1B1AE3	23.70	91.38	111.08	64.62	36.37	81.02	94.15	41.95	73.68	183.64	29.66	290.86	2.00	6.43	1.72	44.11	886.56	46.42	11.49	7.87
F1B1AE4									78.79	225.49	29.04	244.08	13.51	8.11				33.20	13.74	188.39
F1B1AE5	23.30	90.35	108.39	62.94	34.82	56.38	92.50	100.43	72.96	186.53	27.57	283.68	1.65	81.57	0.58	41.90	364.75	45.72	10.96	188.47
F1B1J1									84.05	194.24	30.75	307.42	14.18	7.31				18.56	13.60	50.05
F1B1J2	28.07	108.51	120.58	154.42	107.41	66.95	114.55	245.08	117.27	198.01	36.02	316.06	9.19	372.15	2.37	44.53	359.74	91.62	12.00	1763.67
F1B1O1	23.38	90.23	108.63	63.59	36.81	70.00	90.97	38.14	78.45	157.89	29.82	255.60	1.52	6.65	1.95	41.81	545.20	40.60	10.84	3.31
F1B1O3	23.75	91.38	107.98	63.52	37.03	56.55	92.81	76.82	67.44	191.00	27.77	278.80	2.53	27.77	3.42	44.08	1088.52	42.67	10.21	122.81
F1B1O4	23.47	91.81	111.49	67.18	35.48	58.70	93.29	68.38	74.44	190.89	30.58	288.43	4.08	16.61	3.25	42.00	490.59	43.81	11.29	143.87
F2B1AE1	23.03	85.01	103.12	59.73	34.26	53.66	86.93	41.64	61.58	179.33	23.40	248.14	0.78	10.44	0.32	42.63	1032.26	39.04	9.14	24.96
F2B1AE2									61.73	293.12	22.78	239.27	12.61	29.80				17.57	14.40	156.12
F2B1 AE3									79.75	207.79	28.95	256.89	13.77	53.01				33.51	13.32	241.71
F2B1 AE4									79.17	228.83	29.43	249.10	13.36	8.15				34.14	14.14	189.12
F2B1AE5	24.39	101.08	115.47	64.08	32.91	56.23	100.21	88.97	89.37	191.72	28.80	300.69	6.08	64.27	2.49	43.51	902.42	43.52	12.00	447.00
F2B1AE6	24.36	94.34	113.02	69.54	41.33	61.02	103.37	90.87	74.26	178.09	32.00	295.82	3.40	27.71	0.00	41.43	362.44	44.85	11.77	138.17
F2B1AE7	27.89	104.88	115.03	69.31	44.35	60.19	99.02	158.55	75.74	191.04	23.44	288.62	<d.l.	271.11	2.54	42.24	334.89	62.33	11.27	589.08
F2B1AE8	25.41	103.81	114.95	67.65	45.31	59.41	94.13	108.26	76.43	244.57	31.40	299.09	<d.l.	178.70	1.93	46.81	2439.49	55.45	11.36	262.65
F2B1AE9	24.41	98.50	115.59	67.00	40.64	60.40	105.57	48.11	84.29	200.58	28.20	262.77	5.00	18.21	2.08	43.14	1117.58	46.45	12.28	272.32
F2B1AE10	27.08	97.87	111.01	68.43	47.75	66.47	90.32	111.80	68.13	199.13	29.76	284.08	<d.l.	455.55	0.51	42.63	600.99	80.22	11.65	519.34
F2B1AJ1									86.60	197.01	35.07	286.28	14.87	42.24				41.30	14.94	490.89
F2B1AJ2	24.07	89.10	106.92	65.64	36.89	55.50	90.38	63.07	66.89	186.93	28.68	290.18	1.60	11.76	0.01	43.35	942.61	43.00	11.18	32.77
F3B1AE1									84.86	201.26	38.16	282.49	14.36	13.01				68.63	15.13	217.44
F3B1AE2									65.50	200.82	26.75	225.31	11.56	3.42				17.62	11.37	7.02
F3B1AE3	23.00	96.69	110.58	61.55	37.58	151.37	95.92	72.33	72.66	177.80	29.27	320.01	2.64	6.57	1.92	43.15	597.20	41.32	11.23	52.49
F3B1AE4	23.98	99.06	115.41	65.64	39.51	67.57	95.92	37.41	102.24	166.40	36.14	274.91	3.10	6.33	0.99	41.38	528.29	44.17	12.33	<d.l.
F3B1AE5	22.96	88.64	108.07	64.02	38.26	227.57	96.10	51.07	66.08	155.35	31.89	289.20	1.90	6.58	2.52	42.58	366.89	44.54	10.66	47.57
F3B1AE6									73.86	148.01	26.09	231.62	11.79	1.93				21.70	10.62	2.74
F3B1AE7	23.92	92.35	112.96	64.34	38.60	66.43	95.48	37.11	91.96	159.54	33.33	266.07	1.99	6.42	0.98	41.18	449.05	40.53	11.25	<d.l.
F3B1AE8									71.85	212.74	20.46	246.30	12.59	15.75				20.30	12.14	92.00
F3B1AE9									77.94	187.54	26.96	246.02	13.33	10.68				34.59	13.44	245.52
F3B1O1	23.73	87.85	108.36	65.58	38.82	70.44	93.70	37.62	76.56	162.27	30.18	269.05	1.97	6.62	3.90	40.83	363.88	40.64	10.24	<d.l.
F4B1AE1	33.51	112.97	126.96	188.25	196.03	112.27	149.44	858.54	236.06	195.27	28.31	391.51	76.69	105.05	1.11	45.93	646.52	185.77	5.79	6816.01
F4B1 AE2									71.71	203.91	26.29	273.95	13.02	6.69				29.98	13.11	101.74
F4B1AE3									71.67	200.10	25.40	268.74	13.04	12.30				29.44	13.26	170.84
F4B1 AE4									73.71	204.71	26.83	262.43	13.13	4.77				36.56	12.01	30.75
F4B1AE5	23.17	91.85	114.49	64.24	37.48	89.94	95.64	70.41	73.20	177.33	29.30	288.89	2.19	6.88	1.94	42.22	470.99	45.38	10.81	19.50
F4B1AE6	24.70	90.91	108.58	67.34	41.69	61.14	97.39	97.34	82.98	203.98	29.01	298.49	7.39	54.50	4.49	42.34	805.29	64.83	10.78	627.79
F4B1AJ1	24.27	92.58	109.99	64.10	39.30	65.60	99.04	64.87	77.28	189.95	26.76	293.25	5.14	8.41	0.46	41.99	888.83	46.30	10.95	249.59
F4B1O1	24.22	92.41	108.91	70.39	42.95	58.40	104.62	91.06	82.51	189.65	45.65	242.21	8.49	9.17	3.09	42.52	859.29	58.92	8.96	606.03
F4B1J1									79.78	231.97	28.92	266.30	13.71	7.68				25.81	13.87	42.94
F1B2S1	22.64	79.96	105.11	63.47	34.54	56.23	81.37	36.73	63.49	138.58	25.47	279.19	0.33	6.35	2.04	41.45	542.74	41.81	9.46	<d.l.
F1B2S2	23.32	94.81	112.39	66.04	36.57	59.24	90.78	37.30	70.27	134.01	30.85	399.22	1.94	6.48	1.55	42.43	516.59	47.32	11.45	<d.l.
F1B2S3	22.44	85.85	106.95	64.89	35.27	56.74	88.66	36.74	60.18	132.55	23.42	203.92	<d.l.	6.58	0.72	41.32	579.61	41.79	8.68	<d.l.
F2B2S1	24.39	94.08	115.89	67.81	38.89	59.35	98.16	37.15	91.81	145.17	31.27	234.84	1.33	6.34	4.10	42.05	573.77	41.31	10.16	<d.l.
F2B2S2	22.92	94.93	112.61	66.11	37.23	59.26	89.88	36.86	77.97	147.77	31.46	409.25	1.85	6.49	0.47	44.02	1280.33	44.93	11.79	<d.l.
F2B2S3	23.38	93.64	108.35	64.18	36.13	59.16	88.14	37.05	69.84	144.83	27.64	279.30	1.05	6.99	0.08	42.63	929.79	39.94	10.74	<d.l.
F3B2S1	23.50	87.69	109.93	65.13	36.72	57.61	91.24	36.51	79.45	146.34	29.49	255.50	1.24	6.26	2.33	41.66	671.42	39.90	10.37	<d.l.
F3B2S2	23.03	90.85	108.14	63.44	35.38	56.32	86.67	36.14	62.38	143.35	26.06	297.90	0.64	6.38	1.34	41.80	891.04	40.01	9.90	<d.l.
F3B2S3	23.25	90.17	111.57	64.57	36.64	57.74	89.07	36.26	81.09	136.74	31.03	331.58	1.97	6.31	1.89	40.82	577.03	39.72	10.86	<d.l.
F4B2S1	23.13	85.35	108.04	64.47	35.97	56.05	89.77	36.11	67.70	143.28	26.88	246.51	0.15	6.24	1.28	41.21	753.69	40.37	9.09	<d.l.
F4B2S2	23.47	92.52	109.53	64.88	38.70	56.64	96.55	36.36	88.47	143.92	30.73	261.42	1.61	6.29	1.16	41.05	553.85	41.12	11.08	<d.l.
F4B2S3	23.50	91.39	109.36	65.28	36.71	56.94	92.21	36.29	83.34	143.88	29.81	251.68	1.32	6.24	1.04	41.33	566.72	39.24	10.31	<d.l.

Appendix D

D1 ICP-MS

Table D1: Trace elements from selected sandstone samples at Rietkuil mine measured with the ICP-MS.

SAMPLE ICP-MS	45Sc	51V	52Cr	59Co	60Ni	65Cu	66Zn	75As	85Rb	88Sr	89Y	90Zr	93Nb	95Mo	137Ba	140Ce	208Pb	232Th	238U
	ppm	ppm	ppm	ppm	ppm	ppm	ppm	ppm	ppm	ppm	ppm	ppm	ppm	ppm	ppm	ppm	ppm	ppm	ppm
F1B1AE1	14.52	56.43	26.79	8.27	15.84	38.96	64.97	89.52	74.90	199.00	21.37	131.60	10.02	2.70	747.20	65.25	23.54	11.26	42.99
F1B1AE4	11.20	56.92	26.74	10.09	16.13	36.84	63.50	70.00	68.82	210.00	21.21	142.90	9.31	11.96	1635.00	61.88	22.65	10.83	156.40
F1B1J12	14.47	61.56	27.66	192.70	84.28	20.53	77.00	518.80	66.76	213.60	30.60	160.00	10.29	6051.00	203.10	74.59	27.10	11.85	2046.00
F1B1OJ4	7.22	58.26	25.38	10.38	14.73	17.05	57.50	124.90	69.68	194.90	21.05	127.90	9.61	132.90	497.00	59.06	17.00	11.34	110.00
F2B1AE3	14.57	56.57	26.69	15.35	16.84	17.19	69.44	39.77	72.86	202.70	21.63	139.10	9.87	95.23	476.00	64.79	22.71	11.08	205.20
F2B1AE9	15.04	60.07	27.79	11.82	20.47	22.11	77.58	34.74	72.96	220.50	19.49	127.40	9.72	151.40	1472.00	64.64	18.61	12.00	265.40
F2B1AE10	6.57	54.87	21.79	14.76	23.83	27.40	47.43	159.00	50.80	220.00	24.75	112.20	8.35	7899.00	674.40	71.44	44.42	10.12	535.20
F4B1AE1	12.66	59.86	25.20	253.30	166.40	87.05	106.40	1173.00	53.63	214.70	35.36	164.30	9.25	1220.00	549.40	129.20	90.71	10.23	7943.00
F4B1AE2	12.65	51.17	25.23	9.83	16.09	13.24	57.46	59.35	61.54	192.10	18.85	131.60	8.90	9.06	266.80	57.15	20.50	9.99	80.84
F4B1AE4	13.16	55.60	26.27	11.80	15.99	57.08	62.28	161.10	64.69	196.30	19.08	129.90	9.47	5.95	813.00	53.90	28.37	10.13	27.34
F4B1AE5	13.04	54.53	26.45	8.83	16.23	73.45	63.85	96.88	69.43	195.50	20.61	130.50	9.67	7.82	445.00	64.84	25.57	10.91	25.33
F4B1AE6	11.78	52.23	26.81	19.19	21.47	22.15	67.94	164.40	68.18	228.60	23.67	145.00	9.41	641.50	1022.00	57.43	25.44	10.66	637.40
F4B1AJ1	7.54	55.20	26.90	14.20	17.76	30.83	70.72	75.00	71.63	214.80	19.81	133.30	9.40	24.26	1158.00	62.38	19.86	11.74	260.80
F2B2S1	12.60	57.19	26.22	8.62	16.61	17.35	66.70	4.83	90.66	158.20	20.92	121.00	9.04	1.58	611.70	55.98	17.77	10.13	3.54

Table D2: Comparison of the trace element data from selected sandstone samples measured with ICP-MS and XRF.

SAMPLES	45sc		51V		52Cr		59Co		60Ni		65Cu		66Zn		75As		85Rb		88Sr		89Y		90Zr		93Nb		95Mo		137Ba		140Ce		208Pb		232Th		238U	
	ppm		ppm		ppm		ppm		ppm	%	ppm		ppm		ppm		ppm		ppm		ppm		ppm		ppm		ppm		ppm		ppm		ppm		ppm			
	ICP-MS	XRF	ICP-MS	XRF	ICP-MS	XRF	ICP-MS	XRF	ICP-MS	XRF	ICP-MS	XRF	ICP-MS	XRF	ICP-MS	XRF	ICP-MS	XRF	ICP-MS	XRF	ICP-MS	XRF	ICP-MS	XRF	ICP-MS	XRF	ICP-MS	XRF	ICP-MS	XRF	ICP-MS	XRF	ICP-MS	XRF	ICP-MS	XRF	ICP-MS	XRF
F1B1AE4	11.20	-	56.92	-	26.74	-	10.09	-	16.13	-	36.84	-	63.50	-	70.00	-	68.82	78.79	210.00	225.49	21.21	29.04	142.9	244.08	9.314	13.51	11.96	8.1140	1635	-	61.88	-	22.65	33.20	10.83	13.74	156.4	188.39
F2B2S1	12.60	23.63	57.19	97.85	26.22	116.07	8.623	68.14	16.61	0.004	17.35	61.09	66.70	92.65	4.826	38.00	90.66	80.37	158.2	152.31	20.92	32.43	121.0	421.83	9.038	1.91	1.575	6.6885	611.7	1319.68	55.98	-	17.77	46.31	10.13	12.16	3.543	2.00
F1B1J12	14.47	30.03	61.56	116.07	27.66	128.98	192.7	165.18	84.28	0.014	20.53	71.62	77.00	122.53	518.8	262.15	66.76	125.44	213.6	211.80	30.60	38.53	160.0	338.08	10.29	9.83	6051	398.0716	203.1	384.80	74.59	-	27.10	98.00	11.85	12.84	2046	1886.53
F2B1AE9	15.04	25.62	60.07	103.34	27.79	121.28	11.82	70.30	20.47	0.004	22.11	63.37	77.58	110.76	34.74	50.47	72.96	88.43	220.5	210.45	19.49	29.59	127.4	275.69	9.721	5.25	151.4	19.1101	1472	1172.57	64.64	-	18.61	48.73	12.00	12.89	265.4	285.72
F1B1AE1	14.52	-	56.43	-	26.79	-	8.266	-	15.84	0.004	38.96	-	64.97	-	89.52	-	74.90	83.92	199.0	209.53	21.37	29.09	131.6	262.39	10.02	13.55	2.696	2.8270	747.2	-	65.25	-	23.54	33.71	11.26	13.26	42.99	48.98
F2B1AE3	14.57	-	56.57	-	26.69	-	15.35	-	16.84	0.004	17.19	-	69.44	-	39.77	-	72.86	81.93	202.7	213.45	21.63	29.74	139.1	263.90	9.870	14.14	95.23	54.4594	476.0	-	64.79	-	22.71	34.42	11.08	13.69	205.2	248.30
F4B1AE2	12.65	-	51.17	-	25.23	-	9.826	-	16.09	0.003	13.24	-	57.46	-	59.35	-	61.54	73.64	192.1	209.40	18.85	27.00	131.6	281.33	8.900	13.37	9.057	6.8683	266.8	-	57.15	-	20.50	30.78	9.993	13.46	80.84	104.49
F4B1AE4	13.16	-	55.60	-	26.27	-	11.80	-	15.99	0.004	57.08	-	62.28	-	161.1	-	64.69	75.91	196.3	210.80	19.08	27.63	129.9	270.24	9.473	13.52	5.946	4.9099	813.0	-	53.90	-	28.37	37.65	10.13	12.36	27.34	31.67
F4B1AE5	13.04	23.93	54.53	94.84	26.45	118.21	8.831	66.33	16.23	0.005	73.45	92.87	63.85	98.75	96.88	72.70	69.43	75.58	195.5	183.10	20.61	30.26	130.5	298.29	9.671	2.26	7.815	7.1018	445.0	486.31	64.84	-	25.57	46.86	10.91	11.16	25.33	20.14
F4B1AE1	12.66	37.22	59.86	125.47	25.20	141.00	253.3	209.07	166.4	0.027	87.05	124.69	106.4	165.97	1173	953.51	53.63	262.17	214.7	216.87	35.36	31.44	164.3	434.82	9.250	85.17	1220	116.6647	549.4	718.04	129.2	-	90.71	206.32	10.23	6.43	7943	7569.98
F4B1AE6	11.78	25.81	52.23	95.02	26.81	113.48	19.19	70.38	21.47	0.005	22.15	63.90	67.94	101.79	164.4	101.73	68.18	86.72	228.6	213.19	23.67	30.32	145.0	311.97	9.406	7.72	641.5	56.9586	1022	841.64	57.43	-	25.44	67.76	10.66	11.27	637.4	656.13
F1B1OJ4	7.223	24.54	58.26	95.99	25.38	116.58	10.38	70.25	14.73	0.004	17.05	61.37	57.50	97.55	124.9	71.50	69.68	77.83	194.9	199.59	21.05	31.98	127.9	301.58	9.612	4.26	132.9	17.3673	497.0	512.96	59.06	-	17.00	45.81	11.34	11.81	110.0	150.43
F2B1AE10	6.571	28.86	54.87	104.31	21.79	118.31	14.76	72.93	23.83	0.006	27.40	70.84	47.43	96.26	159.0	119.15	50.80	72.60	220.0	212.22	24.75	31.72	112.2	302.76	8.353	<1	7899	485.5003	674.4	640.51	71.44	-	44.42	85.49	10.12	12.42	535.2	553.49
F4B1AJ1	7.540	25.31	55.20	96.54	26.90	114.70	14.20	66.85	17.76	0.006	30.83	68.41	70.72	103.28	75.00	67.65	71.63	80.59	214.8	198.08	19.81	27.91	133.3	305.80	9.398	5.36	24.26	8.7731	1158	926.88	62.38	-	19.86	48.2798	11.74	11.42	260.8	260.27

Appendix E

E1 LECO analyzer

Table E1: Total carbon % measured by the LECO analyzer for sandstone samples from Rietkuil mine.

Sample name		Mass (g)	% C
F1B1AE1	2019/OB27/18	0,2065	0,32
F1B1AE2	2019/OB27/19	0,2094	0,40
F1B1AE3	2019/OB27/21	0,2036	1,33
F1B1AE4	2019/OB27/17	0,1999	0,45
FB1AE5	2019/OB27/52	0,1985	0,50
F1B1J1	2019/OB27/13	0,2062	1,05
F1B1J2	2019/OB27/14	0,1976	0,60
F1B1OJ1	2019/OB27/16	0,2085	0,37
F1B1OJ3	2019/OB27/20	0,2004	0,38
F1B1OJ4	2019/OB27/15	0,2041	0,34
F2B1AE1	2019/OB27/32	0,2079	1,61
F2B1AE2	2019/OB27/25	0,2046	0,66
F2B1AE3	2019/OB27/23	0,2097	1,27
F2B1AE4	2019/OB27/27	0,1989	0,42
F2B1AE5	2019/OB27/30	0,1972	0,36
F2B1AE6	2019/OB27/26	0,209	0,46
F2B1AE7	2019/OB27/33	0,2096	0,50
F2B1AE8	2019/OB27/29	0,207	0,59
F2B1AE9	2019/OB27/24	0,2029	0,37
F2B1AE10	2019/OB27/22	0,2008	0,42
F2B1AJ1	2019/OB27/28	0,1941	0,64
F2B1AJ2	2019/OB27/31	0,201	0,30
F3B1AE1	2019/OB27/37	0,2022	0,38
F3B1AE2	2019/OB27/36	0,1969	0,57
F3B1AE3	2019/OB27/38	0,2051	0,35
F3B1AE4	2019/OB27/39	0,2055	0,31
F3B1AE5	2019/OB27/41	0,2065	0,29
F3B1AE6	2019/OB27/35	0,2009	0,28
F3B1AE7	2019/OB27/42	0,207	0,58
F3B1AE8	2019/OB27/34	0,2007	0,28
F3B1AE9	2019/OB27/53	0,1987	0,28
F3B1OJ1	2019/OB27/40	0,1995	0,30
F4B1AE1	2019/OB27/48	0,206	0,38
F4B1AE2	2019/OB27/46	0,2056	0,40
F4B1AE3	2019/OB27/44	0,1997	0,35
F4B1AE4	2019/OB27/49	0,2104	0,64
F4B1AE5	2019/OB27/47	0,1984	2,17
F4B1AE6	2019/OB27/51	0,2068	0,23
F4B1AJ1	2019/OB27/50	0,2077	0,52
F4B1J1	2019/OB27/45	0,2061	0,40
F4B1OJ1	2019/OB27/43	0,2032	0,48
F1B2S1	2019/OB27/1	0,2013	0,20
F1B2S2	2019/OB27/2	0,1957	0,20
F1B2S3	2019/OB27/3	0,2015	0,19
F2B2S1	2019/OB27/4	0,199	0,18
F2B2S2	2019/OB27/5	0,2035	0,23
F2B2S3	2019/OB27/6	0,196	0,22
F3B2S1	2019/OB27/7	0,2043	0,24
F3B2S2	2019/OB27/8	0,1973	0,21
F3B2S3	2019/OB27/9	0,2085	0,15
F4B2S1	2019/OB27/10	0,2069	0,24
F4B2S2	2019/OB27/11	0,2073	0,21
F4B2S3	2019/OB27/12	0,1996	0,28

E2 Mebius titration method

Due to space constraints and better control over the samples during the preparation of the samples for titrations the samples were divided into batches. Each batch had its own blanks.

Equations used to calculate the organic carbon content were as follows:

The average for the blank samples were calculated and tabulated.

After the titration the amount of $K_2Cr_2O_7$ that didn't react with the carbon was calculated *i.e.* the excess $K_2Cr_2O_7$:

$$V_{(K_2Cr_2O_7) \text{ unreacted}} = \frac{C(Fe(NH_4)_2(SO_4)_2 \cdot 6H_2O) \times V(Fe(NH_4)_2(SO_4)_2 \cdot 6H_2O)}{C(K_2Cr_2O_7)}$$

Then, the amount of $K_2Cr_2O_7$ that reacted with the carbon was calculated:

$$V_{(K_2Cr_2O_7) \text{ reacted}} = V_{(K_2Cr_2O_7) \text{ blank}} - V_{(K_2Cr_2O_7) \text{ unreacted}}$$

According to Walkley & Black (1934), the equivalent amount of carbon in 1 ml 0.5 N $K_2Cr_2O_7$ is 1.5 mg C.

$$V_{(Carbon)} = 1.5 \times V_{(K_2Cr_2O_7) \text{ reacted}}$$

To calculate the % of carbon in the sample:

$$\%OC = \frac{V_{(Carbon)}}{V_{(original \ sample)} \times 1000} \times 100\%$$

Table E2: Illustrates the % of organic carbon, calculated by the Mebius titration method, in the sandstone samples collected from Rietkuil mine.

Sample	Sample Weight	Titration	Vol K2Cr2O7 unreacted	VBlank- Vx reacted K2Cr2O7	Equivalent mg C in 0,5 N K2Cr2O7	%OC
Batch 1						
Blank unboiled		24,900				
Blank boiled		24,806				
Blank average	0,0000	24,853	9,941	0,000	0,000	0,00
F1B1OJ4	0,5088	20,970	8,388	1,553	2,330	0,46
F1B1OJ4(D)	0,5199	20,722	8,289	1,652	2,479	0,48
F1B1J12	0,5134	22,647	9,059	0,882	1,324	0,26
F1B1J12(D)	0,5108	21,920	8,768	1,173	1,760	0,34
F1B1OJ3	0,5068	23,079	9,232	0,710	1,064	0,21
F1B1OJ3(D)	0,5280	22,599	9,040	0,902	1,352	0,26
F1B1AE2	0,5196	24,088	9,635	0,306	0,459	0,09
F1B1AE2(D)	0,5175	23,070	9,228	0,713	1,070	0,21
F1B1AE3	0,5216	22,839	9,136	0,806	1,208	0,23
F1B1AE3(D)	0,5162	23,610	9,444	0,497	0,746	0,14
Batch 2						
Blank unboiled		25,680				
Blank boiled		25,558				
Blank average	0,0000	25,619	10,248	0,000	0,000	0,00
F1B1OJ1	0,5235	23,367	9,347	0,901	1,351	0,26
F1B1J12(B)	0,5282	22,883	9,153	1,094	1,642	0,31
F1B1J11	0,5063	23,847	9,539	0,709	1,063	0,21
F1B1AE4	0,5158	23,132	9,253	0,995	1,492	0,29
F1B1AE1	0,5276	23,844	9,538	0,710	1,065	0,20
F1B2S1	0,5122	24,083	9,633	0,614	0,922	0,18
F1B2S2	0,5260	24,087	9,635	0,613	0,919	0,17
F1B2S3	0,5266	24,325	9,730	0,518	0,776	0,15
F2B2S1	0,5399	23,949	9,580	0,668	1,002	0,19
F2B2S2	0,5370	24,084	9,634	0,614	0,921	0,17
F2B2S3	0,5041	24,044	9,618	0,630	0,945	0,19
Batch 3						
Blank unboiled		25,303				
Blank boiled		24,581				
Blank average	0,0000	24,892	9,957	0,000	0,000	0,00
F2B1AE10	0,5149	21,930	8,772	1,185	1,777	0,35
F2B1AE3	0,5070	23,962	9,585	0,372	0,558	0,11
F2B1AE9	0,5138	20,033	8,013	1,944	2,915	0,57
F2B1AE2	0,5391	23,848	9,539	0,418	0,626	0,12
F2B1AE6	0,5163	22,164	8,866	1,091	1,637	0,32
F2B1AE4	0,5289	22,357	8,943	1,014	1,521	0,29
F2B1AJ1	0,5183	22,890	9,156	0,801	1,201	0,23
F2B1AE8	0,5180	21,887	8,755	1,202	1,803	0,35
F1B1AE5	0,5373	21,442	8,577	1,380	2,070	0,39
F2B1AE5	0,5125	21,212	8,485	1,472	2,208	0,43
F2B1AJ2	0,5331	22,889	9,156	0,801	1,202	0,23
Batch 4						
Blank unboiled		25,581				
Blank boiled		24,992				
Blank average	0,0000	25,287	10,115	0,000	0,000	0,00
F2B1AE1	0,5249	24,714	9,886	0,229	0,344	0,07
F2B1AE7	0,5056	22,412	8,965	1,150	1,725	0,34
F2B1AE6(B)	0,5368	23,817	9,527	0,588	0,882	0,16
VKK1	0,5233	23,925	9,570	0,545	0,817	0,16
F3B1AE8	0,5036	23,373	9,349	0,766	1,148	0,23
F3B1AE8(B)	0,5278	22,408	8,963	1,152	1,727	0,33
F3B1AE6	0,5187	23,160	9,264	0,851	1,276	0,25
F3B1AE2	0,5063	23,620	9,448	0,667	1,000	0,20
F3B1AE1	0,5101	23,129	9,252	0,863	1,295	0,25
F3B1AE3	0,5133	23,849	9,540	0,575	0,863	0,17
F3B1AE4	0,5349	23,312	9,325	0,790	1,185	0,22
Batch 5						
Blank unboiled		24,807				
Blank boiled		24,585				
Blank average	0,0000	24,696	9,878	0,000	0,000	0,00
F3B1OJ1	0,5190	23,369	9,348	0,531	0,796	0,15
F3B1AE5	0,5153	23,843	9,537	0,341	0,512	0,10
F3B1AE7	0,5067	23,081	9,232	0,646	0,969	0,19
F3B2S1	0,5050	24,568	9,827	0,051	0,077	0,02
F3B2S2	0,5278	24,045	9,618	0,260	0,391	0,07
F3B2S3	0,5202	23,811	9,524	0,354	0,531	0,10
F4B2S1	0,5207	23,609	9,444	0,435	0,652	0,13
F4B2S2	0,5135	23,795	9,518	0,360	0,541	0,11
F4B2S3	0,5339	23,793	9,517	0,361	0,542	0,10
F4B1AE6	0,5055	23,061	9,224	0,654	0,981	0,19
F4B1AJ1	0,5144	22,643	9,057	0,821	1,232	0,24
F4B1AE1	0,5065	22,886	9,154	0,724	1,086	0,21
F4B1AE4	0,5013	23,562	9,425	0,454	0,680	0,14
F4B1AE5	0,5088	22,642	9,057	0,822	1,232	0,24
F4B1AE2	0,5399	22,884	9,154	0,725	1,087	0,20
F4B1J11	0,5430	23,082	9,233	0,646	0,968	0,18
F4B1OJ1	0,5074	22,406	8,962	0,916	1,374	0,27
F4B1AE3	0,5151	22,889	9,156	0,723	1,084	0,21

Appendix F

Pearson correlation coefficient matrix constructed to illustrate relationships between elements hosted in minerals identified in sandstones from Rietkuil mine.

Table F1: Illustrated the 17 samples with complete data sets for all geochemical analyses.

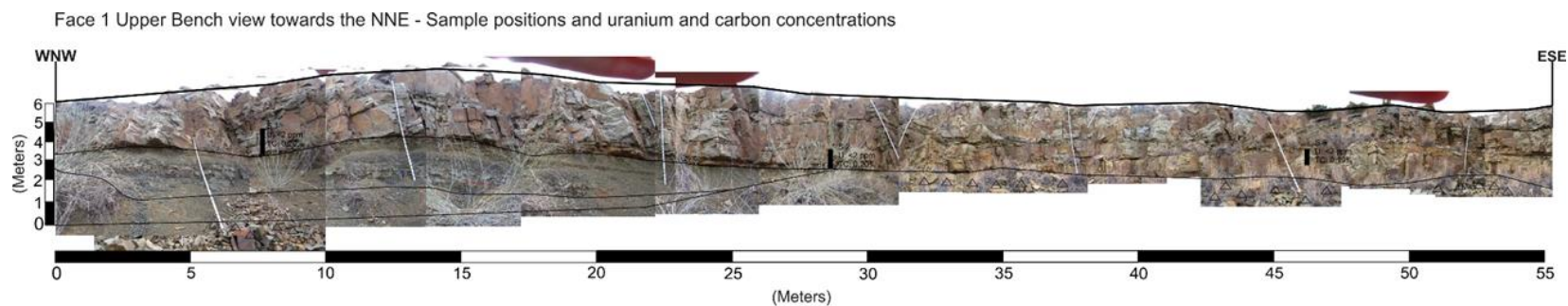
Sample name	SiO ₂ (%)	TiO ₂ (%)	Al ₂ O ₃ (%)	Fe ₂ O ₃ (%)	MgO(%)	MnO(%)	CaO(%)	K ₂ O(%)	P ₂ O ₅ (%)	Na ₂ O(%)	Sc	V	Cr	Co	Ni	Cu	Zn	As	Rb	Sr	Y	Zr	Nb	Mo	Sn	Sb	Ba	Pb	Th	U	%OC	% C
F1B1AE3	71.29	0.54	13.62	3.16	0.87	0.07	1.21	1.88	0.11	2.60	23.70	91.38	111.08	64.62	36.37	81.02	94.15	41.95	73.68	183.64	29.66	290.86	2.00	6.43	1.72	44.11	886.56	46.42	11.49	7.87	0.19	1.33
F1B1AE5	71.13	0.53	13.37	3.05	0.78	0.06	0.86	1.78	0.12	2.79	23.30	90.35	108.39	62.94	34.82	56.38	92.50	100.43	72.96	186.53	27.57	283.68	1.65	81.57	0.58	41.90	364.75	45.72	10.96	188.47	0.39	0.50
F1B1I12	65.49	0.57	14.37	3.16	0.97	0.16	4.08	1.84	0.30	2.25	28.07	108.51	120.58	154.42	107.41	66.95	114.55	245.08	117.27	198.01	36.02	316.06	9.19	372.15	2.37	44.53	359.74	91.62	12.00	1763.67	0.30	0.60
F1B1OJ1	71.72	0.53	13.55	2.86	0.85	0.05	0.97	2.05	0.11	2.57	23.38	90.23	108.63	63.59	36.81	70.00	90.97	38.14	78.45	157.89	29.82	255.60	1.52	6.65	1.95	41.81	545.20	40.60	10.84	3.31	0.26	0.37
F1B1OJ3	71.15	0.53	13.22	3.08	0.84	0.07	1.03	1.70	0.13	2.74	23.75	91.38	107.98	63.52	37.03	56.55	92.81	76.82	67.44	191.00	27.77	278.80	2.53	27.77	3.42	44.08	1088.52	42.67	10.21	122.81	0.23	0.38
F1B1OJ4	70.82	0.55	13.92	3.76	0.76	0.07	0.71	1.90	0.12	2.55	23.47	91.81	111.49	67.18	35.48	58.70	93.29	68.38	74.44	190.89	30.58	288.43	4.08	16.61	3.25	42.00	490.59	43.81	11.29	143.87	0.47	0.34
F2B1AE1	72.36	0.47	12.96	2.42	0.75	0.08	1.32	1.55	0.11	3.11	23.03	85.01	103.12	59.73	34.26	53.66	86.93	41.64	61.58	179.33	23.40	248.14	0.78	10.44	0.32	42.63	1032.26	39.04	9.14	24.96	0.07	1.61
F2B1AE5	69.62	0.59	14.34	3.46	1.09	0.07	0.71	2.04	0.15	2.47	24.39	101.08	115.47	64.08	32.91	56.23	100.21	88.97	89.37	191.72	28.80	300.69	6.08	64.27	2.49	43.51	902.42	43.52	12.00	447.00	0.43	0.36
F2B1AE9	69.10	0.57	14.29	3.56	1.09	0.09	1.28	2.04	0.13	2.31	24.41	98.50	115.59	67.00	40.64	60.40	105.57	48.11	84.29	200.58	28.20	262.77	5.00	18.21	2.08	43.14	1117.58	46.45	12.28	272.32	0.57	0.37
F2B1AJ2	71.89	0.53	13.21	2.64	0.79	0.07	1.09	1.72	0.12	2.93	24.07	89.10	106.92	65.64	36.89	55.50	90.38	63.07	66.89	186.93	28.68	290.18	1.60	11.76	0.01	43.35	942.61	43.00	11.18	32.77	0.23	0.30
F3B1AE3	70.53	0.54	13.37	2.86	0.85	0.07	1.25	1.89	0.12	2.62	23.00	96.69	110.58	61.55	37.58	151.37	95.92	72.33	72.66	177.80	29.27	320.01	2.64	6.57	1.92	43.15	597.20	41.32	11.23	52.49	0.17	0.35
F3B1AE5	72.82	0.51	12.82	3.05	0.84	0.09	1.26	1.63	0.12	2.81	22.96	88.64	108.07	64.02	38.26	227.57	96.10	51.07	66.08	155.35	31.89	289.20	1.90	6.58	2.52	42.58	366.89	44.54	10.66	47.57	0.10	0.29
F4B1AE1	59.78	0.48	12.54	2.20	0.69	0.29	8.84	1.44	0.76	2.41	33.51	112.97	126.96	188.25	196.03	112.27	149.44	858.54	236.06	195.27	28.31	391.51	76.69	105.05	1.11	45.93	646.52	185.77	5.79	6816.01	0.21	0.38
F4B1AE5	70.81	0.54	13.50	3.04	0.94	0.08	1.40	1.85	0.11	2.97	23.17	91.85	114.49	64.24	37.48	89.94	95.64	70.41	73.20	177.33	29.30	288.89	2.19	6.88	1.94	42.22	470.99	45.38	10.81	19.50	0.24	2.17
F4B1AE6	69.90	0.53	13.63	2.72	1.26	0.12	2.15	1.76	0.18	2.63	24.70	90.91	108.58	67.34	41.69	61.14	97.39	97.34	82.98	203.98	29.01	298.49	7.39	54.50	4.49	42.34	805.29	64.83	10.78	627.79	0.19	0.23
F4B1AJ1	70.53	0.55	13.73	2.70	1.57	0.12	2.05	1.91	0.14	2.74	24.27	92.58	109.99	64.10	39.30	65.60	99.04	64.87	77.28	189.95	26.76	293.25	5.14	8.41	0.46	41.99	888.83	46.30	10.95	249.59	0.24	0.52
F4B1OJ1	69.58	0.50	13.58	2.77	0.93	0.12	2.06	1.79	0.15	2.76	24.22	92.41	108.91	70.39	42.95	58.40	104.62	91.06	82.51	189.65	45.65	242.21	8.49	9.17	3.09	42.52	859.29	58.92	8.96	606.03	0.18	0.40

Table F2: Pearson correlation coefficient matrix constructed to view the relationships between the different elements hosted in minerals identified in the sandstone samples from Rietkuil mine. Green=strong positive relationships, Red= strong negative relationships, Black= weak correlations.

	SiO ₂	TiO ₂	Al ₂ O ₃	Fe ₂ O ₃	MgO	MnO	CaO	K ₂ O	P ₂ O ₅	NiO	Na ₂ O	Sc	V	Cr	Co	Ni	Cu	Zn	As	Rb	Sr	Y	Zr	Nb	Mo	Sn	Sb	Ba	Pb	Th	U	%OC	% C
SiO ₂	1	0,0933	0,0520	0,2811	0,0706	-0,9349	-0,9396	0,3074	-0,9488	-0,9295	0,6128	-0,9731	-0,9212	-0,9033	-0,9409	-0,9531	0,0122	-0,9734	-0,9312	-0,9618	-0,4890	-0,1504	-0,7680	-0,9029	-0,5694	-0,0021	-0,7398	0,1256	-0,9522	0,5596	-0,9446	-0,1363	0,1746
TiO ₂	0,0933	1	0,8773	0,7665	0,4738	-0,3190	-0,3644	0,8288	-0,3215	-0,3157	-0,5356	-0,1974	0,2249	0,2292	-0,1734	-0,2944	-0,2362	-0,1686	-0,3519	-0,2461	0,2846	-0,0074	-0,0289	-0,3819	0,2518	0,2350	-0,0910	-0,0208	-0,3337	0,8226	-0,3417	0,7246	-0,1680
Al ₂ O ₃	0,0520	0,8773	1	0,7156	0,4942	-0,2664	-0,3345	0,8279	-0,3335	-0,3133	-0,5502	-0,1811	0,2046	0,1742	-0,1373	-0,2899	-0,4641	-0,1568	-0,3837	-0,2552	0,4197	0,2211	-0,2488	-0,4068	0,3452	0,3160	-0,1614	0,0746	-0,3178	0,7416	-0,3457	0,6953	-0,0993
Fe ₂ O ₃	0,2811	0,7665	0,7156	1	0,0691	-0,4804	-0,5297	0,6696	-0,4523	-0,4658	-0,3960	-0,3891	-0,0227	0,0429	-0,3245	-0,4281	-0,1069	-0,3143	-0,4614	-0,3905	0,1019	0,0985	-0,2661	-0,4713	0,0497	0,4195	-0,2163	-0,1066	-0,4590	0,7296	-0,4571	0,7390	-0,0995
MgO	0,0706	0,4738	0,4942	0,0691	1	-0,0082	-0,1180	0,9834	0,4426	-0,1989	-0,1700	-0,1091	0,0041	-0,0199	-0,1970	-0,2232	-0,2024	-0,0693	-0,2529	-0,1709	0,3325	-0,0278	-0,0948	-0,2094	0,0018	0,1369	-0,2837	0,2678	-0,1843	0,3545	-0,2087	0,1511	-0,1197
MnO	-0,9349	-0,3190	-0,2664	-0,4804	-0,0082	1	0,9834	-0,5251	0,9502	0,9609	-0,4139	0,9547	0,7733	0,7674	0,9142	0,9508	0,1294	0,9542	0,9295	0,9325	0,4019	0,1647	0,7410	0,9163	0,4730	-0,0214	0,6717	-0,1147	0,9679	-0,6971	0,9473	-0,1196	-0,1475
CaO	-0,9396	-0,3644	-0,3345	-0,5297	-0,1180	0,9834	1	-0,5419	0,9780	0,9859	-0,3931	0,9705	0,7755	0,7734	0,9384	0,9826	0,1363	0,9507	0,9652	0,9623	0,3125	0,0966	0,7705	0,9444	0,4674	-0,1077	0,7082	-0,1521	0,9875	-0,7331	0,9746	-0,1560	-0,0976
K ₂ O	0,3074	0,8288	0,8279	0,6696	0,4426	-0,5251	-0,5419	1	-0,5191	-0,5312	-0,3936	-0,4313	-0,0406	-0,0298	-0,4233	-0,5038	-0,2888	-0,3616	-0,5451	-0,4164	0,0123	0,1017	-0,3649	-0,5230	-0,0645	0,2005	-0,3984	0,0333	-0,5266	0,7684	-0,5229	0,6136	-0,1014
P ₂ O ₅	-0,9488	-0,3215	-0,3335	-0,4523	-0,1989	0,9502	0,9780	-0,5191	1	0,9717	-0,4342	0,9782	0,8011	0,8022	0,9247	0,9827	0,1191	0,9566	0,9952	0,9916	0,3187	0,0310	0,8133	0,9803	0,4254	-0,0875	0,7373	-0,1454	0,9931	-0,7324	0,9987	-0,0537	-0,1628
NiO	-0,9295	-0,3157	-0,3133	-0,4658	-0,1700	0,9609	0,9859	-0,5312	0,9717	1	-0,4066	0,9746	0,7866	0,7979	0,9648	0,9913	0,1395	0,9367	0,9603	0,9556	0,2726	0,0798	0,7796	0,9255	0,5195	-0,1388	0,7272	-0,2059	0,9771	-0,6855	0,9650	-0,1120	-0,0916
Na ₂ O	0,6128	-0,5356	-0,5502	-0,3960	-0,1565	-0,4139	-0,3931	-0,3936	-0,4342	-0,4066	1	-0,5283	-0,7744	-0,7201	-0,5371	-0,4648	0,0407	-0,5648	-0,3845	-0,5020	-0,4147	-0,2055	-0,4241	-0,3644	-0,5446	-0,3464	-0,4628	0,1120	-0,4364	-0,1664	-0,4201	-0,5728	0,4784
Sc	-0,9731	-0,1974	-0,1811	-0,3891	-0,1091	0,9547	0,9705	-0,4313	0,9782	0,9746	-0,5283	1	0,8578	0,8421	0,9605	0,9815	0,0170	0,9606	0,9599	0,9749	0,4209	0,0839	0,7833	0,9313	0,5504	-0,0760	0,7726	-0,1022	0,9794	-0,6236	0,7221	0,0239	-0,1895
V	-0,9212	0,2249	0,2046	-0,0227	0,0041	0,7733	0,7755	-0,0406	0,8011	0,7866	-0,7744	0,8578	1	0,9498	0,8630	0,8276	0,0451	0,8818	0,7765	0,8368	0,4515	0,1655	0,7511	0,7282	0,6624	0,0480	0,7462	-0,1655	0,7910	-0,2589	0,7891	0,3006	-0,2353
Cr	-0,9033	0,2292	0,1742	0,0429	-0,0199	0,7674	0,7734	-0,0298	0,8022	0,7979	-0,7201	0,8421	0,9498	1	0,8410	0,8236	0,0758	0,8842	0,7851	0,8471	0,3902	0,1233	0,7546	0,7508	0,5644	0,0466	0,6853	-0,2413	0,7976	-0,2707	0,7931	0,3473	-0,0658
Co	-0,9409	-0,1734	-0,1373	-0,3245	-0,1970	0,9142	0,9384	-0,4233	0,9247	0,9648	-0,5371	0,9605	0,8630	0,8410	1	0,9736	0,0823	0,9115	0,9062	0,9152	0,3304	0,1640	0,7524	0,8387	0,7064	-0,0708	0,7571	-0,2780	0,9375	-0,5376	0,9122	-0,0101	-0,1219
Ni	-0,9531	-0,2944	-0,2899	-0,4281	-0,2232	0,9508	0,9826	-0,5038	0,9827	0,9913	-0,4648	0,9815	0,8276	0,8236	0,9736	1	0,1363	0,9510	0,9739	0,9724	0,2896	0,0796	0,7942	0,9358	0,5384	-0,1151	0,7573	-0,2138	0,9847	-0,6748	0,9770	-0,0644	-0,1232
Cu	0,0122	-0,2362	-0,4641	-0,1069	-0,2024	0,1294	0,1363	-0,2888	0,1191	0,1395	0,0407	0,0170	0,0451	0,0758	0,0823	0,1363	1	0,1434	0,1326	0,0942	-0,5969	0,0528	0,3231	0,1364	-0,1203	0,0481	0,0895	-0,4580	0,1151	-0,1339	0,1147	-0,4190	-0,0904
Zn	-0,9734	-0,1686	-0,1568	-0,3143	-0,0693	0,9542	0,9507	-0,3616	0,9566	0,9367	-0,5648	0,9606	0,8818	0,8842	0,9115	0,9510	0,1434	1	0,9414	0,9696	0,3771	0,1861	0,7583	0,9356	0,4547	-0,0153	0,7242	-0,1237	0,9588	-0,6229	0,9578	0,0716	-0,1993
As	-0,9312	-0,3519	-0,3837	-0,4614	-0,2529	0,9295	0,9652	-0,5451	0,9952	0,9603	-0,3845	0,9599	0,7765	0,7851	0,9062	0,9739	0,1326	0,9414	1	0,9852	0,2870	0,0068	0,8195	0,9837	0,3890	-0,1293	0,7231	-0,1708	0,9845	-0,7563	0,9959	-0,0580	-0,1408
Rb	-0,9618	-0,2461	-0,2552	-0,3905	-0,1709	0,9325	0,9623	-0,4164	0,9916	0,9556	-0,5020	0,9749	0,8368	0,8471	0,9152	0,9724	0,0942	0,9696	0,9852	1	0,3188	0,0483	0,7993	0,9774	0,4158	-0,0839	0,7208	-0,1472	0,9822	-0,6897	0,9922	0,0301	-0,1677
Sr	-0,4890	0,2846	0,4197	0,1019	0,3325	0,4019	0,3125	0,0123	0,3187	0,2726	-0,4147	0,4209	0,4515	0,3902	0,3304	0,2896	-0,5969	0,3771	0,2870	0,3188	1	0,0432	0,2631	0,2772	0,3778	0,2010	0,3609	0,3917	0,3388	-0,0069	0,3130	0,4400	-0,1832
Y	-0,1504	-0,0074	0,2211	0,0985	-0,0278	0,1647	0,0966	0,1017	0,0310	0,0798	-0,2055	0,0839	0,1655	0,1233	0,1640	0,0796	0,0528	0,1861	0,0068	0,0483	0,0432	1	-0,1743	-0,0022	0,2437	0,4160	0,0101	-0,2160	0,1014	-0,0575	0,0386	-0,0575	-0,2108
Zr	-0,7680	-0,0289	-0,2488	-0,2661	-0,0948	0,7410	0,7705	-0,3649	0,8133	0,7796	-0,4241	0,7833	0,7511	0,7546	0,7524	0,7942	0,3231	0,7583	0,8195	0,7993	0,2631	-0,1743	1	0,7788	0,3931	-0,0817	0,6844	-0,3014	0,7909	-0,3991	0,7951	-0,0300	-0,1767
Nb	-0,9029	-0,3819	-0,4068	-0,4713	-0,2094	0,9163	0,9444	-0,5230	0,9803	0,9255	-0,3644	0,9313	0,7282	0,7508	0,8387	0,9358	0,1364	0,9356	0,9837	0,9774	0,2772	-0,0022	0,7788	1	0,2446	-0,1081	0,6820	-0,0755	0,9648	-0,7952	0,9868	-0,0558	-0,1588
Mo	-0,5694	0,2518	0,3452	0,0497	0,0018	0,4730	0,4674	-0,0645	0,4254	0,5195	-0,5446	0,5504	0,6624	0,5644	0,7064	0,5384	-0,1203	0,4547	0,3890	0,4158	0,3778	0,2437	0,3931	0,2446	1	0,0726	0,4661	-0,3833	0,4618	0,0698	0,3961	0,1549	-0,1054
Sn	-0,0021	0,2350	0,3160	0,4195	0,1369	-0,0214	-0,1077	0,2005	-0,0875	-0,1388	-0,3464	-0,0760	0,0480	0,0466	-0,0708	-0,1151	0,0481	-0,0153	-0,1293	-0,0839	0,2010	0,4160	-0,0817	-0,1081	0,0726	1	-0,0491	-0,0518	-0,0503	0,1534	-0,0987	0,1279	-0,2792
Sb	-0,7398	-0,0910	-0,1614	-0,2163	-0,2837	0,6717	0,7082	-0,3984	0,7373	0,7272	-0,4628	0,7726	0,7462	0,6853	0,7571	0,7573	0,0895	0,7242	0,7231	0,7208	0,3609	0,0101	0,6844	0,6820	0,4661	-0,0491	1	0,1671	0,7218	-0,3995	0,7237	-0,0699	-0,0802
Ba	0,1256	-0,0208	0,0746	-0,1066	0,2678	-0,1147	-0,1521	0,0333	-0,1454	-0,2059	0,1120	-0,1022	-0,1655	-0,2413	-0,2780	-0,2138	-0,4580	-0,1237	-0,1708	-0,1472	0,3917	-0,2160	-0,3014	-0,0755	-0,3833	-0,0518	0,1671	1	-0,1750	-0,0290	-0,1331	0,0209	-0,0089
Pb	-0,9522	-0,3337	-0,3178	-0,4590	-0,1843	0,9679	0,9875	-0,5266	0,9931	0,9771	-0,4364	0,9794	0,7910	0,7976	0,9375	0,9847	0,1151	0,9588	0,9842	0,9822	0,3388	0,1014	0,7909	0,9648	0,4618	-0,0503	0,7218	-0,1750	1	-0,7254	0,9910	-0,0774	-0,1467
Th	0,5596	0,8226	0,7416	0,7296	0,3545	-0,6971	-0,7331	0,7684	-0,7324	-0,6855	-0,1664	-0,6236	-0,2589	-0,2707	-0,5376	-0,6748	-0,1339	-0,6229	-0,7563	-0,6897	-0,0069	-0,0575	-0,3991	-0,7952	0,0698	0,1534	-0,3995	-0,0290	-0,7254	1	-0,7525	0,4588	-0,0367
U	-0,9446	-0,3417	-0,3457	-0,4571	-0,2087	0,9473	0,9746	-0,5229	0,9987	0,9650	-0,4201	0,9721	0,7891	0,7931	0,9122	0,9770	0,1147	0,9578	0,9959	0,9922	0,3130	0,0386	0,7951	0,9868	0,3961	-0,0987	0,7237	-0,1331	0,9910	-0,7525	1	-0,0489	-0,1598
%OC	-0,1363	0,7246	0,6953	0,7390	0,1511	-0,1196	-0,1560	0,6136	-0,0537	-0,1120	-0,5728	0,0239	0,3006	0,3473	-0,0101	-0,0644	-0,4190	0,0716	-0,0580	0,0301	0,4400	-0,0575	-0,0300	-0,0558	0,1549	0,1279	-0,0699	0,0209	-0,0774	0,4588	-0,0489	1	-0,2724
% C	0,1746	-0,1680	-0,0993	-0,0995	-0,1197	-0,1475	-0,097																										

Appendix G

Shows the uranium and carbon results obtained from the XRF and LECO analyzer, respectively, in the upper bench on Face 1,2,3, and 4. The results are displayed on photo panoramas illustrating the sampling position see Figure G1 to Figure G4.



LEGEND		LEGEND	
Symbol	Discription	Carbon Samples	
	Contact		Sample number
	Upper most contact of a bench		U: uranium concentration in ppm, measured with the XRF
	Rubble		TC: Total carbon (%) measured with the LECO

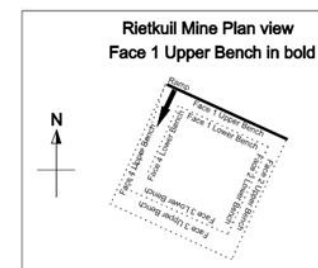
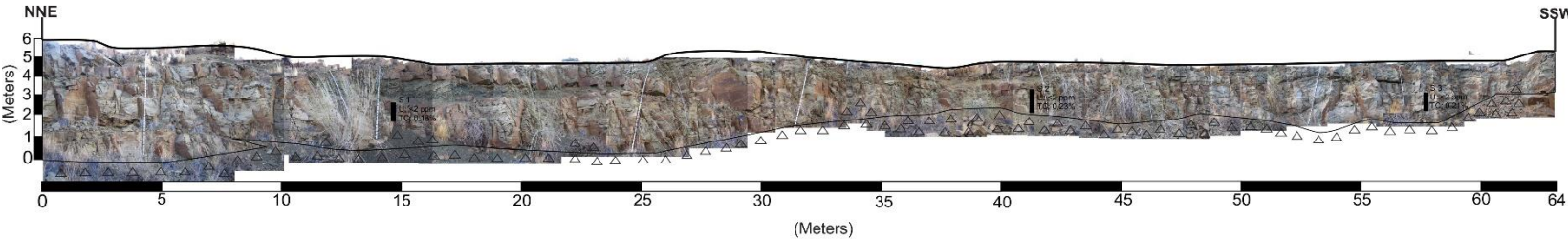


Figure G1: Represent the uranium and carbon concentrations in Face 1 Upper Bench measured with the XRF and LECO analyzer, respectively. Shows a photo-panorama of Face 1 shows sample collection localities.

Face 2 Upper Bench view towards the ESE - Sample positions and uranium and carbon concentrations



LEGEND		LEGEND	
Symbol	Discription	Carbon Samples	
	Contact	<div>Sample number</div> <div>U: uranium concentration in ppm, measured with the XRF</div> <div>TC: Total carbon (%) measured with the LECO</div>	
	Upper most contact of a bench		
	Rubble		

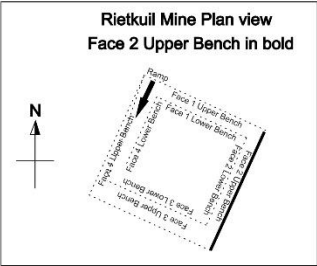
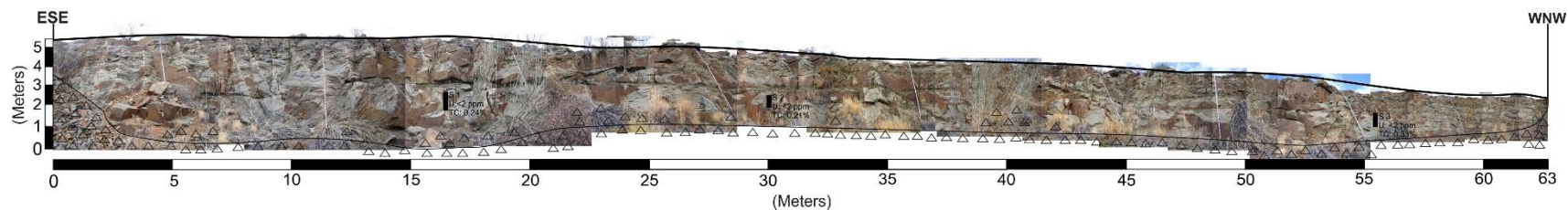


Figure G2: Represent the uranium and carbon concentrations in Face 2 Upper Bench measured with the XRF and LECO analyzer, respectively. Shows a photo-panorama of Face 2 shows sample collection localities.

Face 3 Upper Bench view towards the SSW - Sample positions and uranium and carbon concentrations



LEGEND		LEGEND	
Symbol	Discription	Carbon Samples	
	Contact	Sample number	
	Upper most contact of bench	U: uranium concentration in ppm, measured with the XRF	
	Rubble	TC: Total carbon (%) measured with the LECO	

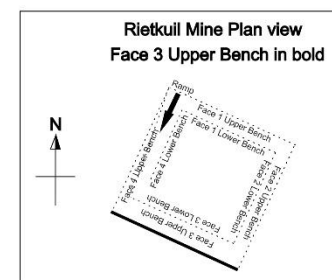
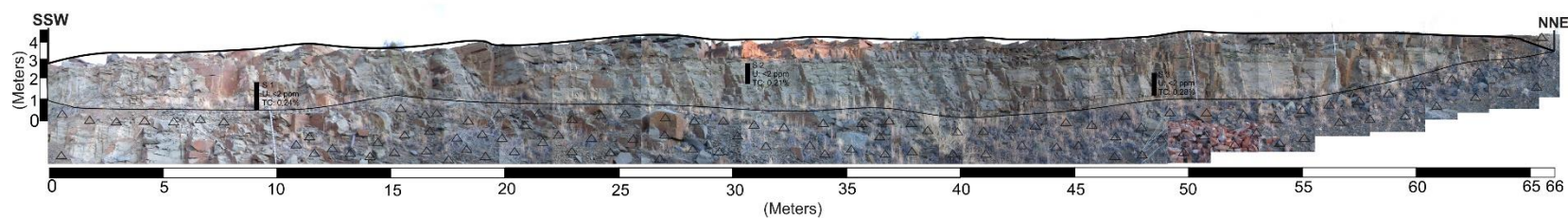


Figure G3: Represent the uranium and carbon concentrations in Face 3 Upper Bench measured with the XRF and LECO analyzer, respectively. Shows a photo-panorama of Face 3 shows sample collection localities.

Face 4 Upper Bench view towards the WNW - Sample positions and uranium and carbon concentrations



LEGEND		LEGEND	
Symbol	Discription	Carbon Samples	
	Contact	Sample number U: uranium concentration in ppm, measured with the XRF TC: Total carbon (%) measured with the LECO	
	Upper most contact of bench		
	Rubble		

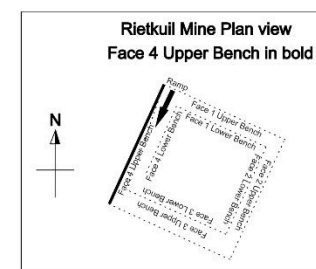


Figure G4: Represent the uranium and carbon concentrations in Face 4 Upper Bench measured with the XRF and LECO analyzer, respectively. Shows a photo-panorama of Face 4 shows sample collection localities.